JAEA-Technology
2019-023
DOI:10.11484/jaea-technology-2019-023

Final Report on Feasibility Study of Pu Monitoring and Solution Measurement of High Active Liquid Waste containing Fission Product at Reprocessing Facility

Megumi SEKINE, Takuya MATSUKI, Satoshi SUZUKI, Koichi TSUTAGI
Naoki NISHIDA, Takahiko KITAO, Hirofumi TOMIKAWA, Hironobu NAKAMURA
Adrienne LaFleur and Michael Browne

Integrated Support Center for Nuclear Nonproliferation and Nuclear Security

March 2020
Japan Atomic Energy Agency
日本原子力研究開発機構

JAEA-Technology

本レポートは国立研究開発法人日本原子力研究開発機構が不定期に発行する成果報告書です。
本レポートの入手並びに著作権利用に関するお問い合わせは、下記あてにお問い合わせ下さい。
なお、本レポートの全文は日本原子力研究開発機構ホームページ（https://www.jaea.go.jp）
より発信されています。

国立研究開発法人日本原子力研究開発機構 研究連携成果展開部 研究成果管理課
〒319-1195 茨城県那珂郡東海村大字白方 2 番地4
電話 029-282-6387, Fax 029-282-5920, E-mail:ird-support@jaea.go.jp

This report is issued irregularly by Japan Atomic Energy Agency.
Inquiries about availability and/or copyright of this report should be addressed to
Institutional Repository Section,
Intellectual Resources Management and R&D Collaboration Department,
Japan Atomic Energy Agency.
2-4 Shirakata, Tokai-mura, Naka-gun, Ibaraki-ken 319-1195 Japan
Tel +81-29-282-6387, Fax +81-29-282-5920, E-mail:ird-support@jaea.go.jp

JAEA-Technology 2019-023

Final Report on Feasibility Study of Pu Monitoring and Solution Measurement of High Active Liquid Waste containing Fission Product at Reprocessing Facility

Megumi SEKINE, Takuya MATSUKI[+1], Satoshi SUZUKI[*1], Koichi TSUTAGI[+1],
Naoki NISHIDA[+1], Takahiko KITAO[+2], Hirofumi TOMIKAWA, Hironobu NAKAMURA[+3]
Adrienne LaFleur[*2] and Michael Browne[*2]

Integrated Support Center for Nuclear Nonproliferation and Nuclear Security
Japan Atomic Energy Agency
Tokai-mura, Naka-gun, Ibaraki-ken

(Received December 25, 2019)

The International Atomic Energy Agency (IAEA) has proposed in its Research and Development plan (STR-385), the development of technology to enable real-time flow measurement of nuclear material as a part of an advanced approach to effective and efficient safeguards for reprocessing facilities. To address this, Japan Atomic Energy Agency (JAEA) has been tackling development of a new detector to enable monitoring of Pu in solutions with numerous FPs as a joint research program with U.S. DOE to cover whole reprocessing process. In this study, High Active Liquid Waste (HALW) Storage Facility in Tokai Reprocessing Plant was used as the test field.

At first, the design information of HALW storage tank and radiation (type and intensity) were investigated to develop a Monte Carlo N-Particle Transport Code (MCNP) model. And then, dose rate distribution outside / inside of the concrete cell where the HALW tank is located was measured to design new detectors and check MCNP model applicability.

Using the newly designed detectors, gamma rays and neutron were continuously measured at the outside / inside of the concrete cell to assess the radiation characteristics and to optimize detector position.

Finally, the applicability for Pu monitoring technology was evaluated based on the simulation results and gamma-ray/neutron measurement results. We have found that there is possibility to monitor the change of Pu amount in solution by combination both of gamma-ray and neutron measurement. The results of this study suggested the applicability and capability of the Pu motoring to enhance safeguards for entire reprocessing facility which handles Pu with FP as a feasibility study. This is final report of this project.

Keywords: Pu Monitoring, High Active Liquid Waste, Reprocessing, Fission Product, Gamma-ray, Neutron

This project was carried out under the support of the Ministry of Education, Culture, Sports, Science and Technology (MEXT) in Japan.

+1 Facility Management Department, TRP Decommissioning Center, Nuclear Fuel Cycle Engineering Laboratories, Sector of Nuclear Fuel, Decommissioning and Waste Management
+2 Technology Development Department, TRP Decommissioning Center, Nuclear Fuel Cycle Engineering Laboratories, Sector of Nuclear Fuel, Decommissioning and Waste Management
+3 Safety and Nuclear Security Administration Department
*1 E&E Techno Service Co., Ltd.
*2 Los Alamos National Laboratory

JAEA-Technology 2019-023

再処理施設における核分裂生成物を含む高放射性溶液中のプルトニウムモニタリング及び溶液測定のフィジビリティスタディに関する最終報告書

日本原子力研究開発機構　核不拡散・核セキュリティ総合支援センター
関根　恵、松木　拓也[+1]、鈴木　敏[*1]、蔦木　浩一[+1]、
西田　直樹[+1]、北尾　貴彦[+2]、富川　裕文、中村　仁宣[+3]
Adrienne LaFleur[*2]、Michael Browne[*2]

（2019 年 12 月 25 日受理）

国際原子力機関 (IAEA) は、再処理施設の保障措置をより効果的・効率的に実施するための手法として、再処理施設全体の核物質の動きをリアルタイムに監視する測定技術開発の必要性を研究開発計画 (STR-385) で技術的課題として掲げている。この課題に対応するため、日本原子力研究開発機構 (JAEA) では、再処理施設の入量計量槽を含め FP 及びマイナーアクチニド (MA) 存在下においても Pu 量のモニタリングが可能な検出器の技術開発を、2015 年から 3 年間の計画で、東海再処理施設の高放射性廃液貯蔵場にて日米共同研究として実施した。

まず、MCNP シミュレーションモデルを作成するためにサンプリングによる高放射性廃液 (HALW) 組成・放射線調査及び HALW 貯槽の設計情報の調査を実施し、シミュレーションモデルを作成した。一方、検出器設計とこのモデルの妥当性を確認するため、コンクリートセル壁内外における線量率分布測定を実施した。さらに、新しく設計された検出器を使用して、コンクリートセル内外においてガンマ線と中性子線を連続的に測定し、放射線特性を把握するとともに検出器の設置位置を最適化した。

最後に、シミュレーション結果とガンマ線及び中性子線測定結果に基づいて、Pu モニタリング技術への適用性を評価した。その結果、ガンマ線測定と中性子線測定の両方を組み合わせることで、溶液中の Pu 量の変化を監視できる可能性があることが分かった。この研究において、FP を含む Pu を扱う再処理工程全体の保障措置を強化するための Pu モータリングが適用可能であることが示唆された。本稿は、本プロジェクトの最終報告書である。

本フィジビリティ研究は、文部科学省の核セキュリティ等強化推進補助事業の一環として実施したものである。

原子力科学研究所：〒319-1195　茨城県那珂郡東海村大字白方 2-4
+1　核燃料・バックエンド研究開発部門　核燃料サイクル工学研究所　再処理廃止措置技術開発センター　施設管理部
+2　核燃料・バックエンド研究開発部門　核燃料サイクル工学研究所　再処理廃止措置技術開発センター　技術部
+3　安全・核セキュリティ統括部
*1　株式会社 E&E テクノサービス
*2　ロスアラモス国立研究所

Contents

目次

Table list

Figure list

1. Introduction

1-1. Background and purpose

The International Atomic Energy Agency (IAEA) in its long-term R&D plan has requested to develop technology for real-time flow measurements of nuclear material as a part of an advanced approach to create effective and efficient safeguards for reprocessing facilities [1]. At the Tokai Reprocessing Plant (TRP), Plutonium (Pu) is stored as inventory and retained wastes (Pu containing Fission Products (FP)) in solid and liquid forms.

These plutonium-bearing materials are subject to inspections by IAEA, as well as by the domestic inspectorate and operator for nuclear material accountancy. However, it is very difficult to accurately measure or continuously monitor or verify the Pu content of these materials because they are generally stored in hot concrete cells that consist of thick concrete and other shielding materials. The solution monitoring and measurement system (SMMS), which has been installed for continuous monitoring for reprocessing safeguards, has been developed to monitor density, temperature, and level of solution. To monitor the Pu content of the solution directly. Japan Nuclear Fuel Limited and JAEA developed the Advanced Monitoring and Measurement System (ASMS) by using neutron coincidence counting in cooperation with LANL to monitor pure Pu (no FP) in annular vessels in 2011 [2]. However, for materials that contain Pu, including FP, ASMS cannot be used to monitor Pu owing to the very high dose rate of the highly active liquid (HAL) solution. Pu containing FP has an extremely high radiation dose rate, making it difficult to access, and it is a challenge to develop a technology for monitoring Pu containing FP. Given that the establishment of monitoring technology is important from the viewpoint of increasing effectiveness of safeguards, as the next step, a feasibility study of the applicability of advanced monitoring technology for solutions containing FP and Minor Actinides (MA) that can be applied to the front end (input accountancy tank) and the back end (HAL waste tanks) of the reprocessing process was performed jointly by Japan (Japan Atomic Energy Agency : JAEA) and the U.S. (LANL and Lawrence Livermore National Laboratory (LLNL)) from 2015 to 2017[3]. This project was mainly conducted in the High Active Liquid Waste Storage (HALWS) in TRP.

1-2. Organization

Technology development was carried out as joint research in Project Arrangement (PA NP-06) in 2015 under the “Implementing Arrangement between the Ministry of Education, Culture, Sports, Science and Technology of Japan (MEXT) and the Department of Energy of the United States of America (DOE) Concerning Cooperation in the Field of Nuclear Energy-Related Research and Development” (*Figure 1- 1*).

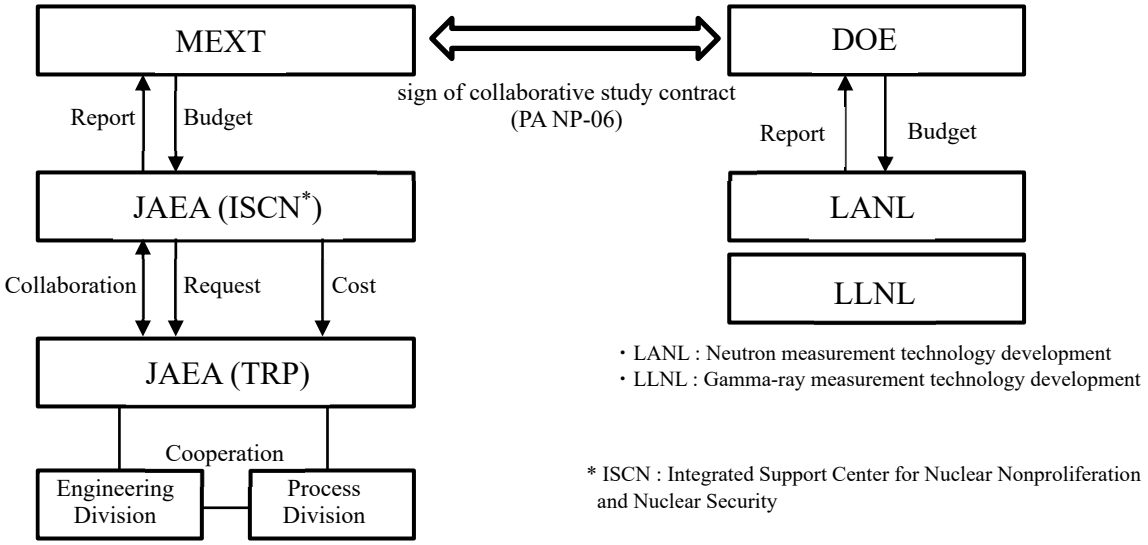

Figure 1- 1 *Organizational diagram for advanced Pu monitoring project*

1-3. Overview and research plan

1-3-1. Flowchart of technology development

A conceptual image of the Pu monitoring technology development process is shown in *Figure 1- 2*. The High Active Liquid Waste (HALW) tank containing a solution with FP and MA is shielded by a concrete cell. Through radiation measurements inside and outside of the concrete cell and Monte Carlo N-Particle Transport Code (MCNP) simulations, a feasibility study was conducted to identify possible solutions and issues for future technology development.

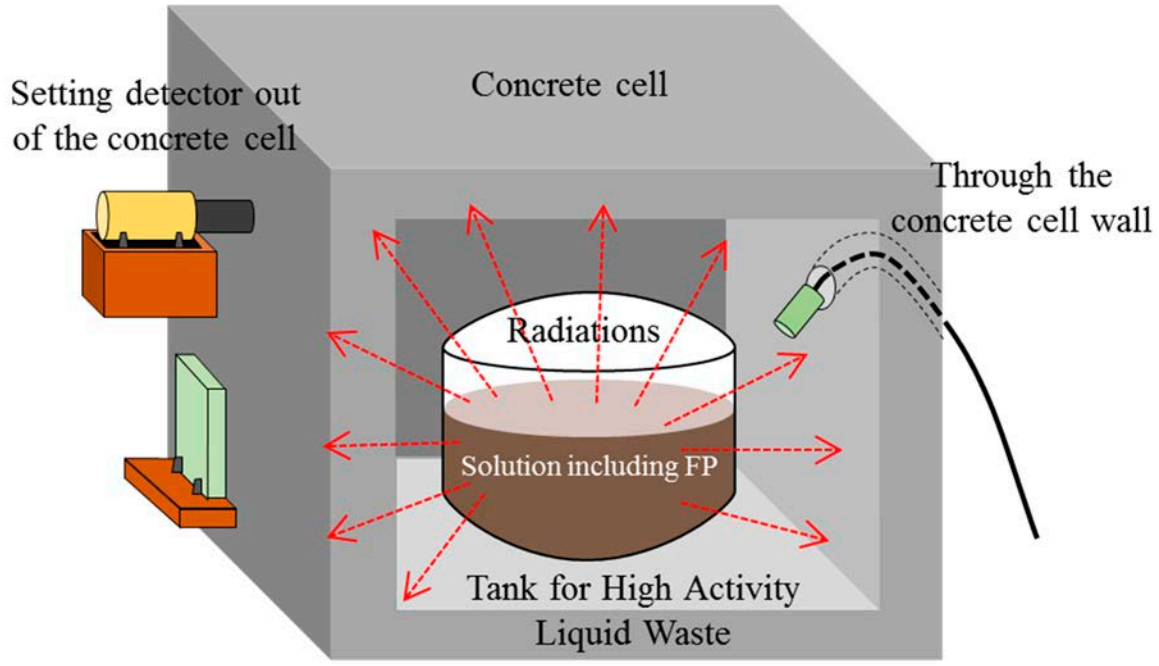

Figure 1- 2 *Conceptual image of technology development*

Figure 1- 3 shows the steps of this technology development process. By performing MCNP simulations and radiation measurements, we evaluated the applicability of the developed Pu monitoring technology.

At first, design information of the HALWS and information about the associated radiation (type and intensity of radiation) were obtained to develop a calculation model by using MCNP.

The chemical components and emitted gamma-rays and neutrons of HALW were analyzed to generate the source input file and create the overall MCNP model.

Gamma-ray count rate measurements were conducted to design detectors for the inside of the concrete cell. The measurement results were used for detector design and checking the applicability of the MCNP model. Gamma rays and neutrons were measured continuously by using the designed detectors both outside and inside the concrete cell in which HALW is located to study detector placement and characteristics of the radiation emitted from the HALW tanks. Gamma-ray spectra of Pu are usually observed in the region from several tens to hundreds of keV, but for the case of Pu solution containing FP, gamma rays from Pu cannot be measured in the region of 0–3 MeV because of Compton scattering caused by the FP. Therefore, to measure gamma-ray spectra, such as those of delayed gamma rays over 3 MeV, which are not affected by gamma-rays with energies less than 3 MeV from FP, the total absorption gamma-ray peaks and the gamma rays induced by the (n, γ) reaction were used as the evaluation indices for Pu monitoring and quantification, as summarized in *Table 1-1*[4,5]. Regarding the evaluation of neutrons, we considered the total neutron emission rate primarily from ^{244}Cm.

By using these results, a MCNP model of the HALW tank was developed, and MCNP benchmark simulations were performed to validate the model. The simulation analysis results and preliminary measurement results obtained outside and inside of the concrete cell were used to evaluate the applicability to use as Pu monitoring technology.

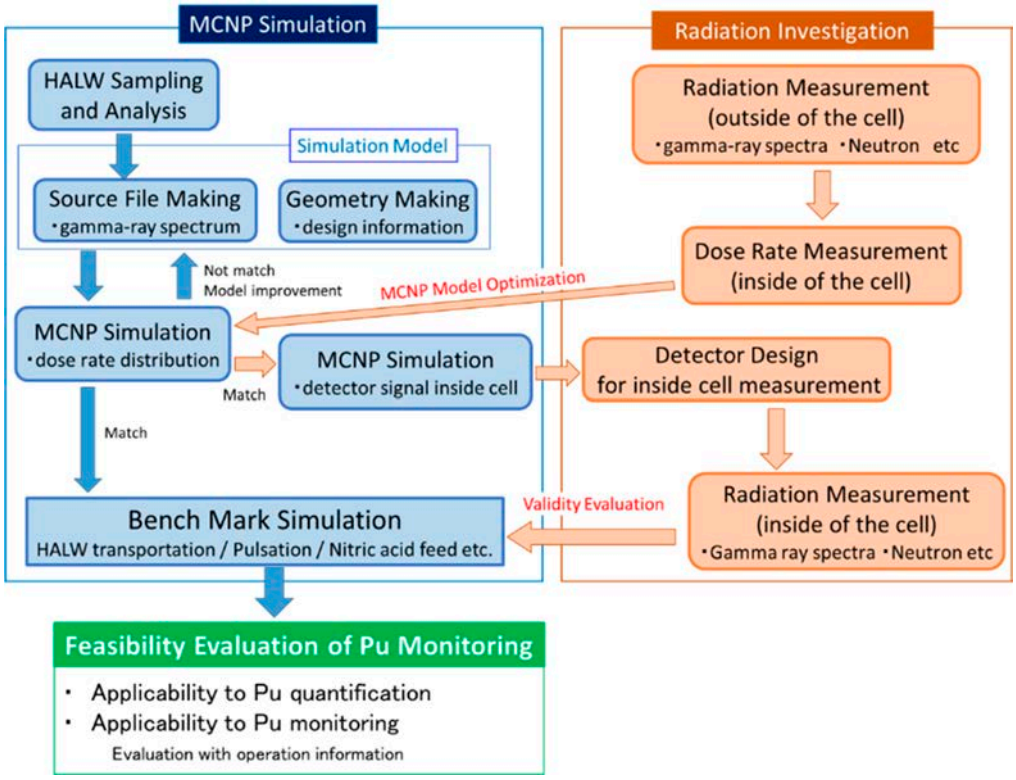

Figure 1- 3 *Steps of this technology development*

Table 1- 1 *Considered and applicable radiations for Pu monitoring technology*

Radiation	Enabled data	Aspects for consideration
Gamma-ray	Energy spectra	Monitoring with delayed gamma rays from Pu fission caused by neutron Isotope ratio with delayed gamma rays from Pu fission caused by neutron
		Monitoring with absorption peak originating from FP Quantification using absorption peak originating from PP and analysis results
		Monitoring using gamma rays originating from (n,γ) reaction
	Gamma-ray count rate	Liquid monitoring based on operational information
Neutron	Neutron count rate	Monitoring based on total neutron number Quantification based on optimized MCNP simulation by using neutron measurement

1-3-2. MCNP and PHITS code

<MCNP code>[6]

MCNP version 6.2 was used to perform both neutron and gamma simulations of the HALW tank

for the ion chamber and the B-10 proportional counter in the holders. MCNP6™ is a general-purpose, continuous-energy, generalized-geometry, time-dependent, Monte Carlo radiation-transport code designed to track many types of particle over broad energy ranges. MCNP 6.2 uses ENDF/B-VII.1 latest cross-section libraries released by the National Nuclear Data Center.

<PHITS code>[7]

PHITS is a Monte Carlo calculation code being developed by JAEA to simulate various radiation behaviors in all substances by using a nuclear reaction model and nuclear data. It is being developed by referring to NMTC, MCNP, and EGS codes among others, and the nuclear data are taken from the JENDL library. JAEA conducted simulation by using the PHITS code.

1-3-3. Experimental locations

The facilities of National Institute for Quantum and Radiological Science and Technology (QST) and National Institute of Standards and Technology (NIST) were used to develop the Pu monitoring technology. Overviews of each of the facilities and their roles in this project are described below.

(1) JAEA (Nuclear Fuel Cycle Engineering Laboratories : NCL, HALWS)

TRP, one of facilities operated by NCL, is the first reprocessing plant in Japan, and it is located in Tokai village of Ibaraki prefecture. The plant commenced hot operations that use spent fuels in 1977. The amount of U reprocessed with LWR and FUGEN (Advanced Thermal Reactor) spent fuels stood at 1,140 tons as of August 2007 (*Figure 1- 4*). Thereafter, TRP was shifted to the decommissioning phase in 2014. The decommissioning plan applied in 2017 was approved on June 2018. In the future, we will advance TRP decommission for about 70 years in accordance with the applied decommissioning plan.

Figure 1- 4 *TRP*

Figure 1- 5 shows a schematic drawing of the reprocessing process at TRP. In TRP, Pu and U are extracted using the PUREX process from the dissolved solution after shearing and dissolution of the spent fuel. The waste liquid remaining after extraction is evaporated and concentrated in an evaporator, and it is called HALW. Thereafter, HALW is stored in HAW tanks. Approximately 340 m^3 of HALW was stored in 6 HAW tanks (including one spare) at HALWS as of Nov 2017. This HALW will be vitrified for 12.5 years from August 2016.

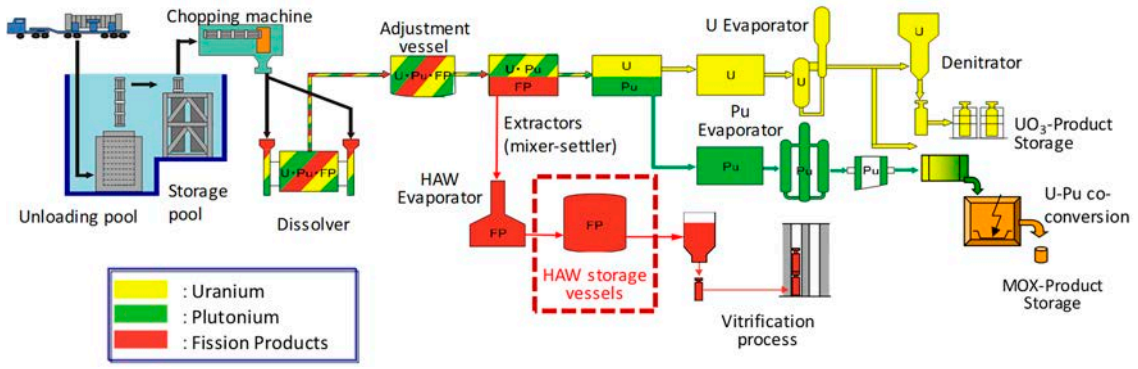

Figure 1- 5 *Schematic drawing of reprocessing process at TRP*

The main process of TRP is important for safeguarding (SG) nuclear material because Pu and U are separated by dissolution through the extraction and refinement of spent fuel during reprocessing. Research on the main process before the extraction of Pu and U is difficult because TRP operation has been completed (i.e., there is no HAL in the input accountability tank). Then, in the request of the future application for the process that is relatively high of Pu concentration of input accountability tank, we selected HALW as measurement target of the research for NP-06 although the Pu concentration is relatively low.

One of the HAW tanks was selected as the target tank from the six available tanks to investigate the feasibility of Pu monitoring in HALW, composition analysis of HALW, and developing the simulation model.

(2) JAEA (Nuclear Science Research Institute, Mock-up facility)

This facility is used as a warehouse in a non-radiation-controlled area. We built rails of actual size (about 6 m in height) and secured the working space because it is a warehouse with height and area. We set up the mock-up equipment and performed experiments in this area. As a result, we could perform the mock-up test with fewer requirements compared to those if the test were performed in a radiation area.

(3) JAEA (Nuclear Science Research Institute, Facility of Radiation Standards: FRS)

FRS is mainly used to perform calibration experiments, and it offers the maximum gamma-ray

irradiation in JAEA. We selected FRS to confirm soundness of the radiation measurement system after it was transported from the U.S.

(4) QST (Takasaki Advanced Radiation Research Institute, Co second building, Fifth irradiation room)

The irradiation room in this facility houses a ^{60}Co source (board shape: 2,003 TBq as of Jan. 10th, 2014), this source is mainly used for energy calibration. In this room, we confirmed the linearity of the calibration formula in the high dose rate range and checked operational ability of the detector (IC: Ionization Chamber) because it was calibrated in and transported from the U.S.

(5) LANL

Both the ion chamber and the B-10 proportional counter were calibrated at LANL by using multiple facilities with different neutron and gamma sources available. The primary calibration facility was the LANL Radiation Physics 2 (RP-2) division dosimetry facility, which is dedicated to high-precision measurements of the effects of irradiation on detectors, instruments, and various samples. The facility utilizes well-characterized and precisely known radiation fields (via fixed geometry) produced by individual NIST-certified sealed sources such as ^{137}Cs, ^{57}Co, and ^{60}Co. The setup uses a pneumatic line to transport a selected sealed source to a fixed location in a shielded room. A table with a movable platform that can be and it can be moved over a ~600-cm range (+/- 1-2 mm) holds the instrument/sample to be irradiated. Through combinations of source strengths and table positions, precise dose rates can be achieved. Moreover, we were able to transport a ^{252}Cf source to this facility to calibrate the B-10 proportional counter neutron count rate in a high gamma-radiation background environment.

2. Preliminary survey

2-1. Target tank for experiment

Figure 2- 1 shows floor plan of the HAW tanks at HALWS. TRP houses six HAW tanks (V31 – V36), with one spare tank at HALWS. Approximately 70 m^3 of HALW was stored in each HAW tank, the capacity of which is 120 m^3, and approximately 5 m^3 nitric acid was stored in the spare tank as of Apr. 1, 2015. The acid concentration of HALW ranges from 2–3 mol/L, density is approximately 1,230 g/L, and radioactivity is ~10^{17} Bq.

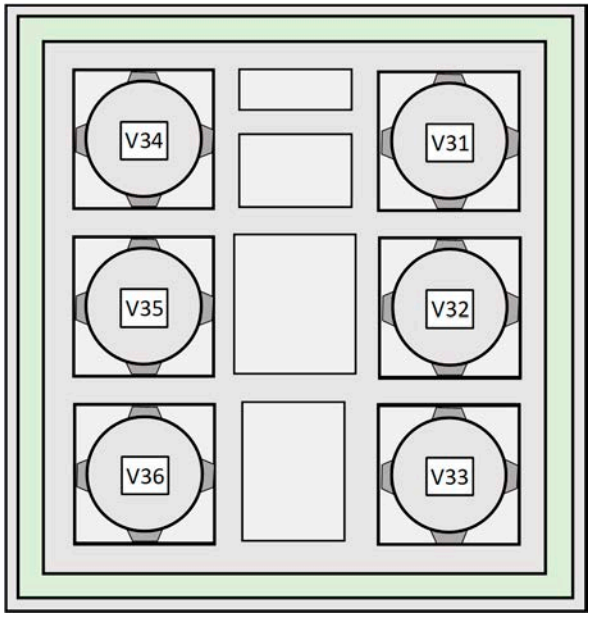

Figure 2- 1 *Floor plan of HAW tanks at HALWS*

In our development plan, after the radiation investigation, which was performed both outside and inside the concrete cell in which the HAW tanks are placed, we evaluated the feasibility of Pu monitoring. Because our first step was radiation investigation outside the thick concreate cell, we selected V35 as the target tank, which has the highest radiation among all tanks at TRP.

However, radiation measurements for another tank were conducted to compare the measurement results, for example, the spare tank or another tank with a radioactivity level different than that of V35.

2-2. Composition analysis of High Active Liquid Waste

2-2-1. About sampling target and method

Composition analysis of the HALW in the target tank was conducted to design the detector for radiation measurement inside the concrete cell and creating the source file for MCNP simulations. *Figure 2- 2* shows the location of the target HAW tank.

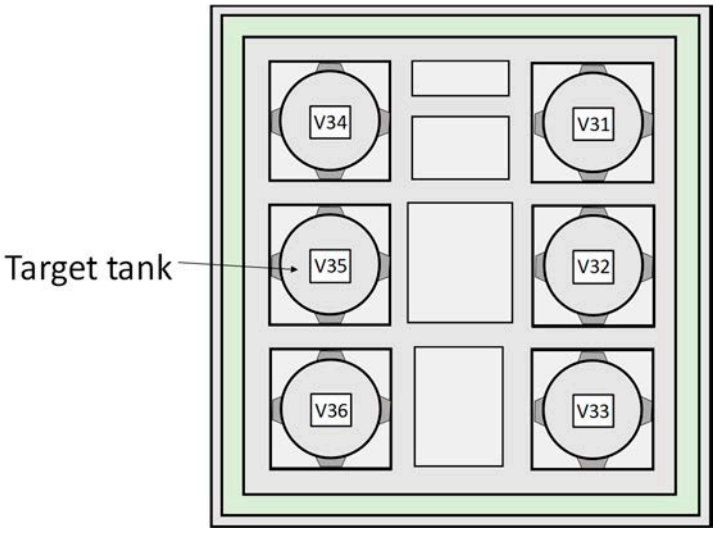

Figure 2- 2 *Location of target HAW tank*

For composition analysis, sampling of the actual HALW and destructive analysis were performed. HALW inside the tank was lifted to the sampling pot in the sampling box by an air lift along the sampling line (bottom), which was installed 500 mm above the bottom of the vessel. *Figure 2- 3* shows the installations inside the HAW tank.

The HALW lifted to the sampling pot was collected in the analysis jug (10 mL), which was maintained under vacuum through the sampling needle (D = 1.2 mm) installed in the sampling pot. *Figure 2- 4* shows an image of the sampling process executed using the sampling pot installed in the sampling box.

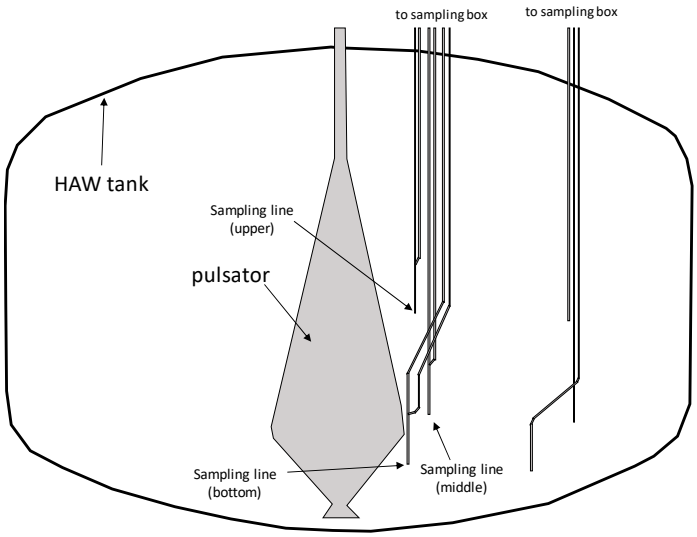

Figure 2- 3 *Installations inside HAW tank*

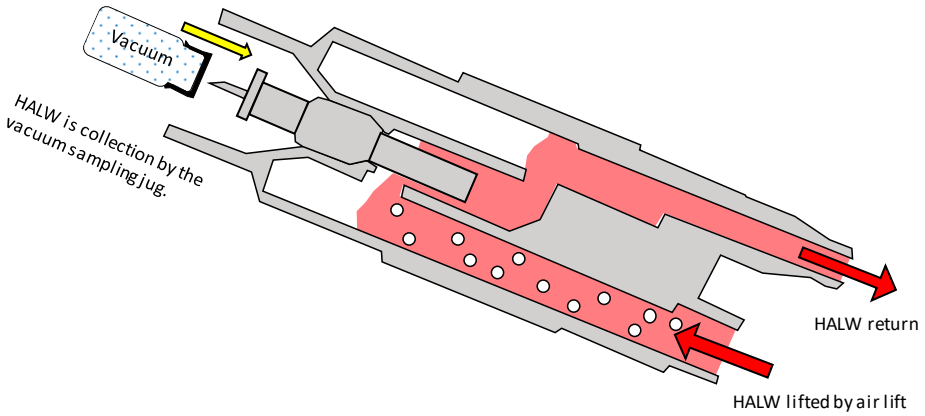

Figure 2- 4 *Sampling executed using sampling pot installed in sampling box*

2-2-2. Sampling of solution and analysis items

Destructive analysis of the HALW sample was conducted. *Table 2- 1* shows the analysis items and the analytical methods employed. The HALW was diluted in a few of the analyses, and sludge dissolution in the sample was conducted as needed.

The entire inventory of the HAW tank was evaluated by multiplying with the liquid volume at the time of sampling.

Table 2- 1 *Analysis item and analytical method (1/2)*

Analytical item	Unit	Methodology
Acid conc.	mol/L	Neutralization titration with NaOH (*Hiranuma COM-1600*)
Density	g/cm^3	Density meter (*Anton-paar DMA-35*) oscillating U-tube type
Cm conc.	Bq/L	*SEIKO EG&G* using detector *"alpha duo"*
Pu conc.	mg/L	Spectrophotometry using cerium nitrate with sludge dissolution by HF
U conc.	g/L	Spectrophotometry (*Shimazu UV-2450*) using TOPO - Ethyl acetate - Dibenzoylmethane (DBM)

Table 2- 1 *Analysis item and analytical method (2/2)*

Gamma measurement	Bq/mL	Canberra using detector *GC-2020*
Pu isotopic composition	wt.%	Mass spectrometer (*Thermo TRITON*) with sludge dissolution by HF, TEVA resin for Pu separation
U isotopic composition	wt.%	Mass spectrometer (*Thermo TRITON*) with sludge dissolution by HF, U-TEVA resin for U separation

2-2-3. Sludge dissolution method

HALW contains undissolved residues, which are assumed to be Zr fines from the cladding tube, which is generated at the time of shearing of spent fuel or sludge generated at the time of evaporate concentration of HALW, of which a major component is zirconium molybdate. Moreover, it is known that Pu and other components are taken up into the sludge during sludge generation.

Therefore, the sludge in the undissolved sample solution as well as that in the dissolved sample solution was analyzed for Pu and Cm.

Figure 2- 5 shows the sludge dissolution method.

To prepare a dissolved sludge sample, the collected sample was heated until the liquid substances in it solidified by means of evaporation after solution (hydrofluoric acid and 8 mol/L nitric acid) dropping on the sample. The solidified liquid substances were then diluted with nitric acid to the same volume as the collected sample. Then, we analyzed Pu and Cm concentrations in the diluted solution after filtering.

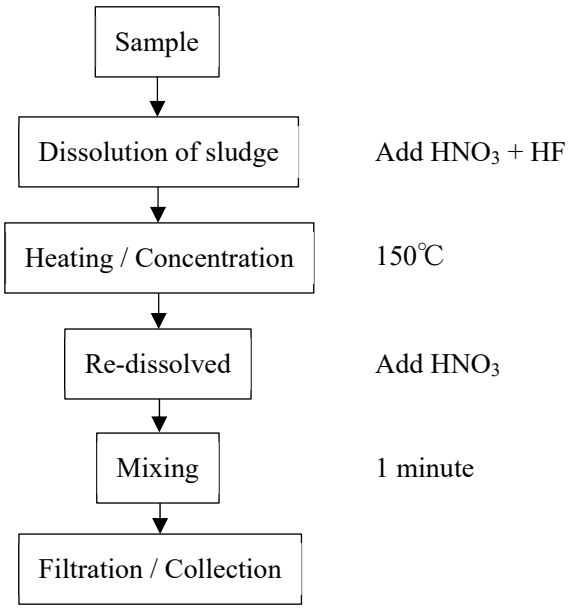

Figure 2- 5 *Sludge dissolution method*

2-2-4. Analysis result

The sampling terms and results of V35, which is the target tank, are as follows (*Table 2-2, 2-3*). The analysis results of the control tank are given in the following chapter.

Sampling date: Dec. 12th, 2017

Volume at the time of sampling: 75.9 m^3

Table 2- 2 *Analysis result*

Analytical item	Unit	Result
Acid conc.	mol/L	2.63
Density	g/cm^3	1.239
Cm conc. *1	Bq/mL	2.5E + 07
Cm conc. *2	Bq/mL	3.7E + 07
Pu conc. *1	mg/L	216
Pu conc. *2	mg/L	326
U conc.	g/L	6.46

All analyses were performed in duplicate (n = 2).

*1: Results from supernatant solution

*2: With sludge dissolution before measurement

Table 2- 3 *Results of gamma-ray spectrometry*

Nuclides	Gamma radiation [Bq/mL]
^{241}Am	7.2E + 07
^{144}Ce	<3.7E + 06
^{137}Cs	2.6E + 09
^{134}Cs	5.1E + 05
^{125}Sb	<3.7E + 06
^{106}Ru	<3.7E + 06
^{103}Ru	<3.7E + 06
^{95}Zr	<3.7E + 05
^{60}Co	<3.7E + 05

Table 2- 4 *Isotopic composition analysis result*

Isotope	Isotopic composition [wt.%]
^{234}U	0.027
^{235}U	1.006
^{236}U	0.313
^{238}U	98.654
^{238}Pu	1.180
^{239}Pu	61.064
^{240}Pu	30.461
^{241}Pu	2.828
^{242}Pu	4.467

All analyses were performed in duplicate (n = 2).

2-2-5. Consideration of measured gamma-ray spectra

Gamma-ray spectrometry was conducted using a software application for specific nuclides, the ORIGEN values and composition of which must be confirmed for safety reasons. In addition, the Cs isotope ratio ($^{137}Cs/^{134}Cs$) was determined to check whether the cooling time is longer than 5.5 years. The results are given in *Table 2- 4*. We conducted further investigation of the raw spectrum to consider the applicability of the spectrum data for our specific purpose. *Figure 2- 6* shows the measured raw gamma-ray spectrum of the diluted HALW sample. The relationship between energy and channel was calibrated using a calculation curve before the measurement. From the spectrum, we evaluated each full peak energy.

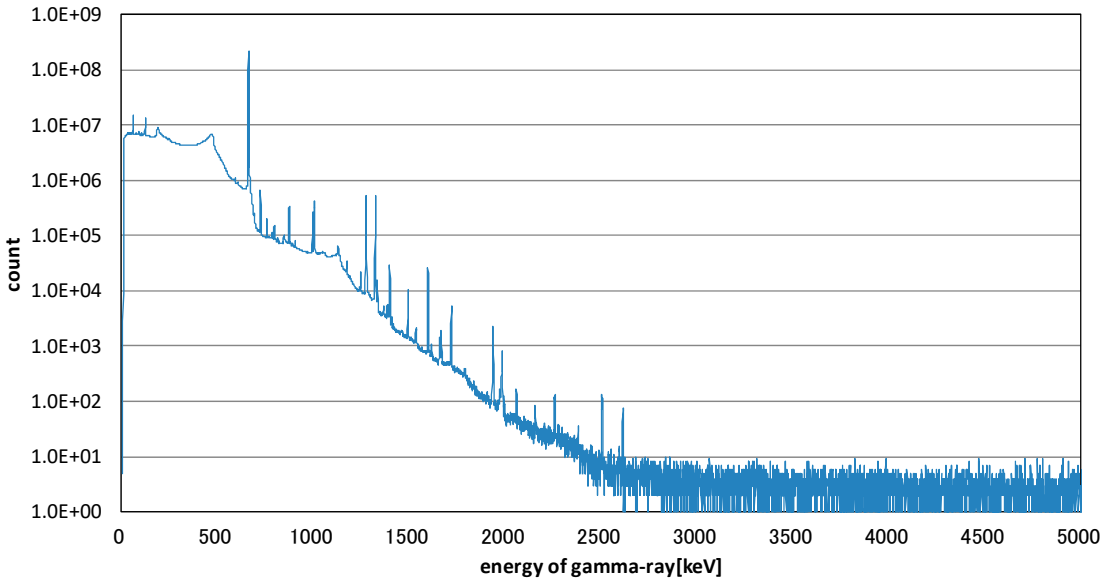

Figure 2- 6 *Gamma-ray spectrum of diluted HALW sample*

Figure 2-7 shows the experimental setup of the gamma-ray spectrometry system. A HPGe [COAXIAL TYPE Ge Detector (GC2020), CANBERRA] and a multi-channel pulse height analyzer (MCA) [DSA1000, CANBERRA] connected to the HPGe were used for gamma-ray spectrometry. The HPGE's relative efficiency was 20% at ^{60}Co 1,332 keV, and the crystal size was ϕ = 61.9 mm and L = 30.8 mm. *Figure 2-8* shows a photograph of the HALW sample bottle and a picture of the experimental setting for gamma-ray measurements. The HPGe detector and the HALW sample were surrounded by Pb to attenuate the background. To reduce dose rate, 1 ml of HALW solution was diluted with nitric acid of the same acid concentration to 10,000 because a very high dose rate increases the dead time in gamma-ray measurements.

Figure 2- 7 *Experimental setup*

Figure 2- 8 *Interior of measurement chamber and sampling bottle*

＜Emitted gamma-ray number evaluation＞

It was necessary to estimate the absolute gamma-ray counts emitted from the HALW sample for using the gamma-ray source data in the MCNP simulations and based on other considerations. The key points considered in preparing the source data are as follows:

(1) Evaluation of gamma-ray energy emitted from HALW sample

(2) Peak count quantity

(3) Estimation of emitted gamma-ray quantity

The peak count was estimated. Then, we calculated the absolute detection efficiency achieved with the employed analysis geometry. As shown in *Figure 2- 9*, each peak spectrum was cut with a straight line in red. The gross counts of each peak were estimated using this original spectrum, as shown in *Figure 2- 10*.

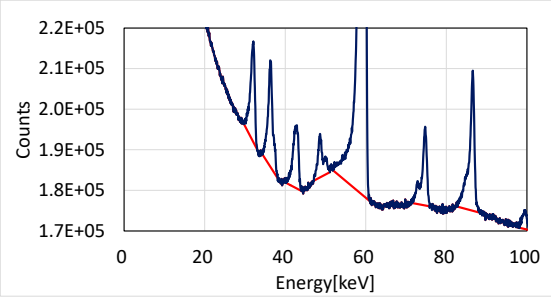

Figure 2- 9 *Cutting spectrum with straight line (gross)*

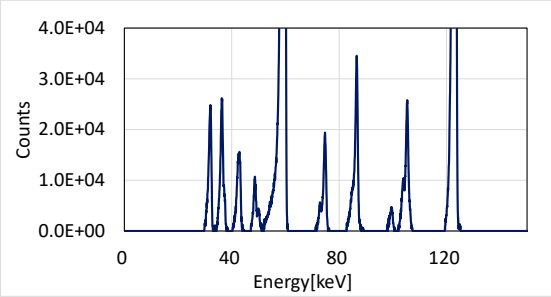

Figure 2- 10 *Net count of each peak*

To determine the effectiveness of the HPGe detector in detecting gamma rays inside the measurement chamber, a model of the measurement chamber was developed, as shown in *Figure 2- 11*. Because the absolute detection efficiency of each peak was different for each gamma-ray energy, we calculated the absolute detection efficiency of each gamma ray for the given analysis geometry by using the PHITS code, as shown in *Figure 2- 12*. The cut off energy was set to 1 keV.

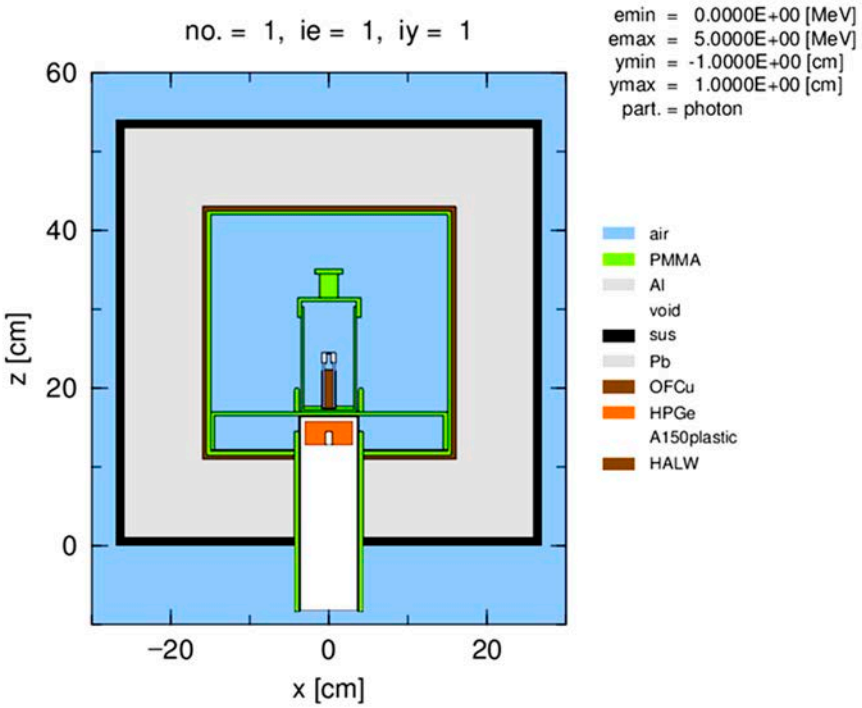

Figure 2- 11 *Model of measurement chamber*

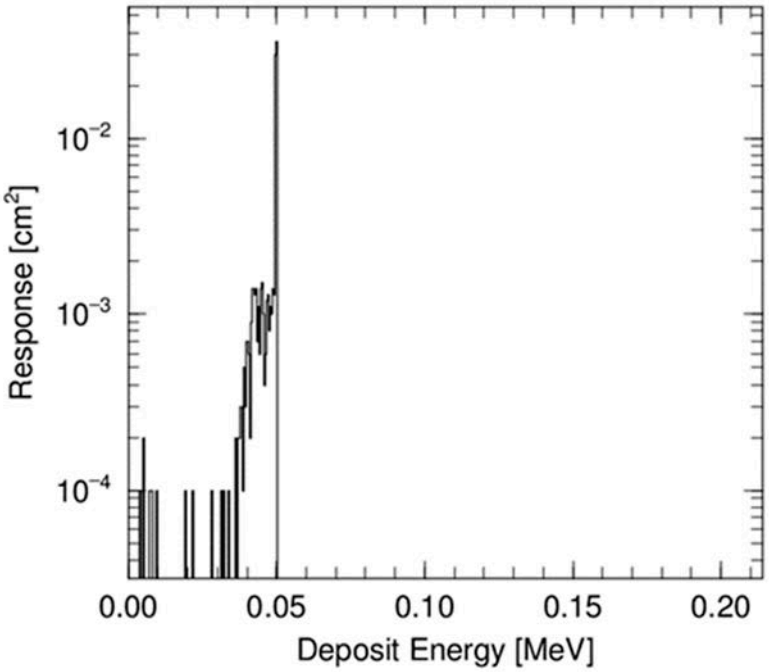

Figure 2- 12 *Example of absolute detection efficiency of 50 [keV]*

The absolute detection efficiency was multiplied by the net counts. Then, the gamma-ray number in V35 tank for each energy was calculated. *Table 2- 5* presents a few examples of the calculation results.

Table 2- 5 *Net counts, absolute detection efficiency, and total gamma-ray number in V35 tank*

Energy [keV]	Net counts from 1 mL HALW [count]	Absolute detection efficiency (PHITS) [deposit/source]	Measurement time [s]	Emitted gamma-ray number (V35) [Bq]
59.54	1.352E + 08	6.084E-02	5.615E + 04	1.85E + 15
123.07	1.120E + 08	5.785E-02	5.615E + 04	1.53E + 15
604.80	6.983E + 06	1.432E-02	5.615E + 04	9.56E + 13
661.66	2.191E + 10	1.343E-02	5.615E + 04	3.00E + 17
795.95	6.794E + 06	1.144E-02	5.615E + 04	9.31E + 13

＜Estimation of gamma-ray emitting nuclides＞

To investigate the nuclides related to each full energy peak, the following items were investigated or calculated.

(1) Nuclides that emit gamma-ray with the same energy as that of the full energy peak (within ± 1 keV) and their branching ratio according to table of isotopes.

(2) Nuclides in HALW and their activities, as calculated using ORIGEN 2.2; these values were estimated using spent fuel data of TRP and liquid transfer record.

We investigated the nuclides common to (1) and (2) and calculated their activities by using ORIGEN 2.2. Then, the nuclide with gamma-ray activity with the order closest to that of the gamma-ray activity evaluated for the previous consideration (evaluation of emitted gamma-ray number) was identified because the nuclides are related to each full energy peak except for the case that the activity difference between calculation and measurement result is more than 100 times.

As a result, in the measured 75 energy peaks within the full energy peak, 46 gamma-ray energy peaks were confirmed to be associated with related nuclides. *Table 2- 6* shows those gamma-ray peaks and the related nuclides. Twenty-four gamma-ray energy peaks were sum peaks of gamma rays, and they were confirmed to be associated with related nuclides. *Table 2- 7* shows those gamma-ray energies and the related gamma-ray energies. Although the other gamma rays which were not matched through (1) and (2) is 5 energy peaks, it is assumed that two of these five gamma-ray energy peaks were derived from ^{60}Co. Because ^{60}Co is not a FP, it was not matched with (1)–(3). It seems that ^{60}Co was generated in the power plant by the neutron capture reaction with the Fe contained in the cladding tube, and it was taken up during shearing of the cladding tube.

Table 2- 8 shows three gamma-ray energy peaks related to Pu. Because the energies of these gamma-ray peaks are relatively low, it may be difficult to detect these gamma-rays inside the concrete cell. However, with destructive analysis, it might be possible to analyze the amount of Pu easily by using a detector with a higher energy resolution.

Table 2- 6 *Forty-six energy peaks of gamma rays confirmed to be related to nuclides (1/2)*

Full peak energy [keV]	Generated gamma-ray number [Bq]	E_g [keV]	Related nuclides	Gamma-ray radiation (calculated value) [Bq]
32.0	1.93E + 14	31.40	^{241}Am	1.61E + 14
42.7	1.09E + 14	43.42	^{241}Am	1.18E + 13
59.5	1.85E + 15	59.54	^{241}Am	5.79E + 15
74.7	8.13E + 13	74.66	^{243}Am	4.58E + 13
86.5	1.84E + 14	86.55	^{155}Eu	1.65E + 14
99.5	2.28E + 13	98.97	^{241}Am	3.28E + 12
103.8	4.21E + 13	102.98	^{241}Am	3.15E + 12
105.3	1.06E + 14	105.31	^{155}Eu	1.14E + 14
		106.13	^{239}Np	1.83E + 13
123.1	1.52E + 15	123.07	^{154}Eu	1.56E + 15
228.1	3.01E + 13	228.18	^{243}Cm	3.70E + 12
		228.18	^{239}Np	7.25E + 12
		227.83	^{239}Np	3.44E + 11
248.0	2.23E + 14	247.93	^{154}Eu	2.66E + 14
277.6	4.02E + 13	277.60	^{243}Cm	4.89E + 12
		277.60	^{239}Np	9.69E + 12
569.5	1.91E + 13	569.33	^{134}Cs	1.60E + 13
582.2	2.47E + 13	582.10	^{154}Eu	3.42E + 13
591.9	1.55E + 14	591.76	^{154}Eu	1.91E + 14
604.8	9.23E + 13	604.72	^{134}Cs	1.02E + 14
607.0	1.98E + 12	606.72	^{125}Sb	3.74E + 12
661.7	2.93E + 17	661.66	^{137}Cs	2.06E + 17
692.5	4.20E +13	692.42	^{154}Eu	6.90E + 13
715.2	2.75E + 13	715.82	^{154}Eu	7.24E + 12
723.3	6.17E + 14	723.30	^{154}Eu	7.74E + 14
756.9	1.53E + 14	756.76	^{154}Eu	1.75E + 14
796.0	9.18E + 13	795.86	^{134}Cs	8.90E + 13
801.7	5.58E + 12	801.95	^{134}Cs	9.05E + 12
		800.73	^{154}Eu	1.23E + 12
815.5	2.34E + 13	815.51	^{154}Eu	1.98E + 13
846.0	5.09E + 13	845.46	^{154}Eu	2.26E + 13
850.5	3.24E + 13	850.64	^{154}Eu	9.34E + 12

Table 2- 6 *Forty-six energy peaks of gamma rays confirmed to be related to nuclides (2/2)*

873.3	4.16E + 14	873.19	^{154}Eu	4.70E + 14
880.0	1.07E + 13	880.63	^{154}Eu	3.10E + 12
892.9	2.02E + 13	892.78	^{154}Eu	1.98E + 13
904.0	2.88E + 13	904.08	^{154}Eu	3.44E + 13
996.3	4.11E + 14	996.26	^{154}Eu	4.06E + 14
1004.7	6.76E + 14	1004.73	^{154}Eu	6.90E + 14
1118.3	2.59E + 12	1118.23	^{154}Eu	4.17E + 12
1128.0	3.80E + 13	1128.56	^{154}Eu	1.23E + 13
1168.4	8.54E + 11	1167.97	^{134}Cs	1.86E + 12
1241.5	4.95E + 12	1241.30	^{154}Eu	5.13E + 12
1246.1	2.56E + 13	1246.15	^{154}Eu	3.33E + 13
1274.4	1.16E + 15	1274.44	^{154}Eu	1.35E + 15
1365.1	3.94E + 12	1365.19	^{134}Cs	3.14E + 12
1408.0	1.22E + 12	1408.01	^{152}Eu	2.22E + 12
		1408.20	^{154}Eu	8.88E + 11
1494.0	2.40E + 13	1494.05	^{154}Eu	2.70E + 13
1537.9	2.15E + 12	1537.82	^{154}Eu	2.03E + 12
1596.5	7.49E + 13	1596.50	^{154}Eu	6.89E + 13
2615.0	3.91E + 11	2614.53	^{208}Tl	2.82E + 10

Table 2- 7 *Sum peak of gamma-ray (Twenty-four energy peaks of gamma-ray) (1/2)*

Full peak energy [keV]	Generated gamma-ray number [Bq]	Related gamma-ray energy of sum peak
371.0	3.55E + 13	123.1 keV(^{154}Eu) and 248.0 keV(^{154}Eu)
784.7	5.11E + 13	123.07 keV(^{154}Eu) and 661.66 keV(^{137}Cs)
909.3	8.92E + 12	247.93 keV(^{154}Eu) and 661.66 keV(^{137}Cs)
1253.0	2.07E + 12	591.76 keV(^{154}Eu) and 661.66 keV(^{137}Cs)
1323.1	1.20E + 15	dabble 661.66 keV(^{137}Cs)
1348.5	1.09E + 12	591.9 keV(^{154}Eu) and 756.76 keV(^{154}Eu)
1369.2	1.04E + 12	123.07keV(^{154}Eu) and 1246.15 keV(^{154}Eu)
1384.8	4.94E + 12	661.66 keV(^{137}Cs) and 723.3 keV(^{154}Eu)
1397.5	6.60E + 13	123.07 keV(^{154}Eu) and 1274.44 keV(^{154}Eu)
1534.6	2.88E + 12	661.66 keV(^{137}Cs) and 873.19 keV(^{154}Eu)
1617.0	1.07E + 12	123.07 keV(^{154}Eu) and 1494.05 keV(^{154}Eu)

Table 2- 7 *Sum peak of gamma-ray (Twenty-four energy peaks of gamma-ray) (2/2)*

1657.8	3.45E + 12	661.66 keV(^{137}Cs) and 996.26 keV(^{154}Eu)
1666.2	5.06E + 12	661.66 keV(^{137}Cs) and 1004.73 keV(^{154}Eu)
1719.5	1.61E + 13	1596.50 keV(^{154}Eu) and 123.07keV(^{154}Eu)
1789.2	3.98E + 11	123.07 keV(^{154}Eu), 661.66 keV(^{137}Cs) and 1004.73 keV(^{154}Eu)
1936.0	8.12E + 12	661.66 keV(^{137}Cs) and 1274.44 keV(^{154}Eu)
1969.6	1.96E + 11	723.3keV(^{154}Eu) and 1246.15keV(^{154}Eu)
1984.2	3.11E + 12	triple 661.66 keV(^{137}Cs)
1993.8	1.08E + 11	661.66 keV(^{137}Cs) and 1332.5 keV(^{60}Co) or double 996.26 keV(^{154}Eu)
2059.0	4.57E + 11	123.07 keV(^{154}Eu), 661.66 keV(^{137}Cs) and 1274.44 keV(^{154}Eu)
2155.0	2.92E + 11	661.66 keV(^{137}Cs) and 1494.05 keV(^{154}Eu) or 123.07 keV(^{154}Eu), 756.76 keV(^{154}Eu) and 1274.44 keV(^{154}Eu)
2258.0	6.00E + 11	591.76 keV(^{154}Eu), 661.66 keV(^{137}Cs), and 1004.73 keV(^{154}Eu), or 661.66 keV(^{137}Cs) and 1596.5 keV(^{154}Eu)
2381.5	1.07E + 11	123.07 keV(^{154}Eu), 591.76keV(^{154}Eu), 661.66 keV(^{137}Cs) and 1004.73 keV(^{154}Eu), or 123.07 keV(^{154}Eu), 661.66 keV(^{137}Cs) and 1596.50 keV(^{154}Eu),
2505.5	6.79E + 11	247.93 keV(^{154}Eu), 591.76 keV(^{154}Eu), 661.66 keV(^{137}Cs) and 1004.73 keV(^{154}Eu) or 1173.24 keV(^{60}Co) and 1332.5 keV(^{60}Co)

Table 2- 8 *Three gamma-ray energy peaks related to Pu isotopes*

Full energy peak energy [keV]	Generated gamma-ray number [Bq]	Eg [keV]	Related nuclides	Gamma-ray radiation (calculation value) [Bq]
42.7	1.09E + 14	43.42	^{241}Am	1.18E + 13
		42.73	^{241}Am	8.88E + 11
		42.82	^{244}Cm	5.99E + 11
		43.50	^{238}Pu	8.15E + 10
		43.18	^{243}Am	4.72E + 10
		42.64	^{126}Sn	1.66E + 10
99.5	2.28E + 13	98.97	^{241}Am	3.28E + 12
		98.86	^{244}Cm	4.04E + 10
		99.85	^{238}Pu	1.52E + 10
103.8	4.21E + 13	102.98	^{241}Am	3.15E + 12
		103.97	^{233}Pa	1.24E + 10
		104.23	^{240}Pu	4.79E + 09
		103.68	^{241}Pu	3.31E + 09

2-2-6. Consideration about neutron emission number from HAW tank

HALW contains a few nuclides that can probable undergo spontaneous fission, such as ^{244}Cm and Pu isotopes. In order to generate the neutron source data for MCNP simulation, we performed neutron number calculation in the HAW tank. We calculated the total number of neutrons emitted from each nuclide by multiplying the spontaneous fission yield of each nuclide with the total mass of each nuclide based on analysis result. *Table 2- 9* shows a few examples of the calculation results.

Table 2- 9 *Number of neutrons generated in V35 (1/2)*

Nuclides	Weight [g]	Spontaneous fission yield [n/s-g]	Neutron yield [n/s]
^{234}U	1.28E + 04	5.02E-03	6.42E + 01
^{235}U	5.14E + 05	2.99E-04	1.54E + 02
^{236}U	1.60E + 05	5.49E-03	8.79E + 02
^{238}U	5.05E + 07	1.36E-02	6.86E + 05
^{238}Pu	3.28E + 04	2.59E+03	8.50E + 07
^{239}Pu	1.64E + 06	2.18E-02	3.58E + 04
^{240}Pu	8.62E + 05	1.02E+03	8.79E + 08
^{241}Pu	7.98E + 04	5.00E-02	3.99E + 03

Table 2- 9 *Number of neutrons generated in V35 (2/2)*

^{242}Pu	1.20E + 05	1.72E+03	2.06E + 08
^{241}Am	4.19E + 04	1.18E+00	4.94E + 04
^{244}Cm	1.04E + 03	1.08E+07	1.12E + 10

The Sources4C capability of OrigenARP was used to calculate the (α,n) neutron source term for the HALW. The results are shown in *Figure 2- 13*. Based on these results, the (α,n) neutron source term is considerably smaller than the spontaneous fission source term. Moreover, the average energy of spontaneous fission and that of the (α,n) neutrons are very similar. Therefore, it is not necessary to perform two separate calculations for spontaneous fission and (α,n) neutron sources. Instead, one calculation was performed using the spontaneous fission neutron source term, and the overall neutron yield was corrected to include the (α,n) neutron source term.

```
total (alpha,n) neutron source from all sources and targets:                    7.898E+07 n/s
total spontaneous fission neutron source from all sources and targets:          1.036E+10 n/s
total delayed neutron source from all sources and targets:                      0.000E+00 n/s
total neutron source from all sources and targets:                              1.044E+10 n/s
average (alpha,n) neutron energy:                                               2.459E+00 mev
average spontaneous fission neutron energy:                                     2.11121E+00 mev
average delayed neutron energy:                                                 0.000E+00 mev
average neutron energy from all sources:                                        2.114E+00 mev
portion of total neutron source rate accounted for in the energy spectrum:       99.9999%
portion of (a,n) neutron source rate accounted for in the energy spectrum:       99.9938%
portion of spontaneous fission neutron source rate accounted for in the energy spectrum:  100.0000%
```

Figure 2- 13 *Sources4C calculation results*

Based on these results, the neutron spectrum and the amount of ^{244}Cm were used as inputs to generate the neutron source data to be used in the MCNP simulation.

2-2-7. Analysis results of other tanks

The target tank was 272V35, and we used this tank to optimize the simulation model. Comparison with different HALW compositions was necessary in the development of the Pu monitoring technology. Therefore, we sampled HALWs from other tanks and analyzed their compositions.

Table 2- 10 to Table 2- 12 show the analysis results.

Table 2- 10 *Analysis results of other tanks (1/2)*

Analysis item	Date	2/7/2017	12/12/2017		2/8/2017	12/11/2017
	Tank	272V35	272V35	272V35	272V34	272V33
Acid conc. (mol/L)		2.34	2.63	-	2.24	1.73
Density (g/cm^3)		1.249	1.239	-	1.191	1.252

Table 2- 10 *Analysis results of other tanks (2/2)*

Cm conc.*1 (Bq/mL)	2.90E + 07	2.50E + 07	4.20E + 07	3.80E + 07	1.60E + 07
Cm conc.*2 (Bq/mL)	4.10E + 07	3.70E + 07	4.00E + 07	3.00E + 07	1.60E + 07
Pu conc.*1 (mg/L)	238	216	217	177	81
Pu conc.*2 (mg/L)	356	326	326	250	110
U conc. (g/L)	6.65	6.46	-	5.18	2.74

*1 Undissolved
*2 Dissolved

Table 2- 11 *Results of gamma-ray spectrometry of other tanks*

Nucleus	Gamma radiation (Undissolved)					
	Date	2/7/2017	12/12/2017		2/8/2017	12/11/2017
	Tank	272V35	272V35	272V35	272V34	272V33
^{241}Am	Bq/mL	6.90E + 07	7.20E +07	-	1.00E + 08	5.50E + 07
^{144}Ce	Bq/mL	<3.7E + 06	<3.7E + 06	-	<3.7E + 06	<3.7E + 06
^{137}Cs	Bq/mL	2.90E + 09	2.60E + 09	-	3.50E + 09	1.80E + 09
^{134}Cs	Bq/mL	6.40E + 05	5.10E + 05	-	8.80E + 05	<3.7E + 05
^{125}Sb	Bq/mL	<3.7E + 06	<3.7E + 06	-	<3.7E + 06	<3.7E + 06
^{106}Ru	Bq/mL	<3.7E + 06	<3.7E + 06	-	<3.7E + 06	<3.7E + 06
^{103}Ru	Bq/mL	<3.7E + 06	<3.7E + 06	-	<3.7E + 06	<3.7E + 05
^{95}Zr	Bq/mL	<3.7E + 05	<3.7E + 05	-	<3.7E + 05	<3.7E + 05
^{60}Co	Bq/mL	<3.7E + 05	<3.7E + 05	-	<3.7E + 05	<3.7E + 05

Table 2- 12 *Isotopic composition analysis results of other tanks*

Isotope	Isotopic composition (Dissolved)					
	Date	2/7/2017	12/12/2017		2/8/2017	12/11/2017
	Tank	272V35	272V35	272V35	272V34	272V33
^{234}U	wt%	0.025	0.027	-	0.023	0.024
^{235}U	wt%	1.006	1.006	-	1.039	1.056
^{236}U	wt%	0.313	0.313	-	0.287	0.279
^{238}U	wt%	98.656	98.654	-	98.651	98.641
^{238}Pu	wt%	1.199	1.180	-	1.192	1.178
^{239}Pu	wt%	60.033	61.064	-	60.422	61.684
^{240}Pu	wt%	31.469	30.461	-	31.350	30.441
^{241}Pu	wt%	2.916	2.828	-	2.796	2.523
^{242}Pu	wt%	4.383	4.467	-	4.240	4.174

2-3. Mock-up test

2-3-1. Outline

The HAW tanks at HALWS are behind thick concrete cells that block the radiation generated by the HALW (*Figure 2- 14*). The concrete cells house the HALW tanks and the drip trays under the tanks to catch any leaked liquid, as well as six guide rails to insert detector holders for safety purposes. The guide rails are laid in a route from which one can observe the upper and the central parts of the tank, drip tray, and other components. Then, we can insert the radiation detector inside the concrete cell from the entrance of the inspection pipe on the corridor side.

In this study, we inserted the radiation detector into the guide rail and performed radiation measurements inside the concrete cell. However, radiation measurement in the concrete cell by using the guide rail was the first challenge at HAWS. Therefore, we fabricated an actual-sized rail (same shape, materials, and dimensions) and performed a mock-up test with this rail in advance to ensure that the radiation detector does not get stuck inside the concrete cell.

We selected the rail with the most severe curve for the mock-up test (*Figure 2- 14*). Then, we confirmed its workability and safety in terms of performing measurements.

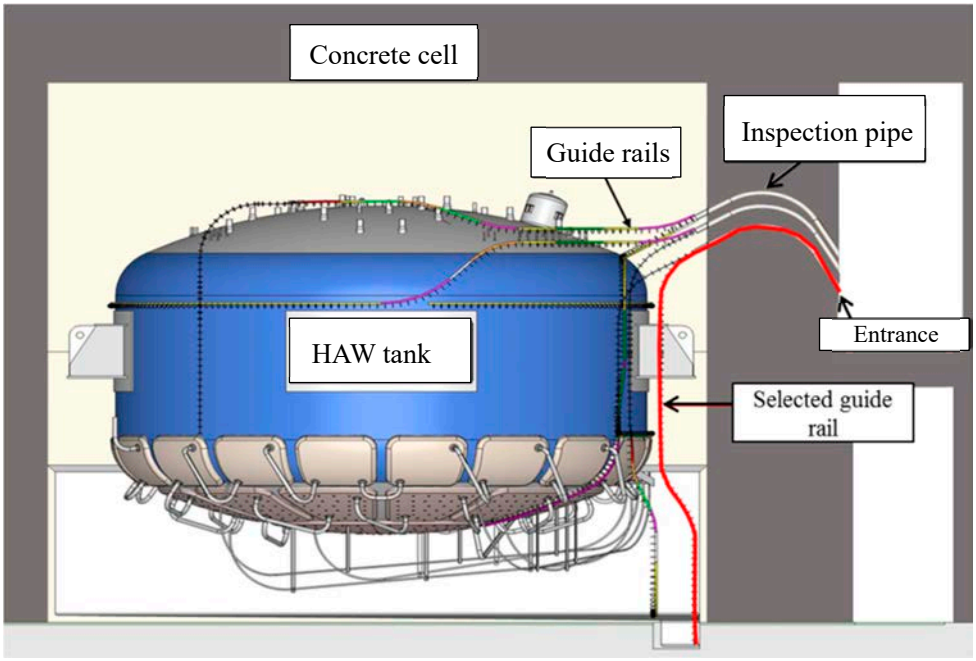

Figure 2- 14 *Layout of equipment around tank at HALWS*

【Specifications of HAW tank】

(1) Size: Dia. = 6.8 m, Height = 4.8 m, t = 22 mm

(2) Volume: approximately 120 m^3/tank

(3) Material: SUS316ULC

2-3-2. Mock-up equipment

Figure 2- 15 shows the mock-up test equipment. The height of the mock-up test rails is approximately 8,600 mm. The rail can be divided into four parts and fabricated. The mock-up test equipment consists of the rail and the support frame.

The entrance of the rail is at approximately 4,850 mm from the floor level. The rail inclines upward at the start and then inclines downward toward the floor in a helicoidal fashion. The work platform for operation is at the rail entrance.

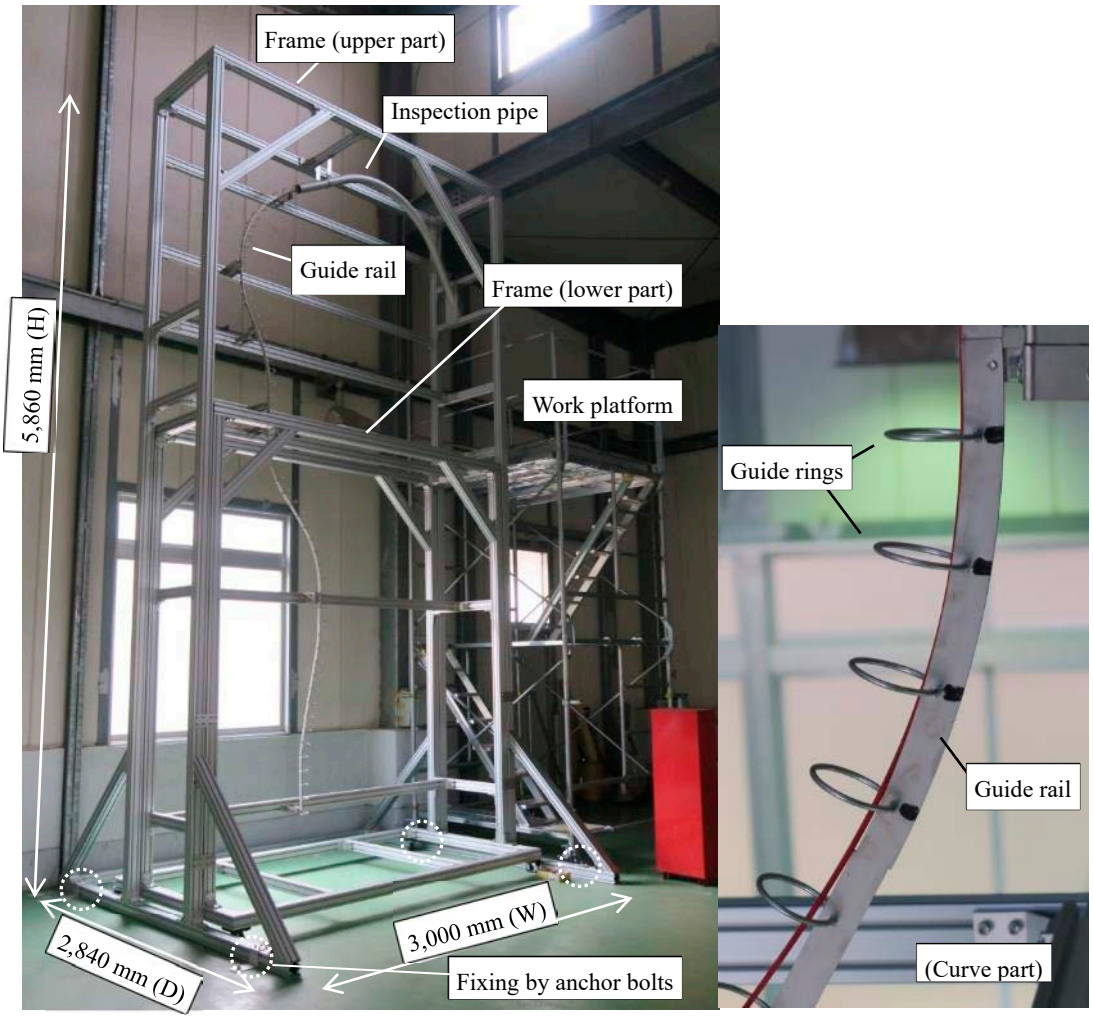

Figure 2- 15 *Mock-up test equipment*

【Specifications】

(1) External size: 3,000 mm (Width) × 2,840 mm (Depth) × 5,860 mm (Height)

(2) Rail: 4 divisions (5 mm thickness, 30 mm width, SUS304)

(3) Rings: Inner diameter 58 mm and 62 mm (Fabricated using SUS304 round bar of diameter 5 mm at every 10 cm)

* Rings with larger inner diameter are used at the curves on the ring side.

(4) Inspection pipe: Inner diameter = 69.3 mm

* Guide wire (5 mm diameter) is set from the concrete entrance to the rail.

(5) Frame material: Aluminum

(6) Total weight: 492.2 kg

2-3-3. Holder for detector and scope

Radiation measurements inside the concrete cell were performed by mounting the detector on the rail. The detector was mounted using a holder. A tough and flexible fiber-reinforced plastic (FRP) rod was connected to the holder for insertion. The holder had an upper-lower bisection. After connecting FRP rod, we fixed the upper and the lower parts by screws (Helisert).

Figure 2- 16 shows inside the configuration of the IC holder and storage situation of the IC, *Figure 2- 17* shows the storage situation of the scope, and *Figure 2- 18* shows the connection details of the holder and the FRP rod.

【Specifications】

(1) External size: Diameter 55 mm, Length 315 mm, cylinder type (Both ends are conical)

(2) Material: PEEK (Poly Ether Ether Ketone) or POM (Polyacetal)

* PEEK has good characteristics in terms of radiation hardness, heat resistance, strength, low combustibility, low abrasiveness (sliding), and electrical insulation.

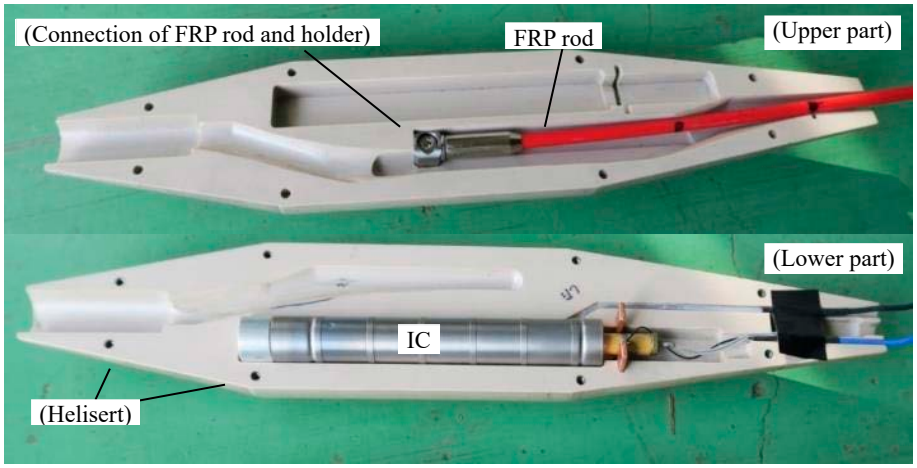

Figure 2- 16 *Inside of holder and IC storage*

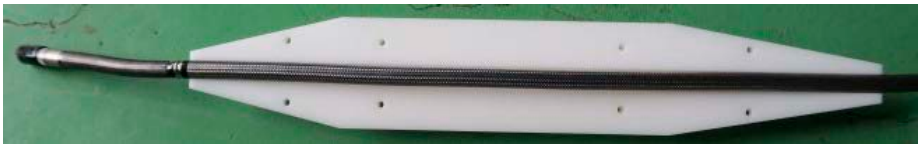

Figure 2- 17 *Placement of scope in scope holder*

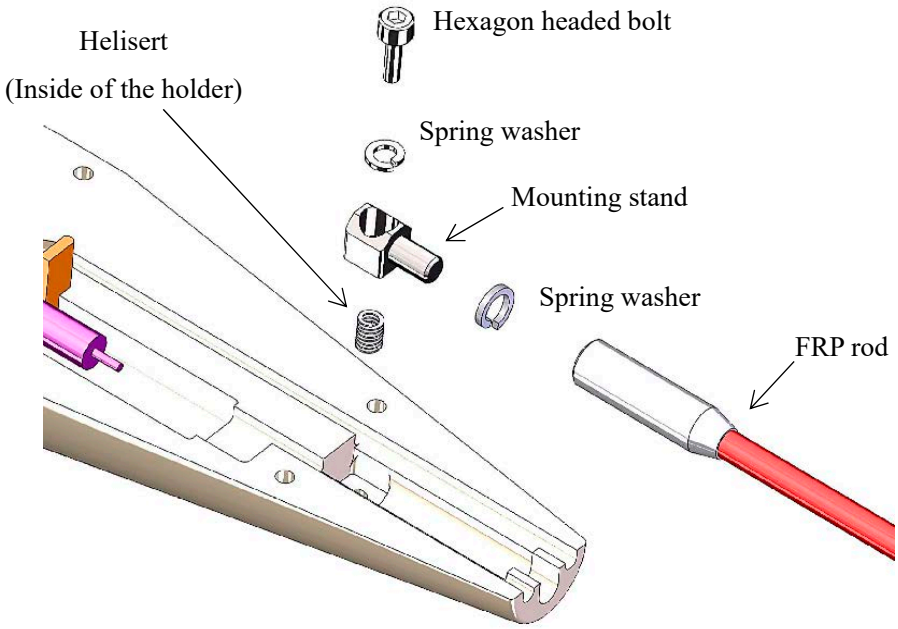

Figure 2- 18 *Connection details of holder and FRP rod*

2-3-4. Mock-up test

Figure 2- 19 shows an example of the work situation. We obtained the following knowledge in the mock-up test.

(1) Regarding the direction of insertion of the holder, the front side should have a shorter taper and the rear side should have a longer taper. If the tapers are reversed, the holder will get stuck on the way.

(2) FRP rod should be set centrally on the holder to press uniform and to ensure the holder moves smoothly.

(3) When the holder is stuck on the rail, we can rotate the FRP rod to take it out.

(4) If the insertion speed is slow (about 5 cm/s), the holder can get stuck easily. We must operate the holder faster (about 15 cm/s).

(5) After the holder is inserted to the deepest position, it is pulled out.

(6) Detector cables should be set in the space inside the holder.

(7) PEEK or POM are suitable holder materials because they are not shaved off easily (less dust).

(8) A mark should be made on the FRP rod to measure insertion distance (ID).

(9) The external form of the holder should be ground to improve holder insertion if holder movement is not smooth (*Figure 2- 20*).

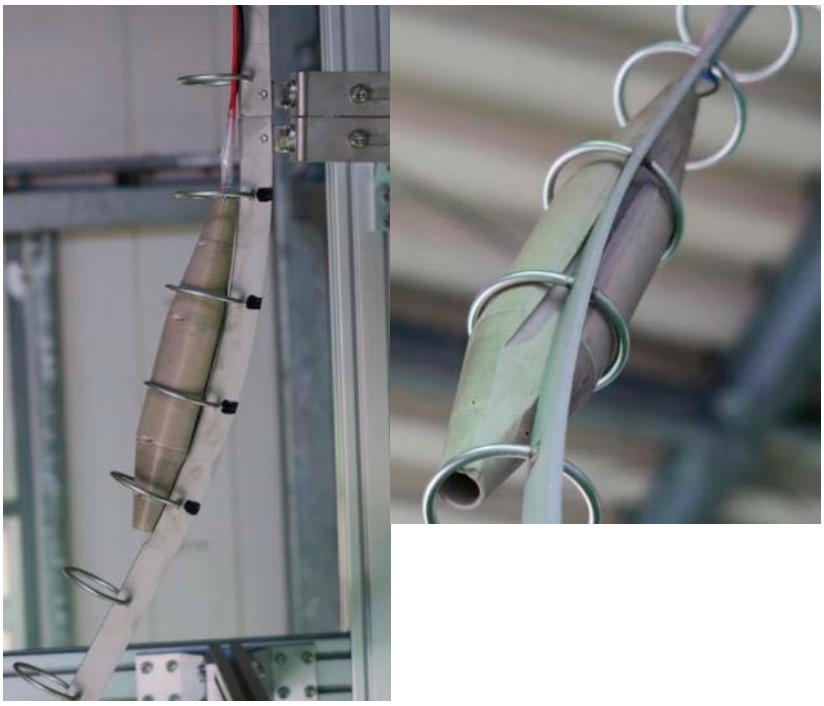

Figure 2- 19 *Example of mock-up test scenario*

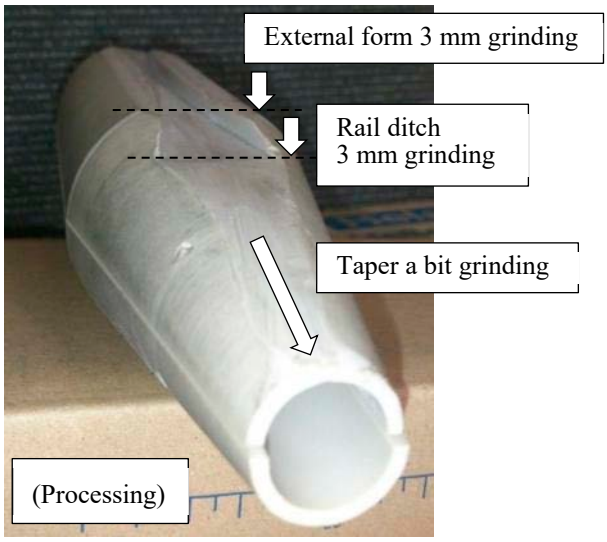

Figure 2- 20 *Holder improvement (Grinding of external form)*

2-3-5. Preliminary investigation of the inside of concrete cell for HAW tank

(1) Outline

We confirmed the situation inside the inspection pipe, rail, and rings in the concrete cell by using a

fiber scope at HAW as a preliminary investigation of the measurement points. We measured the ID by using the FRP rod. We made marks at intervals of approximately 100 mm over the entire rod length of 8,500 mm. The holder was located between the rings at intervals of 100 mm based on the mock-up tests.

(2) Results

① No obstacles were found inside the inspection pipe during the planned measurements, and the guide wire did not present any problems (*Figure 2- 21*).

② We confirmed no bucking up of the rail or falling off and rusting of the rings inside the concrete cell. Thus, we confirmed there were no problems with detector insertion toward the inside of the concrete cell (*Figure 2- 22*).

③ The holder was located between the rings by moving it to the marks on the FRP rod. We confirmed that the holder could be set at the planned measurement points (deepest approximately 8,500 mm) (*Figure 2- 23*).

Figure 2- 21 *Inside of inspection pipe and guide wire*

Figure 2- 22 *Rail and inside of concrete cell (ID approximately 3,000 mm)*

Figure 2- 23 *Rail and ring inside concrete cell (ID approximately 8,500 mm)*

3. Radiation investigation

3-1. Feasibility study with gamma-ray for Pu monitoring

3-1-1. Feasibility study for gamma-ray outside concrete cell

In this technology development process, applicable levels of radiation and the corresponding energies were investigated, and measurements were conducted to decide the type of detector and measurement location.

As the first step, we measured gamma rays over a wide energy range outside the concrete cell to confirm whether it is possible to measure the gamma rays emitted from the HAW tank at a position outside the concrete cell.

A. Gamma-ray dose rate measurement

Gamma-ray dose rates outside the concrete cell were measured using an ion chamber (IC) and NaI(Tl) (NaI(Tl) is usually used for radiation at the facility). As a result, no specific count rate was detected.

B. Gamma-ray spectra measurement

B-1. Purpose of measurement

Gamma-rays are emitted by the HALW containing fission products. The gamma-ray spectra were measured outside the concrete cell. *Figure 3- 1* shows the measurement point for the gamma-ray spectra. We selected two tanks (V35, V36) for these measurements. Tank V36 contained only nitric acid solution, and it is a spare tank. The results obtained in the case of V36 were compared to those obtained in the case of V35, which contained HALW.

Upper floor ① In front of shield plug, ② Middle width of V35

Lower floor ③ Middle width of V35, 1.5 m from floor

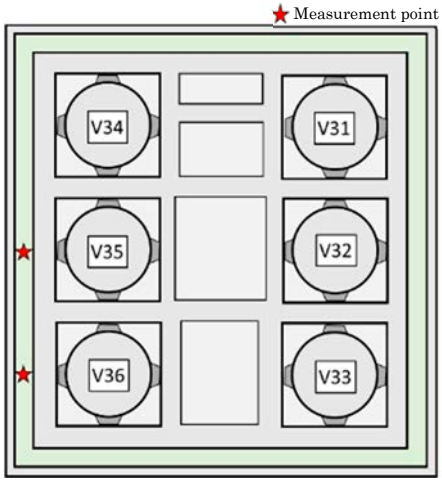

Figure 3- 1 *Gamma-ray measurement location outside concrete cell*

Figure 3- 2 shows the measurement setup outside the concrete cell. There is concrete between the detector and the HALW tank outside the wall of the HALW. The largest solid angle point was selected as the measurement point, and it was at the same level as the liquid in the HALW tank. The detector was surrounded by Pb to reduce background.

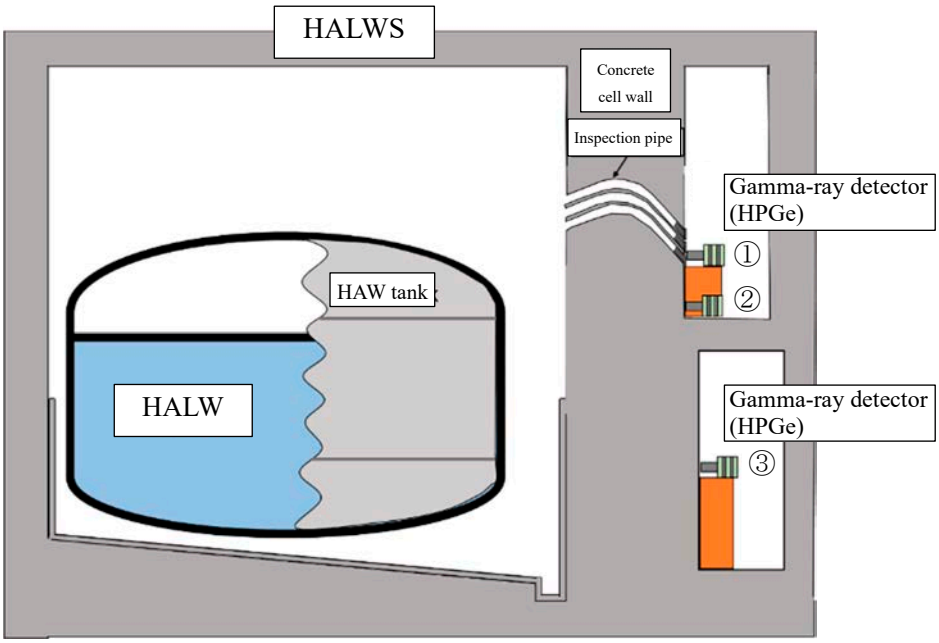

Figure 3- 2 *Measurement setup (cross section view)*

B-2. Detector for experiment

HPGe [GMX50-83-A ORTEC] was used for gamma-ray measurements, and its energy range was up to 10 MeV. *Figure 3- 3* shows the HPGe detector setup.

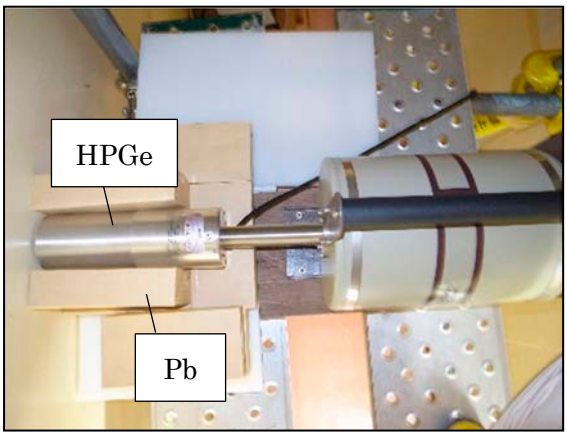

Figure 3- 3 *HPGe detector*

・Ortec: GMX50-83-A
・Crystal size: φ63 cm × 74.5 cm
・Detector shape: N type
・Efficiency: 50%
・Resolution: 2.15 keV (FWHM at 1.33 MeV, ^{60}Co)
・Energy range: about 40 keV~10 MeV
・Weight: ~18 kg (with full liquid N_2)

B-3. Measurement setup

High voltage was supplied from the portable MCA, and the signal from the detector was counted by the MCA. Gamma-ray spectra were measured by using a laptop PC with a software application called gamma station (see *Figure 3- 4*).

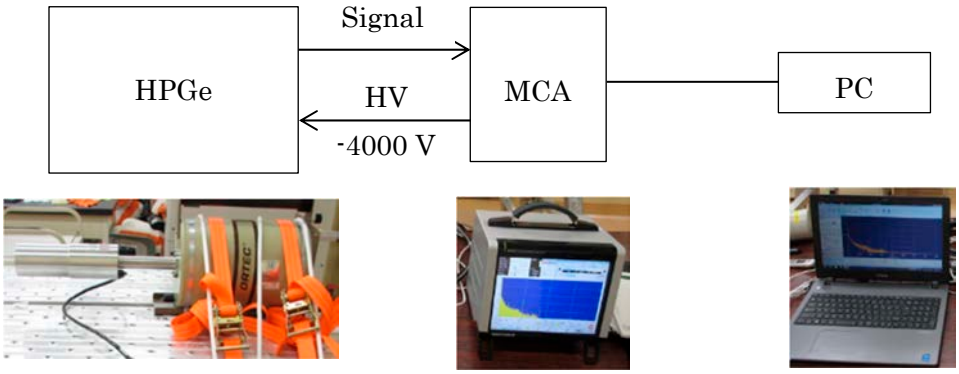

Figure 3- 4 *HPGe measurement setup*

B-4. Calibration test

Energy calibration between the channel and energy were conducted using ^{137}Cs (662 keV) and ^{60}Co (1,332 keV) sources.

B-5. Result

In terms of HPGe measurement (live time: 3,600 s, location Fig.3-2②), we could find only background peaks (see *Figure 3- 5*). Although we expected to detect high-energy gamma rays, such as delayed gamma rays with short lifetime, we understood that Pu monitoring by gamma-ray measurement outside the concrete cell seems to be difficult. Measurements should be conducted at locations of with poor shielding, such as inside the penetration pipe or the concrete cell.

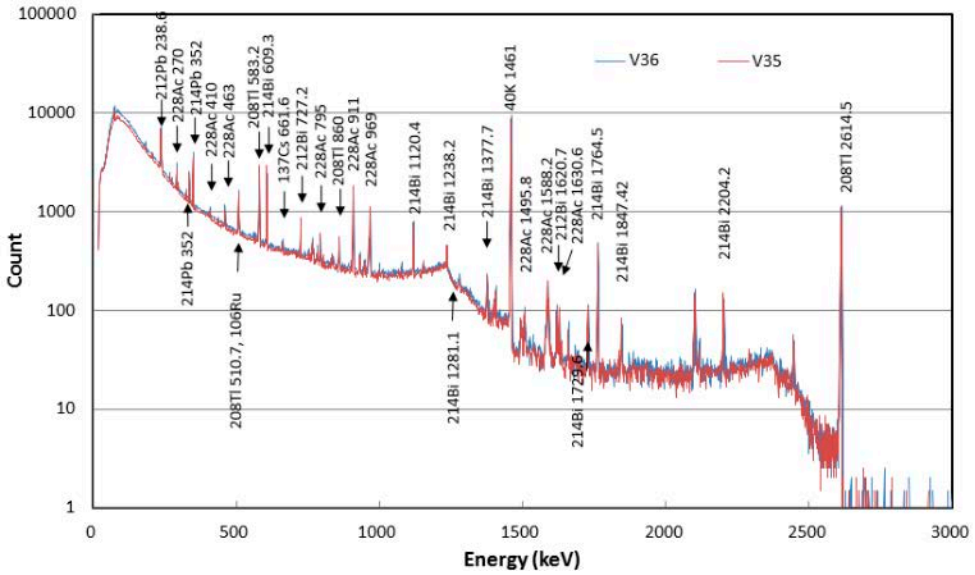

Figure 3- 5 *Searched gamma-ray peaks outside concrete cell*

B-6. Comparison with simulation model (PHITS)

<Model>

To confirm model validity by means of comparison with measured values, simulations using a simple model were performed using PHITS.

Because ^{244}Cm is the dominant source of neutrons in HALW, ^{244}Cm was used as the neutron source term in the simulation to simulate some reactions, such as (n, γ). The input gamma-ray source assumed the gamma-ray spectra measured using an HPGe detector multiplied by the efficiency curve calculated using PHITS code. We assumed the number of particles as 1 million. The simulation model is shown in *Figure 3- 6*.

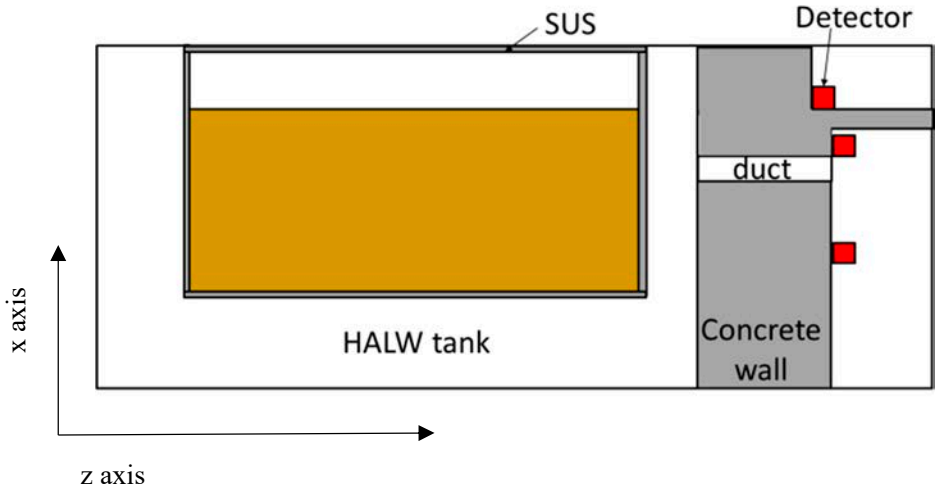

Figure 3- 6 *Model of entire HALW tank (V35)*

<Result>

Gamma rays were simulated using the gamma-ray destructive analysis (DA) spectrum obtained from measurement of the diluted HALW sample (see *Figure 3- 7*). We observed that gamma rays were almost completely shielded at approximately 70 cm from the inner wall (entrance of the concrete cell). Based on the results of PHITS simulation using DA data as the input file, it is seemingly difficult to measure any gamma-rays directly from the HAW tank outside the concrete cell.

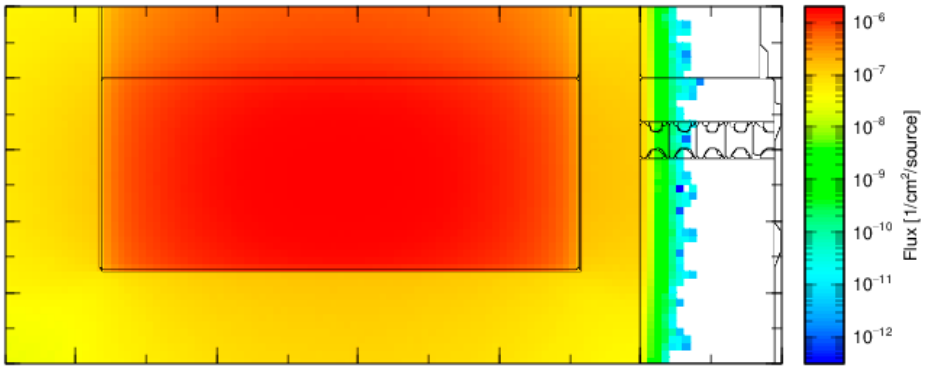

Figure 3- 7 *Gamma-ray simulation result*

B-7. Consideration

We performed actual gamma-ray measurements outside the concrete cell. Gamma-ray peaks emitted from the HALW solution were not found in the measured spectrum because the shielding effect of the HALW tank cell was very strong. We confirmed model validity by comparing the results obtained with actual measurement values and understood the effect of gamma rays at approximately 70 cm from the inner wall. Therefore, we tried to perform gamma-ray spectrum measurements inside the concrete cell, where the shielding effect is weaker than that outside the concrete cell as the next step.

3-1-2. Feasibility study with gamma rays inside the concrete cell

A. Gamma-ray dose rate measurement

A-1. Purpose of measurement

In this measurement, we measured the gamma-ray dose rate inside the concrete cell. The measured data were compared with the evaluation results obtained by in a simulation performed parallel to the gamma-ray dose rate measurement at HAW for Pu monitoring technological development. To confirm the simulation results and optimization of simulation model, we conducted the measurement. The gamma-ray dose rate measurement data were utilized for selection of neutron and gamma ray detectors inside the concrete cell, shielding design, and study of detector position for Pu monitoring.

A-2. Measurement tools

(1) Radiation meter (*Figure 3- 8*)

① Ionization Chamber (IC)

- Model: 52120 Gamma Ionization Chamber (LND, INC.)
- Size: Diameter = 0.63 inch, Length = 5.01 inch (Active length 3.38 inch, Effective volume 17 cm^3)
- Sensitivity: 1.5E-11 A/R/h (^{137}Cs), 2.0E-12 A/R/h (^{60}Co)
- Measurement range: ~1,000 Gy/h
- Fill gas (atm): Nitrogen (1 atm)

***Figure 3- 8** IC*

【Reasons for selection】

- ^{137}Cs (662 keV) is about 97% based on sampling analysis.
- The estimated gamma-ray dose rate near the tank surface was about 120 Gy/h, as measured using an alanine cumulative dose meter.
- The effective length of detection part was less than 10 cm because the space between rings was approximately 10 cm.

(2) IC holder and operation tools

① IC holder (*Figure 3- 9*)

- External form: Diameter = 55 mm, Length = 315 mm, Cylinder type (Both ends conical)
- Material: PEEK
- Structures: Storage on inside of the IC and scope, and connection to inside of FRP rod are possible.

Figure 3- 9 *IC holder*

② FRP rod (*Figure 3- 10*)

- Diameter: 5 mm
- Load-withstanding capacity: Tensile fracture strength = 7.3 kN, Bending strength = 400 N/mm^2
- Minimum radius: 140 mm

Figure 3- 10 *FRP rod*

(3) Signal processing and control system – Unattended Dual Current Monitor (UDCM)[8]

① Instrument for HV supply and data acquisition: UDCM (Made in LANL) (*Figure 3- 11*)

- HV supply to IC
- It was used to correct changing data, such as trend data.

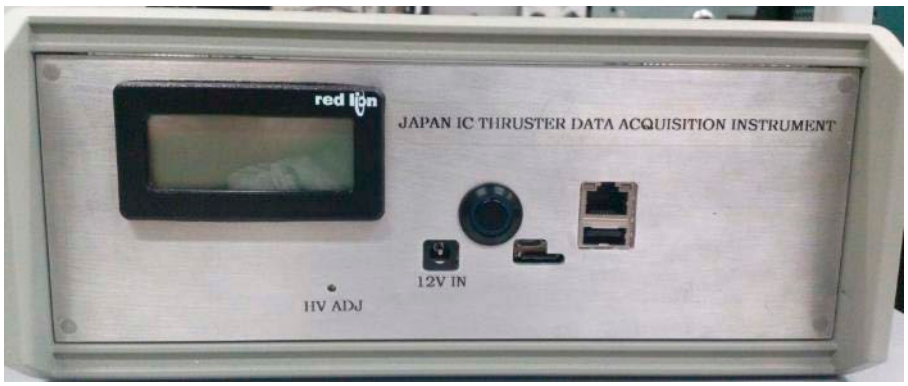

Figure 3- 11 *UDCM*

② Current measurement instrument: Picoammeter (KEITHLEY 6485) (*Figure 3- 12*)
It is used to acquire high-rate data

Figure 3- 12 *Picoammeter*

A-3. Experimental setup

(1) Device structure

Figure 3- 13 shows the IC structure. *Figure 3- 14* and *Figure 3- 15* show the measurement system. A cable for HV supply and two cables for signal are connected to the IC. We checked the conduction (Ω1 to Ω3) of the cables before use because the cable length is 30 m. The measurement system consists of the IC, IC holder, UDCM, and picoammeter. In addition, the FRP rod is connected to the inside of the IC holder for inserting and pulling out the IC holder.

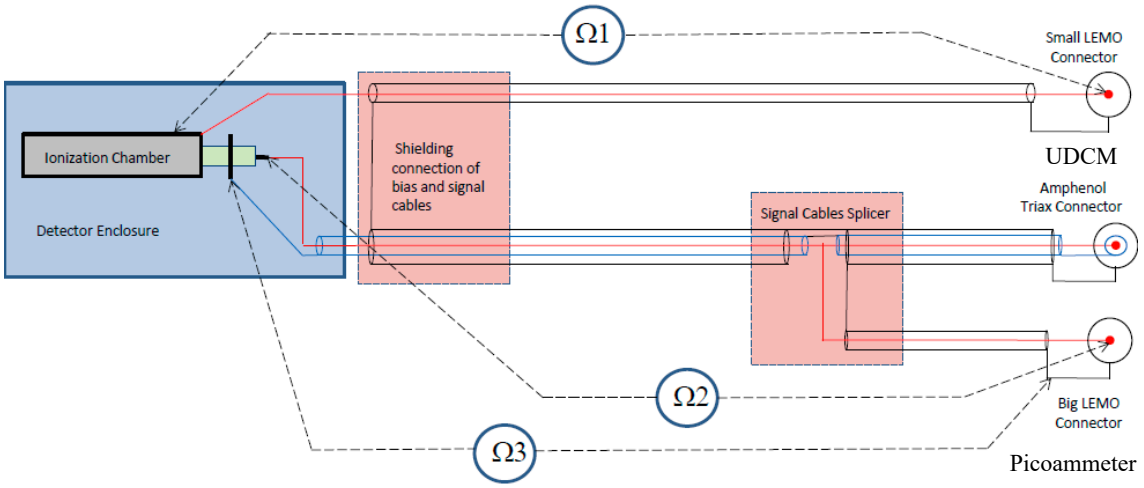

Figure 3- 13 *IC structure*

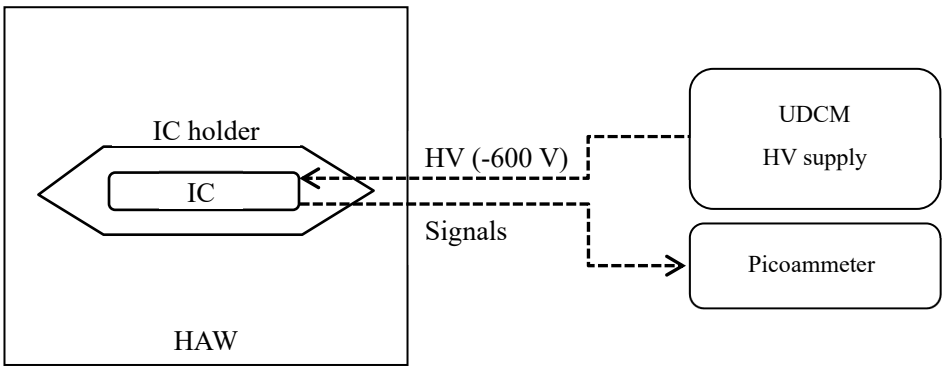

Figure 3- 14 *Data measurement system using picoammeter*

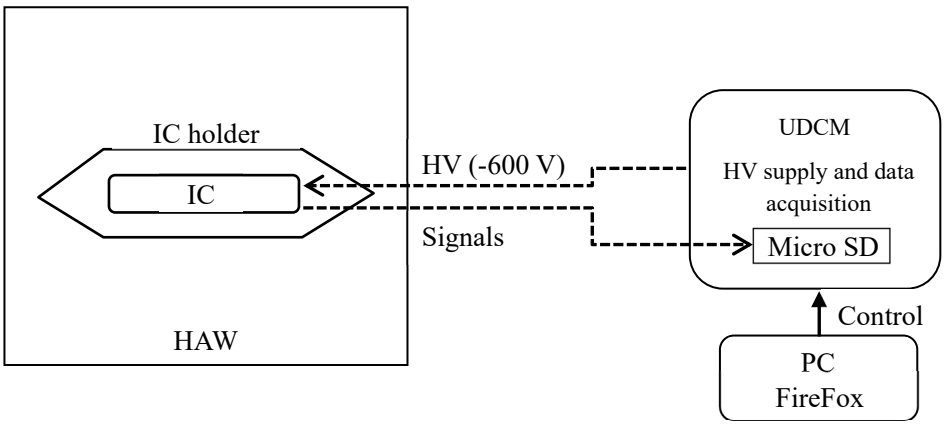

Figure 3- 15 *Data measurement system using UDCM*

(2) IC holder setup

Figure 3- 16 shows the structure of the IC inside the holder. The IC and FRP rod are set and connected around the center of the IC holder. The FRP rod is fixed tightly by using a mounting stand and a hexagon-headed bolt. The IC surface is covered with insulation grease to prevent corrosion current and to provide insulation. During assembly of the IC holder, we fixed the cables with tape to prevent insertion into the IC holder.

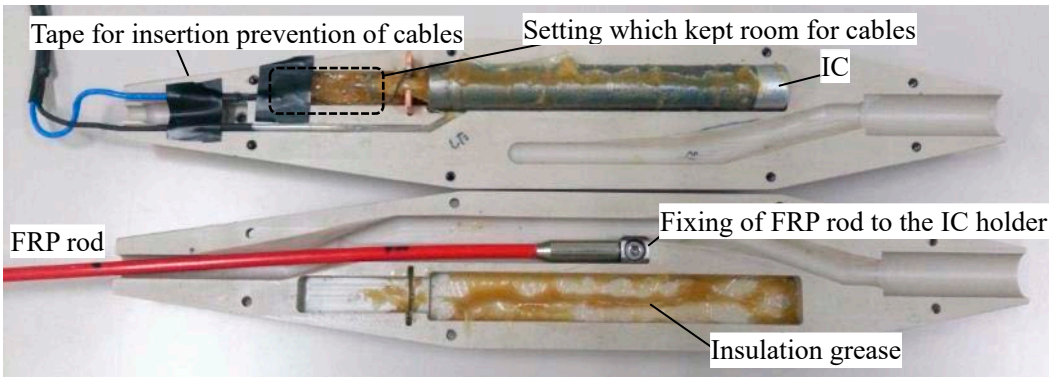

Figure 3- 16 *IC storage and fixing of FRP rod to inside of IC holder*

(3) Device connection

① Data correction using picoammeter

(*Figure 3- 17*)

- Connect test current device to picoammeter, and check indicated values of picoammeter for normal current (-12 nA and -120 nA)

(*Figure 3- 18*)

Connect of coaxial cable (double shield) of IC to picoammeter (coaxial cable of IC is kept free to ensure that the current does not diverge.)

(*Figure 3- 19*)

- Connect power supply cable of UDCM (front), and set HV to -600 V
- Connect HV cable of IC to rear HV terminal of UDCM
- Set measurement point of IC holder, measure using picoammeter

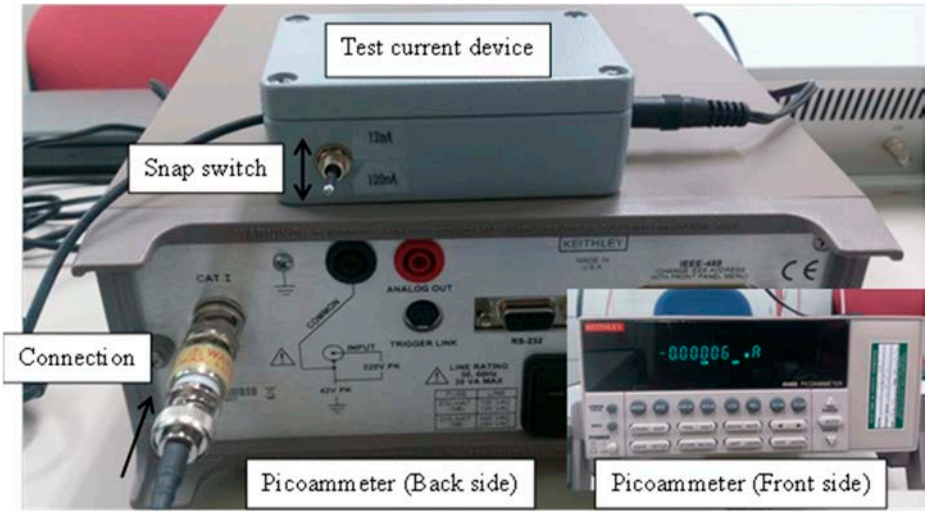

Figure 3- 17 *Connection of test current device*

Figure 3- 18 *Connection of IC cables*

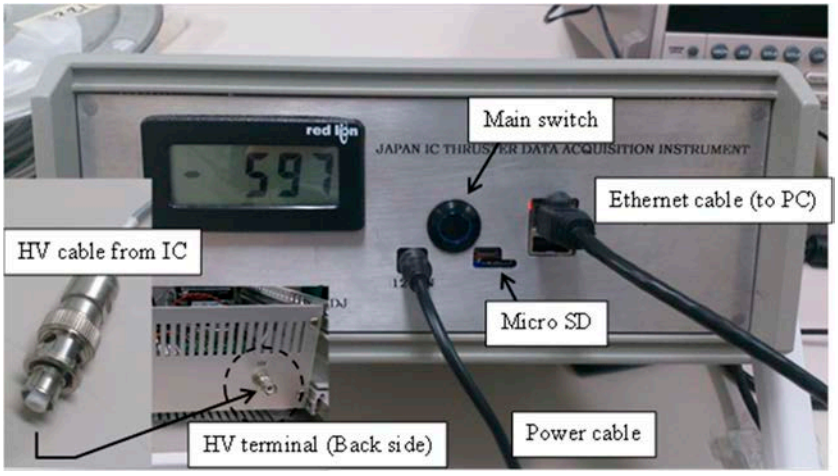

Figure 3- 19 *Connection of cables to UDCM*

② Data acquisition using UDCM

(*Figure 3- 19*)

- Insert micro SD card into UDCM
- Connect power supply cable of UDCM (front), and set HV to -600 V
- Connect HV cable of IC to rear HV terminal of UDCM
- Connect NIM cable of IC to rear ch1 of UDCM (Coaxial cable of IC is kept free to ensure the current does not diverge)
- Connect LAN cable between PC and UDCM, and start automatic network communication by pushing switch (on)

(*Figure 3- 20*)

Start Web browser (FireFox), and confirm communication status

- Start measurement at the same time as the start of communication. Stop measurement by pushing [STOP]
- In the case of a change in settings, reflect it by pushing [Submit]
- Arrange measurement point on IC holder, and start measurement by pushing [START] (Data are stored in micro SD card automatically.)

  * One data file is created in one day of measurement. In the case of repetitive measurement, data are added to the file.

(Measurement data)

- Read data (CSV file) on micro SD card by using Linux.
- File name is “measurement data.csv.” For example, the file is named “2017-01-31.csv” automatically.
- Data consists of 11 lines, and the details of every line are as follows.

line 1: Date and time
line 2: Signal of channel 1 (current (nA))
line 3: Standard deviation of channel 1
line 4: Signal of channel 2 (current (nA))
line 5: Standard deviation of channel 2
line 6: Measurement time (data acquisition time (s))
line 7: Number of data (about measurement time/100 ms)
line 8: Not used
line 9: High voltage
line 10: Gain of channel 1
line 11: Gain of channel 2

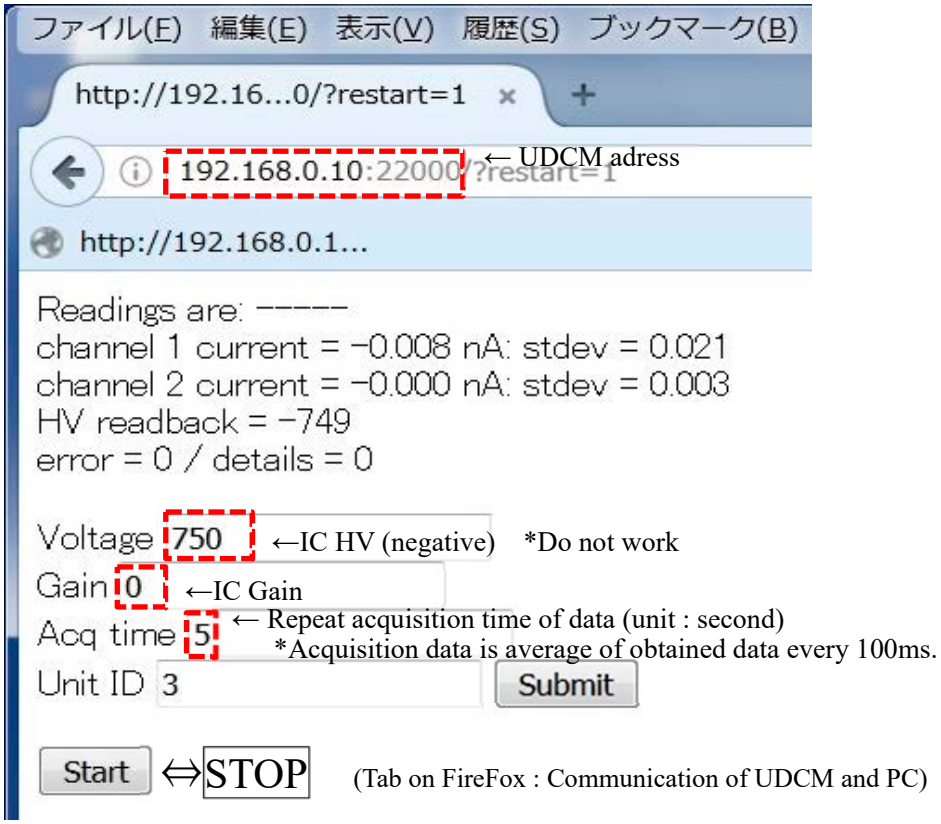

Figure 3- 20 *Measurement control display in FireFox*

A-4. Calibration Tests

(1) Calibration at LANL

Before shipping the IC to JAEA, calibration tests were performed at LANL to determine the IC response (current) as a function of dose rate. Based on preliminary information that the expected radiation is of the order of thousands of R*/h, we selected a less sensitive 1-atm N-filled ionization chamber LND model #52120 instead of the commonly used highly sensitive 10-atm Xe-filled IC model 52110. The added advantage of this choice is the more uniform sensitivity versus energy graph of the incident gamma radiation. The calibration measurement setup is shown in *Figure 3- 21*.

＊Unit of radiation

R: Roentgen (CGS units)

Irradiation radiation dose is quantity of electric charge per unit weight of air ionized by photons such as X-rays and gamma rays. SI unit is coulomb per kilogram [C/kg] (1 R = 2.58E-4 C/kg).

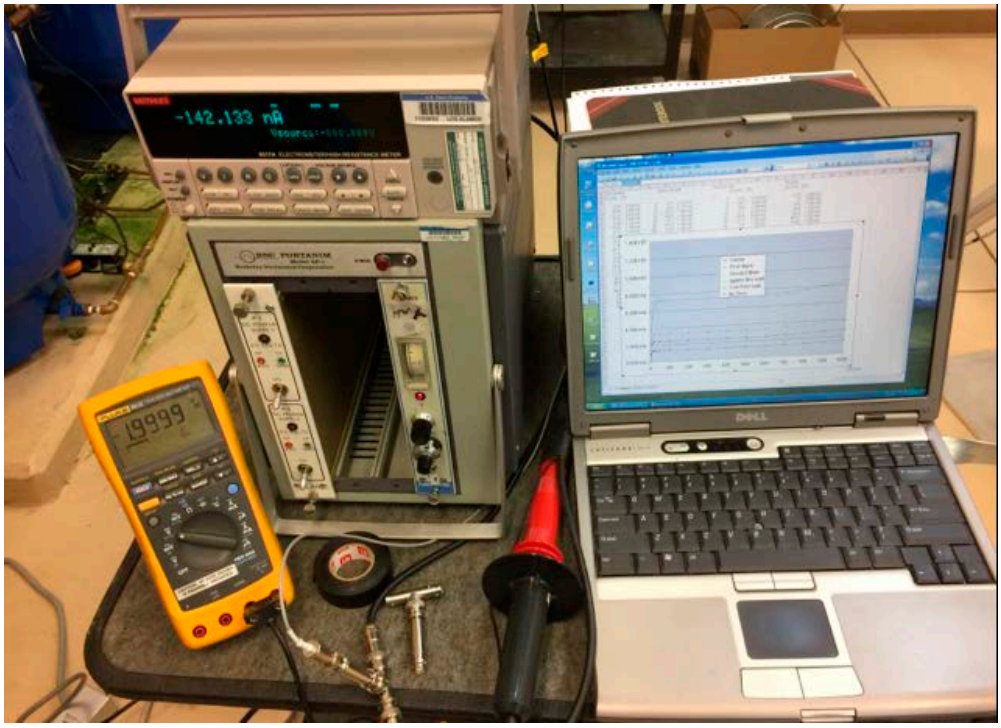

Figure 3- 21 *Measurement Setup: Canberra HV Bias Supply; Keithley DMM for control of HV bias; and Keithley electrometer mod 6517A for measuring of IC anode current*

Calibration at 500 R/h using ^{137}Cs Calibration Sources

The sensitivity of the IC gamma holder was calibrated using the gamma calibration system at the LANL RP-2 facility (see *Figure 3- 22*), which can generate gamma fields of the orders of mR/h to 750 R/h with NIST-traceable accuracy of +/-5%. The gamma IC was exposed to dose rates ranging from 1R/h to 750 R/h by changing the distance and strength of the ^{137}Cs radiation sources. The calibration measurement results are shown in *Figure 3- 23*. The plotted experimental data were used to determine the gamma sensitivity of the gamma holder as 2.05 pA/R/h. The good R^2 of the linear fit indicated good linear response in the calibration range of up to 750 R/h.

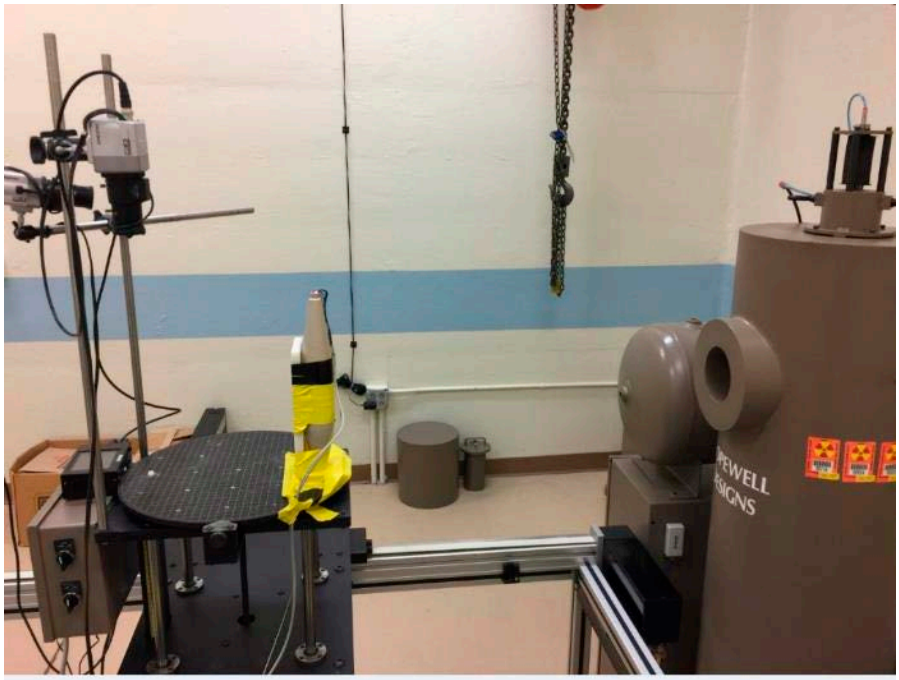

Figure 3- 22 *Experimental setup for calibration of gamma holder. The detector was placed with an offset of 15 cm order to extend the dose rate exposure to 750 R/h*

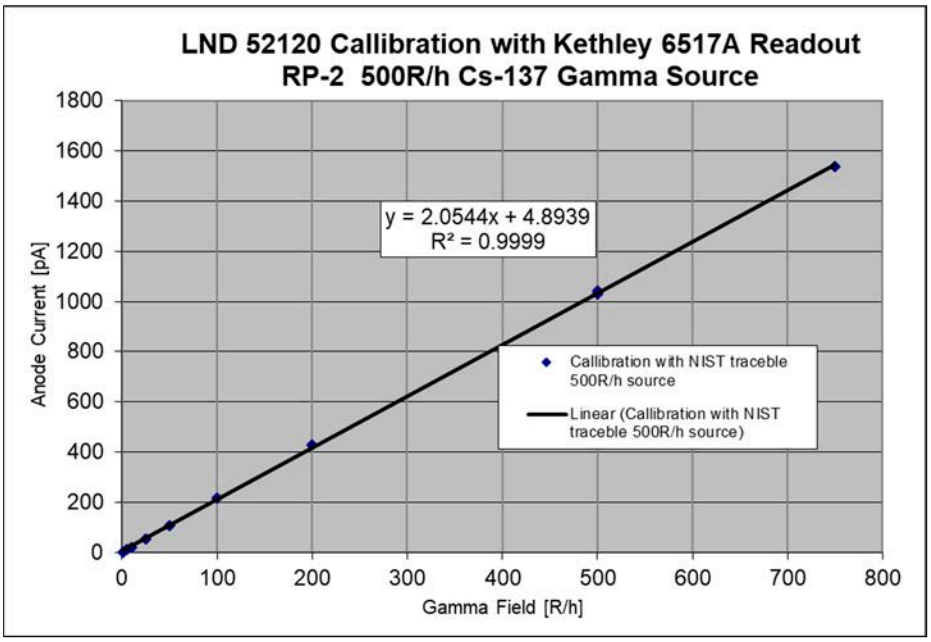

Figure 3- 23 *LND52120 calibration results showing anode current versus dose rate*

Calibration of Unattended Dual Current Monitor (UDCM) Instrument

As an alternative approach to the classical Keithley electrometer, LANL developed the UDCM, and

direct data readout to the computer was calibrated with a Keithley current calibrator mod 263 and used for the measurements. *Figure 3- 24* shows the experimental setup and a plot of the measured versus the calibration current. The calibration shows that UDCM can be used to record data automatically.

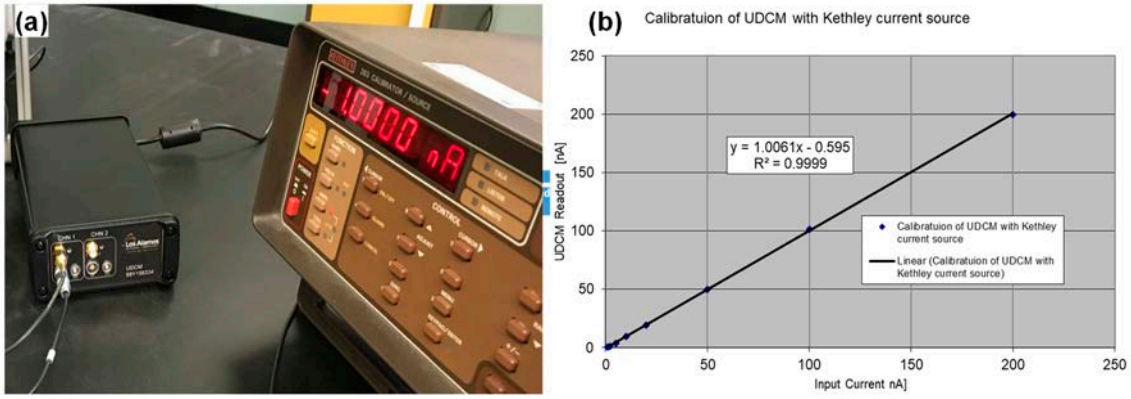

Figure 3- 24 *(a) Calibration setup with UDCM and Keithley 263 charge calibrator and (b) Plot of input value (Keithley 263 calibrator) versus value reported by UDCM currents*

Verification of Linearity of Gamma Holder for High Gamma Field

Additional calibration measurements at higher gamma dose rates were conducted at LANL by using the MARK-I Irradiator (see *Figure 3- 25*) to verify linearity by using a strong ^{137}Cs source that can provide a dose rate of up to 100 kR/h at the source and approximately 11 kR/h at the enclosure door.

Figure 3- 25 *Picture of ion chamber holder in MARK-I Irradiator*

A dummy enclosure was designed, in which we installed the MARK-I IC and used it to measure the gamma field inside the holder body and verify the linear response of the detector in the kR/h range gamma field. At the time of the experiments, the internal IC malfunctioned. Therefore, we conducted a more sophisticated experiment to verify detector linearity. We measured the anode current saturation plots versus anode voltage (called I-V plots in the literature) under different gamma fields (*Figure 3- 26a*). We exploited the fact that the nonlinear effects in the detector owing to charge carrier recombination will change the shape of the I-V plateau. Accordingly, we compared the shapes of I-V plateaus, as shown in *Figure 3- 26b*.

The results shown in *Figure 3- 26* indicate that the LND52120 IC saturates well below 100 V and can be operated under high gamma fields similar to those of typical spent fuel assemblies without signs of nonlinearity in the I-V characteristics.

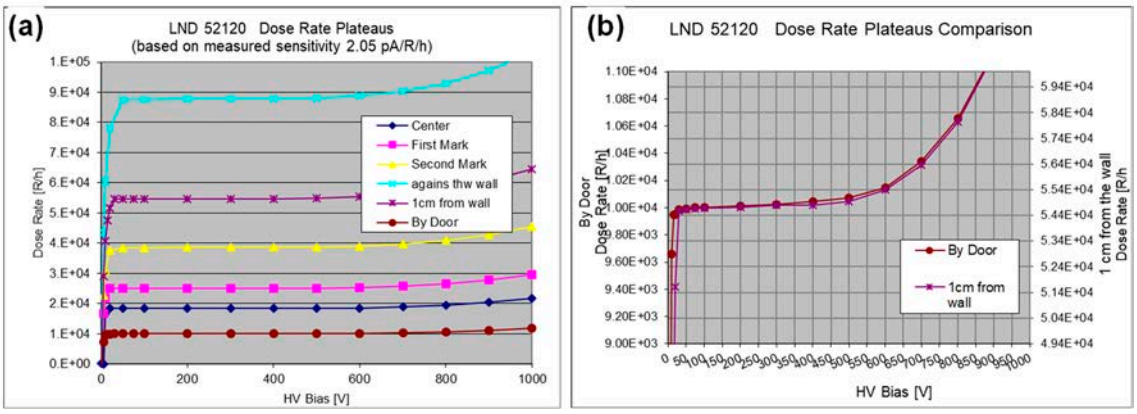

Figure 3- 26 *(a) I-V Plateau at different positions in MARK-I. The vertical scale was calibrated in dose rate units by using the calibration in 500 R/h source and (b) normalized at 300 V I-V Plateau taken at 11 kR/h (at door and 50 kR/h (1 cm from wall))*

(2) Confirmation of operation at JAEA

① Outline

We performed an irradiation experiment at JAEA (FRS) and compared the results with the calibration results obtained at LANL. We evaluated damages due to IC shipping from the U.S. to Japan and confirmed the soundness of the IC and the measurement system.

② Date and facility

Dec. 22, 2016

JAEA, Nuclear Science Research Institute, Facility of Radiation Standards (FRS)

③ Instruments used

IC, IC holder, picoammeter, and UDCM

④ Source and irradiation dose rates

・ Source: ^{60}Co, 7.4 TBq (Feb 2006)

・ Irradiation dose rates: 10 R/h, 25 R/h, 50 R/h, 75 R/h, 100 R/h

⑤ Measurement details

Figure 3- 27 shows the measurement scenario at FRS.

In the measurement, we set the IC holder with the IC detector on the irradiation base. Radiation dose rates were measured by changing distance from the source to the IC and converting the output current to the radiation dose rate. Irradiation dose rate settings were the same as those given under ④, and IC was irradiated for 5 min (the signals were averaged 10 times at intervals of 30 s).

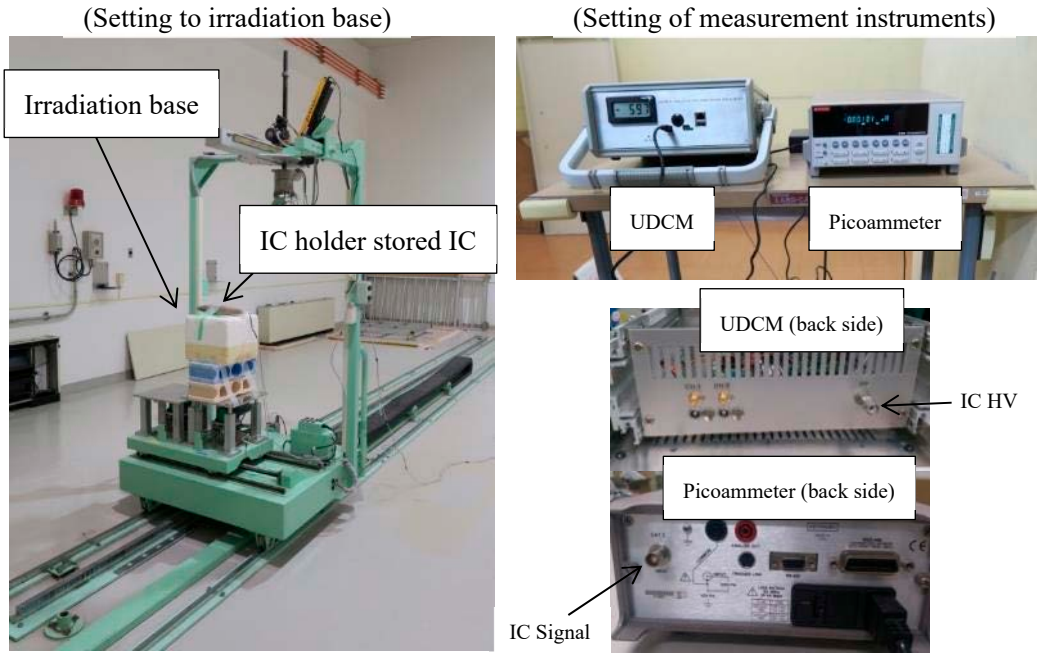

Figure 3- 27 *Measurement situation at FRS*

⑥ Results

Figure 3- 28 and *Table 3- 1* show the relationship between the irradiation dose rates and the output current of IC.

Relationship formula y [nA] = -1.9525E-3 x [R/h] – 1.4106E-3

We compared the results obtained using the LANL calibration formula with our measured data and found that our data was equivalent to the results obtained using the LANL calibration formula. The formula slope was about -5% with the LANL calibration formula. We suppose that differences of in geometrical condition and sensitivity to source (^{137}Cs at LANL) caused these differences. Because we confirmed the linearity of formula until 100 R/h, we checked for any damage owing to shipping from the U.S., and we could confirm that the IC and its measurement system work well.

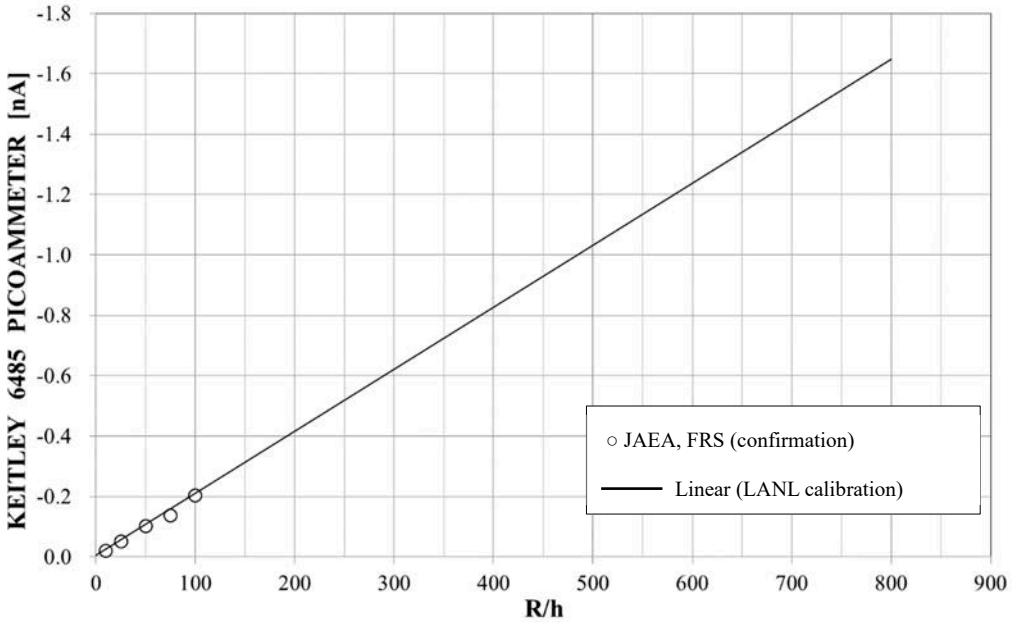

Figure 3- 28 *Correlation of irradiation dose rates and IC output current*

Table 3- 1 *Measurement results*

Measurement No.	Irradiation dose rates			Picoammeter average [nA]
	C/kg/h	R/h	Gy/h	
1	2.58E-03	1.00E+01	0.1	-0.021
2	6.45E-03	2.50E+01	0.2	-0.052
3	1.29E-02	5.00E+01	0.4	-0.102
4	1.94E-02	7.50E+01	0.7	-0.138
5	2.58E-02	1.00E+02	0.9	-0.202

(3) Confirmation of linearity at QST

① Outline

We confirmed the validity of the dose rates in the concrete cell, which were evaluated by extrapolating the LANL calibration formula. We confirmed the linearity of the LANL calibration curve at dose rates higher than those measured at LANL. We confirmed the angle dependence of the source because the tank angle changes at every measurement location on the guide rail.

② Date and facility

Feb. 27 and 28, 2017

QST, Takasaki Advanced Radiation Institute, Co., Second building, Fifth irradiation room

③ Instruments used

IC, IC holder, picoammeter, and UDCM

④ Source and irradiation dose rates

・ Source: ^{60}Co, 2,003 TBq (Jan. 10th, 2014) (*Figure 3- 29*)

・ Irradiation dose rates: 2,790 R/h to 23,400 R/h (11 setting values)

・ Angle dependence: 4,190 R/h × 0° to 180° (7 setting values)

⑤ Unit conversion

・ Gy = 33.97* × C/kg

* 33.97: W value of air (W value: Energy of an ion-pair formation in gas)

*Japan Industrial Standard: JIS Z4511 Methods of calibration for exposure meters, air kerma meters, air absorbed dose meters, and dose–equivalent meters

・ 1 R = 2.58E-4 × C/kg

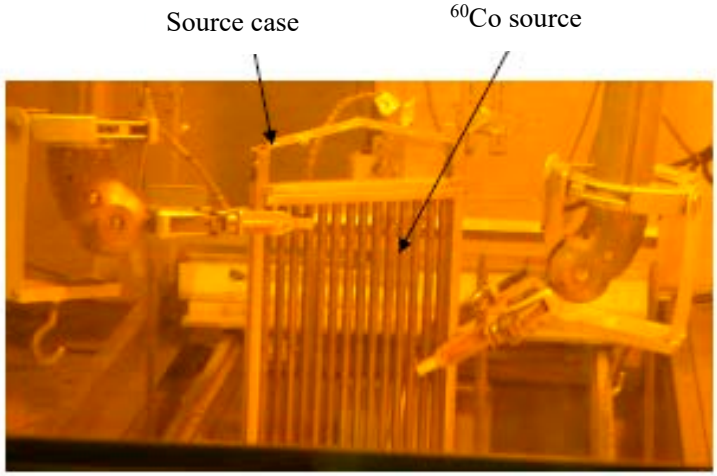

Reference「JAEA-Technology 2008-071」[9]

Figure 3- 29 *Example of ^{60}Co source*

⑥ Measurement detail

Figure 3- 30 shows the measurement schematic, and *Figure 3- 31* to *Figure 3- 35* show the measurement scenarios.

At first, we located the IC holder for storing the IC at any position in the irradiation room. Then, we located the dosimeter* calibrated in QST at the equivalent position. Measurements were performed with two instruments at the same time. The irradiation dose rates were based on the dosimeter. We set the irradiation dose rate in terms of angle dependence of the IC on the source to around the maximum value measured inside the concrete cell. We changed the angle of IC. Direction of the IC tip to source was 0°, and we performed measurements at intervals of 30° until 180°. We used the average of 10 measurement data for the evaluation.

* APPLIED ENGINEERING INC.　Parallel-plate ionization chamber (C-MA)

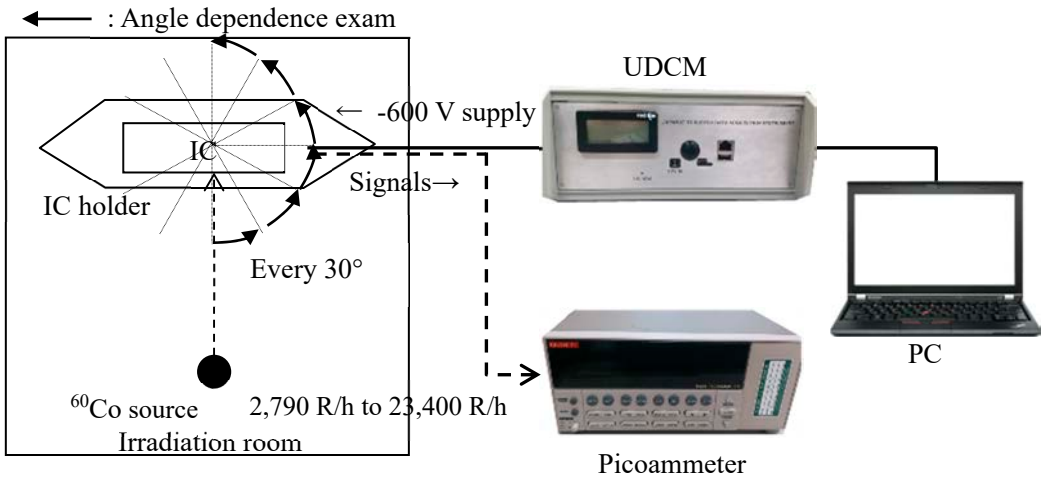

Figure 3- 30 *Measurement schematic*

Figure 3- 31 *Co second building, Fifth irradiation room*

Figure 3- 32 *Measurement situation*

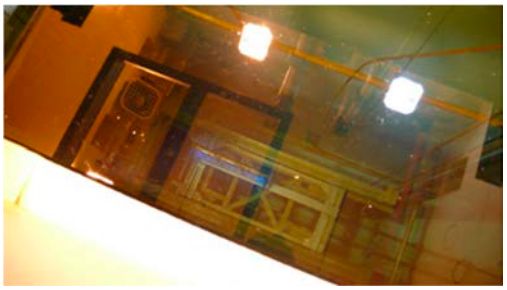

Figure 3- 33 *^{60}Co source*

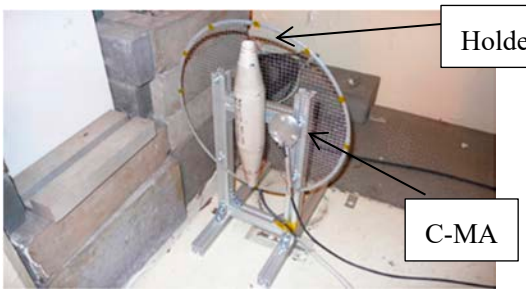

Figure 3- 34 *Irradiation examination situation*

Figure 3- 35 *Angle dependence examination*

⑦ Results

Figure 3- 36 and *Table 3- 2* show the relationship between irradiation dose rates and IC output current.

y [nA] = -2.1982E-3 x [R/h] -9.6646E-2

We compared the above formula to the LANL calibration formula and confirmed that they were equivalent. The formula shows linearity in the high dose rate area (until 23,400 R/h). The slope of the formula was about -7% compared to that of the LANL calibration formula, which is similar to the result at FRS. We suppose that this difference can be ascribed to different geometrical conditions and the type of source used.

Figure 3- 37 and *Table 3- 3* show the results of angle dependence of IC. As for the maximum, IC tip direction with respect to the source was 90°. If the value is 100%, the opposite direction (180°) for the source is approximately 60% of the minimum. Similarly, the value was equally low at 0°.

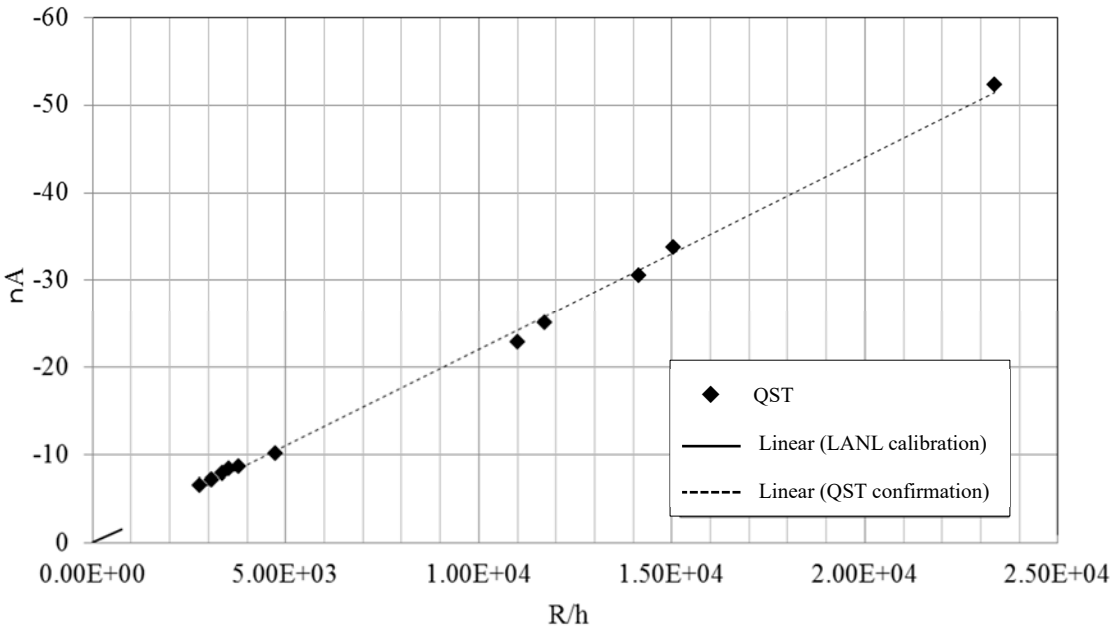

Figure 3- 36 *Relationship between irradiation dose rates and IC currrent*

Table 3- 2 *Measurement results*

Measurement No.	Irradiation dose rates			Picoammeter average [nA]
	C/kg/h	R/h	Gy/h	
1	2.84	1.10E+04	96.5	-22.915
2	3.02	1.17E+04	102.6	-25.126
3	1.22	4.73E+03	41.3	-10.118
4	0.80	3.10E+03	27.1	-7.143
5	0.72	2.79E+03	24.3	-6.532
6	0.87	3.37E+03	29.7	-7.904
7	0.91	3.53E+03	30.9	-8.373
8	0.98	3.80E+03	33.2	-8.671
9	3.88	1.50E+04	131.8	-33.715
10	3.65	1.41E+04	124.0	-30.551
11	6.03	2.34E+04	204.8	-52.343

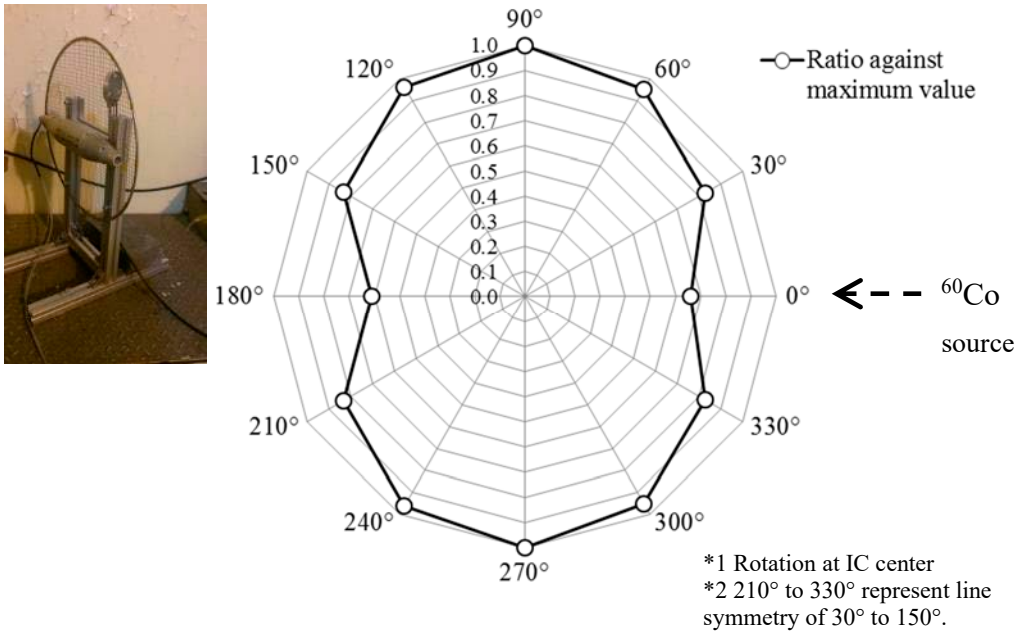

Figure 3- 37 *Angle dependence of IC*

Table 3- 3 *Angle dependence measurement results*

Measurement No.	Direction of IC tip for source	Irradiation dose rates			Picoammeter average [nA]	Difference rate compared with maximum value
		C/kg/h	R/h	Gy/h		
1	0°	1.08	4.19E+03	36.6	-5.939	0.66
2	30°	1.08	4.19E+03	36.6	-7.453	0.83
3	60°	1.08	4.19E+03	36.6	-8.551	0.95
4	90°	1.08	4.19E+03	36.6	-9.003	1.00
5	120°	1.08	4.19E+03	36.6	-8.646	0.96
6	150°	1.08	4.19E+03	36.6	-7.524	0.84
7	180°	1.08	4.19E+03	36.6	-5.483	0.61
―	210°	1.08	4.19E+03	36.6	-7.524	0.84
―	240°	1.08	4.19E+03	36.6	-8.646	0.96
―	270°	1.08	4.19E+03	36.6	-9.003	1.00
―	300°	1.08	4.19E+03	36.6	-8.551	0.95
―	330°	1.08	4.19E+03	36.6	-7.453	0.83

⑧ Summary

- We confirmed the linearity of the IC response up to approximately 23,400 R/h and the validity of the LANL calibration formula in high-dose-rate areas.
- The different slope obtained using the LANL calibration formula was likely because of the different geometric conditions and source type.
- The differences in the angle dependence of IC are up to ~40% along the direction of the IC relative to the source because of the different detection angles of the IC, which are influenced by IC column shape.
- The detection angle of the IC depends on the size of its radiation source. As the size of the radiation source is much larger than the size of IC. We did not need to care of the difference in angle dependence. Therefore, we assumed that dependence of the IC is low when conducting measurement at the HAW tanks.
- Placement of the IC relative to the source is sideways at most points from the drawings. It seems that there is little angle dependence of IC because the solution volume is large enough for the IC. There is little influence of angle dependence in this measurement.

⑨ Gamma-ray dose rate evaluation method

Gamma-ray dose rates were evaluated using the LANL calibration formulas corresponding to each measurement device. For the picoammeter, we applied the calibration formula shown in *Figure 3- 38* (output is negative) and recorded the measured current by visual observation. For the UDCM, we applied the calibration formula shown in *Figure 3- 39* (output is positive) and recorded the measured current by using a PC.

The time constant of IC is 1 s, but we stabilized it to 30 s to 1 min between measurements. For measurements using the picoammeter, the dose rate was calculated using an average of ten measured values. When using UDCM, the measurement time range was 30 s to 1 min. UDCM calculates the dose rate by using current* average as well.

*UDCM acquires the output current of IC at intervals of 100 ms and records the average of the setting time (s).

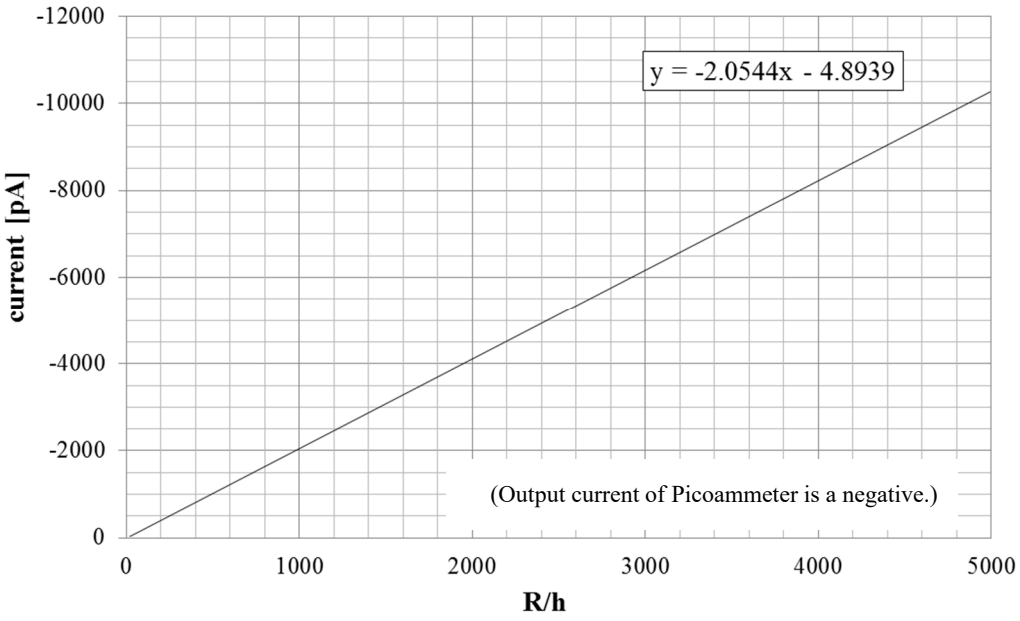

Picoammeter calibration formula $y\,[\mathrm{pA}] = -2.0544 \times [\mathrm{R/h}] - 4.8939$

Figure 3- 38 *Calibration formula (for evaluation using picoammeter)*

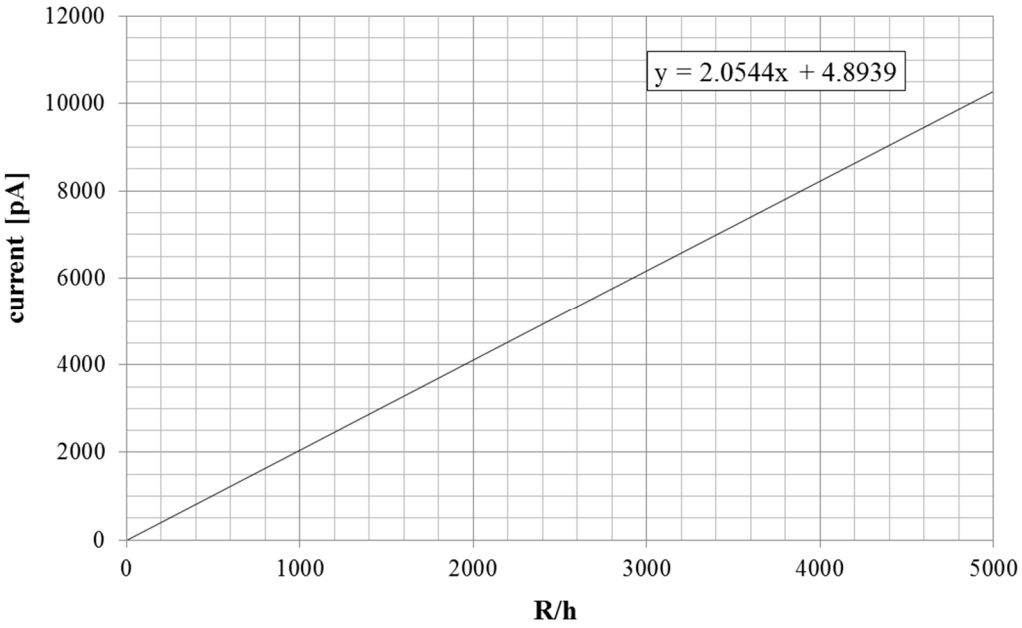

UDCM calibration formula $y\,[\mathrm{pA}] = 2.0544 \times [\mathrm{R/h}] + 4.8939$

Figure 3- 39 *Calibration formula (for evaluation using UDCM)*

A-5. Gamma-ray dose rate distribution measurement

A-5-1. Dose rate distribution measurement on route A

(1) Measurement

Figure 3- 40 shows an outline of the gamma-ray dose rate distribution measurement.

We selected the rail running from the upper to the lower side of the concrete cell for efficient gamma-ray dose rate measurement and the 272V35 tank with relatively high Pu concentration. In the measurement, we inserted the IC holder into the concrete cell and recorded measurements at distance intervals of 10 cm (to prevent shielding by the ring itself).

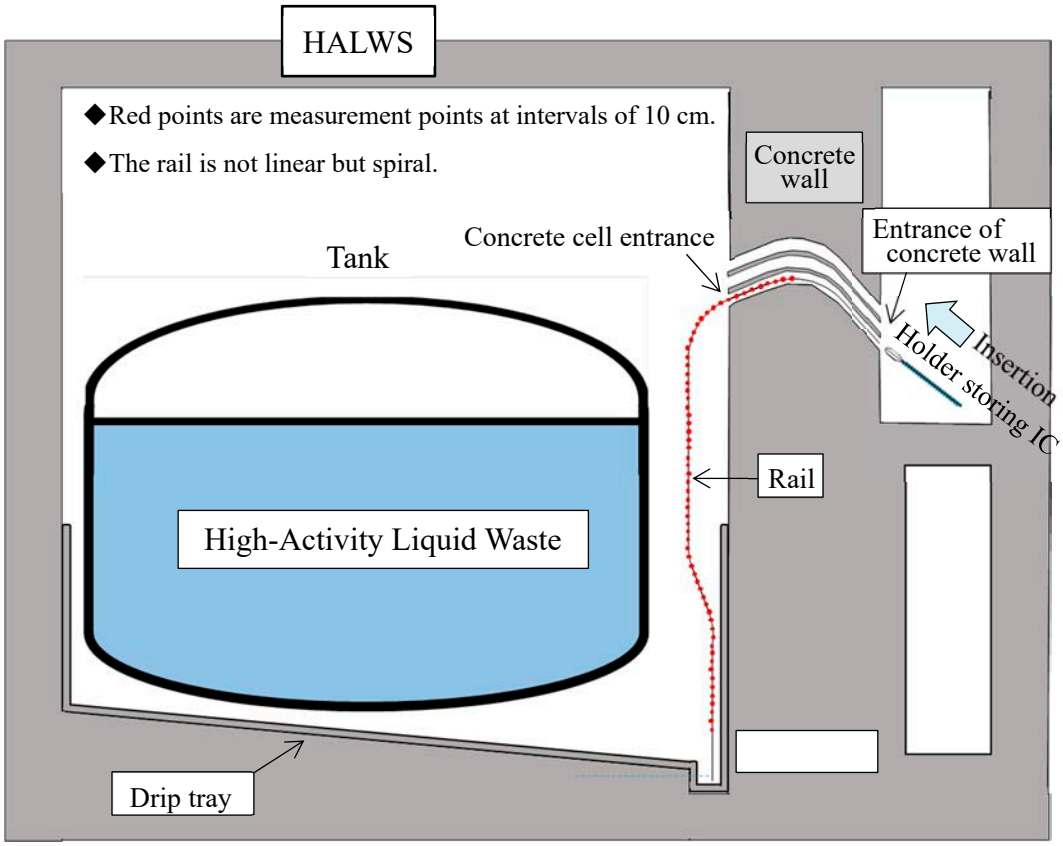

Figure 3- 40 *Outline of gamma-ray dose rate distribution measurement inside concrete cell*

【Conditions】

- Tank: 272V35
- Rail: Left lower inspection pipe (Route Y) at 272V35 (from upper concrete cell to drip tray)
- Measurement points: at intervals of 10 cm from ID 140 cm to ID 760 cm
- HV: -600 V
- Measurement device: Picoammeter
- Data recording: 10 times at every point (evaluation using average)

(2) Results

Figure 3- 41 and *Table 3- 4*, *Table 3- 5* show the gamma-ray dose rate distributions for various ID from the entrance of the concrete wall at 272V35.

① The gamma-ray dose rate increased gradually from ID 190 cm (in front of the concrete cell entrance).

② Gamma-ray dose rate decreased once at ID 320 cm.

③ After ID 320 cm, the gamma-ray dose rate increased with ID. The maximum dose rate was 2,368 R/h at ID 480 cm.

④ The maximum dose rate point was 90 cm lower than the liquid level.

⑤ After ID 480 cm, the gamma-ray dose rate decreased with ID. The dose rate dropped sharply at ID 720 cm.

⑥ Gamma-ray dose rate was not detected until around ID 180 cm.

⑦ We confirmed repeatability of the gamma-ray dose rates based on the data recorded on January 24, 2017 and January 25, 2017.

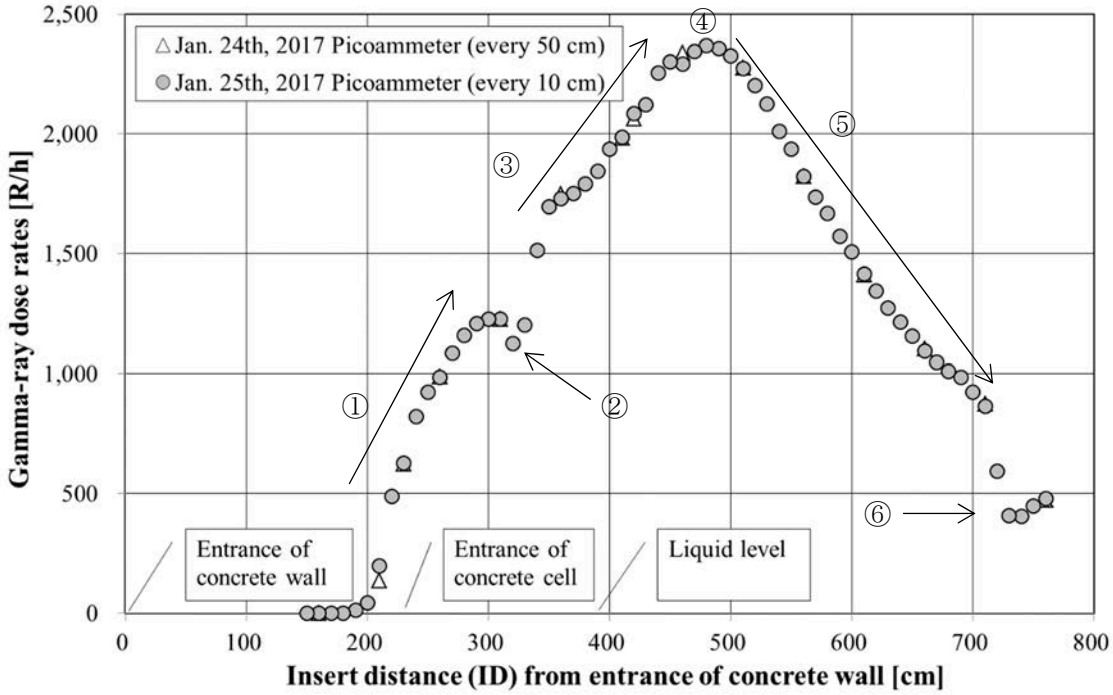

Figure 3- 41 *Gamma-ray dose rate distribution as a function of ID*

Table 3- 4 *Measurement results of gamma-ray dose rates (272V35) (Jan 24, 2017) (1/2)*

Measurement points	ID	Current average [nA]	Standard deviation [σ]	Coefficient variation [%]	R/h	C/kg/h[*1]	Gy/h[*2]
0	760 cm	-0.974	0.009	0.88	472	0.12	4.1
5	710 cm	-1.801	0.003	0.16	874	0.23	7.7
10	660 cm	-2.272	0.003	0.13	1,104	0.28	9.7
15	610 cm	-2.904	0.003	0.10	1,411	0.36	12.4
20	560 cm	-3.749	0.004	0.11	1,822	0.47	16.0
25	510 cm	-4.684	0.003	0.07	2,278	0.59	20.0
30	460 cm	-4.806	0.023	0.47	2,337	0.60	20.5

Table 3- 4 *Measurement results of gamma-ray dose rates (272V35) (Jan 24, 2017) (2/2)*

34	420 cm	-4.243	0.004	0.08	2,063	0.53	18.1
35	410 cm	-4.079	0.002	0.06	1,983	0.51	17.4
40	360 cm	-3.599	0.002	0.07	1,750	0.45	15.3
45	310 cm	-2.524	0.004	0.15	1,226	0.32	10.7
50	260 cm	-2.034	0.003	0.13	988	0.25	8.7
53	230 cm	-1.289	0.008	0.63	625	0.16	5.5
55	210 cm	-0.286	0.004	1.28	137	0.04	1.2
60	160 cm	-0.001	0.002	—	—	—	—

*1 C/kg = 2.58E-4×R

*2 Gy = 33.97×C/kg

Table 3- 5 *Measurement results of gamma-ray dose rates (272V35) (Jan 25, 2017) (1/3)*

Measurement points	ID	Current average [nA]	Standard deviation (σ)	Coefficient of variation (%)	R/h	C/kg/h	Gy/h
0	760 cm	-0.989	0.002	0.20	479	0.12	4.2
1	750 cm	-0.924	0.002	0.26	447	0.12	3.9
2	740 cm	-0.838	0.007	0.86	405	0.10	3.6
3	730 cm	-0.844	0.002	0.24	408	0.11	3.6
4	720 cm	-1.226	0.003	0.23	594	0.15	5.2
5	710 cm	-1.780	0.007	0.40	864	0.22	7.6
6	700 cm	-1.900	0.004	0.19	922	0.24	8.1
7	690 cm	-2.029	0.003	0.13	985	0.25	8.6
8	680 cm	-2.077	0.005	0.26	1,009	0.26	8.8
9	670 cm	-2.156	0.002	0.10	1,047	0.27	9.2
10	660 cm	-2.253	0.004	0.17	1,094	0.28	9.6
11	650 cm	-2.376	0.006	0.26	1,154	0.30	10.1
12	640 cm	-2.497	0.005	0.21	1,213	0.31	10.6
13	630 cm	-2.622	0.009	0.36	1,274	0.33	11.2
14	620 cm	-2.766	0.006	0.23	1,344	0.35	11.8
15	610 cm	-2.911	0.005	0.17	1,415	0.36	12.4
16	600 cm	-3.104	0.010	0.33	1,508	0.39	13.2
17	590 cm	-3.236	0.004	0.11	1,573	0.41	13.8
18	580 cm	-3.433	0.016	0.48	1,669	0.43	14.6

Table 3- 5 *Measurement results of gamma-ray dose rates (272V35) (Jan 25, 2017) (2/3)*

19	570 cm	-3.568	0.003	0.10	1,735	0.45	15.2
20	560 cm	-3.750	0.004	0.10	1,823	0.47	16.0
21	550 cm	-3.986	0.004	0.10	1,938	0.50	17.0
22	540 cm	-4.138	0.002	0.05	2,012	0.52	17.6
23	530 cm	-4.369	0.009	0.21	2,124	0.55	18.6
24	520 cm	-4.529	0.003	0.07	2,202	0.57	19.3
25	510 cm	-4.675	0.004	0.08	2,273	0.59	19.9
26	500 cm	-4.781	0.003	0.06	2,325	0.60	20.4
27	490 cm	-4.847	0.003	0.07	2,357	0.61	20.7
28	480 cm	-4.869	0.003	0.06	2,368	0.61	20.8
29	470 cm	-4.824	0.003	0.06	2,346	0.61	20.6
30	460 cm	-4.715	0.001	0.03	2,293	0.59	20.1
31	450 cm	-4.733	0.034	0.71	2,302	0.59	20.2
32	440 cm	-4.638	0.024	0.53	2,255	0.58	19.8
33	430 cm	-4.363	0.004	0.10	2,121	0.55	18.6
34	420 cm	-4.290	0.036	0.84	2,086	0.54	18.3
35	410 cm	-4.084	0.002	0.04	1,986	0.51	17.4
36	400 cm	-3.985	0.020	0.50	1,937	0.50	17.0
37	390 cm	-3.793	0.001	0.03	1,844	0.48	16.2
38	380 cm	-3.686	0.021	0.58	1,792	0.46	15.7
39	370 cm	-3.606	0.003	0.09	1,753	0.45	15.4
40	360 cm	-3.557	0.004	0.10	1,729	0.45	15.2
41	350 cm	-3.486	0.003	0.09	1,694	0.44	14.9
42	340 cm	-3.114	0.003	0.08	1,513	0.39	13.3
43	330 cm	-2.475	0.012	0.48	1,202	0.31	10.5
44	320 cm	-2.317	0.002	0.08	1,125	0.29	9.9
45	310 cm	-2.525	0.003	0.11	1,227	0.32	10.8
46	300 cm	-2.527	0.003	0.13	1,227	0.32	10.8
47	290 cm	-2.484	0.003	0.11	1,207	0.31	10.6
48	280 cm	-2.386	0.002	0.10	1,159	0.30	10.2
49	270 cm	-2.235	0.002	0.09	1,086	0.28	9.5
50	260 cm	-2.029	0.004	0.18	985	0.25	8.6
51	250 cm	-1.901	0.002	0.09	923	0.24	8.1
52	240 cm	-1.696	0.003	0.19	823	0.21	7.2

Table 3- 5 *Measurement results of gamma-ray dose rates (272V35) (Jan 25, 2017) (3/3)*

53	230 cm	-1.295	0.007	0.55	628	0.16	5.5
54	220 cm	-1.009	0.002	0.19	489	0.13	4.3
55	210 cm	-0.409	0.010	2.33	196	0.05	1.7
56	200 cm	-0.097	0.004	3.80	45	0.01	0.4
57	190 cm	-0.033	0.001	3.51	14	0.00	0.1
58	180 cm	-0.005	0.002	—	—	—	—
59	170 cm	-0.004	0.002	—	—	—	—
60	160 cm	-0.002	0.001	—	—	—	—
61	150 cm	-0.002	0.002	—	—	—	—

(3) Consideration

① Relationship of distance between measurement points and solution

The rail runs from the upper side to the lower side, heading to the drip tray inside the concrete cell. The distance from the rail to the tank changed according to the measurement points. Therefore, we determined the distance from the measurement points to the center of solution.

Figure 3- 42 shows the positional relationship between the rail and the tank. *Figure 3 - 43* shows the change in distance from the measurement points to the center of the solution.

The distance from the measurement points to the center of the solution decreases with ID. The point with the shortest distance from the center of the solution is around ID 460 cm, and decreased the value to drip tray.

- In *Figure 3 - 43*, the relationship between the dose rate distribution and the distance from the measurement points to the center of the solution shows good consistency.
- Based on the relationship between dose rate distribution and distance from the center of the solution in *Figure 3 - 43*, the dose rate distribution is influenced considerably by the distance from the IC to the source. We supposed that the detection angle of the IC for the source increases as IC approaches the source.
- Changes in the gamma-ray dose rate and distance from measurement points to center of the solution are consistent. The gamma-ray dose rate distribution is influenced by distance from IC to source.
- The point at which the gamma-ray dose rate is the maximum is 90 cm lower than the liquid level because at this point, the angle between the IC and the source is the largest, and there is an increase in gamma-ray incidence.
- We may be able to comprehend the concentration distribution (sediment of sludge, etc) in the solution by correcting the attenuation effect of distance.

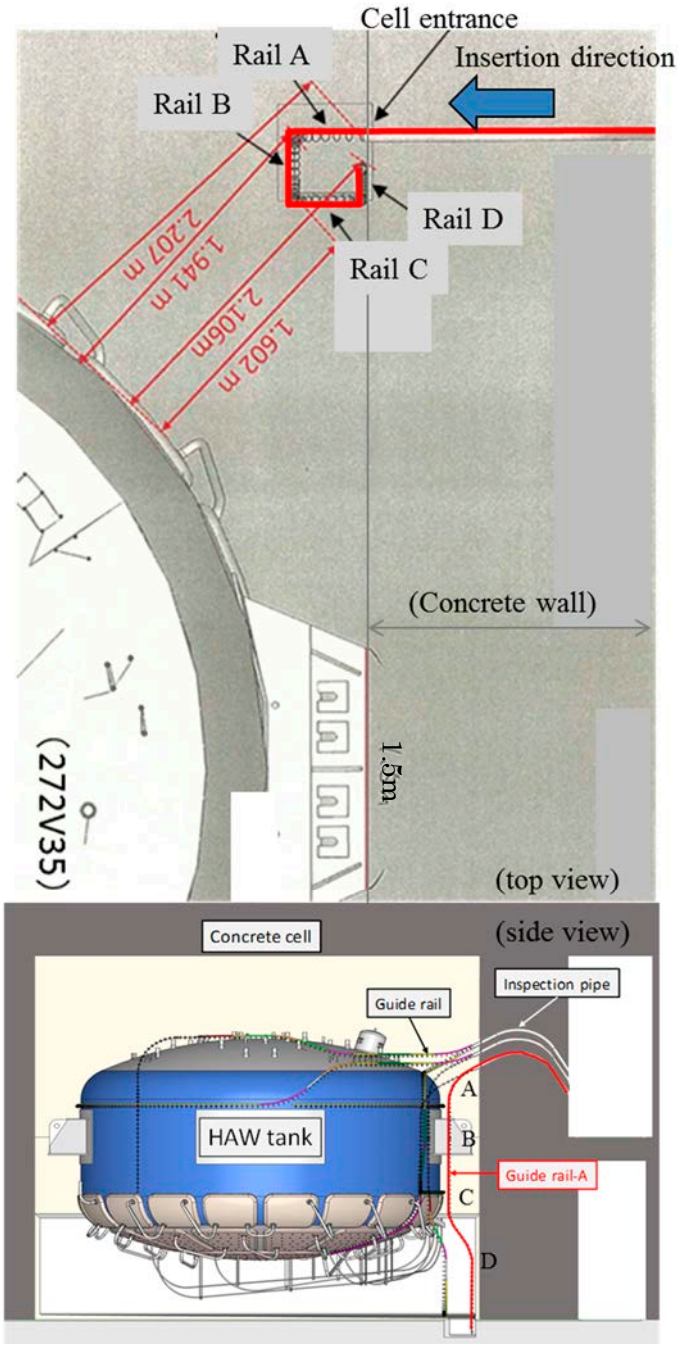

Figure 3- 42 *Positional relationship between rail and tank*

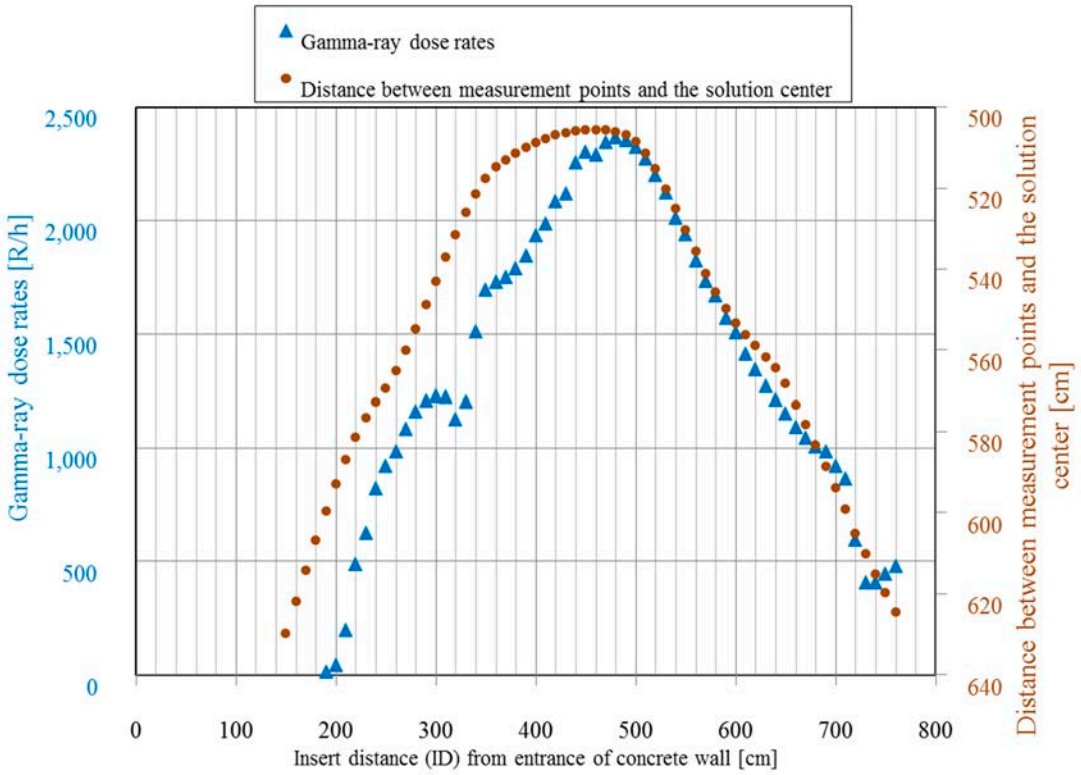

Figure 3- 43 *Relationship between ID and distance from measurement points to the center of solution*

② Cause of discontinuous region of gamma-ray dose rates

Gamma rays are mainly attenuated by shields. Based on the results of an investigation of the structures in the concrete cell, we confirmed that the other five rails, rail supports, pipes, and pipe supports can shield gamma rays.

Figure 3- 44 is a photo taken along the direction from the tank to the rail (around drip tray), and *Figure 3- 45* shows a schematic of the attenuation effect due to the pipe supports. The measurement rail is located behind the pipes and pipe supports.

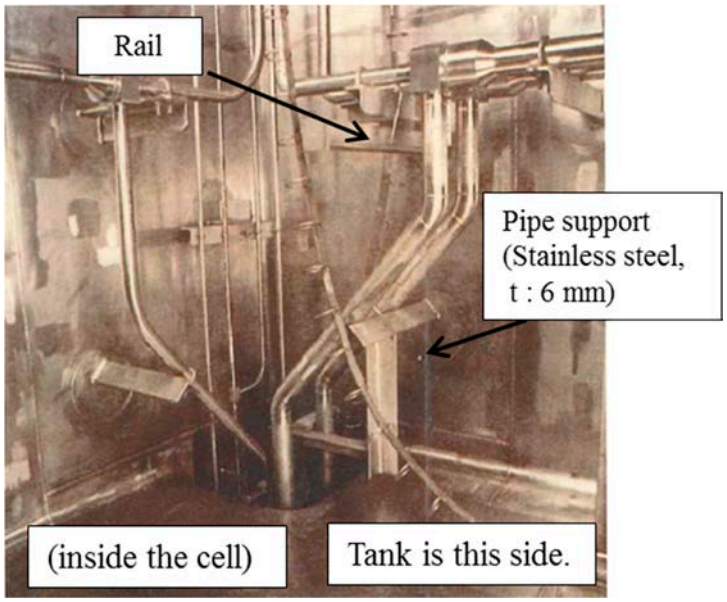

Figure 3- 44 *Photo of lower concrete cell (around drip tray)*

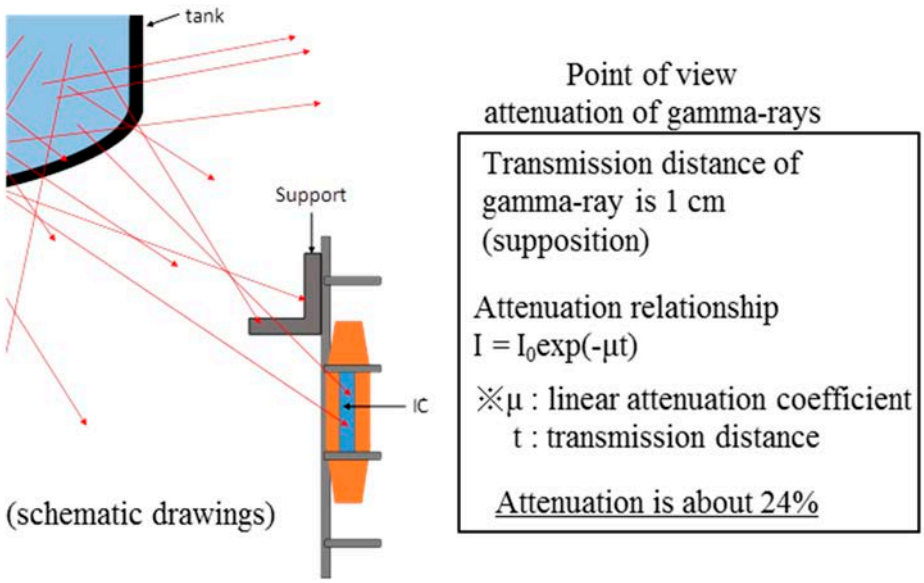

Figure 3- 45 *Attenuation effect of pipe support*

We confirmed that ID 720 cm corresponds to the position of the pipes and pipe supports.

- These 6-cm-thick pipe supports were made of stainless steel (SUS304). We examined the attenuation effect of stainless steel for dominant ^{137}Cs (662 keV).
- Because the steel pipe supports were L-shaped, we assumed a gamma-ray transmission distance of 1 cm and calculated the attenuation rate of 600 keV gamma-rays with a linear attenuation coefficient of 7.611E-2 cm^2/g (refer to Radioisotope pocket data book). As a result, we confirmed that the dose rate decreased by about 24% owing to the pipe supports.

- The reductions in dose rate at ID 320 cm and ID 720 cm were approximately 24% and 43%, respectively. The red dotted lines (*Figure 3- 46*) are assumed linear line. If we consider an attenuation rate of approximately 24%, the red dotted lines (gamma-ray dose rates corrected by straight lines) and the real gamma-ray dose rates show good consistency.
- Other rails and instrumentation pipes are far from the measurement rail. We suppose these components have little influence because the detection angle for the IC is very small relative to that for the tank.
- The rail supports do not have the shielding effect for IC.
- Based on these factors, we believe the decreases in dose rate can mainly be ascribed to the pipe supports. During measurements, it is necessary to confirm these positions in order to understand the measurement results.

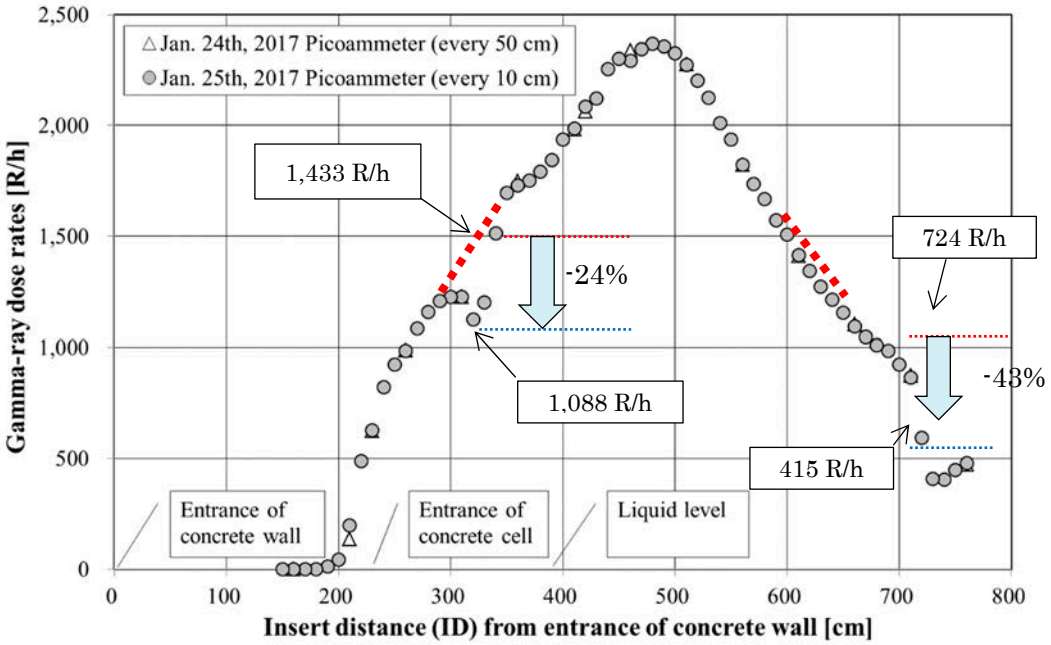

Figure 3- 46 *Gamma-ray dose rate distribution (correlation of attenuation effect)*

(4) Coefficient of variation of measurement data (additional measurement)

① Purpose of evaluation

We confirmed the influence of the distance to source and shielding by structures. Then, we confirmed the coefficient variation (reliability) of the measurement values from these plural data.

② Results

Figure 3- 47 and *Table 3- 4*, *Table 3- 5* show the coefficient of variation of the measurement data.

At low dose rates (until approximately 100 R/h), the coefficient of variation was less than 4%. At dose rate higher than 100 R/h, the coefficient of variation was small. At dose rates higher than 400 R/h, the coefficient of variation was less than 1%.

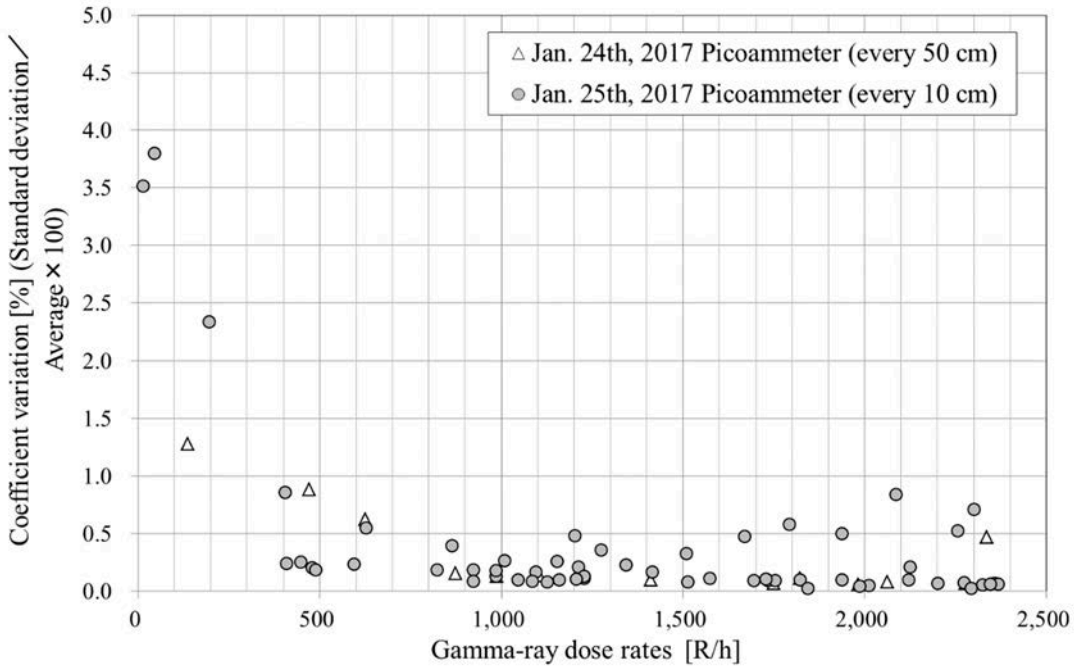

Figure 3- 47 *Coefficient of variation of gamma-ray dose rates (272V35)*

③ Consideration

The dispersion was ~1% at gamma-ray dose rates higher than 400 R/h. In another range, the dispersion was less than 4%. We confirmed that the measured values had good repeatability.

A-5-2. Dose rate distribution measurement on route B

(1) Measurement

Figure 3- 48 shows an outline of the gamma-ray dose rate distribution measurement on route B (red line).

The guide rail of route B was installed in the concrete cell to observe the surfaces of the middle and bottom parts of the 272V35 tank. Thus, the dose rate distribution near the tank and the bottom of the tank could be obtained.

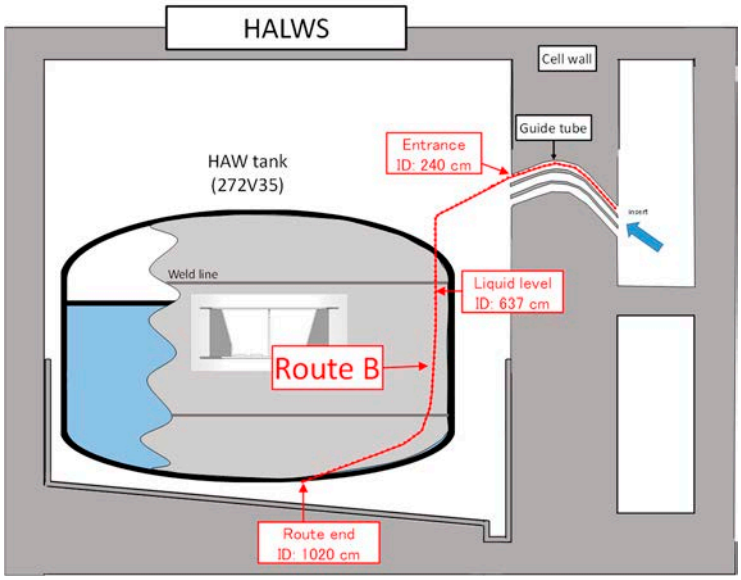

Figure 3- 48 *Outline of gamma-ray dose rate distribution measurement inside concrete cell*

【Conditions】

- Tank: 272V35
- Rail: Left lower inspection pipe (Route B) at 272V35 (from upper concrete cell to drip tray)
- Measurement points: At intervals of 10 cm from ID 180 cm to ID 950 cm
- HV: -600 V
- Measurement device: Picoammeter
- Data: 10 times at every point (evaluation using average)

(2) Result

Figure 3- 49 and *Table 3- 6* show the gamma-ray dose rate distribution for various IDs from entrance of the concrete wall at 272V35.

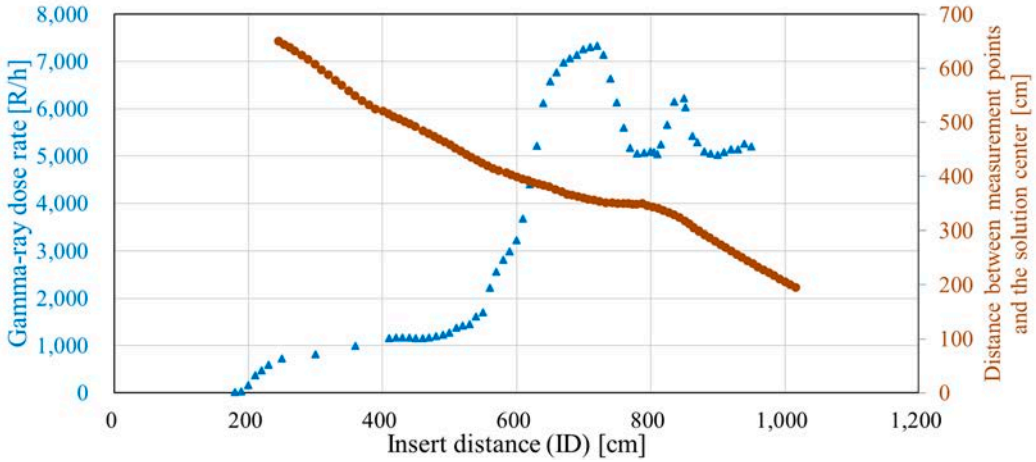

Figure 3- 49 *Gamma-ray dose rate distribution as a function of ID on route B*

Table 3- 6 *Measured gamma-ray dose rates (272V35) (Aug 25, 2017) (1/2)*

ID	Current [nA]	Standard deviation (σ)	Coefficient of variation (%)1	Dose rate [R/h]
950 cm	-10.691	0.005	0.046	5201.7
940 cm	-10.811	0.002	0.021	5259.8
930 cm	-10.559	0.001	0.012	5137.4
920 cm	-10.574	0.001	0.011	5144.7
910 cm	-10.441	0.001	0.012	5079.7
900 cm	-10.317	0.001	0.009	5019.5
890 cm	-10.373	0.001	0.009	5046.7
880 cm	-10.461	0.001	0.008	5089.8
870 cm	-10.857	0.004	0.037	5282.4
863 cm	-11.124	0.004	0.040	5412.5
852 cm	-12.395	0.002	0.016	6031.2
850 cm	-12.791	0.001	0.005	6223.7
835 cm	-12.625	0.004	0.029	6143.1
825 cm	-11.615	0.002	0.014	5651.5
815 cm	-10.765	0.001	0.014	5237.7
810 cm	-10.347	0.001	0.005	5034.2
805 cm	-10.425	0.001	0.012	5072.2
800 cm	-10.482	0.001	0.007	5099.6
790 cm	-10.413	0.001	0.011	5066.4
780 cm	-10.383	0.001	0.009	5051.5
770 cm	-10.619	0.001	0.012	5166.6
760 cm	-11.491	0.022	0.189	5590.9
750 cm	-12.593	0.003	0.027	6127.5
740 cm	-13.641	0.001	0.007	6637.4
730 cm	-14.668	0.004	0.026	7137.5
720 cm	-15.076	0.001	0.007	7336.0
710 cm	-15.017	0.001	0.008	7307.5
700 cm	-14.915	0.001	0.007	7257.7
690 cm	-14.658	0.002	0.011	7132.5
680 cm	-14.530	0.001	0.008	7070.1
670 cm	-14.321	0.001	0.007	6968.6
660 cm	-13.909	0.002	0.012	6767.7

Table 3- 6 *Measured gamma-ray dose rates (272V35) (Aug 25, 2017) (2/2)*

650 cm	-13.506	0.001	0.009	6571.9
640 cm	-12.556	0.124	0.988	6109.6
630 cm	-10.699	0.001	0.011	5205.7
620 cm	-9.031	0.002	0.019	4393.5
610 cm	-7.545	0.001	0.016	3670.4
600 cm	-6.630	0.001	0.019	3224.8
590 cm	-6.149	0.001	0.023	2990.6
580 cm	-5.788	0.001	0.009	2815.0
570 cm	-5.267	0.001	0.016	2561.2
560 cm	-4.556	0.001	0.030	2215.4
550 cm	-3.499	0.001	0.020	1700.8
540 cm	-3.302	0.010	0.305	1605.0
530 cm	-2.980	0.011	0.363	1448.2
520 cm	-2.928	0.001	0.019	1422.8
510 cm	-2.821	0.001	0.028	1371.0
500 cm	-2.610	0.000	0.017	1268.2
490 cm	-2.533	0.001	0.021	1230.5
480 cm	-2.473	0.001	0.022	1201.6
470 cm	-2.394	0.000	0.020	1162.7
460 cm	-2.377	0.001	0.040	1154.7
450 cm	-2.378	0.000	0.018	1155.4
440 cm	-2.388	0.001	0.025	1159.8
430 cm	-2.389	0.008	0.347	1160.7
420 cm	-2.408	0.003	0.141	1169.8
410 cm	-2.370	0.003	0.133	1151.0
360 cm	-2.038	0.000	0.013	989.5
300 cm	-1.679	0.000	0.023	815.1
250 cm	-1.475	0.000	0.034	715.4
230 cm	-1.227	0.003	0.227	594.8
220 cm	-0.965	0.003	0.346	467.6
210 cm	-0.751	0.000	0.037	363.2
200 cm	-0.325	0.020	6.288	155.9
190 cm	-0.059	0.001	1.125	26.5
180 cm	-0.013	0.000	0.872	3.9

(3) Consideration

Figure 3- 50 shows the arrangement between IC position and ID on route B. Dose rate distribution increases from ID 0 cm to ID 640 cm because the distance between the HALW and the IC decreases. The maximum dose rate was measured at ID 720 cm, 80 cm below the liquid level. This trend is same as that for route A.

After ID 720 cm, the dose rate distribution is complex, although the distance between the solution and the IC does not differ significantly. Moreover, after ID 720 cm, there is no equipment inside the tank, such as supports, as shown in *Figure 3- 51*. Therefore, it can be said that the dose rate distribution at the tank bottom is affected by sludge deposition.

A comparison of the dose rate distributions calculated by MCNP simulation and the measurement result can reveal information about distribution of the deposited sludge because the dose rate distribution obtained by MCNP simulation is not affected by sludge.

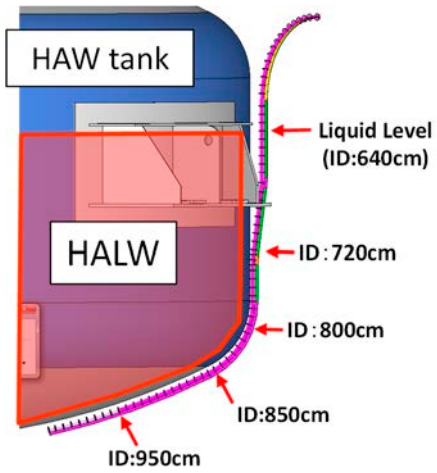

Figure 3- 50 *Arrangement between IC position and ID on route B*

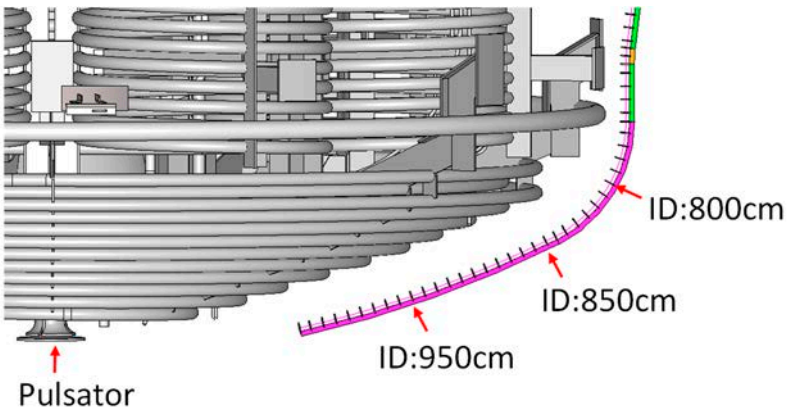

Figure 3- 51 *Arrangement of equipment inside tank after ID 800 cm*

A-6. Comparison between 272V35 and 272V34

(1) Purpose of measurement

We measured the gamma-ray dose rate distribution of 272V34 to confirm the correlation between total quantity of gamma rays and the gamma-ray dose rate. We selected the same positional entrance for comparison at the same positional relationship for the tank, but these rails(V34 route Z and V35 route X) were on a different route. Even if these rails were on different routes, their positional relationship with each tank would be the same until ID 300 cm. We confirmed the same positional relationship on the drawings (*Figure 3- 52*).

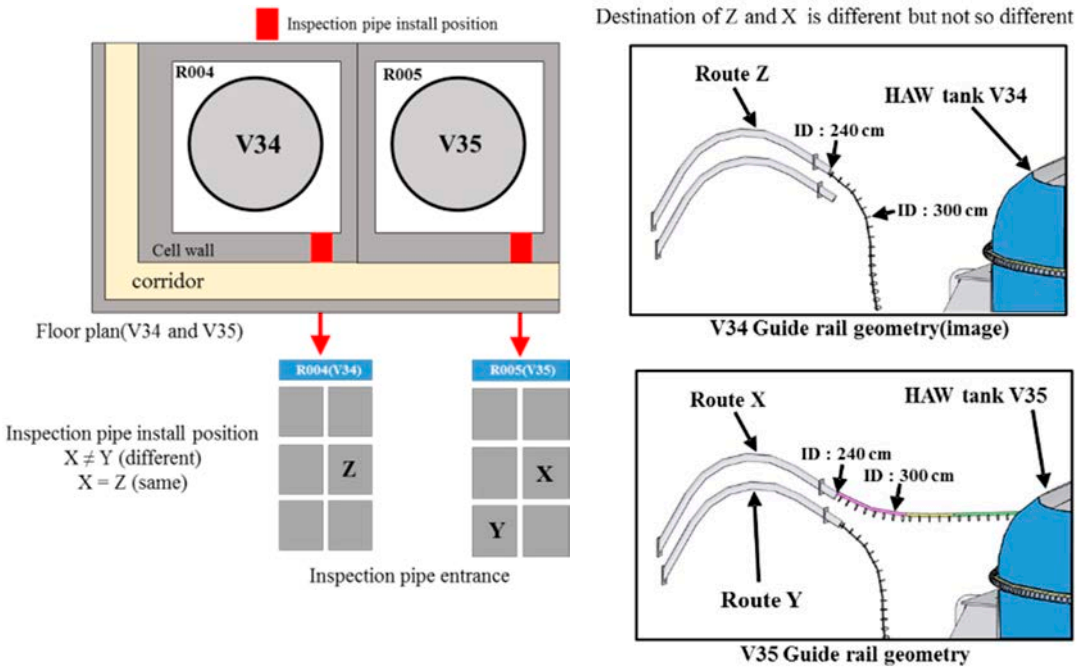

Figure 3- 52 *Positional relationship of routes for comparison*

【Conditions】

・Tanks: 272V35 (Route X), 272V34 (Route Z)

・Rails: Right and middle inspection pipes at both tanks

・Measurement points: at intervals of 10 cm from ID 160 cm to ID 300 cm

・High voltage: - 600 V

・Measurement device: Picoammeter

・Data recording: 10 times at every point (evaluation using average)

(2) Results

Figure 3- 53 and *Table 3- 7* show the measured gamma-ray dose rate distributions for various IDs

from the entrance of the concrete wall at 272V35 and 272V34. *Table 3- 8* shows the analysis results of the solution for each tank.

① Gamma-ray dose rate increased in small steps from ID 190 cm.

② Gamma-ray dose rate was approximately 650 R/h at ID 230 cm (entrance of concrete cell).

③ A significant gamma-ray dose rate was measured from ID 190 cm at tanks 272V35 and 272V34.

④ Gamma-ray dose rates at 272V34 and 272V35 were approximately the same inside the concrete wall.

⑤ We confirmed differences in gamma-ray dose rates for ID ≥ 270 cm inside the concrete cell.

・ Total gamma-ray activity based on the analytical data of ^{137}Cs in 272V34 was approximately 30% higher than that in 272V35. By contrast, the measured dose rate at 272V35 was higher than that at V34 from ID 270 to ID 300 cm.

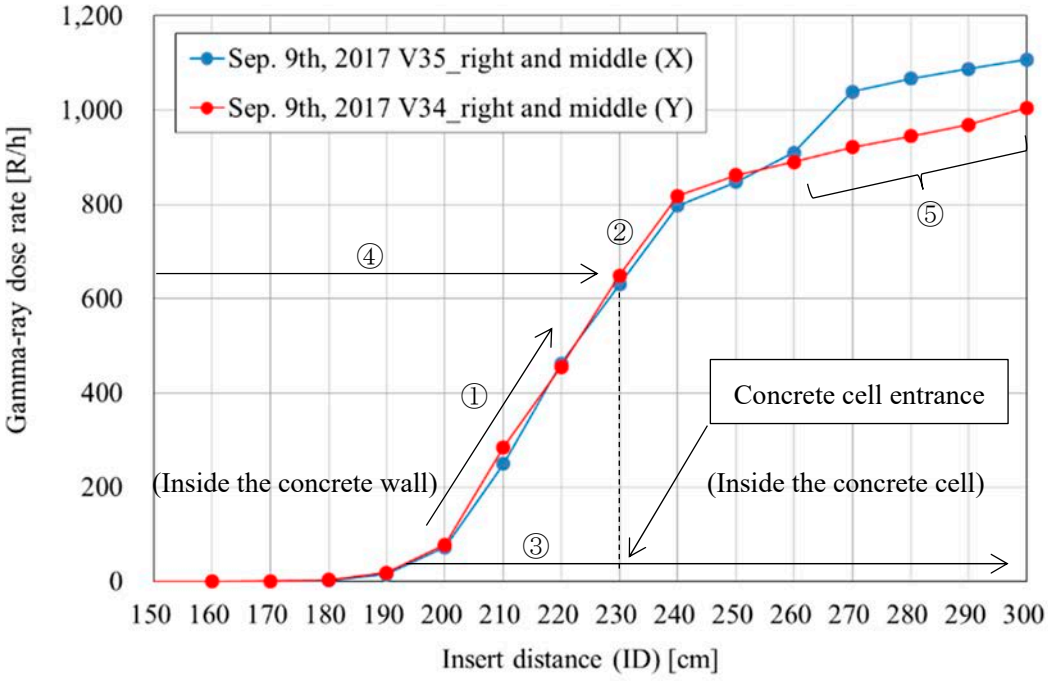

Figure 3- 53 *Gamma-ray dose rate distribution as a function of ID*
(Comparison of 272V35 and 272V34)

Table 3- 7 *Comparison of gamma-ray dose rates in 272V35 and 272V34*

Measurement routes	ID	Current [nA]	Standard deviation	Coefficient of variation [%]	Gamma-ray dose rates [R/h]
Sep 26, 2017 Right and middle Route X at 272V35	300 cm	-2.280	0.001	0.04	1,107.4
	290 cm	-2.239	0.000	0.02	1,087.7
	280 cm	-2.197	0.001	0.02	1,067.2
	270 cm	-2.141	0.003	0.12	1,039.6
	260 cm	-1.874	0.001	0.03	910.0
	250 cm	-1.747	0.000	0.02	848.2
	240 cm	-1.643	0.000	0.03	797.5
	230 cm	-1.299	0.000	0.02	630.1
	220 cm	-0.955	0.000	0.04	462.4
	210 cm	-0.517	0.000	0.06	249.3
	200 cm	-0.155	0.000	0.09	72.9
	190 cm	-0.036	0.000	0.68	15.1
	180 cm	-0.009	0.000	1.26	1.8
	170 cm	-0.003	0.000	4.82	-1.0
	160 cm	-0.001	0.000	10.00	-1.7
	150 cm	-0.001	0.000	18.76	-2.1
Sep 26, 2017 Right and middle Route Y at 272V34	300 cm	-2.069	0.001	0.03	1,004.9
	290 cm	-1.996	0.000	0.02	969.1
	280 cm	-1.945	0.000	0.02	944.6
	270 cm	-1.897	0.000	0.03	921.2
	260 cm	-1.834	0.000	0.03	890.2
	250 cm	-1.777	0.000	0.03	862.6
	240 cm	-1.686	0.000	0.03	818.4
	230 cm	-1.339	0.000	0.02	649.3
	220 cm	-0.940	0.000	0.03	455.4
	210 cm	-0.590	0.000	0.03	284.9
	200 cm	-0.166	0.000	0.09	78.4
	190 cm	-0.044	0.001	1.45	19.0
	180 cm	-0.012	0.000	1.95	3.4
	170 cm	-0.007	0.000	0.78	1.0
	160 cm	-0.005	0.000	1.51	0.1
	150 cm	-0.004	0.000	2.76	-0.3

Table 3- 8 *Solution analysis results of 272V35 and 272V34*

Tank No. Items	272V35		272V34	
Sampling date	Feb 7, 2017		Feb 8, 2017	
Density (g/mL)	1.249		1.191	
Pu (mg/L)	Filtrated	Dissolved sludge	Filtrated	Dissolved sludge
	238	356	177	250
Cm (Bq/mL)	2.9×10^{7}	4.1×10^{7}	3.8×10^{7}	3.0×10^{7}
U (g/L)	6.65		5.18	
^{241}Am (Bq/mL)	6.9×10^{7}		1.0×10^{8}	
^{137}Cs (Bq/mL)	2.9×10^{9}		3.5×10^{9}	
Total-gamma*	2.2×10^{17} Bq		2.8×10^{17} Bq	

* Total intensity because ^{137}Cs is dominant gamma-ray

(3) Consideration

① We confirmed the difference in gamma-ray dose rate based on gamma intensity, but we couldn't confirm the correlation between the total gamma intensity and the gamma-ray dose rates inside the concrete wall (Penetration pipe, until ID 230 cm). The attenuation effects of the gamma rays inside the concrete wall were high, and we believe it is mainly because of scattering of gamma rays, as opposed to direct radiation.

② After ID 270 cm, the gamma-ray dose rates of 272V35 rose more than those of 272V34. We believe that the gamma rays permeated easily because the density of 272V35 was lower than that of 272V34.

③ It is necessary to obtain additional measurement data inside the concrete cells and compare the results with those of other tanks to confirm the influence of different solution compositions on the gamma-ray dose rates.

A-7. Gamma-ray dose rate monitoring

A-7-1. Route A

(1) Purpose of measurement

Figure 3- 54 shows a schematic drawing of gamma-ray dose rate monitoring.

The solution in the tank is stirred regularly using a pulsator to ensure that the solution is relatively uniform at the center of the tank. Stirring was performed by downward pulsator of air at the center of the tank. However, the air was not transferred into the solution. The pulsator was operated automatically at intervals of 6 min, and the liquid level rose by approximately 45 mm as a result. This

measurement target confirmed the relationship between the change in solution level and the gamma-ray dose rate.

We set the measurement time to longer than the 6-min pulsator operation interval and selected three measurement points in the concrete cell, namely, entrance of the concrete cell, at liquid level, and bottom of the tank. These measurements were performed in the 272V35 tank, in which a significant gamma-ray dose rate distribution was measured on the same route.

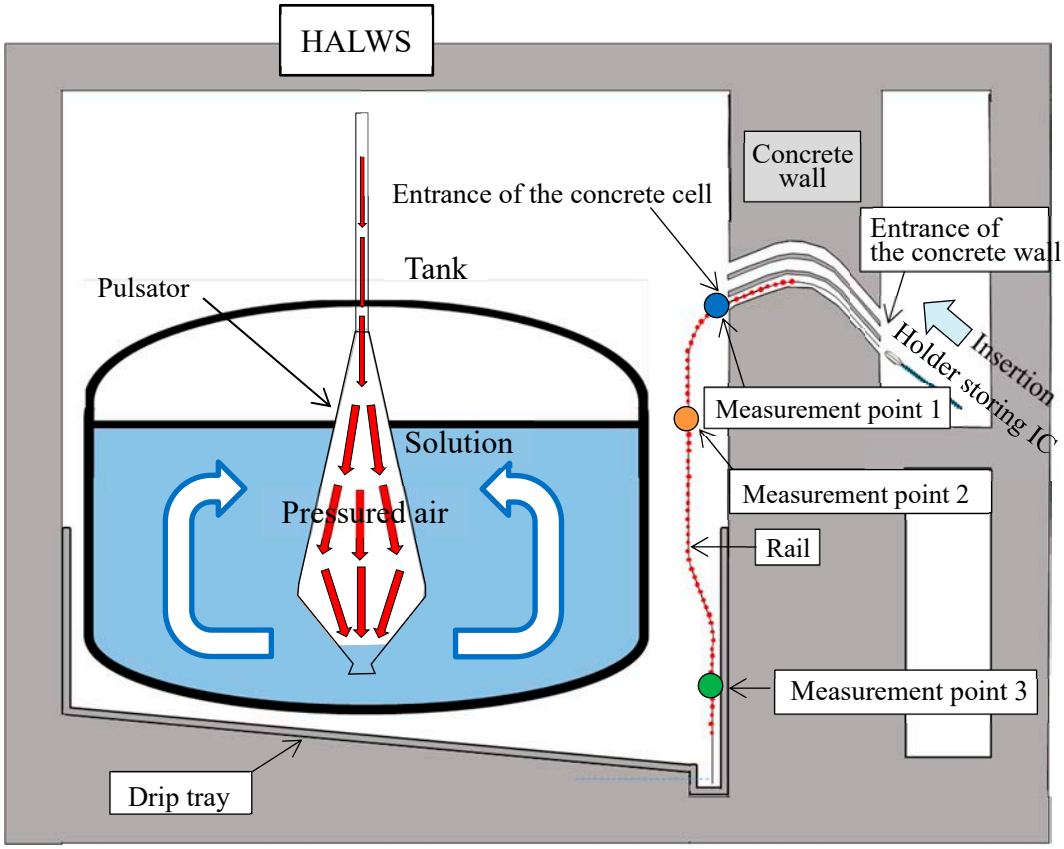

Figure 3- 54 *Schematic drawing of gamma-ray dose rate monitoring*

【Conditions】

・Tank: 272V35

・Rail: Left lower inspection pipe (Route Y)

・Measurement points: ID 230 cm (entrance of concrete cell), ID 400 cm (liquid level), ID 760 cm (bottom of tank)

・HV: -600 V

・HV and data acquisition device: UDCM

・Measurement time: approximately 20 min

・Data recording: at intervals of 1 s (the data acquired were averages of the data obtained at intervals of 100 ms)

(2) Point 1 measurement result (Concrete cell entrance: ID 230 cm) (*Figure 3- 55*)

① The gamma-ray dose rate changed in conjunction with the change in liquid level as a result of pulsator operation, but there was no significant correlation.

② Gamma-ray dose rate increased in the cycle longer than the 6-min pulsator operation cycle from about 15:10 to 15:20.

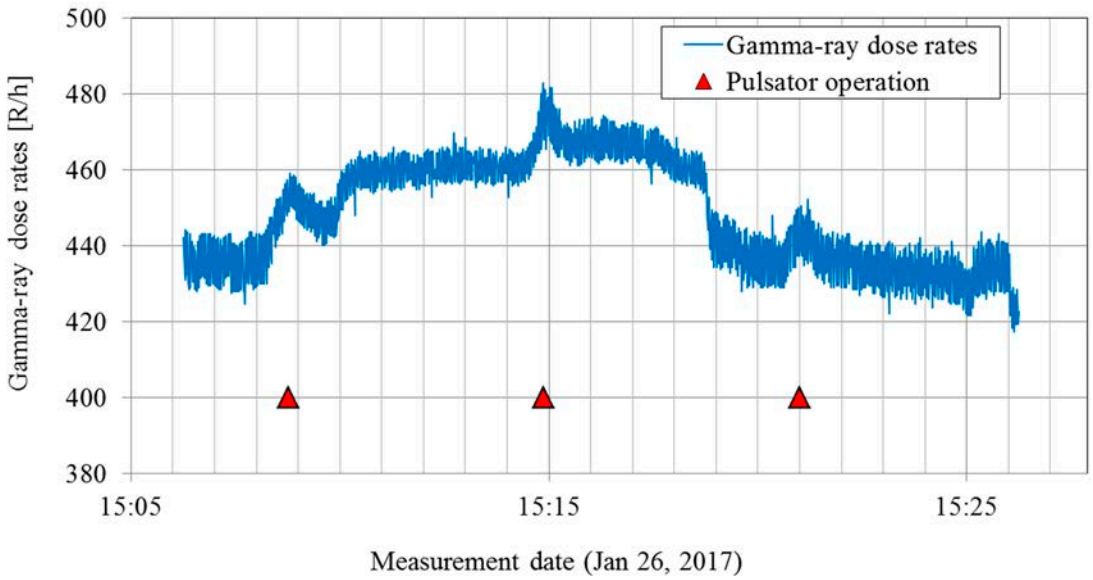

Figure 3- 55 *Result of gamma-ray dose rate monitoring at point 1*

(3) Point 2 measurement result (Around liquid level: ID 400 cm) (*Figure 3- 56*)

① We confirmed a significant correlation between changes in the liquid level and changes in the gamma-ray dose rate.

② It is possible to monitor the liquid level based on changes in the gamma-ray dose rate.

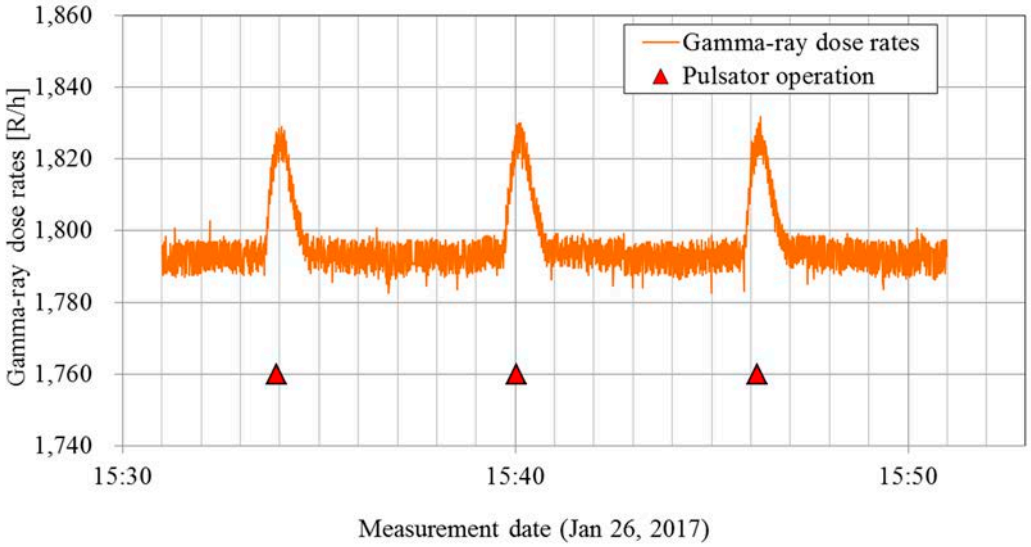

Figure 3- 56 *Result of gamma-ray dose rate monitoring at point 2*

(4) Point 3 measurement result (Bottom of tank : ID 760 cm) (*Figure 3- 57*)

There was no correlation between changes in the liquid level and changes in the gamma-ray dose rate.

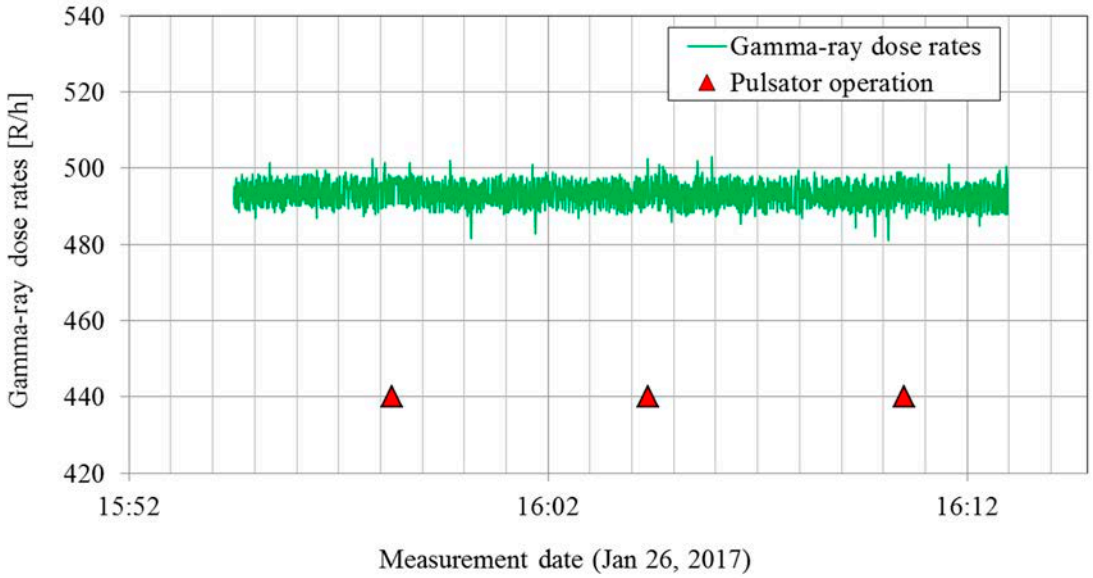

Figure 3- 57 *Result of gamma-ray dose rate monitoring at point 3*

(5) Consideration

① At (around) the liquid level in the HALW tank, we observed a correlation between the change in the liquid level (change in source figure) and the change in the gamma-ray dose rate. Therefore,

the gamma-ray dose rate measured at (around) the liquid level in the tank can possible be applied for source figure monitoring.

② If we select the optimum measurement points depending on the liquid surface, it would be feasible to perform continual monitoring based on the gamma-ray dose rate.

③ In monitoring from the concrete cell entrance, we could not confirm a positive correlation between the liquid level and the gamma-ray dose rate because the gamma-ray scatter increased considerably owing to changes (wave, flow, etc) in the liquid surface and shielding effects of the by structure.

④ We could not confirm dose rate fluctuation at the bottom of the tank. The cause is unknown, but it may be caused either by shielding effects of the cooling jackets or zero variance of source intensity.

⑤ We will perform measurements when the source intensity changes, and it is necessary to confirm the possibility of monitoring depending on source intensity.

⑥ If we can confirm the correlation between the change in source intensity and the gamma-ray dose rate, we may utilize this measurement for continual Pu monitoring or confirmation of decontamination during cleaning of tank interior and decomposition.

A-7-2. Route B

(1) Measurement

Figure 3- 58 shows a schematic drawing of the gamma-ray dose rate monitoring points on route B. The dose rate was monitored at a few points on route B in the 272V35 tank in the same way as that described in chapter A-7-1.

Table 3- 9 *Insert distance at each monitoring point*

Point	ID
A	638 cm (Liquid level)
B	790 cm
C	810 cm
D	830 cm
E	850 cm
F	900 cm
G	950 cm

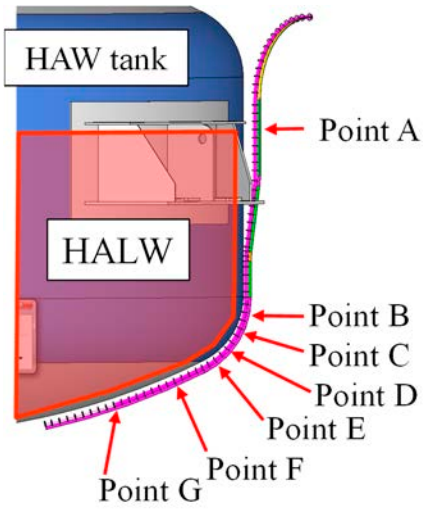

Figure 3- 58 *Schematic drawing of monitoring points*

【Conditions】

・Tank: 272V35

・Rail: Left lower inspection pipe (Route B)

・Measurement points: *Table 3- 9*

・HV: -600 V

・HV and data acquisition device: UDCM

・Measurement time: approximately 20 min

・Data: at intervals of 1 s (Acquired data were averages of data obtained at intervals of 100 ms)

(2) Result

i. Point A

Figure 3- 59 shows the dose-rate monitoring measurement result at point A. Each red symbol represents pulsator operation timing. The dose rate increases in accordance with pulsation, which is the same as that in the case of result 2 in chapter A-7-2. It is caused owing to decrease in the distance between the IC and the source by each pulsation.

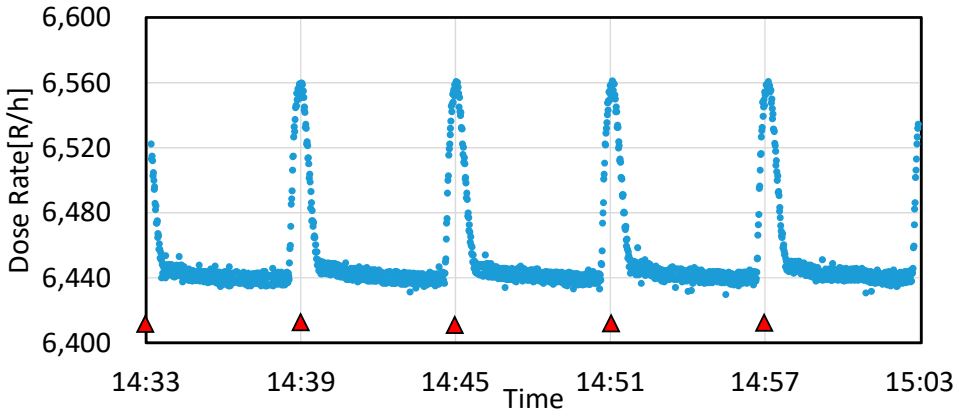

Figure 3- 59 *Dose-rate trend at point A*

ii. Point B

Figure 3- 60 shows the dose-rate monitoring measurement result at point B. Each red symbol denotes pulsator operation timing. The dose rate does not change in accordance with pulsation, which is the same as result 3 in chapter A-7-2. The dose rate trend data may not have changed because the distance between the IC and the source did not change below the liquid level with each pulsation.

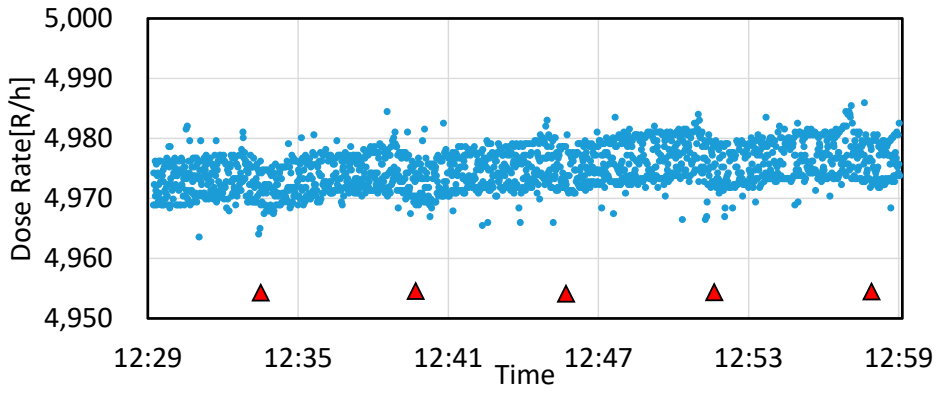

Figure 3- 60 *Dose-rate trend data at point B*

iii. Point C, D, E

Figure 3- 61, *Figure 3- 62*, and *Figure 3- 63* show the dose-rate monitoring measurement results obtained at points C, D, and E, respectively. Each red symbol denotes pulsator operation timing. The dose-rate trend data show a unique trend from ID 810 cm to ID 850 cm. This ID range is consistent with the ID range in which interesting dose rate peaks in the dose rate distribution were measured on route B. The dose rate decreases with each pulsation. Thereafter, the dose rate increases until the next pulsation. The maximum increase in dose rate is measured at point D.

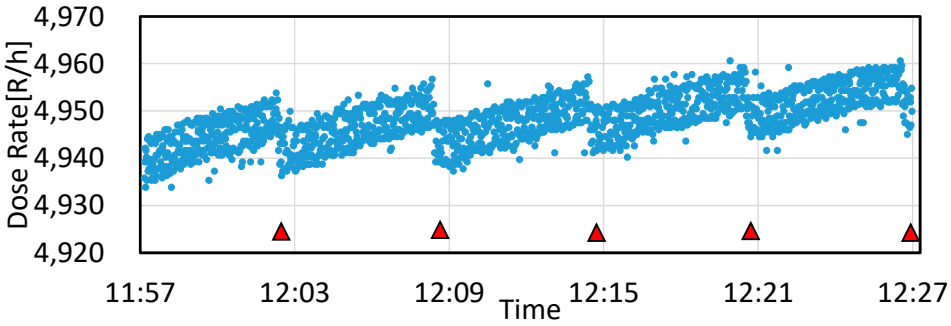

Figure 3- 61 *Dose-rate trend data at point C*

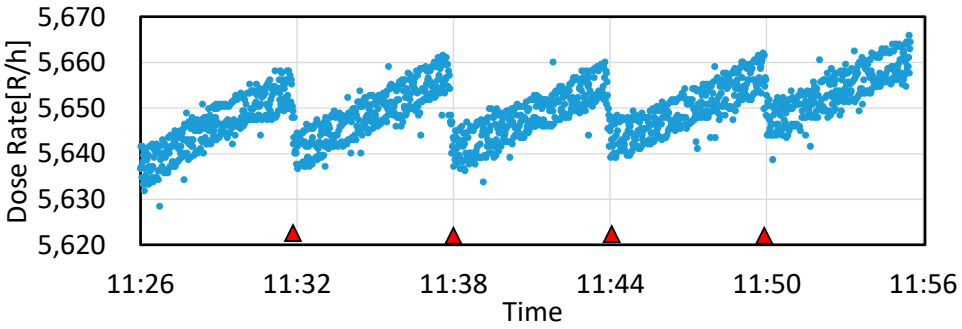

Figure 3- 62 *Dose-rate trend data at point D*

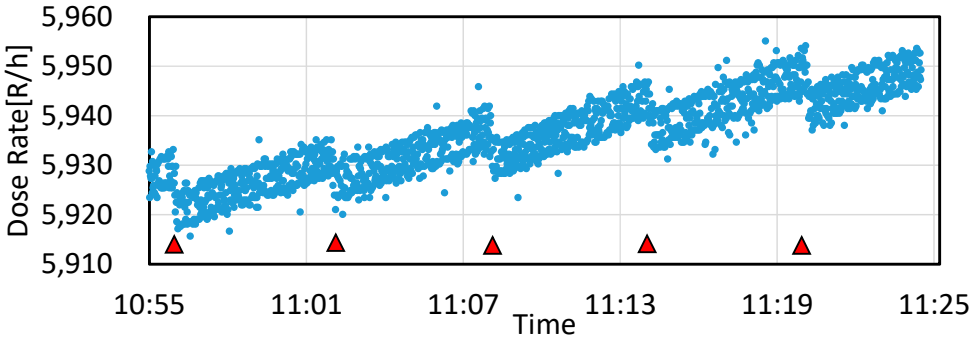

Figure 3- 63 *Dose-rate trend data at point E*

iv. Point F, G

Figure 3- 64 and *Figure 3- 65* show the dose-rate monitoring measurement results obtained at points F and G, respectively. Each red symbol denotes pulsator operation timing. The dose rate changes intricately after ID 850 cm.

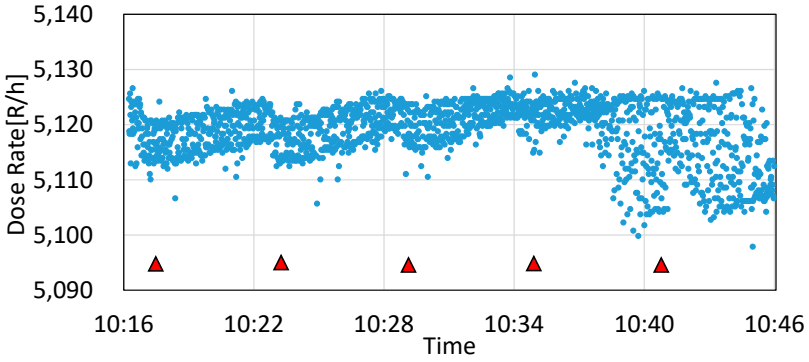

Figure 3- 64 *Dose-rate trend data at point F*

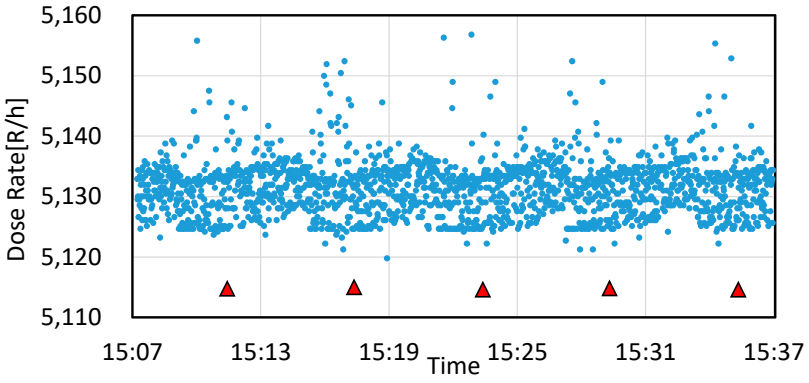

Figure 3- 65 *Dose-rate trend data at point G*

A-8. Comparison with simulation model

< LANL and LLNL using MCNP >

A detailed input model for Tank 35 was created for use with the radiation transport code MCNP [8]. Simulations were performed using the input in conjunction with ENDF/B-VII photoatomic data to calculate dose-rate profiles outside the tank for comparison with the measured data provided by JAEA. In addition, detailed gamma spectra were estimated at locations outside the tank.

The geometric model was created based on CAD drawings, and it was sufficiently detailed to reflect the actual as-built system. *Figure 3- 66* shows the vertical cross-sectional view of the tank, and *Figure 3- 67* shows the various instrumentation tracks present.

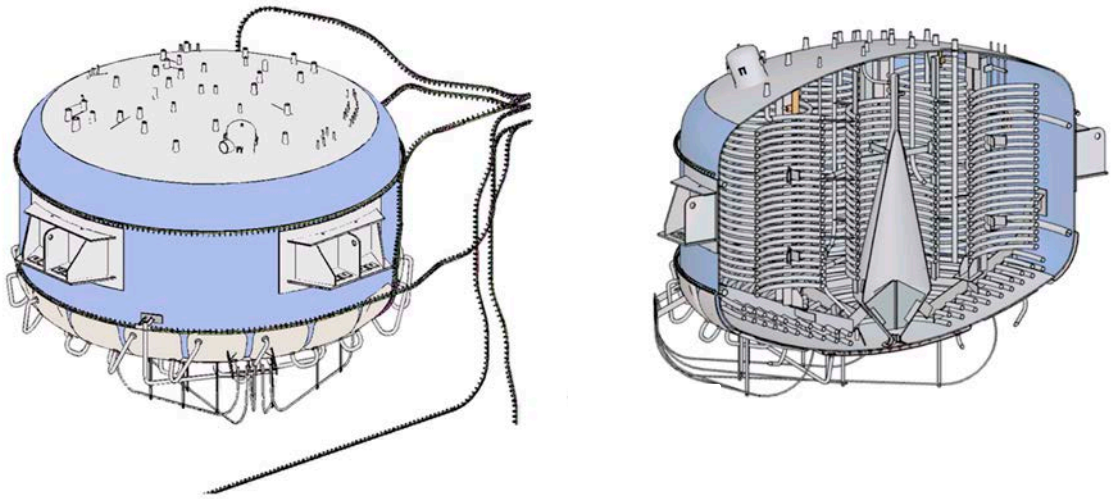

Figure 3- 66 *Design schematic of HALW Tank V35 provided by JAEA. Instruments are passed into the containment structure by inspection pipes that travel along tracks around the tank. The 3D PDF file was imported into Auto CAD® Inventor to obtain the dimensions of each component of the structure.*

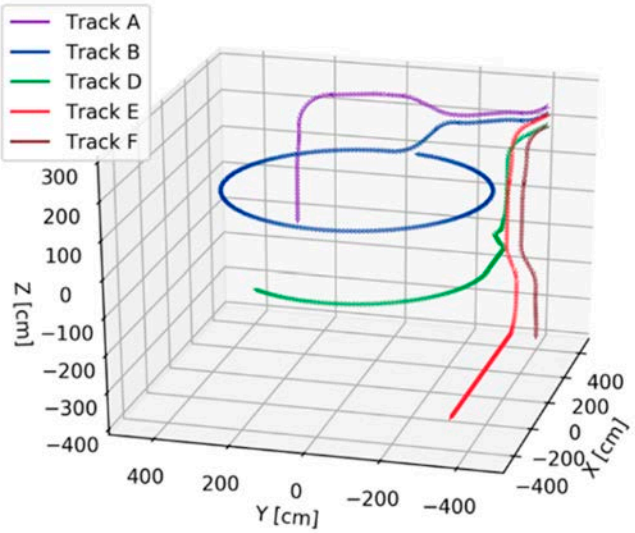

Figure 3- 67 *Location of instrumentation tracks around tank*

The vertical and horizontal cooling coils inside the tank and the cooling coils outside the tank can be seen in the MCNP model in *Figure 3- 68*. *Figure 3- 69* shows horizontal cuts of the vertical cooling tubes at different axial levels. *Figure 3- 70* shows the model with the surrounding building structures.

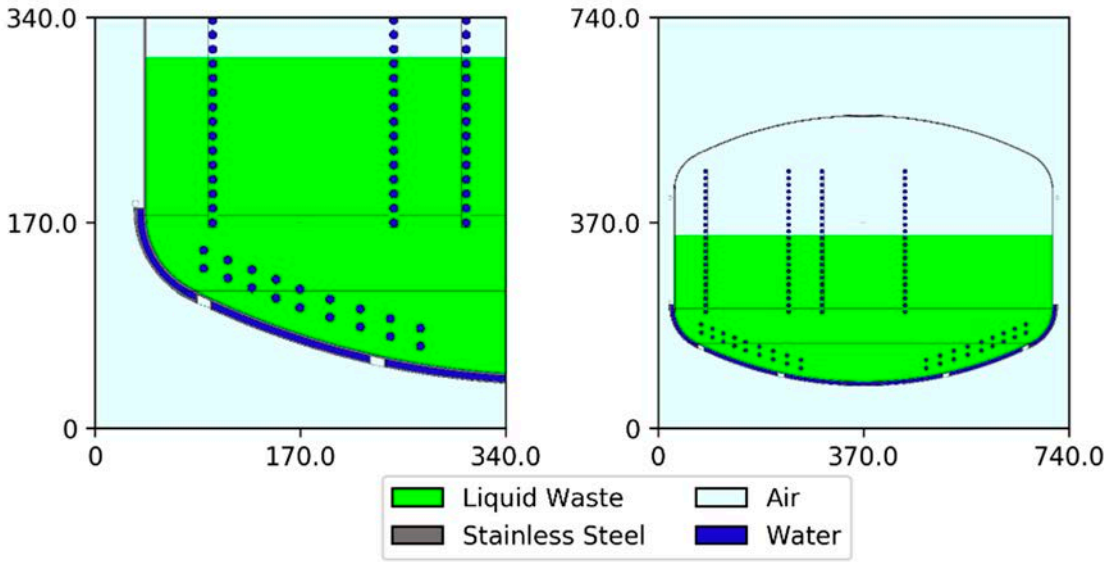

Figure 3- 68 *Tank 35 with cooling coils (unit: cm)*

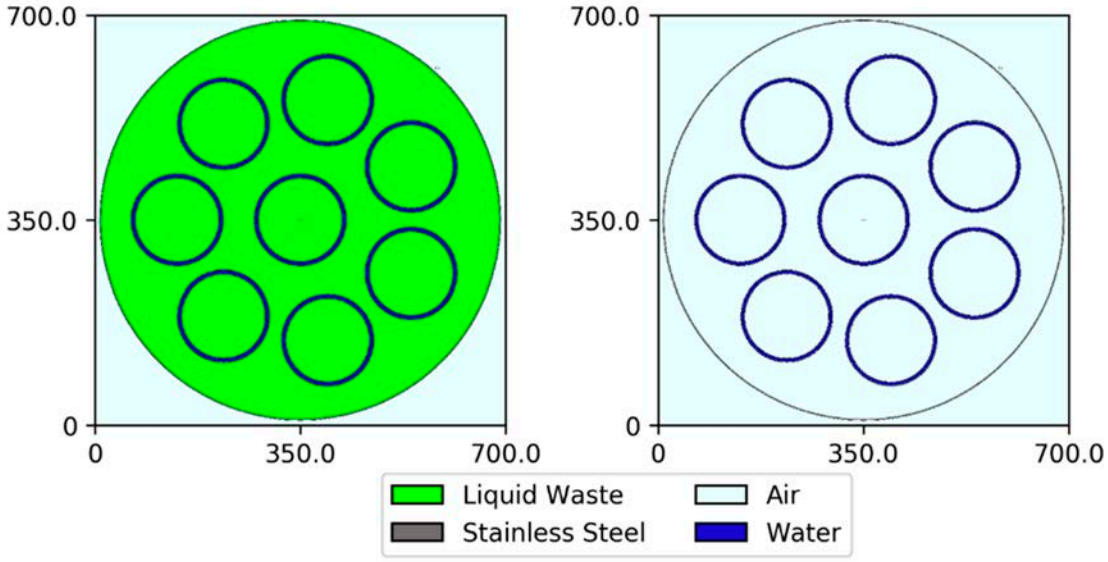

Figure 3- 69 *Vertical cooling coils in tank below liquid level (left) and above liquid level (right) (unit: cm)*

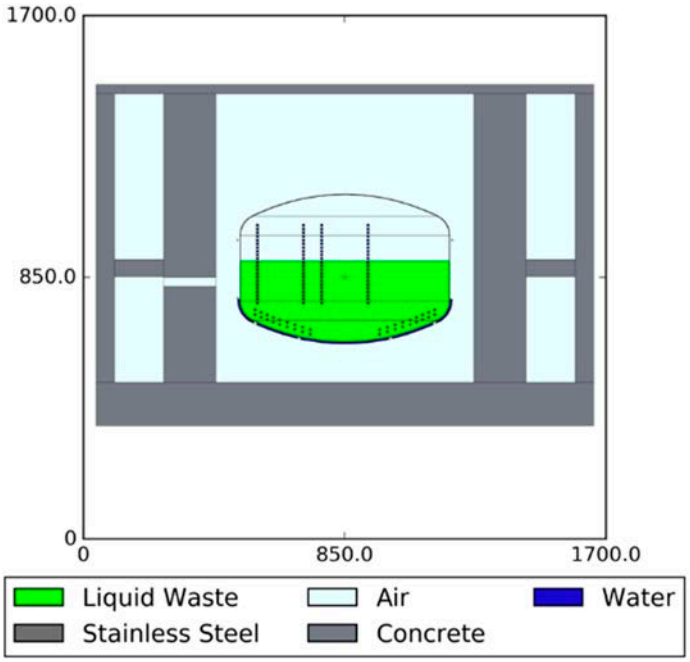

Figure 3- 70 *Tank model with surrounding structures (unit: cm)*

The model incorporated the inspection pipes in the wall through which the holder with the IC is inserted into the tank chamber to measure dose rates at different locations. The IC and holder were modeled per the drawings provided by JAEA. Dose-rate measurements were performed along Track

F (see *Figure 3- 67*). A single IC model was developed (*Figure 3- 72*) and translated and rotated to the correct positions to simulate the actual measurement locations as the detector system is moved along the track. Fifty-three positions were modeled for establishing the dose profile. *Figure 3- 71* shows the inspection pipes through which the detector system is inserted into the chamber.

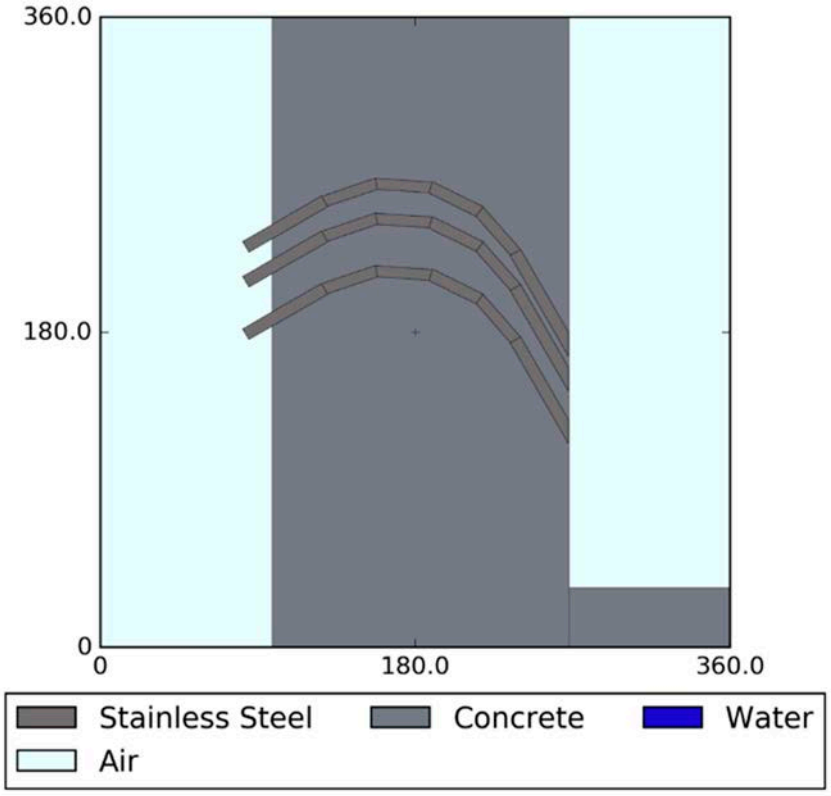

Figure 3- 71 *Inspection pipes in MCNP model (unit:cm)*

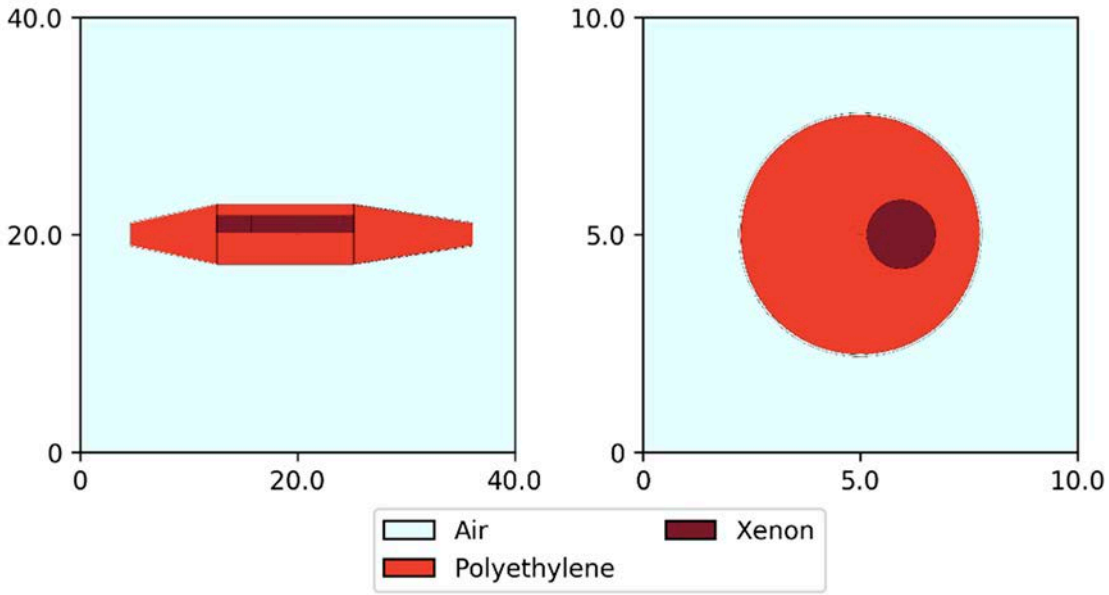

Figure 3- 72 *Cross-sectional view of ion chamber (unit:cm)*

The IC holder combination was modeled accurately and placed at various locations along Track F for dose estimation. *Figure 3- 72* shows the MCNP geometry of the IC.

Material Specifications

The specifications of standard materials were obtained from a compendium of material compositions [3]. The liquid in the tank was modeled with the density and composition obtained from a sampling run conducted by JAEA [3]. The density obtained was 1.234 g/mL based on a nitric acid concentration of 2.25 mol/L and considering the presence of residual amounts of actinides and other elements. *Table 3- 10* presents the composition of the liquid. Although the actual composition was included in the input for the sake of completeness, the actual radiation transport of photons does not require isotopic breakdown because photoatomic cross sections are exclusively element-dependent.

Table 3- 10 *Isotopic composition of liquid in tank*

Isotope	Mass fraction	Isotope	Mass fraction
H	9.925E-02	^{235}U	4.228E-05
N	8.607E-01	^{236}U	1.315E-05
O	3.376E-02	^{238}U	4.146E-03
^{238}Pu	8.591E-07	^{244}Cm	1.074E-09
^{239}Pu	4.469E-05	^{137}Cs	2.022E-07
^{240}Pu	2.127E-05	^{54}Fe	1.163E-04
^{241}Pu	2.248E-06	^{56}Fe	1.875E-03
^{242}Pu	3.249E-06	^{57}Fe	4.370E-05
^{234}U	1.135E-06	^{58}Fe	5.929E-06

Source Specification

The liquid was modeled to be 131.3 cm from the bottom of the cylindrical portion of the tank. This represented the nominal level of the liquid in the model and was based on the nominal volume obtained from JAEA [3]. Source sampling was performed homogeneously over the entire liquid volume. Angular biasing of the source was employed to focus source particles toward Track F. The measured energy spectrum [3], spanning from 10 keV to 2.6 MeV in 3,326 groups, was used to sample the energy of the source gammas.

Gamma Dose Rate along Track F

The gamma dose rate was calculated at 53 axial locations along Track F for comparison with the measured data provided by JAEA (see *Figure 3- 73*). In addition to the dose rates with the nominal liquid level, three sensitivity studies were conducted to determine the effect of changing the liquid level: 50 cm above and below nominal level and a low level at the bottom of the cylindrical portion of the tank. All four calculations were performed by sampling 10 billion histories for acceptable convergence of the individual estimates. In these cases, the “f6” tally in MCNP was used. This estimator provides the energy absorbed in the IC per unit mass, and thus, provides a direct estimate of the gamma dose. The calculated values were normalized with a factor determined based on the nominal case value corresponding to the peak measured dose rate. This factor was used to renormalize all values in the four sets.

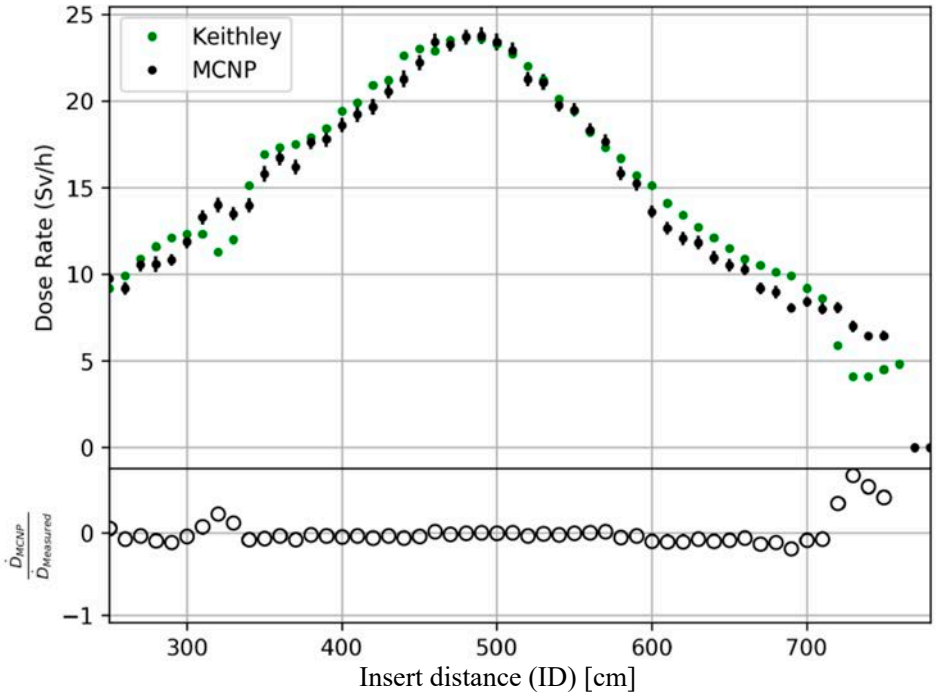

Figure 3- 73 *Comparison of measured dose rate to simulated dose rate for various positions along Track F*

Figure 3- 74 shows a comparison of the nominal set to the measured set, as well to the values obtained from the three sensitivity runs. The shape of the calculated dose rates shows very good agreement with the measured set. The case with the liquid level 50 cm above the nominal level is higher at high elevations and drops back to match the tail of the profile in the nominal level case. Similarly, the case with the liquid level 50 cm below the nominal level behaves as expected—lower at high elevations and matching the tail of the profile. The low-level case is very low for the most part, as expected.

Table 3- 11 *Volume of liquid waste for varying liquid levels*

Liquid level (Global coordinates)	Liquid volume (L)
1.0m	9.04×10^4
0.5m (Base Case)	7.36×10^4
0.02m	5.70×10^4
-0.8m	2.97×10^4

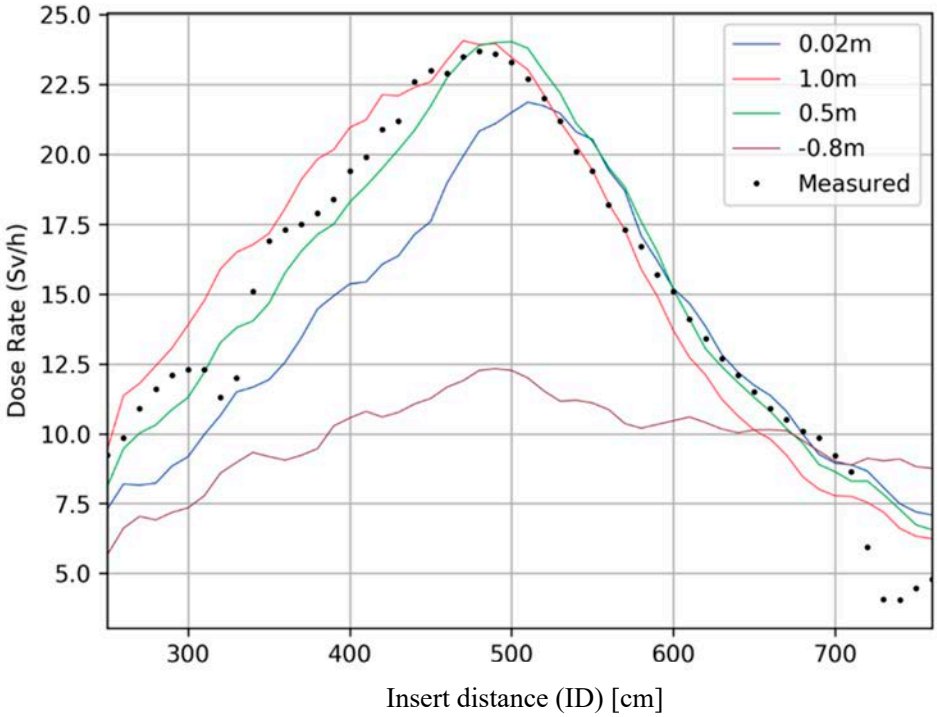

Figure 3- 74 *Expected dose rate as a function of increase in liquid level*

Gamma Spectra in Track F

The gamma spectrum along Track F was determined at four ion-chamber four positions. The elevations of these locations were 93 cm above the nominal liquid level, and 14.5, 186, 328 cm below the nominal liquid level, as summarized in *Table 3- 12*. The simulations were performed by sampling one billion histories. Point detector tallies were used, and the resulting source spectrum was tallied in a 67-group structure with emphasis on capturing the main expected peaks. *Figure 3- 75* presents the four spectra together with the source spectrum. The strong ^{137}Cs peak and a few of the prominent ^{154}Eu peaks in the range 0.7-1.3 MeV are visible. As expected, the spectra in line with the bulk of the liquid have higher magnitudes than the one above the liquid level and the one near the tank bottom. The spectra converge well, with standard errors lower than 5% in the important regions of the energy spectrum.

Table 3- 12 *Gamma-ray detector position on Track F*

Detector location (Global coordinates)	Height from liquid surface (m)
(361.8, 395, 144.6)	0.926
(360, 355.2, 14.5)	-0.375
(365, 355, -133.9)	-1.859
(403, 358.9, -275.7)	-3.277

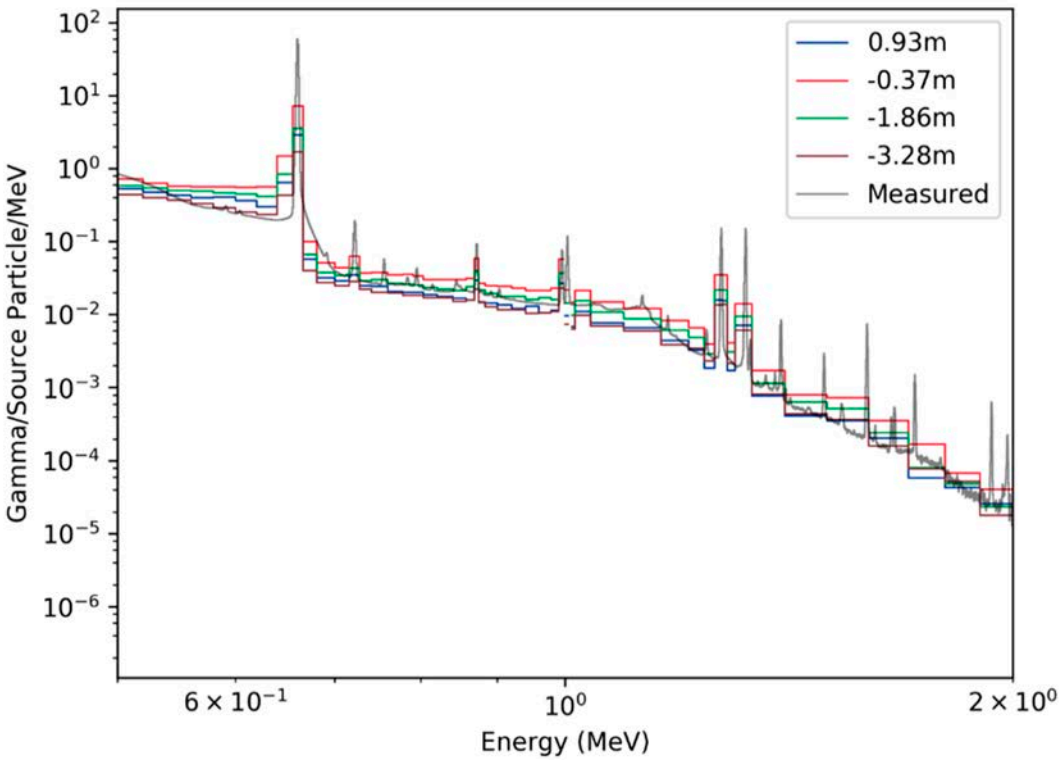

Figure 3- 75 *Gamma-ray spectra as a function of position along Track F*

< JAEA using PHITS code >

The input model for Tank 35 was created using the radiation transport code, PHITS ver 2.92[6]. Dose rate calculation was performed using the input source file and model. The dose rate at each point at which dose rate measurement was conducted, was calculated for comparing the measured data and the data calculated using MCNP with the data calculated using PHITS.

- Source file

HALW composition in V35 was investigated by destructive analysis and non-destructive assay, as described in chapter 2.2. One analysis item was gamma-ray spectrum measurement of the gamma rays discharged from the actual diluted HALW sample in V35 by using a high-purity Ge detector. The gamma-ray number and each of the energies discharged from the HALW in V35, calculated from the gamma-ray spectrum obtained by gamma-ray spectrum analysis as described in chapter 2-2-5, were used as gamma-ray source data in the MCNP simulation.

As for neutron source data, the neutron dose rate caused by ^{244}Cm, the major neutron-discharged nuclide in HALW, and its spectrum were used as neutron source data in the MCNP simulation. The analysis result of α spectrum of the diluted HALW sample was used to determine the neutron dose rate due to ^{244}Cm, as described in chapter 2-2-5.

➢ Model

The MCNP simulation model consists of the HALW solution, HALW tank, cooling jacket at the tank bottom, concrete cell, and inspection pipe. No material region is filled with air (*Figure 3- 76* to 78). As for the cooling jacket, water layer was made on the bottom of the outside the tank, except for the route of the guide rail along the bottom of the tank. The route of the guide rail was filled with air (*Figure 3- 79*).

Concentration of the nitric acid solution was set to 2.25 mol/L, which is the same as the analysis value of actual HALW, in the HALW solution model. An SUS tank housing a container with the same thickness as that of the HALW tank was set as the HALW tank model. Its dimensions (i.e. diameter, height) were the same as those of the HALW tank. A concrete cell wall with the inspection pipe installed on it, as in case of the actual concrete cell, was set as the concrete cell and inspection pipe model.

The average density inside the tank calculated using CAD data was used for the air part and the solution inside the tank to consider self-shielding by internal equipment, such as cooling jacket and so on.

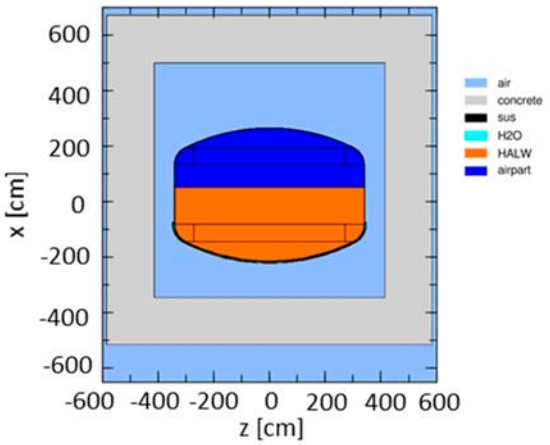

Figure 3- 76 *MCNP simulation model*

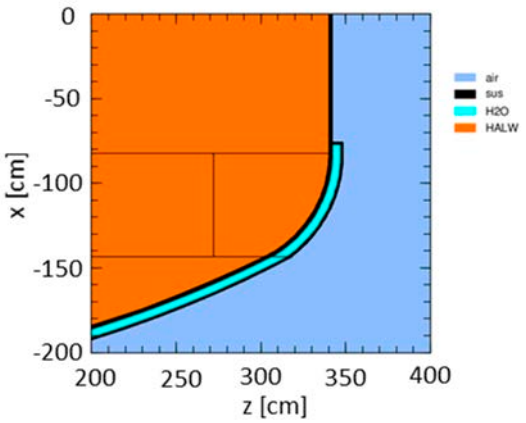

Figure 3- 77 *HAW tank and cooling jacket*

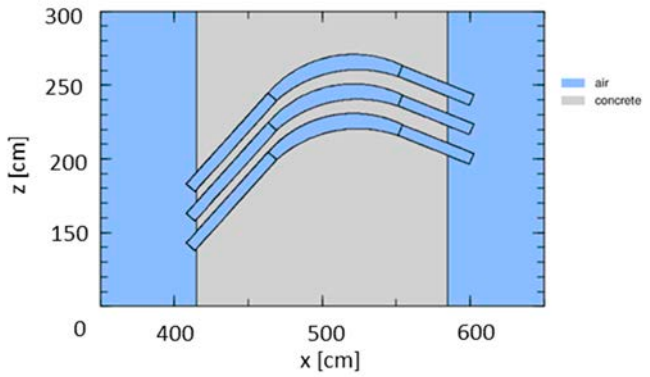

Figure 3- 78 *Inspection pipe*

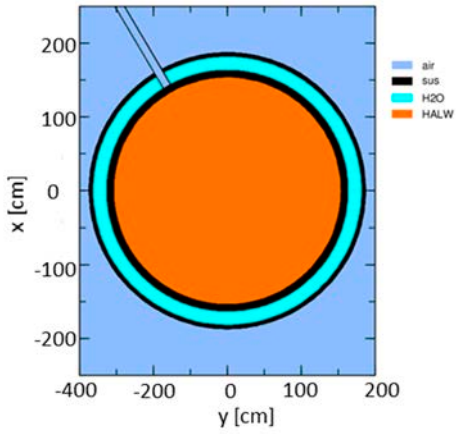

Figure 3- 79 *Bottom of tank (horizontal view)*

➢ Simulation method

Coordination of the center of the guide ring was investigated using CAD data. We set the evaluation-sphere on each measurement route to calculate acceleratory setting specific angle from the source and obtained flux and Gy the output.

➢ Result

Dose rate calculation was conducted on route A (*Figure 3- 80*). Dose rate distribution on route A as calculated using PHITS agrees well with the measurement result, except for the dose rate drop point. We assumed that the decrease in dose rate was caused by pieces of equipment that were not modeled, such as guide rail support.

The dose rate on route B was calculated (*Figure 3- 81*). Dose rate distribution on route B as calculated by PHITS agrees well with the measurement result, except for the dose rate distribution after ID 850 cm. We assumed that the dose rate distributions at measurement positions after 850 cm were attenuated by sludge.

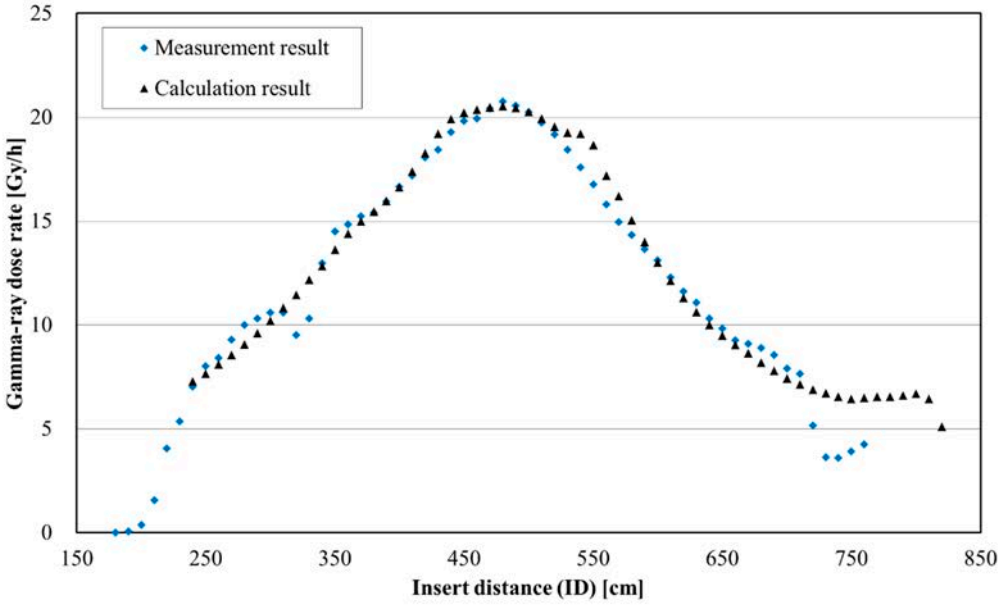

Figure 3- 80 *Comparison between measurement result and calculation result by PHITS on route A*

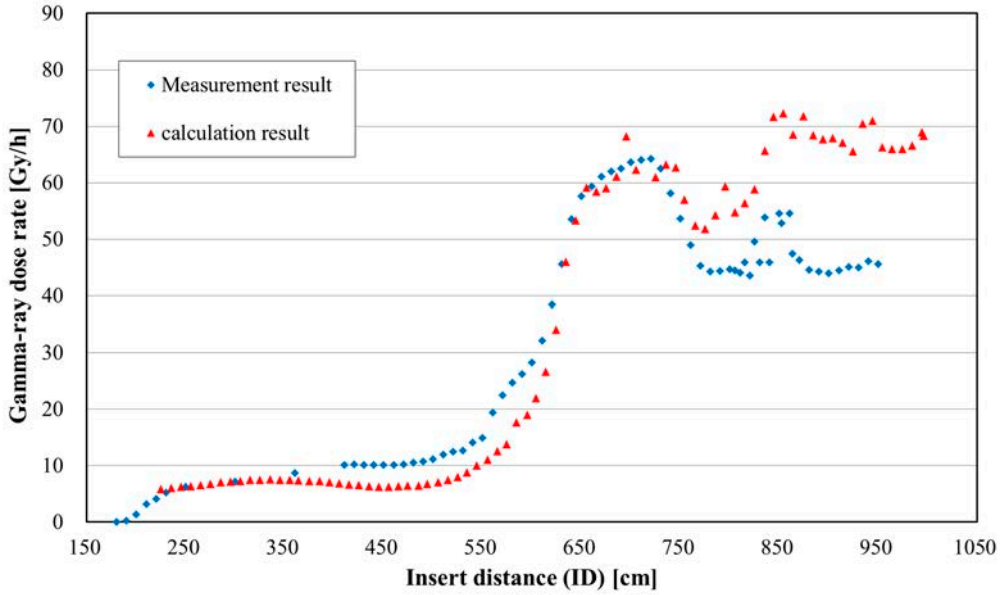

Figure 3- 81 *Comparison between measurement result and calculation result by PHITS on route B*

A-9. Summary

(1) We developed a gamma-ray dose rate measurement system for areas with very high radiation levels, where operators cannot enter.

(2) The measured gamma-ray dose rates reflected the effect of distance between the IC and the source and attenuation effects of the pipe supports in the concrete cell. As a result, we obtained minute gamma-ray dose rate distributions with slight dispersion. These data are valid for comparison in the process of model simulation and optimization.

(3) We measured the gamma-ray dose rate inside the concrete cell and applied the measured value to design detectors, such as gamma-ray spectrum measurement detector, and shielding for gamma rays.
(4) We could not confirm the difference in gamma-ray dose rate based on the difference in solution composition in the concrete cell.
(5) We confirmed the possibility of monitoring changes in source figure in the tank based on the results of gamma-ray dose rate monitoring around the liquid level.

B. Gamma spectra measurement

B-1. Purpose of measurement

We measured gamma-ray spectra inside the concrete cell of HAW to confirm applicability to Pu monitoring. We evaluated the energy and intensity of gamma rays from the measured gamma-ray spectra. The measured gamma rays, including delayed gamma rays, which are absorbing peaks in the high-energy range useful for Pu monitoring. This is because the low-energy area (<1 MeV) is dominated by FPs, such as Cs, and it is difficult to detect Pu-origin gamma rays.

This measurement was performed to evaluate the possibility of solution monitoring by using gamma-ray spectra. The measurement target was delayed gamma rays derived from the nuclear fission of Pu and the total absorption peak derived from Pu at energies higher than 3 MeV. The measurement was performed under a high dose rate of radioactivity, and the measurement range was 12 MeV.

B-2. Selection of detector

At first, we shortlisted detectors that can be used for gamma-ray spectra measurement, such as the ones listed in *Table 3- 13*, and selected the GAGG detector from the following viewpoints. We designed the device size considering radiation condition, limited storage space, and measurement of gamma-ray energy.

・ Short dead time (large number of signals processed per unit time)

  Reason: The gamma-ray dose rate inside the concrete cell was high at the past measurement and pile up was considered.

・ Miniaturization

  Reason: It is necessary to install the detector inside the holder and insert it inside the concrete cell. Wide energy range in spectra (approximately 10 MeV) and high density. For measurement of high-energy delayed gamma rays with good energy resolution. Gamma rays with several energy peaks of energy are emitted from HALW.

Table 3- 13 *Selection of detector for gamma-ray spectrum measurement*

Type of detector	Type of device		FWHM (Full Width at Half Maximum)	Decay time μs	Density g/cm^3	Special mention
Semiconductor	CdTe	Cadmium telluride	2.6% at 60 keV 6% at 122 keV	—	5.85	Downsizing is possible
	CdZnTe	Cadmium zinc telluride	10% at 60 keV 6% at 122 keV	—	~5.8	Downsizing is possible
	Ge	Germanium	~1% at 100 keV ~0.1% at 1 MeV	—	5.33	Cooling is necessary
Scintillator	NaI(Tl)	Sodium iodide	10% at 150 keV	0.23	3.67	Deliquescency
	BGO	BiGeO	20% at 511 keV	0.3	7.13	No deliquescency
	GSO(Ce)	GdSiO(Ce)	15% at 662 keV	0.06	7.13	No deliquescency
	CsI(Tl)	Cesium iodide	8% at 662 keV	1	4.51	Deliquescency
	$LaBr_3$(Ce)	Lanthanum bromide	3~4% at 662 keV	0.026	5.29	BG : La-138 (1,435 keV) Deliquescency
	$CeBr_3$	Cerium bromide	4% at 662 keV	0.017	5.2	Deliquescency
	SrI_2(Eu)	Strontium iodide	~4% at 662 keV	1~5	4.59	Activation by neutron
	GAGG	Gadolinium Aluminun Gallium Garnet	5% at 662 keV	0.05	6.63	No deliquescency Downsizing is possible

B-3. Measurement tools

(1) Radiation meter (*Figure 3- 82*)

① GAGG scintillator: $Gd_3Al_2Ga_3O_{12}$ (Ce), Gadolinium Aluminum Gallium Garnet

・Size: 25 mm × 25 mm × 25 mm

・Density: about 6.6 g/cm^3

・Resolution: about 9% (^{137}Cs, 662 keV)

・Decay time: about 50 ns

② Signal amplification: Photomultiplier Tube (PMT)

③ Cables: Radiation hardness (for signal and high voltage) 10 m

Figure 3- 82 *GAGG scintillator*

(2) Holder and operation tool

① Holder *Figure 3- 83*, *Attachment 3*)

・Material: Polyacetal resin (POM)

・External form: Diameter = 55 mm, Length = 315 mm, and Cylinder type (conical ends)

・Structures: With tungsten for shielding and space to store GAGG inside

・Weight: 3.5 kg

② FRP rod

・Diameter: 8 mm

・Load-withstanding capacity: Tensile fracture strength = 19.6 kN, Bending strength = 400 N/mm^2

・Minimum radius : 290 mm

Figure 3- 83 *Holder for GAGG scintillator*

(3) Processing of signals and HV control

① DSP: Digital Signal Processor (*Figure 3- 84*)

Number of channels: 2, Sampling frequency: 1 GHz

Wave pattern mode: Histogram, List

LEMO connector

② HV: HV device (*Figure 3- 84*), Range: ±1 to ±5 kV, SHV connector

Figure 3- 84 *DSP and HV device*

B-4. Experimental setup

(1) Device composition

Figure 3- 85 shows the detector composition, and *Figure 3- 86* shows a schematic drawing of the measurement system.

The measurement system is connected to the DSP (Digital Signal Processor) and the HV device by 10-m-long radiation hardness cables (for signal and HV) connected to the photomultiplier tube (PMT). Each device is connected to a PC via a HUB, and it is possible to control measurement and HV supply by using a software application on the PC. For measurement control, FPGA (Field-Programmable Gate Array) was used to fine-tune parameters (height of rise time, integral time, threshold, et al.) on the user side in anticipation of detector pile up under high levels of radiation. FPGA is an integrated circuit that can be used to design hardware freely, and it is effective for radiation measurement with high count rates because the parameters can be changed depending on measurement conditions. As the measurement principle, luminescence due to radiation entering the GAGG device was acquired as signal from PMT.

The shield for the high-radiation condition was designed and manufactured with tungsten, which can provide shielding from gamma rays from the viewpoint of device decay time and holder size limitation based on gamma-ray dose rate distribution measurement. In addition, the periphery of the PMT was covered with a ferromagnetic permalloy because the PMT is affected by magnetic field drift.

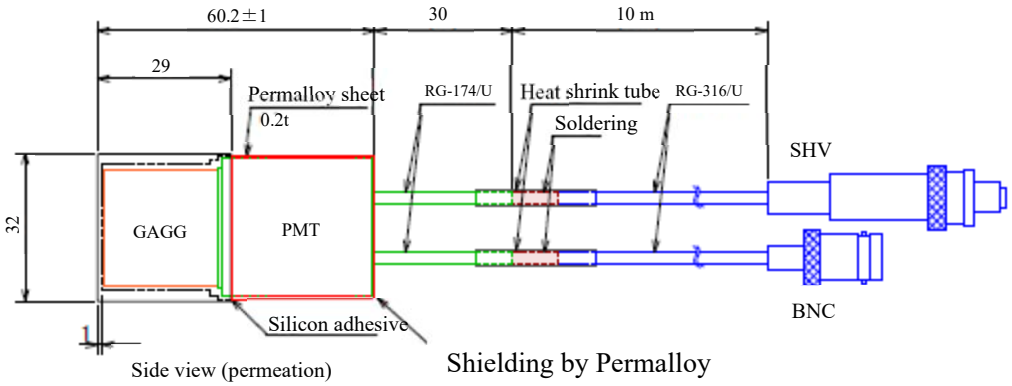

Figure 3- 85 *Detector composition*

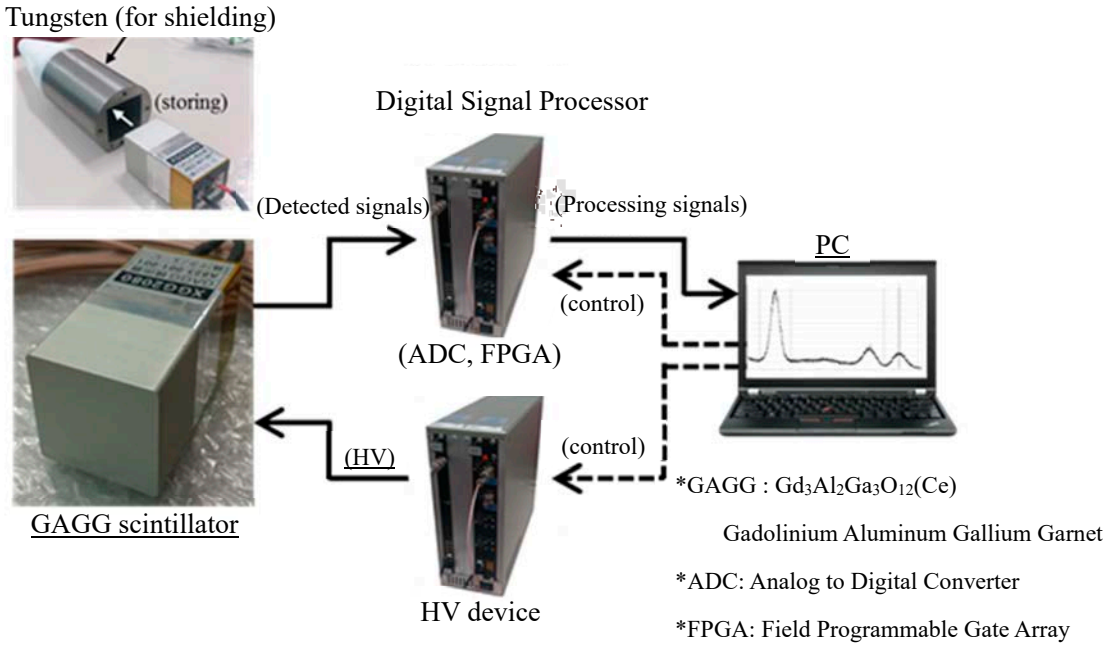

Figure 3- 86 *Schematic drawing of measurement system*

(2) Internal structures of holder and storage of detector

Figure 3- 87 shows a schematic drawing of the GAGG holder, and *Figure 3- 88* shows detector storage.

The cylindrical front and rear of the holder were manufactured with POM. The column body was manufactured with tungsten for shielding. The holder is divided into three parts. The body part of tungsten can store the GAGG, shield gamma ray from solid angle (4π steradian). It is designed such that the detection part shows the opposite radiation condition in gamma-ray spectrum measurement.

The tungsten body is one-piece, except for the lid. The lid serves as the maze structure for prevention of gamma-ray streaming. The holder is heavy and made by tungsten. Therefore, we adopted a FRP rod which is thicker than the one used in gamma-ray dose rate distribution measurement by IC.

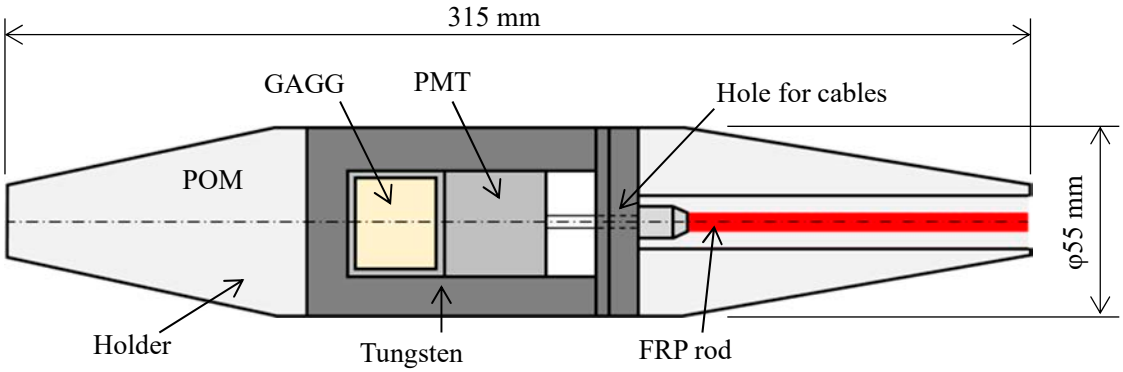

Figure 3- 87 *Schematic drawing of GAGG holder*

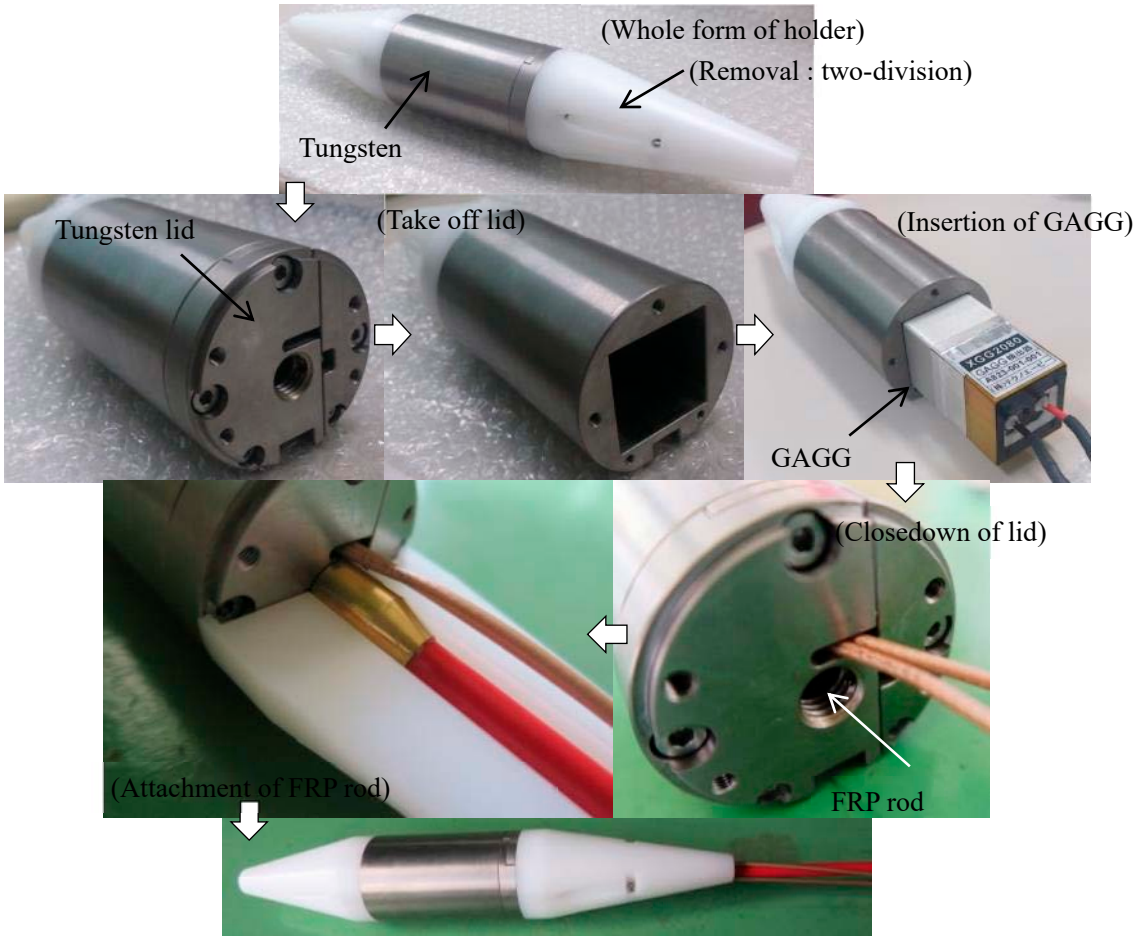

Figure 3- 88 *Detector storage*

(3) Connection of measurement system

Figure 3- 89 shows the method for connecting the measurement system.

We connected two GAGG cables going out the rear of the holder to the DSP and the HV device. The cable connected to the DSP was a BNC connector, and the cable connected to the HV device was a SHV connector. The DSP, HV device, and PC were connected by ethernet cables via a HUB because measurement control and HV are operated by means of a software application on the PC.

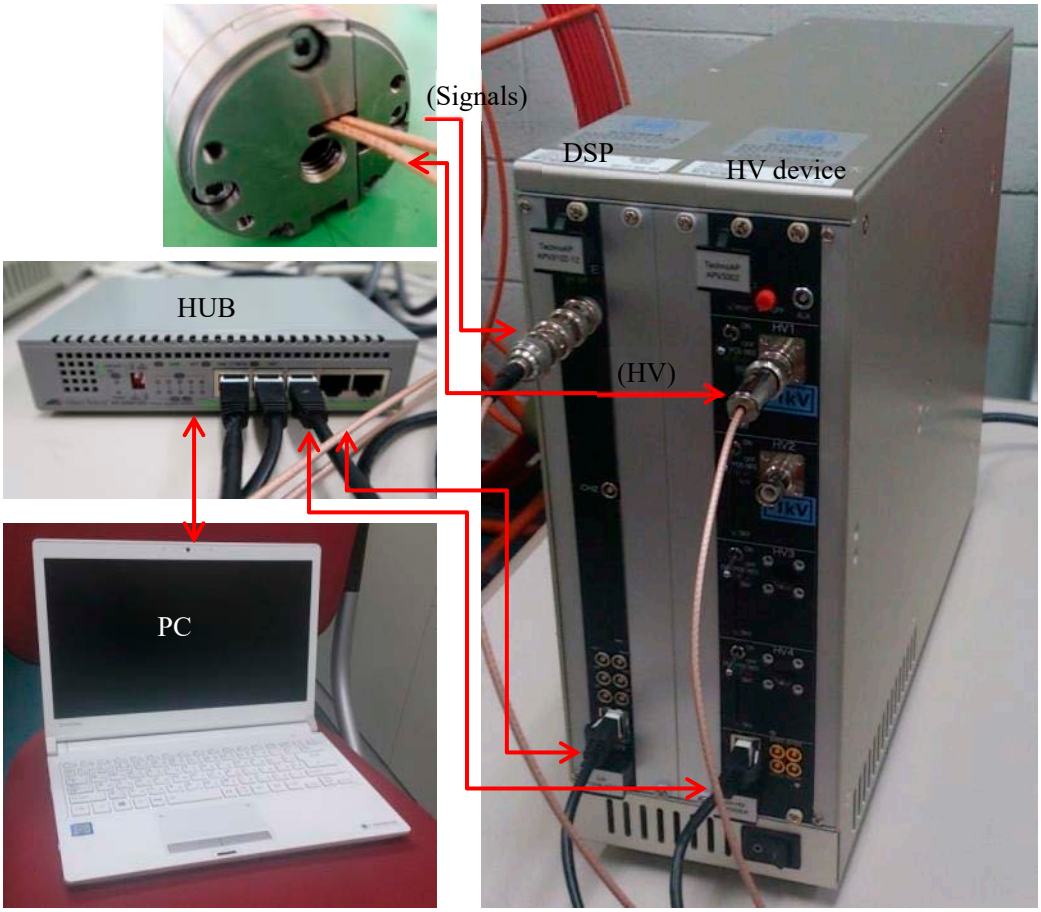

Figure 3- 89 *Connection of measurement system*

B-5. Calibration test

(1) Outline

The GAGG scintillator performs measurements at room temperature without maintaining a fixed temperature, unlike a Germanium semiconductor detector. The scintillator causes channel drift based on measurement conditions, such as temperature. Therefore, we performed energy calibration before the measurement, and it is necessary to calibrate the relationships between channel and energy.

In addition, we performed gain adjustment to observe the energy range for effective measurement, and it is necessary to optimize the acquisition spectra.

(2) Method

① Arrangement of energy range

The spectrum display is 8,192 ch. We performed gain adjustment so that the maximum energy at measurement would be allotted to this maximum ch.

For example, in case of measurement to 12 MeV, a channel becomes about 1.46 keV/ch (12 MeV/8, 192 ch). When using ^{60}Co (1,332 keV), we performed gain adjustment so that the peak center was near

913 ch (1,332 keV/1.46 keV).

② Energy calibration

We measured the known standard source and performed calibration based on the detected gamma-ray peak. The standard sources used to this end were point sources of ^{137}Cs (662 keV) and ^{60}Co (1,332 keV). ^{137}Cs (662 keV) was the main nuclide in the HAW solution. ^{60}Co (1,332 keV) is the maximum energy in the available standard sources. We confirmed keV/ch based on these two energy peaks and the center ch of the peaks.

Figure 3- 90 shows an example of energy calibration.

The nuclides corresponding to the gamma-ray peaks detected during measurement were identified by using the relationship between energy and ch.

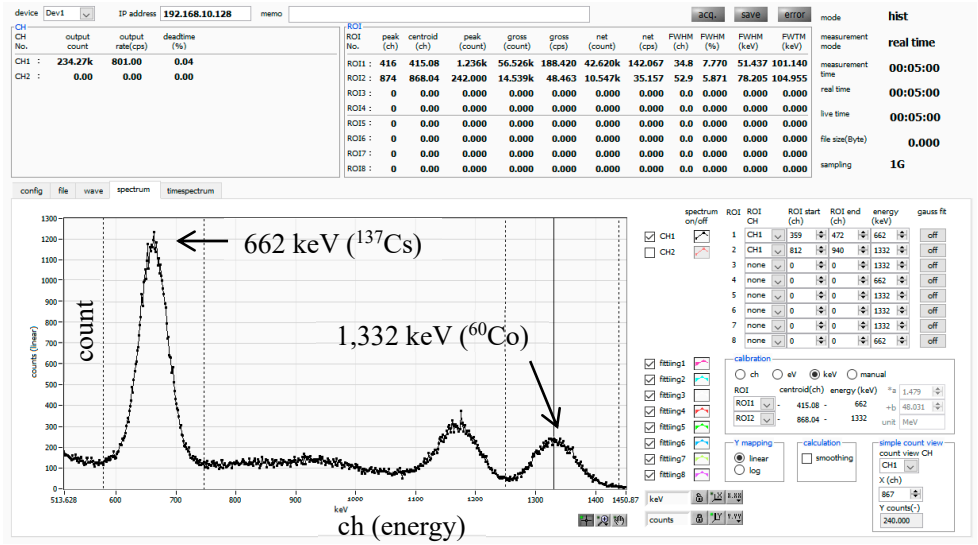

Figure 3- 90 *Example of energy calibration*

B-6. Measurement

We used route to show with red at 272V35 of HAW for measurement (*Figure 3 - 91*) and inserted the holder into inspection pipe (*Figure 3- 92*). The detector piled up at ID 210 cm near the entrance of the concrete cell, and the baseline fluctuated *Figure 3- 93*). The dead time became 0.1% without pile up at ID 170 cm (*Figure 3- 94*), and we confirmed the validity of the measurement. We decided to measure gamma-ray spectra in detail at ID 170 cm. In addition, after acquisition of spectra over a wide energy range, and we performed measurements in the low energy range (~3 MeV) and the high energy range (3 MeV~).

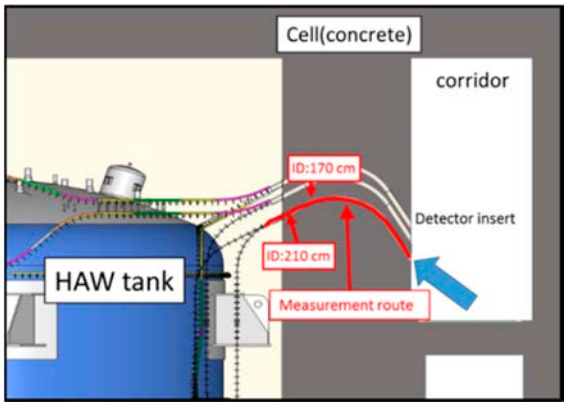

Figure 3- 91 *Measurement route*

Figure 3- 92 *Insertion of holder*

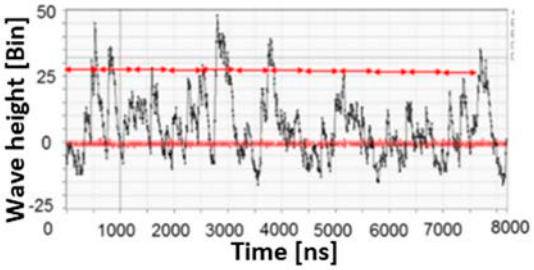

Figure 3- 93 *Detected signal (ID: 210 cm)*

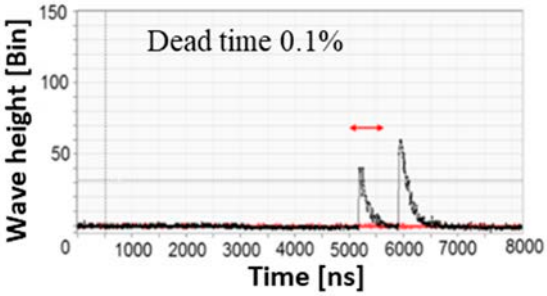

Figure 3- 94 *Detected signal (ID: 170 cm)*

【Conditions】

- Tank: 272V35
- Rail: Left lower penetration pipe (Rail A) (same route as IC measurement)
- HV: -790 V
- Measurement point: ID 170 cm (from entrance of concrete wall)

B-7. Result

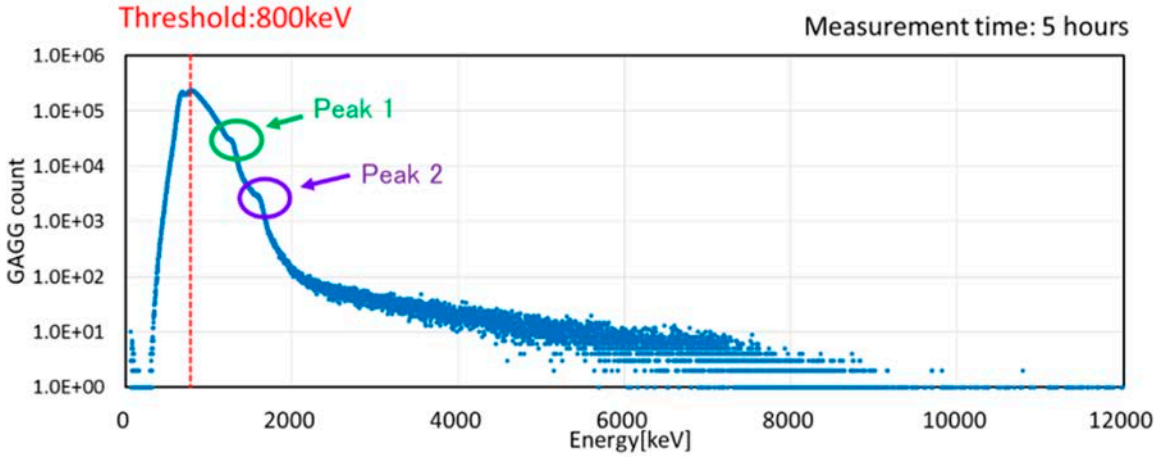

Figure 3- 95 *Gamma-ray spectra measurement result*

As a result of gamma-ray spectra measurement at ID 170 cm, two peaks were detected over 1 MeV, as shown in *Figure 3- 95*. The threshold was set to 800 keV to cut off gamma rays emitted mainly from ^{137}Cs. Two peaks detected at 1,279 keV and 1,604 keV were ascribed to gamma rays from ^{154}Eu based on Gaussian fitting (see *Figure 3- 96*).

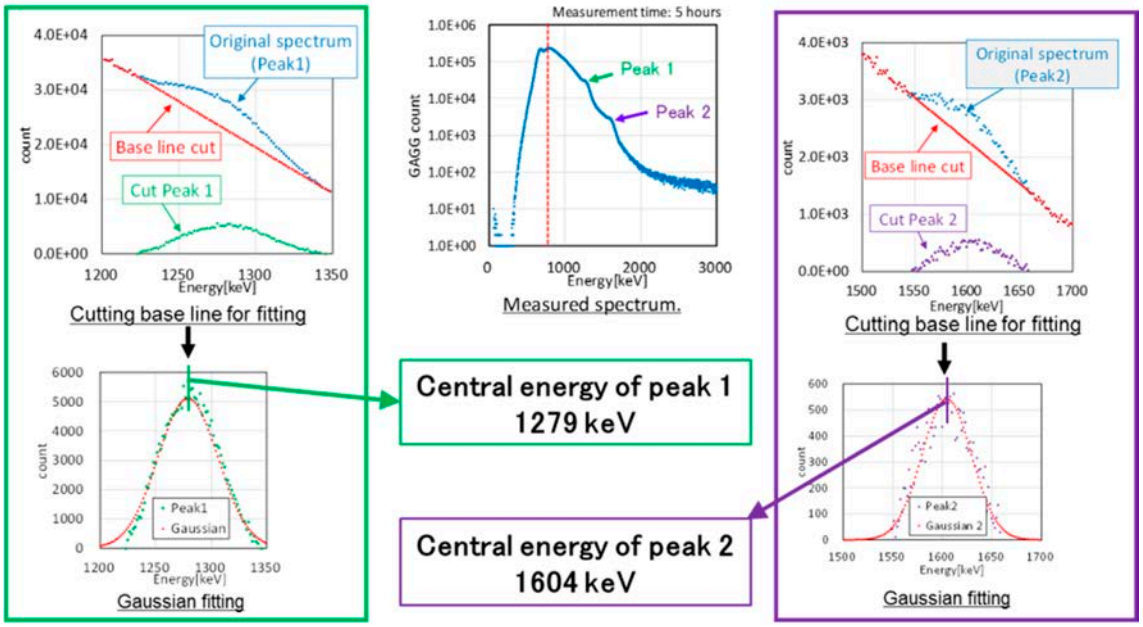

Figure 3- 96 *Fitting by Gaussian distribution*

B-8. Consideration

Figure 3- 97 shows a comparison of the results obtained by analyzing the sample from the HAW diluted to 10,000 times and using the HPGe detector to those obtained using the GAGG. The two peaks measured by GAGG were assigned to ^{154}Eu. The results of measurements focusing on the high energy region as an additional test are shown in *Figure 3- 98*.

From the comparison with the analysis results in *Figure 3- 97*, we expected to measure a 10.8 MeV peak from ^{14}N(n, γ)^{15}N that could not be identified in an analysis of the diluted sample. There is a broad peak around 6,400 keV (see *Figure 3- 98*), which can be ascribed to the spread of energy and full width at half maximum, possibly because of a (n, γ) reaction of the ^{56}Fe contained in stainless steel and concrete. To analyze the region with energy higher than 3 MeV, we considered the effects of neutrons in the field.

In the region lower in energy than ^{137}Cs, no peak was detected because of Compton scattering (see *Figure 3- 99*).

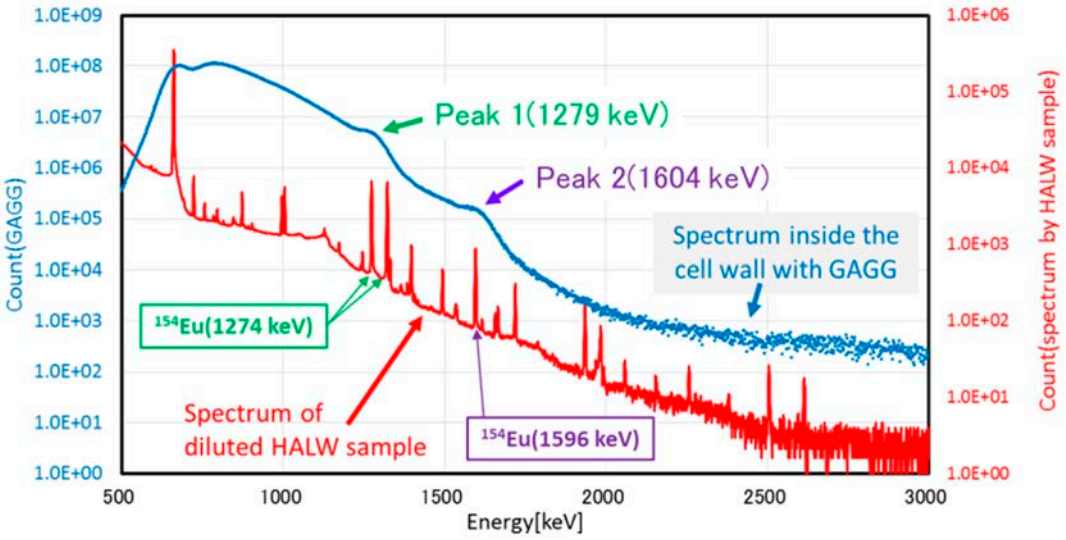

Figure 3- 97 *Comparison between measurement result by GAGG and analysis data by HPGe*

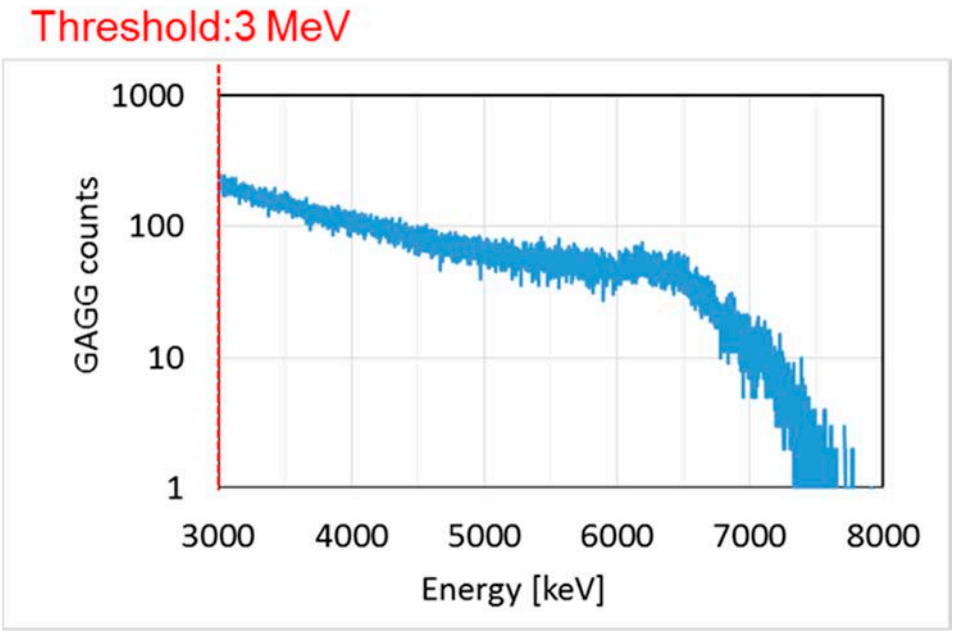

Figure 3- 98 *Gamma-ray measurement focusing on high energy range*

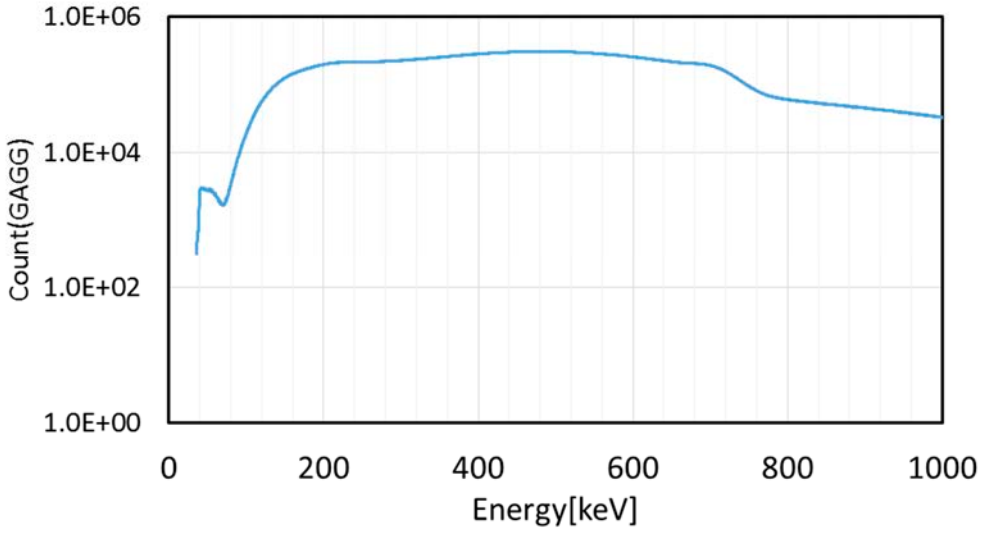

Figure 3- 99 *Gamma-ray measurement focusing on low energy range*

3-2. Feasibility study with neutrons for Pu monitoring

3-2-1. Feasibility study with neutrons outside of concrete cell

A. Neutron count rate measurement

A-1. Purpose of measurement

^{244}Cm and Pu contained in the HALW emit neutrons created by spontaneous fission. Generally, because neutrons have strong penetrability, it may be possible to measure neutron count outside the thick concrete cell. Therefore, to investigate the feasibility of Pu monitoring by neutron monitoring outside the concrete cell, we conducted neutron measurements outside the concrete cell that housed the target HAW tank (V35).

In addition, to measure background (BG) neutron count rate and confirm the neutron count rate difference due to different radioactive compositions of HALW, neutron measurements were conducted for the spare tank (V36) and the HAW tank (V34), which have different radioactive components from those in V35. *Figure 3- 100* shows the floor plan of the HAW tanks and the measurement points.

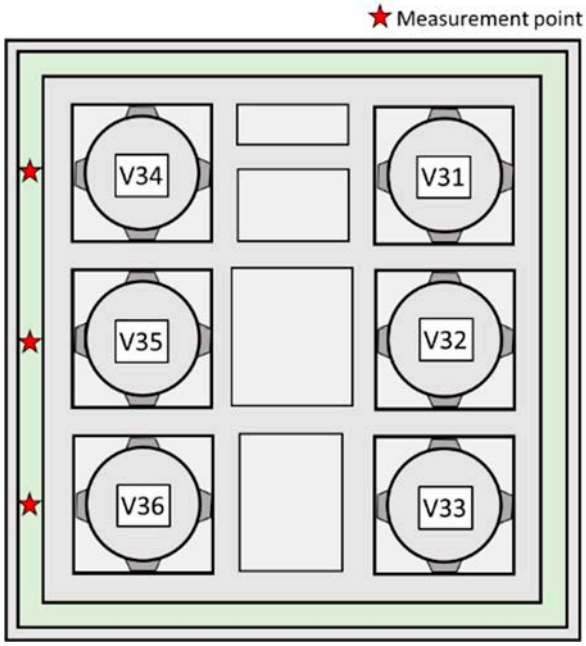

Figure 3- 100 *Relationship between target tank and measurement point*

Neutron count rate measurements outside the concrete cell were conducted using the neutron detectors (GBAS, BCAT) installed on the external surfaces of the concrete cells housing the HAW tanks. *Figure 3- 101* shows the installed neutron detectors.

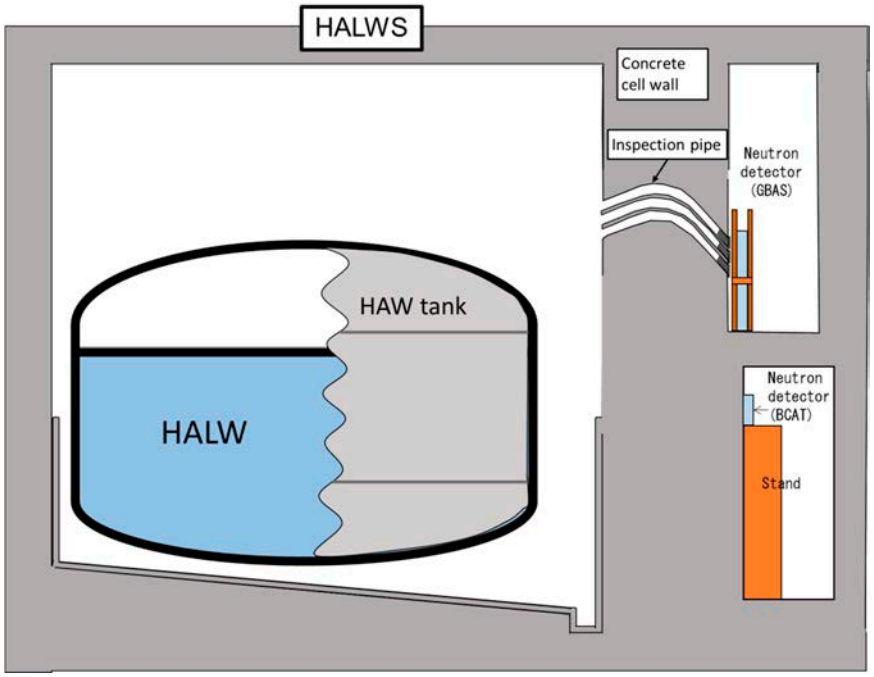

Figure 3- 101 *Installed neutron detectors*

A-2. Detector for experiment (GBAS, BCAT)

GBAS (Glove Box Assay System) was one of the neutron measurement systems used to measure held-up plutonium in GB. GBAS comprises 12 He-3 gas tubes (D: 2.54 cm, L: 152 cm). These tubes are set up inside high-density polyethylene with Cd and Al liners on the outside. The signal from the detector element is processed by the upper electric installation by using AMSR. *Figure 3- 102* shows an image of the measurement conducted with the GBAS, as well as specifications of the GBAS.

Figure 3- 102 *GBAS (Glove Box Assay System)*

【Specification】
- Detector element: He-3 gas tube × 12
- Weight: approximately 130 kg

Neutron measurements at the locations where measurement could not be performed using GBAS or GBAS could not be installed were conducted using BCAT (Glove Box Cleanout Assistant Tool), which is lighter and more portable than GBAS. BCAT comprises six He-3 gas tubes (D: 2.54 cm, L: 33 cm). These tubes are set up inside high-density polyethylene. The signal from the detector element was processed by the upper electric installation by using AMSR. BCAT has lower detector efficiency for neutrons compared to that of GBAS. *Figure 3- 103* shows an image of the measurement conducted with BCAT, as well as the specifications of BCAT.

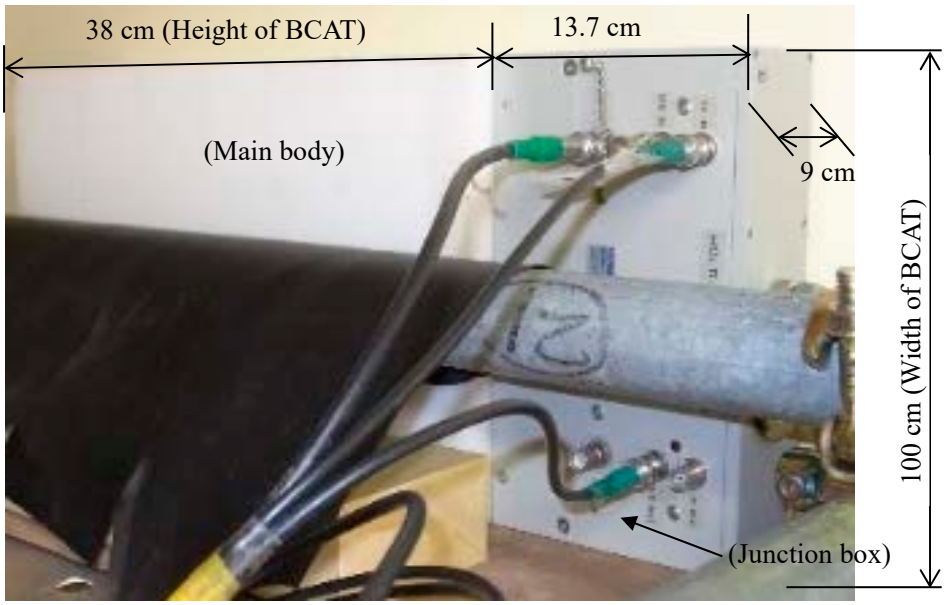

Figure 3- 103 *BCAT (Glove Box Cleanout Assistant Tool)*

【specification】

- Detector element: He-3 gas tube × 6
- Weight: approximately 8 kg

A-3. Experimental setup

(1) GBAS

Figure 3- 104 shows the experimental setup of GBAS. A high input voltage is supplied from a shift register (AMSR-150). Signals from the detector generated by the detected neutrons are transmitted to the shift register. Thereafter, the neutron count is recorded by the laptop PC connected to the shift register. The INCC software application is used for the measurement.

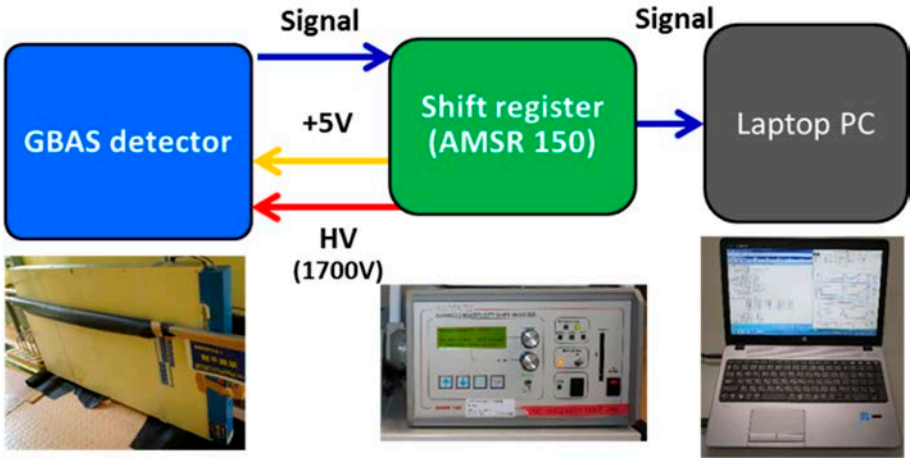

Figure 3- 104 *Experimental setup of GBAS*

【Measurement parameter】

Table 3- 14 shows the neutron measurement parameters of GBAS.

Table 3- 14 *Neutron measurement parameters of GBAS (software: INCC)*

Parameter	Set value	Units
Pre-delay	4.5	μ s
Gate length	64	μ s
2nd gate length	64	μ s
High voltage	1700	V
Die away time	61	μ s
Efficiency	0.05	—
Multiplicity dead time	0.00	ns
Coefficient A	0.68	(1E-6)
Coefficient B	0.22	(1E-12)
Coefficient C	0.000	(1E-9)
Double gate fraction	0.0001	—
triple gate fraction	0.0001	—

(2) BCAT

Figure 3- 105 shows the experimental setup of BCAT. High input voltage is supplied from the shift register (AMSR-150). Signals from the detector generated by the detected neutrons are transmitted to the shift register. Thereafter, the neutron count is recorded by the laptop PC connected to the shift register. The software application used for the measurement is INCC.

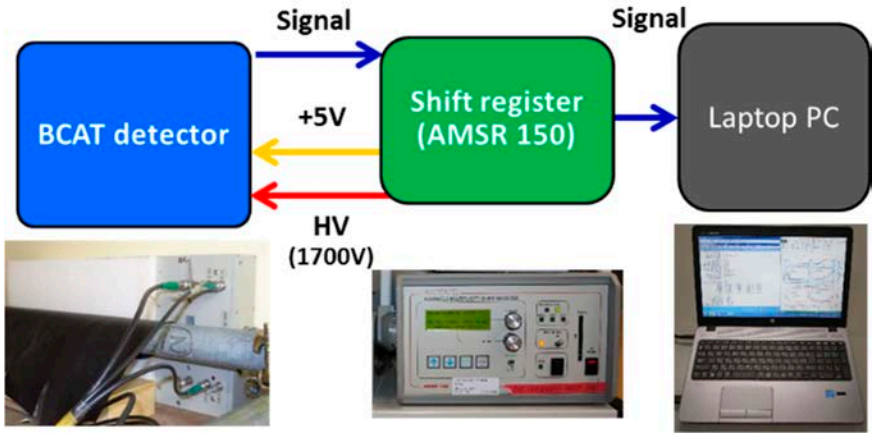

Figure 3- 105 *Experimental setup of BCAT*

【Measurement parameter】

Table 3- 15 shows neutron measurement parameters of BCAT.

Table 3- 15 *Neutron measurement parameters of BCAT (software: INCC)*

Parameter	Set value	Units
Pre-delay	3.0	μ s
Gate length	32	μ s
2nd gate length	64	μ s
High voltage	1700	V
Die away time	40.1	μ s
Efficiency	0.0082	—
Multiplicity dead time	0.00	ns
Coefficient A	0.00	(1E-6)
Coefficient B	0.00	(1E-12)
Coefficient C	0.000	(1E-9)
Double gate fraction	0.0001	—
triple gate fraction	0.0001	—

A-4. Validation

A ^{252}Cf check source was used to confirm the integrity of each device to validate the functionality of GBAS and BCAT. *Figure 3- 106* shows the ^{252}Cf check source specification.

Radiation	Neutron
Source	^{252}Cf
Image	
Source No.	G3-400
Activity	3.6 MBq (8/15/2009)

Figure 3- 106 *^{252}Cf check source*

A-5. Measurement

Measurement time and count target are as follows.

(1) GBAS

Measurement time: 60 s × 60 cycles (=1 h)

60 s × 900 cycles (=15 h)

Target: Singles

(2) BCAT

Measurement time: 60 s × 60 cycles (=1 h)

Target: Singles

A-6. Result

(1) Neutron count rate measurement outside concrete cell with GBAS (upper liquid level)

The neutron count rate measurement was conducted with GBAS installed at the floor level, which is approximately the same height as the HALW liquid level. The thickness of the concrete cell at this point was 20 cm less than that of the bottom floor.

Figure 3- 107 shows the measured count rates at each point. The neutron count rate was about 40–50 counts per minute, and the uncertainty at each point was within 2%. Based on these results, we could confirm that the evaluation of nuclear materials was difficult during neutron measurement with GBAS outside the concrete cell because the neutron count rates were low, and we were unable to confirm the difference in the HAW solutions.

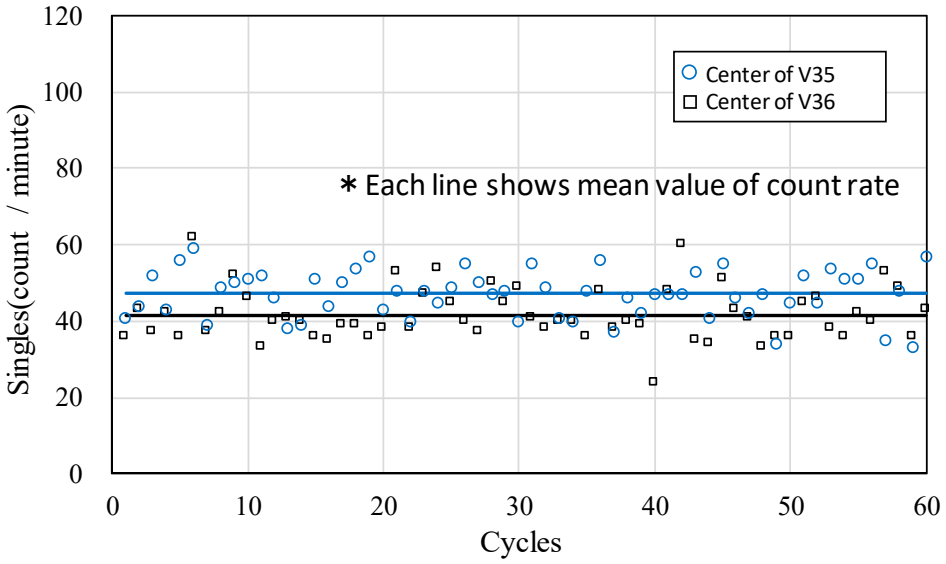

Figure 3- 107 *Neutron count rate outside concrete cell on upper floor (GBAS)*

(2) Neutron count rate measurement outside concrete cell with BCAT (center of HALW)

Neutron count rate measurement was conducted with BCAT installed at the point where the surface of the wall is located at the center of HALW. The concrete cell thickness at this point was 20 cm more than that of the upper floor.

Figure 3-108 shows the measured count rate at each point. The neutron count rate was approximately few tens per minute, and the uncertainty at each point was within 5%. Based on these results, we could confirm that the evaluation of nuclear material was difficult based on neutron measurement with BCAT outside the concrete cell because the neutron count rate was low, and we were unable to confirm the difference in the HAW solutions.

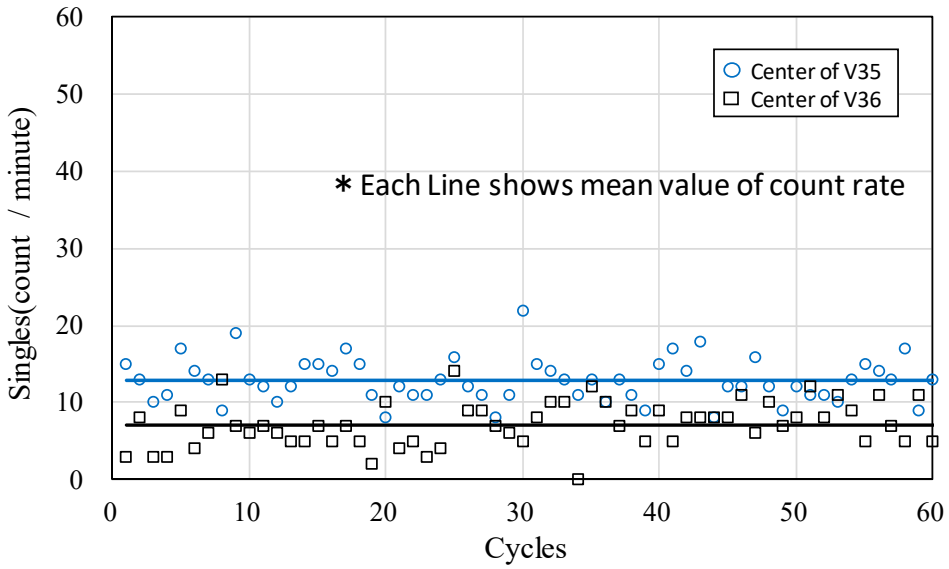

Figure 3- 108 *Neutron count rate outside concrete cell at bottom floor (BCAT)*

Since the neutron count rate difference between V35 and V36 at the bottom floor was higher than that in case of the upper floor, neutron count rate measurements outside the concrete cell at the bottom floor for V34, which has a different inventory from V35, were perfomred additionally. *Figure 3- 109* shows the neutron count rates outside the concrete cell at the bottom floor for each tank.

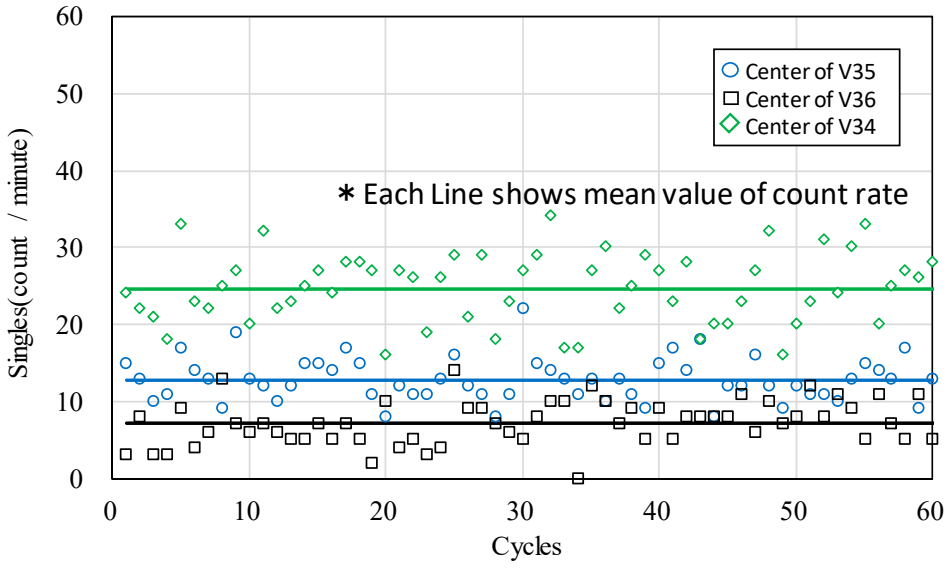

Figure 3- 109 *Comparison of neutron count rate outside concrete cell at bottom floor for each tank (BCAT)*

A-7. Comparison between simulation (PHITS) and measurement result

Neutron distribution was simulated using the neutron analysis data as the input file (see chapter 2). Scattered neutrons were detected by means of simulation, as shown in *Figure 3- 110*. We assumed that the radiation was scattered because of the structure of the screw duct, as shown in 3-1-1 B-6. According to the simulation results, no neutrons were detected. This shows that it is difficult to explain the count difference between V35 and V36.

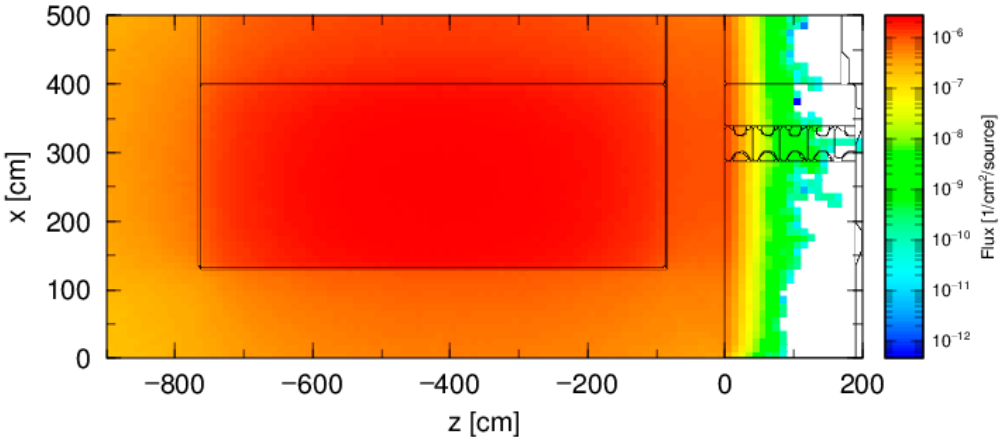

Figure 3- 110 *Neutron simulation result*

A-8. Consideration

Neutron count rate measurements were conducted using the neutron detectors (GBAS and BCAT) installed on the external surface of the concrete cell housing HAW tanks (V34, V35, and V36).

Based on the results of the neutron measurements outside the concrete cell, we were able to obtain a detector response corresponding to the inventory of the HAW tank when the neutron detector was located at the center of the HALW. However, to achieve better monitoring accuracy for solution monitoring, we must improve detector efficiency, increase count rate, or conduct neutron count rate measurement inside the concrete cell or in the concrete cell wall, where it is assumed that a higher count rate can be obtained because the measured neutron count rate on the external surface of the concrete cell is low (GBAS: 0.7 counts/s, BCAT: 0.4 counts/s).

3-2-2. Feasibility study with neutrons inside concrete cell

A. Neutron count rate measurement

A-1. Purpose of measurement

In this measurement, we measured neutron count rate distribution inside the concrete cell and compare the results with the simulation results. These data will be used to validate and optimize the model. Moreover, neutron distribution data will be utilized to study detector position for Pu monitoring.

A-2. Measurement tools

(1) Radiation meter (*Figure 3- 111*)

① B-10 proportional counter

- Size: φ 0.5 inch × L: 7 inch (Active φ: 0.44 inch × L: 5 inch)
- Sensitivity : about 1 cps/nv @ 1,900 V (nv: neutron flux)
- Fill gas (atm): Argon (1 atm)

Figure 3- 111 *B-10 proportional counter*

(2) Holder and operation tool

① Holder (*Figure 3- 112*)

- Material: PEEK
- Size: Diameter 55 mm, Length 315 mm, Cylinder type (both ends are conical)
- Structure: Division into upper and lower, and fixing across the board (Fixed B-10 proportional counter and electrical base).

② FRP rod (same as that used in chapter 3-1-2)

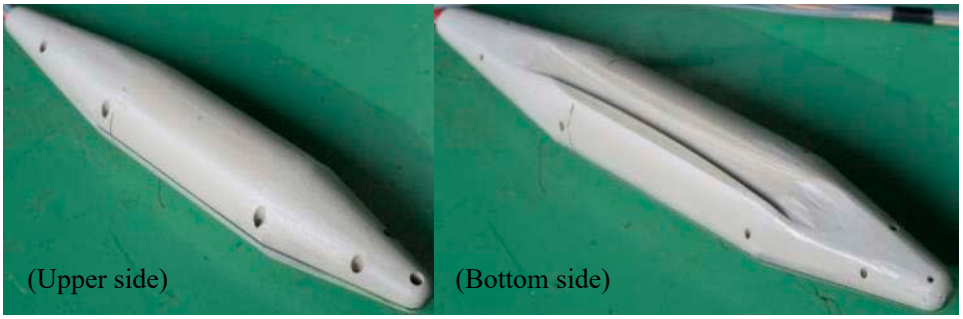

Figure 3- 112 *Holder for B-10 detector*

(3) Signal processing and control

① Shift register: JSR-15, JSR-12 (*Figure 3- 113*)

② Software: INCC ver 5.1.2

(JSR-15) (JSR-12)

Figure 3- 113 *Shift registers*

A-3. Experimental setup

(1) Device structure

Figure 3- 114 shows the composition of the B-10 proportional counter composition, *Figure 3- 115* shows a drawing of the measurement system.

The B-10 proportional counter used is a thermal neutron detector with a large thermal neutron absorption cross section. When neutrons are absorbed by B-10, alpha particles are produced ($^{10}B + n \rightarrow {}^{7}Li + \alpha$). We measured the electrical signal generated by the ionization effect of the alpha particle. The electrical signals were found to be proportional to the quantity of gas ionized (quantity of neutrons absorbed).

The high voltage (HV) and low voltage power (5 V) of the KM200 pre-amplifier were supplied from the shift register (JSR-12). The neutron signals were collected using the JSR-15 shift register. The measurement data were collected and recorded using INCC ver 5.1.2 via a PC. Settings such as measurement time were executed on the PC.

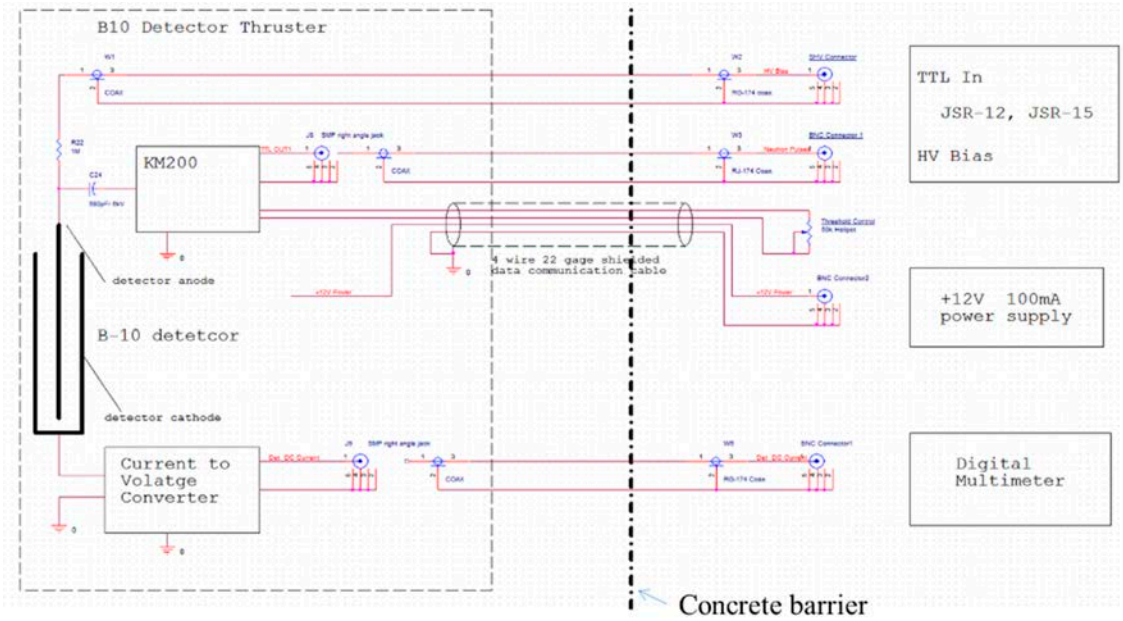

Figure 3- 114 *B-10 proportional counter composition*

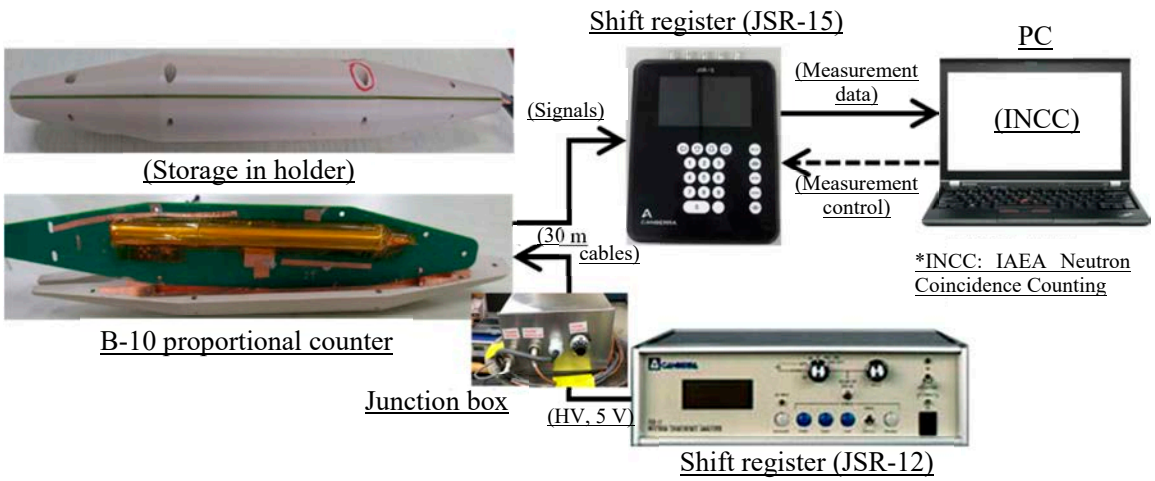

Figure 3- 115 *Drawing of measurement system*

(2) Internal structure of B-10 holder

Figure 3- 116 shows a schematic drawing of the detector, and *Figure 3- 117* shows the internal structure of the holder for the B-10 proportional counter. The B-10 holder is divided into two parts, namely, upper part and lower part. The board to which the B-10 detector and the electrical base (KM200) are attached is sandwiched between the upper and the lower parts. The B-10 detector is fixed on the underside of the board, and the base is fixed to the upper part of the board. The FRP rod is

connected around the center of the B-10 holder and designed to come out with cables from the rear of the B-10 holder. In addition, the internal cavities of the B-10 proportional counter holder are laminated with cooper tape to shield the very sensitive pulse-counting electronics from electromagnetic and electrostatic discharge noise during measurements in the tank. To prevent electrical discharge due to humidity condensation, the HV circuitry and components on the PCB board are conformal coated, and the detector electrodes are covered with HV dielectric grease, similar to the conformal coating and dielectric grease on the gamma IC Holder.

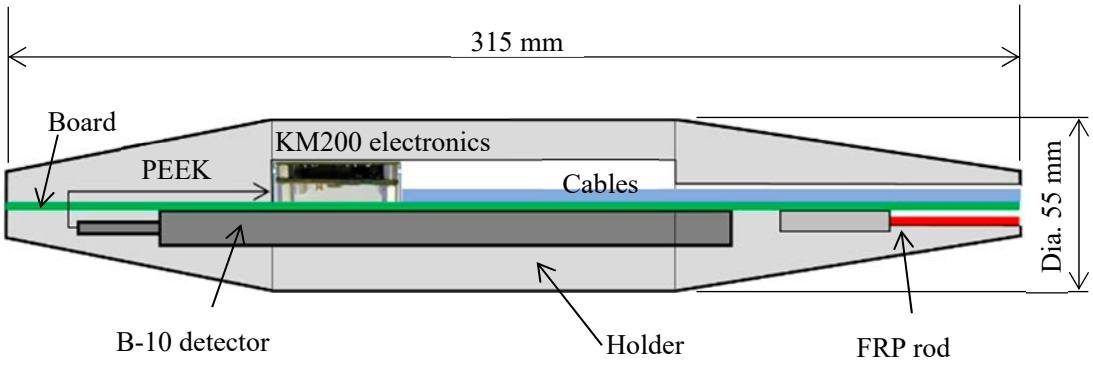

Figure 3- 116 *Schematic drawing of detector*

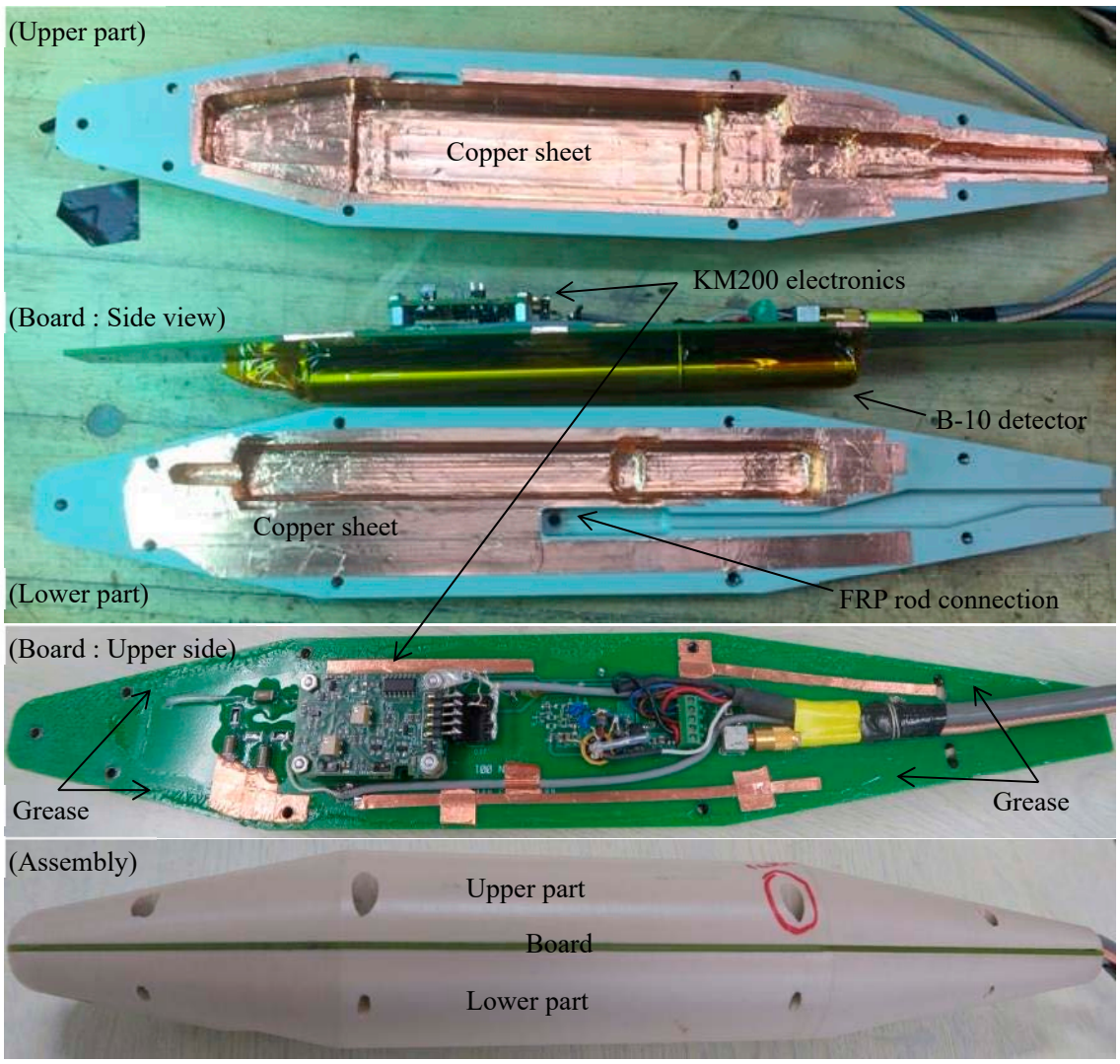

Figure 3- 117 *Internal structure of B-10 holder*

(3) Connection of cables

Figure 3- 118 shows how to connect the cables to the junction box. The cables of the B-10 detector are connected to the shift registers (JSR-12 and JSR-15) via a junction box. Signal and 5 V cables are BNC connectors, and the HV cable is a SHV connector.

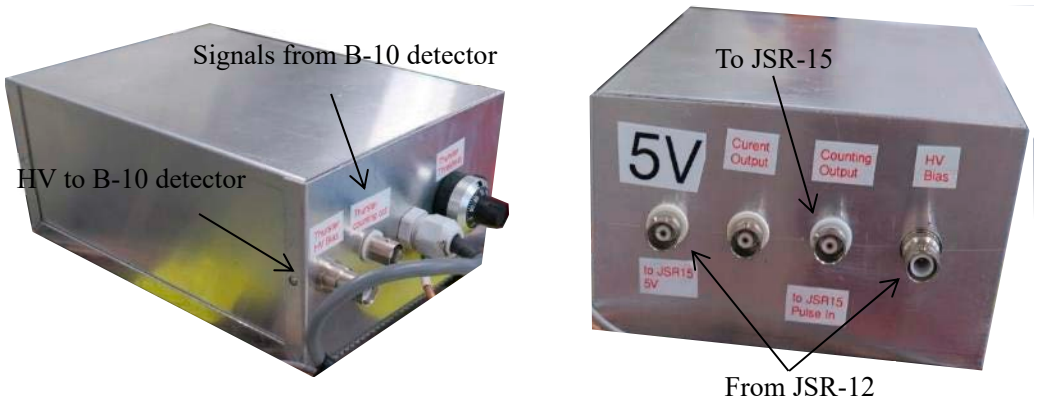

Figure 3- 118 *Connection of cables to junction box*

A-4. Calibration test

The neutron holder is based on a novel radiation-hard B-10 detector and novel electronics for simultaneous readout of neutron and gamma information from the same detector [9]. The detector is operated at a very low gain on the slope of the counting characteristics to cope with the very high gamma radiation. The B-10 detector uses very sensitive low-noise electronics with remote threshold control for operation in over wide ranges of gamma and neutron fields.

The B-10-lined detectors do not have a HV plateau in terms of counting characteristics, such as the ones in the case of He-3 tubes (counting rate equal to detector reaction rate) based on their operating principle. They have a quasi-plateau as a result of gross counting effects at a low threshold. Because this detector is meant to be operated with very low gain on the slope to avoid gamma pile-up and space charge effects, we performed efficiency cross calibration between the RS-P7-0405-202 B-10 detector with passport sensitivity 1 cps/nv and the RS-P4-0812-124 He-3 tube with passport sensitivity 37 cps/nv by using a dedicated HDPE moderator with symmetrical geometry. The measurement setup is shown in *Figure 3- 119*, where the two detectors with KM200 preamplifiers and the A7-866 ^{252}Cf source with 35 μCi activity were installed in the designated holes. The top half of the He-3 tube active length was wrapped with a Cd sheet to ensure its geometry was similar to that of the B-10 detector. The count rate characteristics versus HV bias voltage were measured with each detector by using this fixed geometry. Moreover, only half of the active length of the He-3 tube was exposed in the known reproducible geometry.

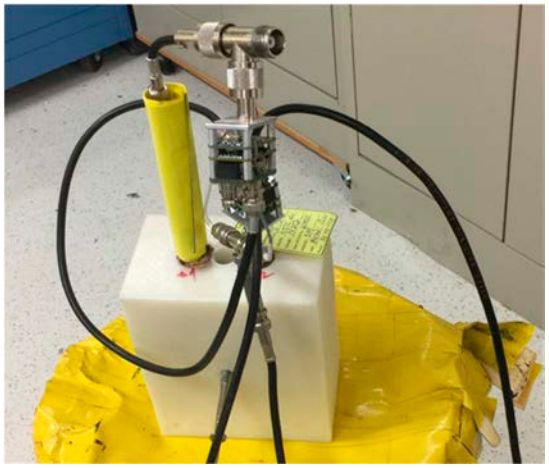

Figure 3- 119 *Measurement setup for efficient cross calibration of B-10 and He-3 tubes*

The JSR-12 shift register was used to power the electronics and collect data. The plateau comparison plots are shown in *Figure 3- 120*(a). We used the constant plateau sensitivity of the He-3 tube to calculate the variable with the HV bias sensitivity of the B-10 tube. The sensitivity plots are shown in *Figure 3- 120*(b). The B-10 detector sensitivity plot is the efficiency calibration characteristic for any given operating voltage, depending of the strength of the gamma field that can be used to calculate the neutron flux in the HALW tank measurement. The sensitivity is comparable to that of the U-235 fission chambers in the FORK detector.

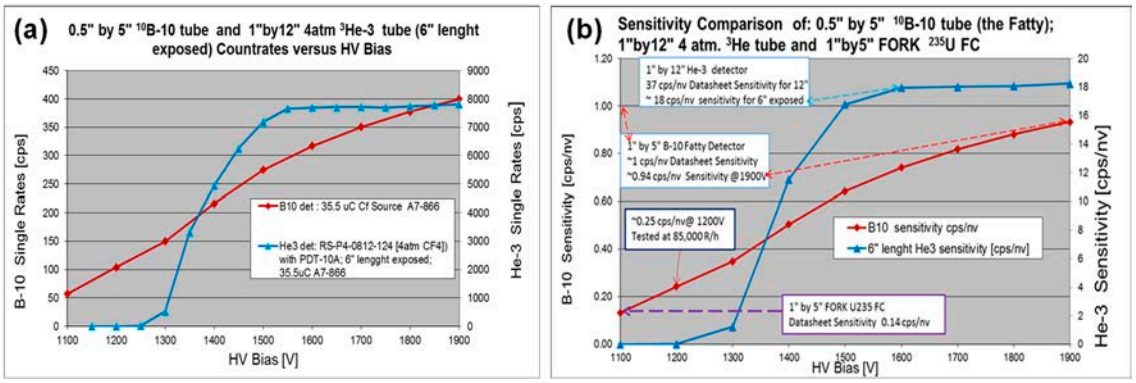

Figure 3- 120 *Results for (a) singles rate versus HV bias and (b) B-10 sensitivity plots versus HV bias*

The overall design configuration of the B-10 neutron holder detector is shown in *Figure 3- 121*. Here, we fabricated a different cylindrical moderator that can accommodate the entire holder and neutron source inside to increase the counting efficiency and accelerate the measurement time with relatively weak neutron sources.

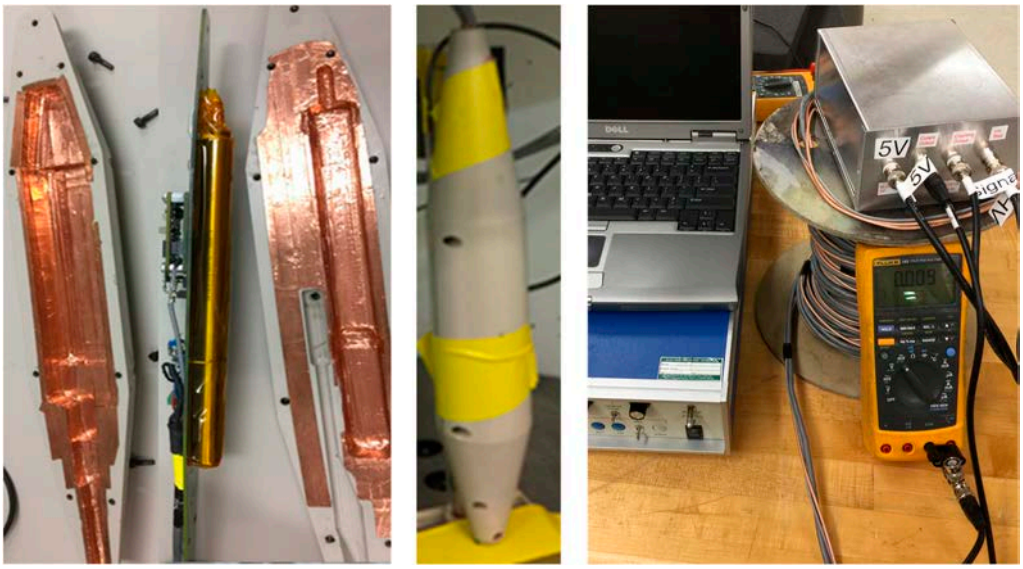

Figure 3- 121 *Neutron Holder configuration. Let to right: open view of holder assembly: assembled holder; 30-m cable with remote threshold control box; and data acquisition system (JSR-12 for power neutron counting and Fluke DMM as total current meter)*

Neutron and Gamma Measurements with B-10 Holder

The sensitivity of the B-10 Neutron holder to high gamma fields was measured using the 500 R/h ^{137}Cs calibration source (setup similar to that used for the IC holder), with the B-10 holder installed in a cylindrical HDPE moderator to increase the neutron-counting efficiency.

The count rate in the neutron channel at a constant HV bias voltage was recorded as a function of the gamma field to determine the boundaries of gamma pile-up and gamma leakage in the neutron channel. The results of these measurements are shown in *Figure 3- 122*(a), and the same data as shown in (a) but expanded with the measurement data obtained using the MARK–1 Irradiator under very strong gamma fields is shown in *Figure 3- 122*(b). These measurement results show that the neutron channel can reliably measure the neutron flux under elevated gamma fields.

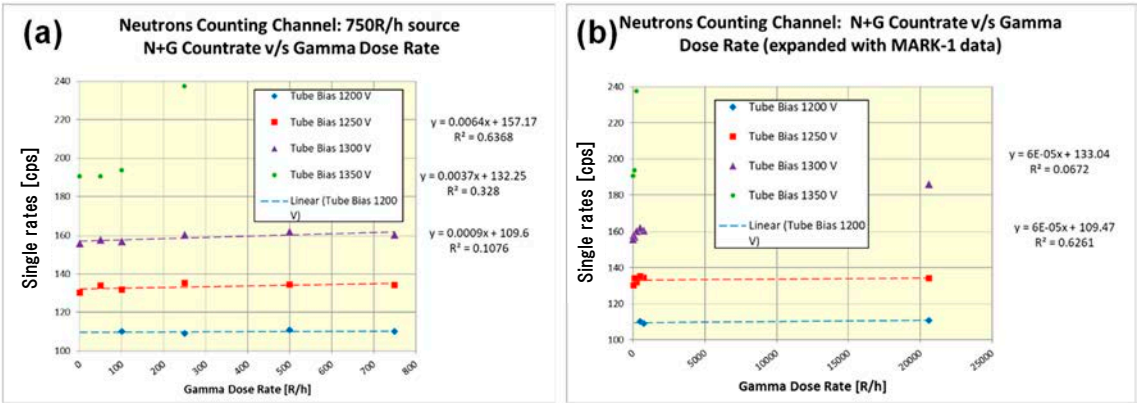

Figure 3- 122 *(a) Neutron channel count rate versus gamma dose rate at different bias voltages and (b) Same data as (a) bu t expanded with data obtained using MARK–1 Irradiator.*

The gamma sensitivity of the current channel was calibrated using the same setup but without external poly and neutron sources. The calibration results are shown in *Figure 3- 123*.

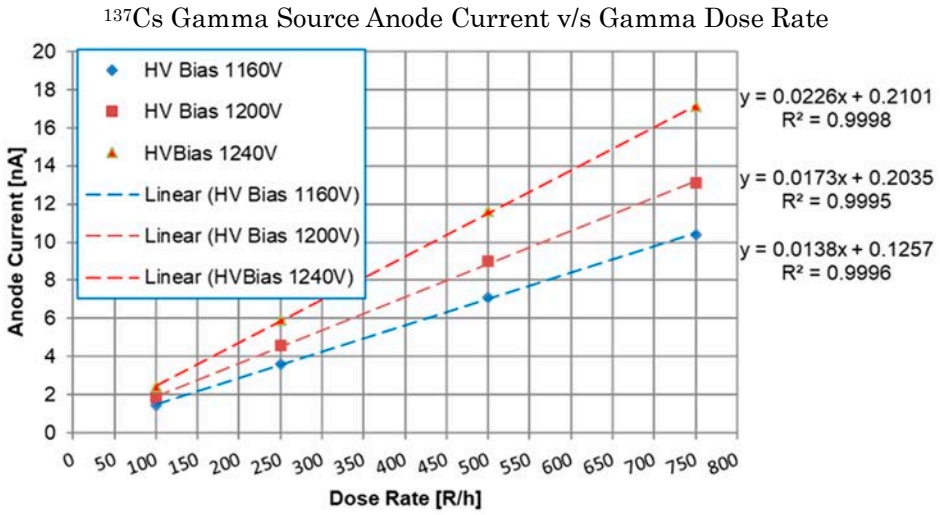

Figure 3- 123 *Calibration plots of gamma sensitivity of current channel as function of HV bias*

A-5. Neutron count rate distribution measurement

(1) Measurement

Figure 3- 124 shows a schematic drawing of the measurement. The measurement method is similar to that specified in clause 3-1-2A. At first, we insert the B-10 holder containing the B-10 detector to the deepest insert position and measure the neutron count rate at intervals of 10 cm from there toward the outside. The deepest insert position is 600 cm based on prior confirmation. Before the measurement, we confirmed that the B-10 proportional counter was functioning normally by using a standard ^{252}Cf source (*Figure 3- 125*).

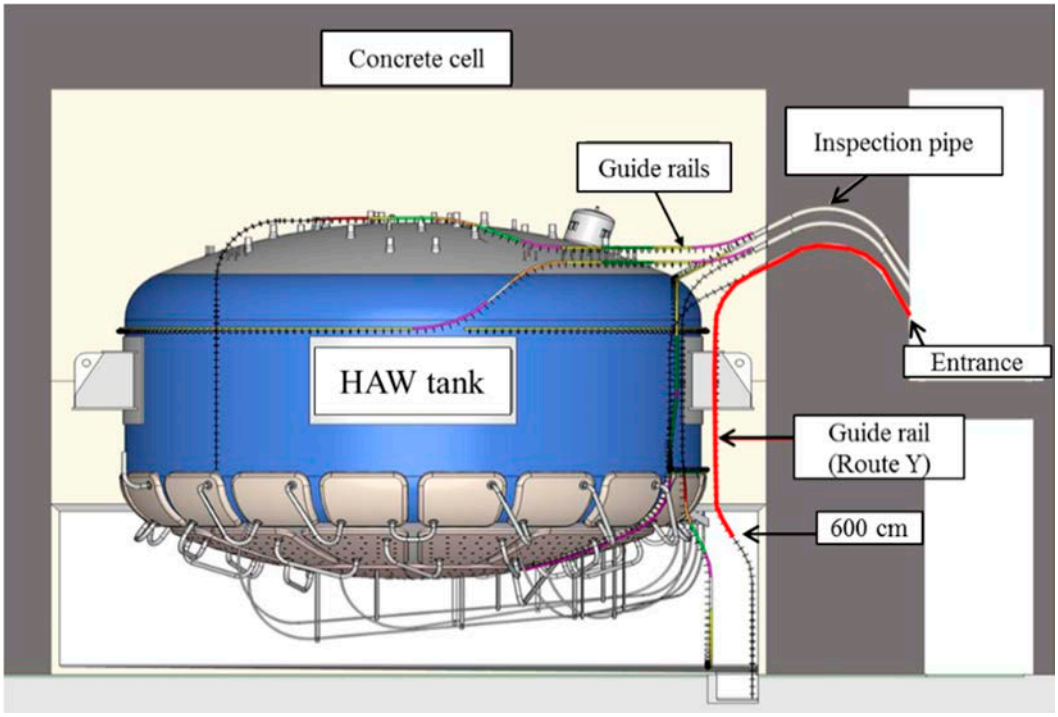

Figure 3- 124 *Schematic drawing of measurement*

[Conditions]

- Tank: 272V35
- Rail: Left lower inspection pipe (Route Y)
- ID: 600 cm
- High voltage: 1,250 V
- Measurement time: 30 s × 4 times (total 2 min)
  (Evaluated value is average of four measurements)
- Measurement points: at intervals of 10 cm from ID 600 cm to 0 toward the outside

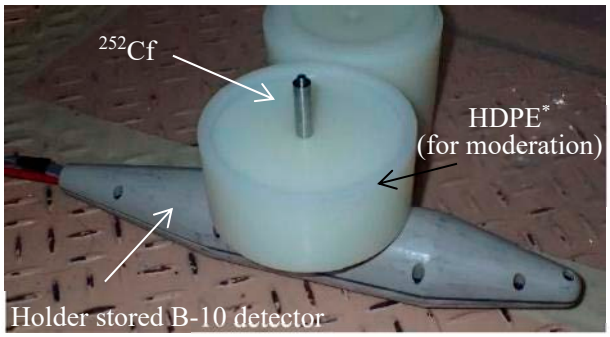

(252Cf specification)

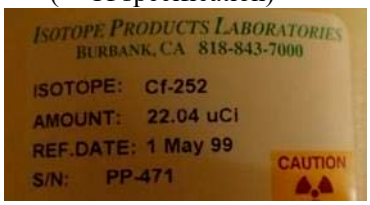

* HDPE : High-density polyethylene

Figure 3- 125 *Calibration using ^{252}Cf source*

(2) Results

Figure 3- 126 and *Table 3- 16* show the neutron count rate distribution obtained at 272V35 by changing ID.

① Neutron count rate increased in small steps from ID 170 cm and decreased once at ID 320 cm.

② After ID 320 cm, the neutron count rate increased with ID. The maximum count rate was approximately 35 cps at ID 490 cm.

③ The maximum count rate point was located 100 cm below the liquid level.

④ After ID 480 cm, the neutron count rate decreased in small steps with increasing ID.

⑤ We confirmed repeatability of the neutron count rate measurement based on the data obtained on September 6, 2017 and September 27, 2017.

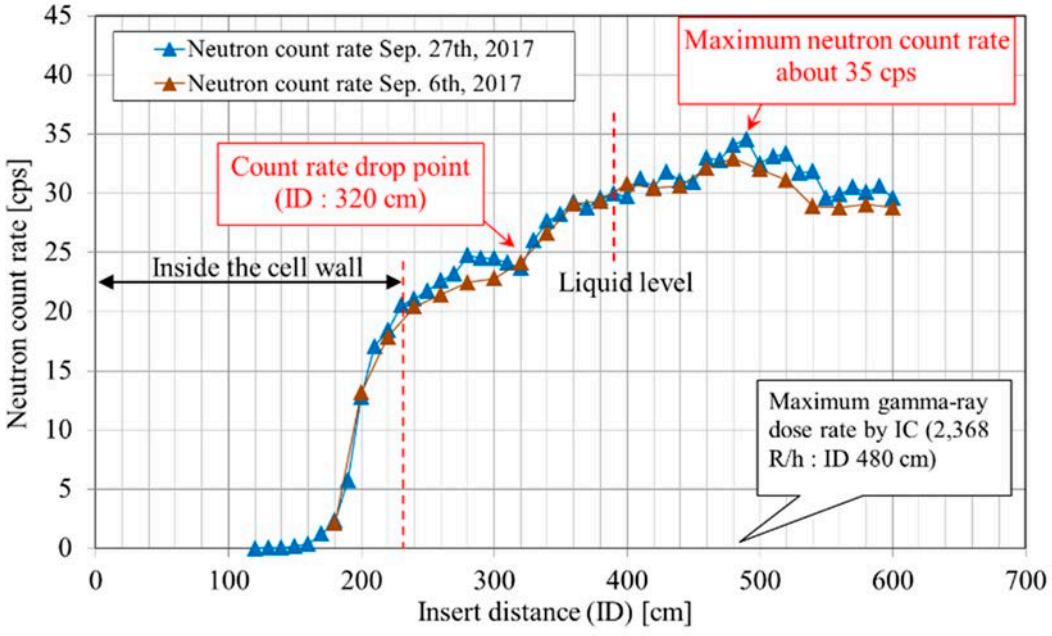

Neutron Intensities v.s. B-10 holder Position at 272V35 (Sep, 2017)

Figure 3- 126 *Neutron count rate distribution inside concrete cell*

Table 3- 16 *Neutron count rate distribution inside concrete cell (1/2)*

ID [cm]	Neutron [cps]					
	Sep. 27, 2017					Sep. 6, 2017
	Number of measurements				AVG	
	1	2	3	4		
600	28.63	29.30	30.87	29.73	29.63	28.80
590	30.57	31.23	31.77	28.77	30.59	-
580	28.13	32.07	31.77	28.33	30.08	29.04
570	29.73	31.07	30.80	30.57	30.54	-
560	30.20	29.60	30.10	29.70	29.90	28.82
550	30.63	29.23	30.07	28.53	29.62	-
540	33.67	29.67	32.13	31.93	31.85	28.88
530	30.63	31.23	33.60	31.50	31.74	-
520	34.77	32.93	34.03	31.63	33.34	31.13
510	31.53	34.03	34.00	33.03	33.15	-
500	32.37	33.70	31.53	32.37	32.49	32.04
490	34.03	33.93	34.77	35.57	34.58	-
480	35.40	33.73	32.63	34.50	34.07	32.94
470	32.30	32.27	33.07	33.63	32.82	-
460	31.60	32.97	33.30	33.97	32.96	32.12
450	30.77	30.00	31.97	30.90	30.91	-
440	31.17	30.87	30.90	31.17	31.03	30.61
430	33.47	31.63	30.53	31.57	31.80	-
420	30.27	29.67	31.73	30.53	30.55	30.43
410	31.03	32.03	31.43	30.43	31.23	-
400	30.00	30.37	29.20	29.33	29.73	30.82
390	29.97	30.10	29.13	30.73	29.98	-
380	29.17	30.53	30.30	28.53	29.63	29.35
370	30.43	28.30	26.73	29.67	28.78	-
360	28.87	28.57	30.10	29.73	29.32	29.13
350	28.13	27.53	29.37	27.97	28.25	-
340	29.20	27.63	27.77	25.93	27.63	26.62
330	26.80	26.03	25.17	26.10	26.03	-
320	24.23	23.73	23.53	23.20	23.67	24.16

Table 3- 16 *Neutron count rate distribution inside concrete cell (2/2)*

310	24.00	25.20	23.37	23.97	24.14	-
300	24.20	25.33	24.30	24.17	24.50	22.79
290	25.43	24.30	23.70	24.73	24.54	-
280	25.53	23.77	24.33	25.43	24.77	22.47
270	22.93	23.80	22.83	23.33	23.22	-
260	23.20	21.97	22.47	22.83	22.62	21.47
250	21.50	21.20	21.13	23.20	21.76	-
240	20.63	21.67	21.17	20.87	21.09	20.42
230	21.10	20.17	20.47	20.47	20.55	-
220	18.33	18.43	18.73	18.23	18.43	17.87
210	16.80	17.30	16.87	17.33	17.08	-
200	13.37	12.50	11.83	13.53	12.81	13.14
190	5.90	6.23	5.40	5.47	5.75	-
180	1.63	2.63	2.63	2.50	2.35	2.12
170	1.13	1.43	1.33	0.97	1.22	-
160	0.23	0.43	0.37	0.43	0.37	-
150	0.17	0.17	0.17	0.23	0.19	-
140	0.00	0.03	0.00	0.03	0.02	-
130	0.13	0.03	0.10	0.03	0.07	-
120	0.00	0.00	0.00	0.00	0.00	-
BG.	0.00	0.00	0.00	0.03	0.01	-

(3) Consideration

① Relationship of distance between measurement points and solution

In addition to gamma-ray dose rate distribution measurement results inside the concrete cell in 3-1-2A, we confirmed the correlation between measurement points and distance from measurement points to the center of the solution (*Figure 3- 127*).

- The relationship between neutron count rates and distance from measurement points to the center of the solution shows good agreement with both measurement data.
- We confirmed that the influence of distance from the detector to the center of the solution was significant. Therefore, we consider the count rate distribution to be accurate based on the influence of the distance.
- The point with the maximum neutron count rate was 100 cm below the liquid level. This point was the closest point to the tank, and we believe that the location of this point depends on the largest

solid angle of the B-10 detector for the source and the increase in neutron incidence (same as gamma-ray dose rate distribution).

- A comparison with the gamma-ray dose rate distribution showed that they had a similar distribution shape (*Figure 3- 128*), but we confirmed the difference between the points corresponding to the entrance of the concrete wall and ID 400 cm. They have the difference of attenuation effect of the radiations, then we suppose that gamma-ray depends on significant impact of attenuation effect by concrete and distance in comparison with neutrons.

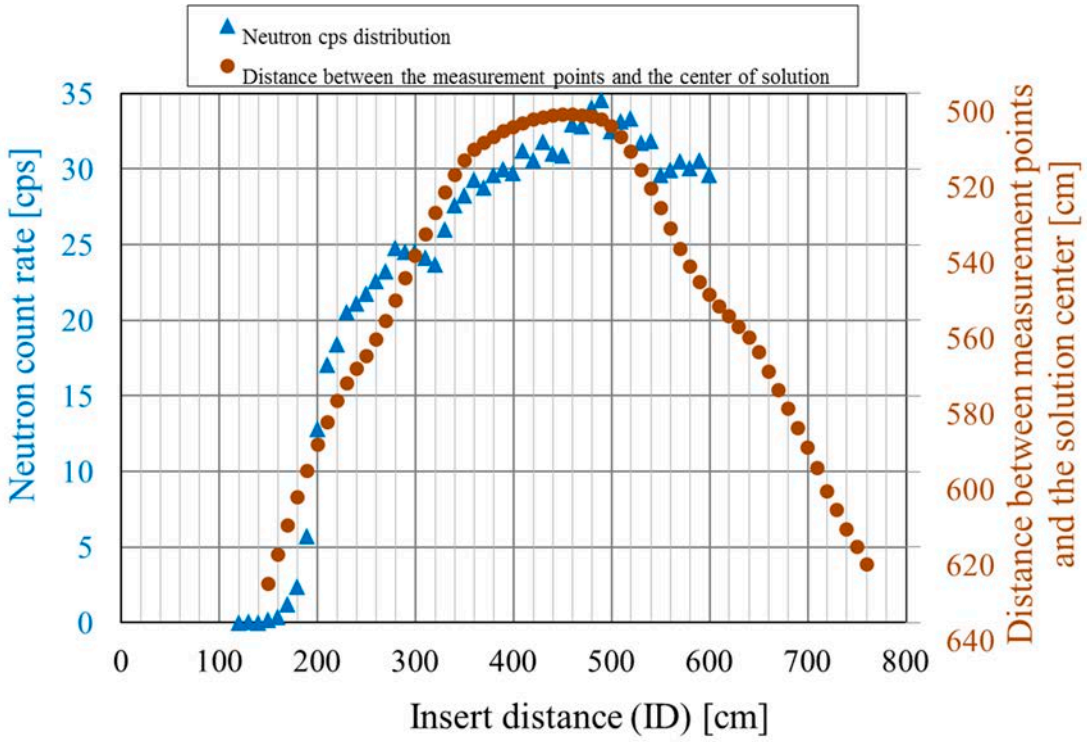

Figure 3- 127 *Relationship between ID and distance between measurement points and center of solution*

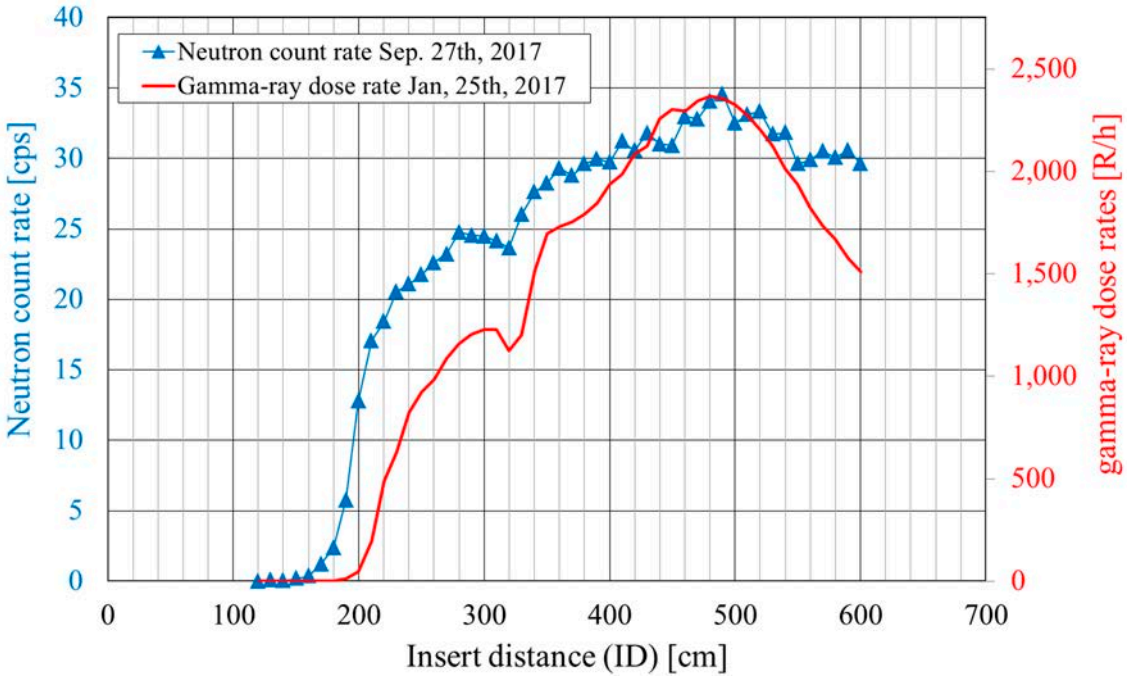

Figure 3- 128 *Comparison between neutron and gamma-ray distributions*

② Factor of discontinuous region of neutron count rates

We confirmed the attenuation effect of radiation at the same point at which the gamma-ray dose rate distribution was recorded. We considered the attenuation effect of the pipe supports to because the point corresponds to the point of attenuation of the gamma-ray dose rate distribution.

A-6. Additional tests

A-6-1. Comparison between tanks, routes

(1) Comparison between 272V35 and 272V34, and routes for the same tank

① Measurement

At the point of gamma-ray dose rate measurement, we measured neutron count rate distribution of the 272V35 and 272V34 tanks (*Figure 3- 129*). Then, we confirmed the correlation between neutron count rates and solution composition, total neutron quantity, and other factors.

In addition, there are six inspection pipes, and different rails are laid on each inspection pipe. To account for measurements with plural instruments, we confirmed the distribution of neutron count rates on different rails for the same tank (*Figure 3- 130*). Insert distance ranged until 300 cm based on prior confirmation.

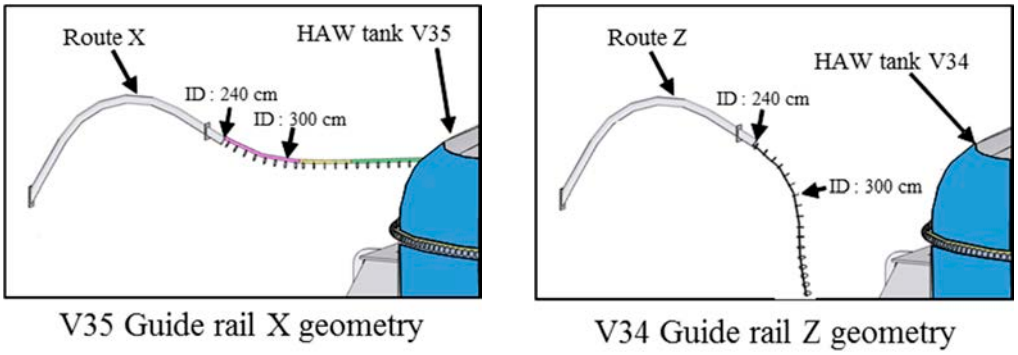

Figure 3- 129 *Geometry of rails of 272V35 and 272V34*

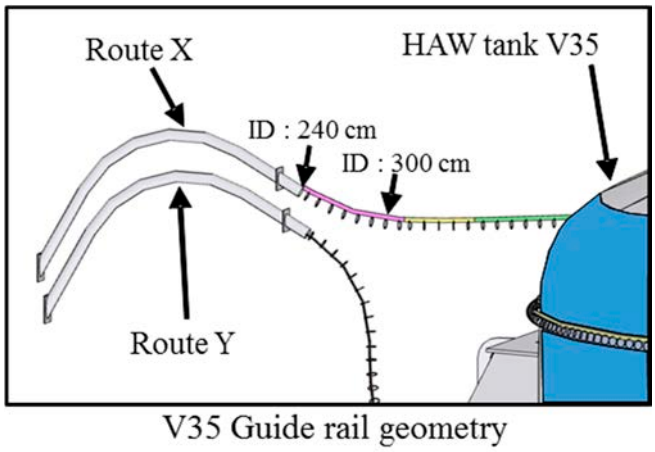

Figure 3- 130 *Geometry of rails of 272V35*

[Conditions]

- Tanks: 272V35 and 272V34
- Rails: Comparison of tanks (*Figure 3- 129*)

  Right middle inspection pipe at both tanks * 272V35 (route X), 272V34 (route Z)
- Rails : Comparison of routes (*Figure 3- 130*)

  Right middle (route X) and Left lower (route Y) inspection pipes
- Measurement points: at intervals of 10 cm from ID 150 cm to ID 300 cm
- High voltage: 1,250 V
- Measurement device: B-10 detector, Shift register (JSR-15)
- Data: 30 s × 4 times (total 2 min) at every point * Evaluation using average

② Results and consideration

Figure 3- 131 and *Table 3- 17* shows the results of comparisons of neutron count rate distributions.

②-1 Comparison between 272V35 and 272V34

We confirmed the difference in neutron count rate distribution depending on the difference in tanks (HALW composition). We confirmed the difference inside the concrete cell, and we confirmed the difference inside the concrete wall. In comparison with the gamma-ray dose rate distribution result of additional examination (2) in chapter 3 Radiation investigation, we confirmed that the neutron count rate inside the concrete cell wall was more effective than the gamma-ray dose rate inside the concrete wall.

②-2 Comparison between routes for same tank

We measured neutron count rate distributions on different routes for the same tank (same composition) but found no influence on neutron count rate across routes until ID 300 cm (inside concrete cell and concrete wall).

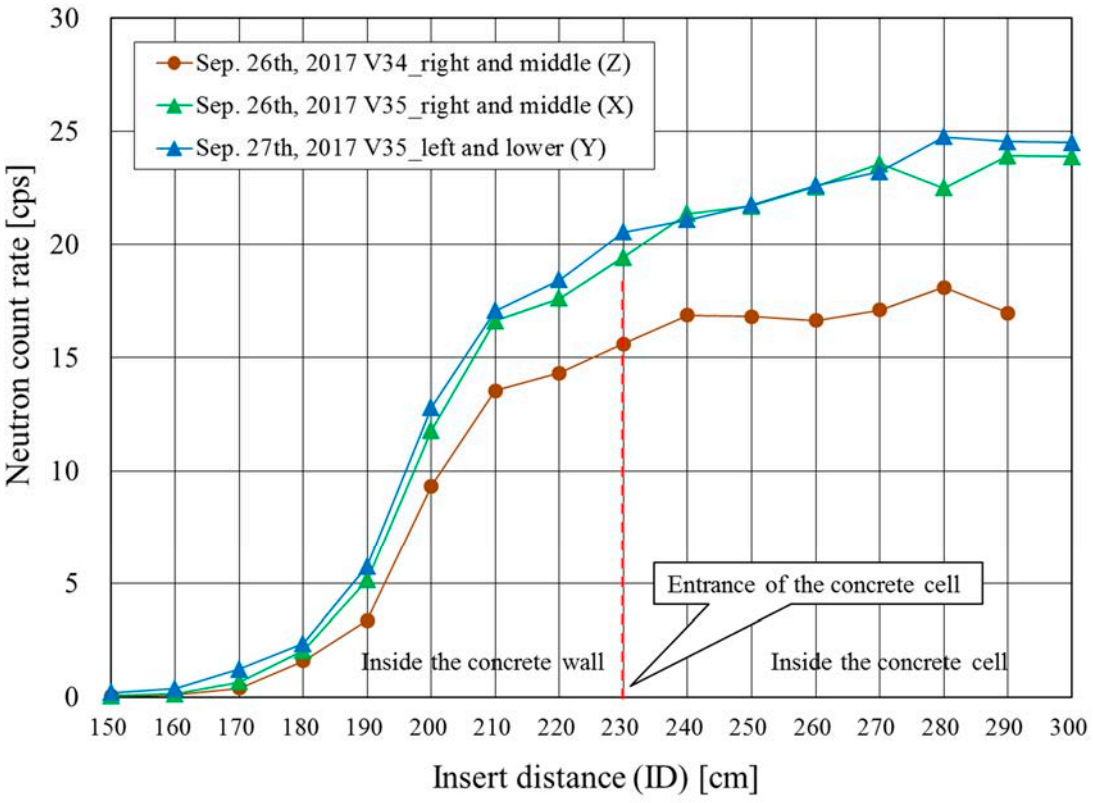

Figure 3- 131 *Neutron count rate distribution in different tanks*

Table 3- 17 *Measurement results of neutron count rate*

Measurement routes	ID	Neutron count rate [cps]
Sep. 26th, 2017 V35_right and middle (X)	300 cm	23.9
	290 cm	23.9
	280 cm	22.5
	270 cm	23.6
	260 cm	22.6
	250 cm	21.7
	240 cm	21.4
	230 cm	19.4
	220 cm	17.6
	210 cm	16.6
	200 cm	11.8
	190 cm	5.1
	180 cm	2.0
	170 cm	0.7
	160 cm	0.1
	150 cm	0.1
Sep. 26th, 2017 V34_right and middle (Z)	290 cm	17.0
	280 cm	18.1
	270 cm	17.1
	260 cm	16.7
	250 cm	16.8
	240 cm	16.9
	230 cm	15.6
	220 cm	14.3
	210 cm	13.5
	200 cm	9.3
	190 cm	3.4
	180 cm	1.6
	170 cm	0.4
	160 cm	0.1
	150 cm	0.0
	140 cm	0.0

(2) Comparison with other tanks

① Measurement

We confirmed that the neutron count rate corresponding to every solution composition (272V35 and 272V34) was different based on the result of an examination. Then, we measured the neutron count rate distribution of other tanks (272V31 and 272V33).

Measurement conditions were similar to those in examination (1). The measurement routes of 272V31 and 272V33 were different from those of 272V35 and 272V34. However, the positional relationship was similar to ID 300 cm, and the relationship of the measurement positions with the source was the same, regardless of route.

② Results

Figure 3- 132 and *Table 3- 18* show the comparison results.

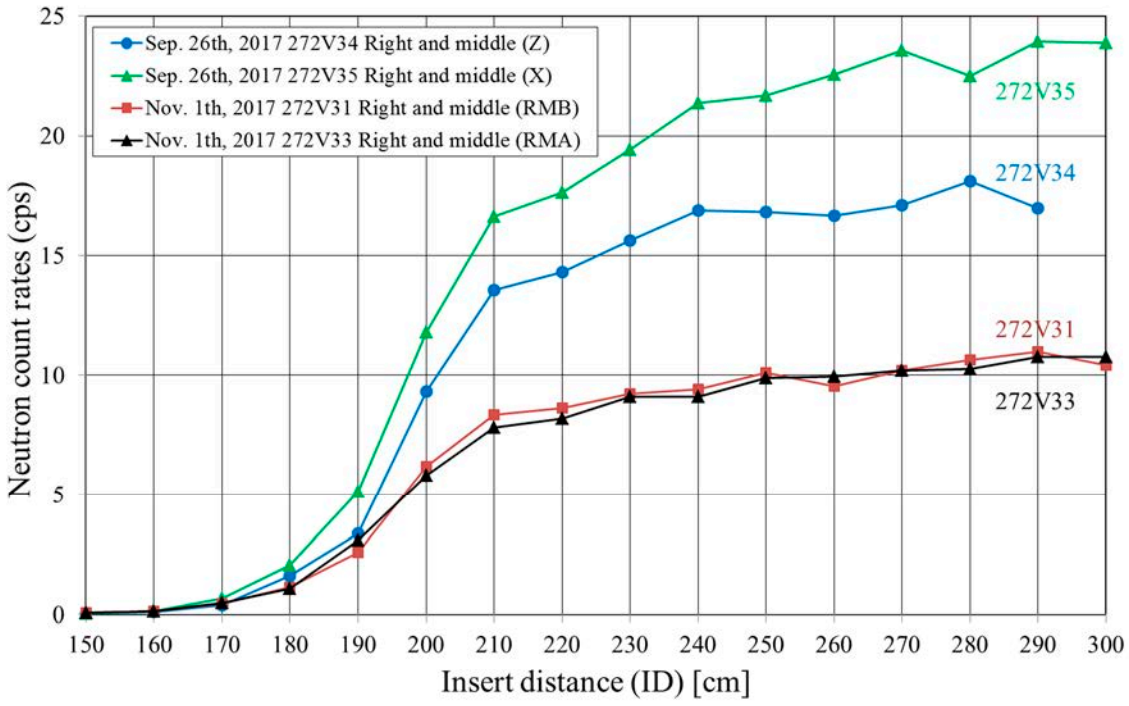

Figure 3- 132 *Comparison with tanks*

We confirmed a difference in the neutron count rate of every tank (solution composition). The neutron count rates of 272V31 and 272V33 were approximately half the count rate of 272V35. The count rate of 272V34 was distributed approximately 22% lower than that of 272V35 at 290 cm. The count rates of 272V31 and 272V33 were approximately identical. However, the ratio of neutron count rate distributions varied slightly across various measurement points.

Table 3- 18 *Measurement results of other tanks (272V31, 272V33)*

Measurement routes	ID	1 cps	2 cps	3 cps	4 cps	AVG cps
Nov. 1th, 2017 272V33 Right and middle (A)	300 cm	11.0	11.4	10.5	10.1	10.8
	290 cm	10.0	11.3	12.0	9.7	10.8
	280 cm	10.4	10.5	10.4	9.9	10.3
	270 cm	11.5	9.1	10.5	9.7	10.2
	260 cm	10.3	9.9	10.0	9.6	10.0
	250 cm	9.9	9.2	10.2	10.3	9.9
	240 cm	9.1	9.1	9.1	9.1	9.1
	230 cm	8.4	9.3	9.3	9.5	9.1
	220 cm	7.8	7.6	8.5	8.9	8.2
	210 cm	7.1	8.1	8.4	7.6	7.8
	200 cm	5.8	5.5	6.1	5.8	5.8
	190 cm	2.8	3.7	2.6	3.1	3.1
	180 cm	0.8	1.3	0.9	1.3	1.1
	170 cm	0.5	0.4	0.3	0.6	0.5
	160 cm	0.1	0.1	0.1	0.2	0.1
	150 cm	0.1	0.1	0.1	0.1	0.1
Nov. 1th, 2017 272V31 Right and middle (B)	300 cm	11.0	10.2	10.6	9.9	10.4
	290 cm	10.2	10.9	11.2	11.6	11.0
	280 cm	10.7	10.3	10.9	10.6	10.6
	270 cm	10.9	10.6	9.6	9.6	10.2
	260 cm	9.8	9.7	9.9	8.8	9.6
	250 cm	9.9	10.5	9.6	10.5	10.1
	240 cm	9.5	9.2	9.0	9.9	9.4
	230 cm	9.0	8.2	10.1	9.6	9.2
	220 cm	7.8	8.8	8.2	9.7	8.6
	210 cm	8.6	8.7	7.9	8.2	8.3
	200 cm	7.0	5.8	6.3	5.7	6.2
	190 cm	3.0	2.5	2.2	2.7	2.6
	180 cm	1.1	1.2	1.1	1.1	1.1
	170 cm	0.4	0.5	0.6	0.3	0.5
	160 cm	0.1	0.1	0.1	0.2	0.1
	150 cm	0.1	0.1	0.1	0.0	0.1

(3) Neutron generation amount comparison in HAW tank

To evaluate the amount of neutron generation in each HAW, composition analysis of each HAW tank was conducted according to the same procedure as used for V35 in chapter 2-2. *Table 3- 19* shows the calculated amounts of neutron generation by analysis and by using ORIGEN. *Table 3- 20* lists the volume of each HAW tank.

Based on these results, the amount of neutrons generated in V31 is of same order as that in V33, although the volume of V31 is half that of V33. The amount of neutrons generated in V34 is of the same order as that in V35. The amounts of neutrons generated in V31 and V33 are those generated in V34 and V35.

Table 3- 19 *Estimation of amount of neutrons generated in each tank*

Tank	Calculation by analytical value		Neutron count rate (^{244}Cm) calculated by ORIGEN [n/s]
	Radioactivity of Cm [Bq]	Neutron count rate [n/s]	
V31	—	—	3.31E+09
V33	1.13E+15	4.02E+09	3.52E+09
V34	2.37E+15	8.42E+09	6.68E+09
V35	3.00E+15	1.07E+10	7.60E+09

Table 3- 20 *Volume of each HAW tank*

Tank	Volume as of sampling [m^3]
V31	38.7
V33	70.9
V34	79.5
V35	75.5

(4) Summary

① We confirmed that the neutron count rates depend on the quantity of neutron generated from the HAW solution.

② The neutron count rate can be applied for monitoring because we could measure the neutron count rate with changing contents in each tank.

③ It is necessary to confirm the correlation with the target nuclide, Pu, to apply the method to source

monitoring because we found that neutrons are generated primarily from Cm.

④ We compared the neutron numbers of ^{244}Cm calculated using ORIGEN code with the values measured in each tank, then 272V34 was -12%, 272V33 was +8%, 272V31 was -2% as for measurement values based on 272V35 values calculated using ORIGEN code.

⑤ Therefore, the quantity of neutrons generated from ^{244}Cm and the ratio of the neutron count rates were constant. Then, we suppose that the neutron count rate is can be applied to Pu monitoring. However, in future, we must evaluate the quantity of neutrons generated from Am and the (α, n) reaction by simulation to confirm the difference between the ORIGEN code values and the measured values, and it would be necessary to evaluate the applicability of neutron count rate to Pu monitoring by performing MCNP simulation.

⑥ The neutron count rates were not affected by the measurement point until ID 300 cm. Therefore, it is possible to install plural detectors under the same radiation environment on different routes as back-up detectors. In addition, we will confirm the reliability of measurement data because multiple identical data can be obtained.

A-6-2. Relationship of measurement time and error

(1) Measurement

We confirmed the dispersion of data at arbitrary measurement times at the maximum neutron count rate point (*Figure 3- 133*). The dispersion as utilized as the standard to set measurement time and to evaluate errors in the data.

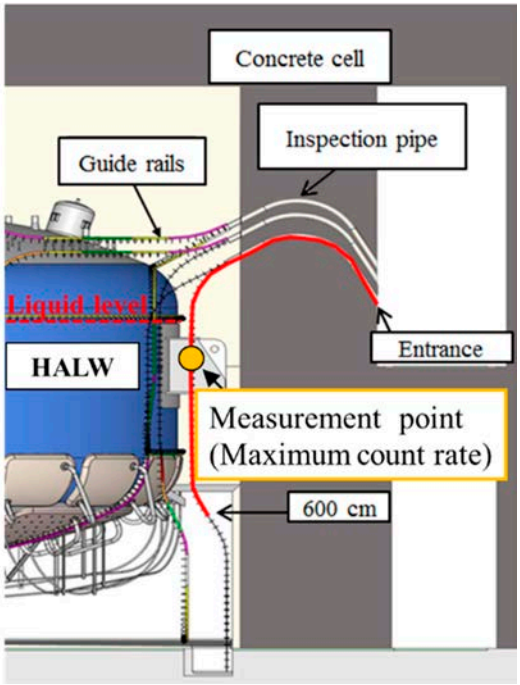

Figure 3- 133 *Measurement point*

【Conditions】

- Tank: 272V35
- Rails: Left lower inspection pipe (Route Y)
- Measurement points: Maximum neutron count rate point (ID 480 cm)
- High voltage: 1,250 V
- Measurement device: B-10 detector, Shift register (JSR-15)
- Measurement time: 1 s, 30 s, 60 s, 300 s, and 600 s
- Data recording: 10 times in every instance of measurement (Only in the case of 600 s, it was five times)
- Evaluation using average

(2) Results and consideration

Figure 3- 134 and *Table 3- 21* show the evaluation results of measurement error.

We confirmed that the measured values varied depending on the measurement time. In the case of 1-s measurement, we confirmed that the dispersion increased by about 15%. In the case of 30-s neutron count rate measurement, the dispersion was about 2%, and in the case of 10-min measurement, we confirmed that it was less than 1%. The dispersion decreased as the measurement time increased. However, it is necessary to set the measurement time depending on the objective dispersion for efficient measurement. In addition, it is necessary to set the measurement time depending on the neutron count rate because it changes at the each measurement point (it was approximately 35 cps in this examination).

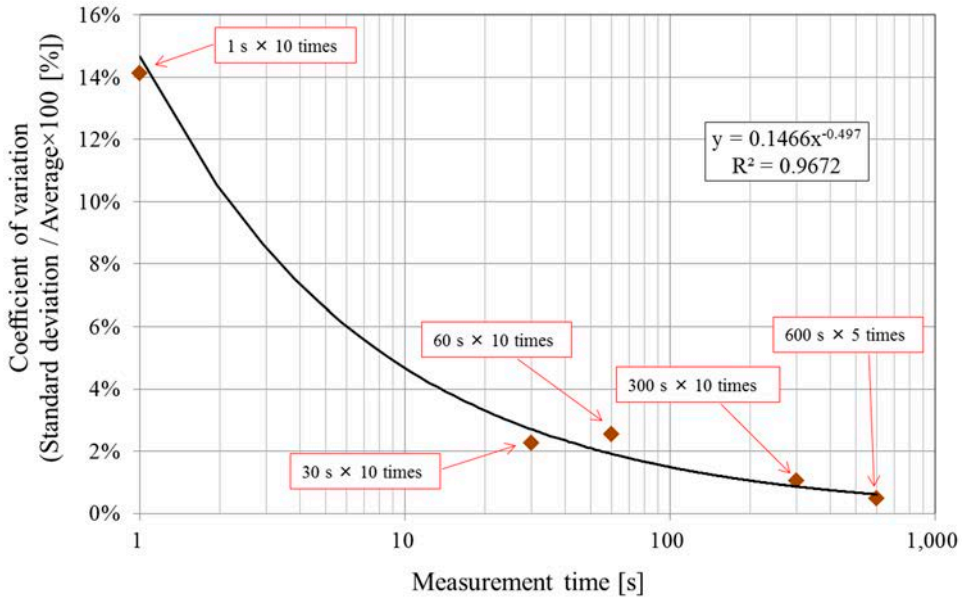

Figure 3- 134 *Relationship between measurement time and variation*

Table 3- 21 *Measurement results of neutron count rate*

Measurement number	Measurement time (s)				
	1	30	60	300	600
1	26	1,014	2,009	10,191	20,048
2	33	1,032	1,984	10,119	20,152
3	31	1,009	1,983	10,195	20,213
4	30	1,023	2,107	10,076	20,048
5	33	1,034	2,024	9,964	19,908
6	42	973	2,106	10,143	-
7	29	1,011	2,040	10,102	-
8	32	972	1,953	9,878	-
9	34	1,046	2,055	9,952	-
10	24	1,036	1,950	9,926	-
Average	31.4	1,015	2,021	10,055	20,074
Standard deviation	4.4	22.9	51.1	104.2	95.1
Coefficient of variation	14.1%	2.3%	2.5%	1.0%	0.5%

A-6-3. Neutron count rate monitoring

(1) Measurement

By using the same method as that for gamma-ray dose rate monitoring, we confirmed the relationships between the neutron count rate and various liquid levels. *Figure 3- 135* shows a schematic drawing of the measurement. We selected two measurement positions as representative points in the concrete cell.

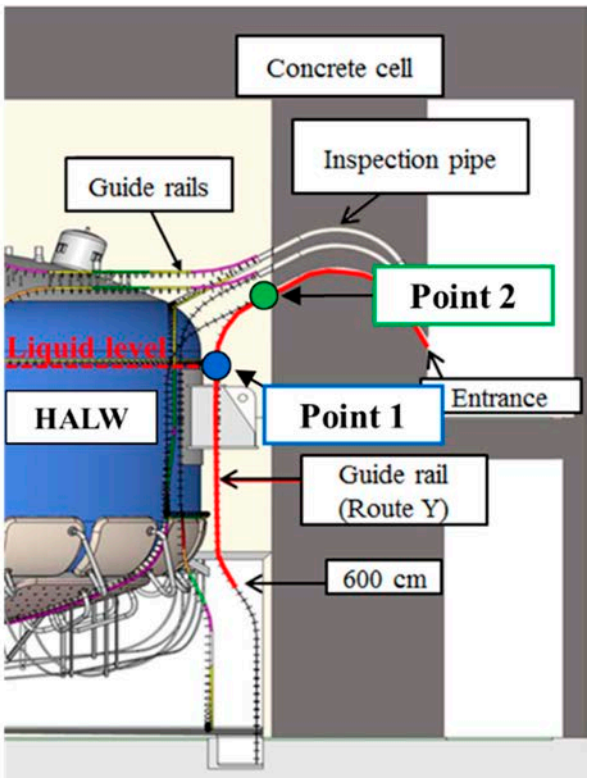

Figure 3- 135 *Schematic drawing of neutron count rate monitoring*

【Conditions】

- Tank: 272V35
- Rail: Left lower inspection pipe (Route Y)
- Measurement points: ID 250 cm (concrete cell entrance), 390 cm (around liquid level)
- High voltage: 1,250 V
- Measurement device: B-10 detector, Shift register (JSR-15)
- Measurement time: 60 min
- Data recording: at intervals of 1 s (continuous)

(2) Results and consideration

Figure 3- 136 and *Figure 3- 137* show the effect of changing source figure due to pulsation on the neutron count rate. Even if the surface fluctuated by pulsation, the neutron count rate remained approximately 30 cps at point 1 and 20 cps at point 2. There was no correlation between surface fluctuation and neutron count rate, irrespective of the measurement point. The difference in neutron count rate was a function of the difference in the measurement positions for the source. There was no correlation with surface fluctuation, but the radioactivity level remained constant. Even if the source shape changes, we can monitor the source quantity. About the applicability of the evaluation to Pu

monitoring, it will be necessary to confirm the change in neutron count rate with changes in the level of radioactivity and transport of Pu solution.

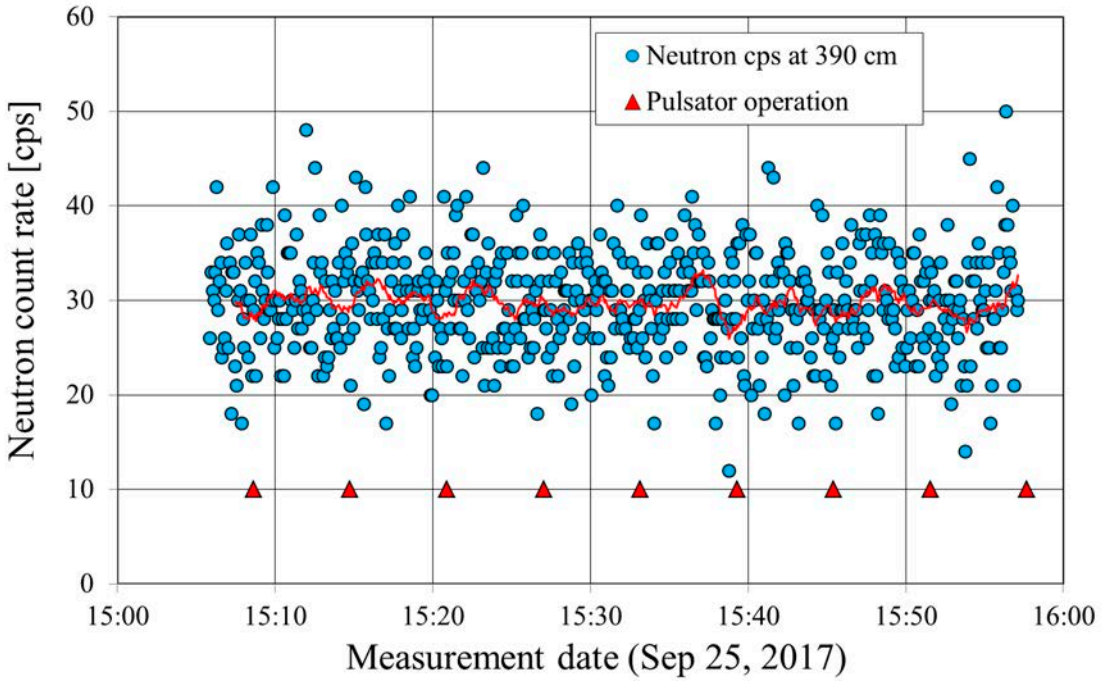

Figure 3- 136 *Neutron count rate monitoring (Point 1: ID 390 cm)*

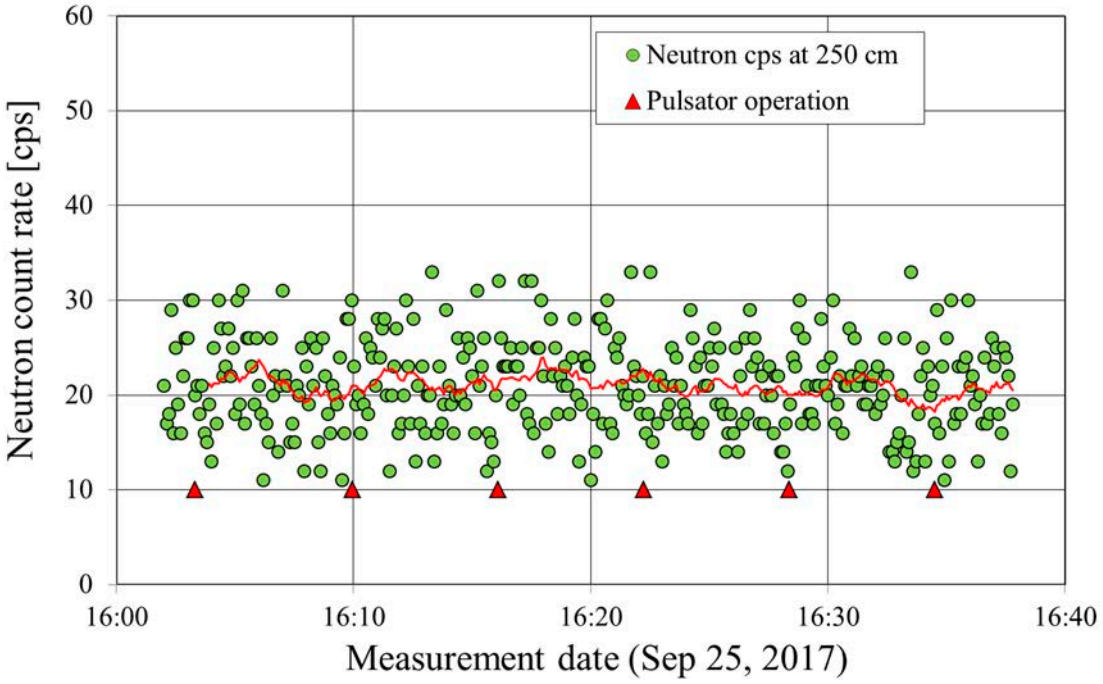

Figure 3- 137 *Neutron count rate monitoring (Point 2: ID 250 cm)*

A-7. Comparison with model of MCNP simulation

The neutron radiation emitted from the HALW tank and detected using the B-10 neutron detector was simulated with MCNP at 39 different axial positions along the height of the HALW tank. The MCNP simulations were compared to the actual experimental measurements in order to validate the MCNP model. Notably, the B-10 tube was not modeled explicitly in MCNP. Instead, the neutron flux entering the detector gas was tallied to improve statistics and save computational time. As a result, the simulated neutron rate was corrected using a constant correction factor to account for the lower efficiency of the B-10 neutron detector. *Figure 3- 138* shows a picture of the holder and the neutron detector modeled in MCNP.

Figure 3- 138 *Picture of holder and neutron detector modeled using MCNP*

Experimental measurements were performed at many axial positions along the height of the HALW tank. The holder with the neutron detector was simulated using MCNP at 39 axial positions. The comparison of the MCNP-simulated neutron rate to experimental measurements is shown in *Figure 3-139*. Based on these results, we obtained very good agreement between the MCNP simulations and neutron measurements. Moreover, the neutron measurements recorded on different days were consistent.

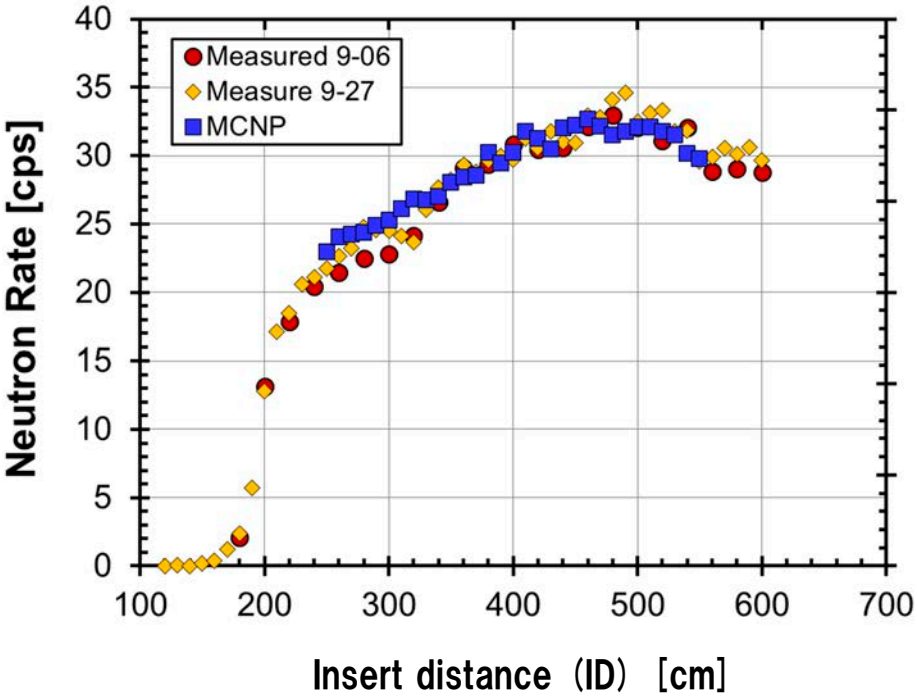

Figure 3- 139 *Comparison of MCNP-simulated neutron rate to experimental measurements*

A-8. Summary

(1) We established a neutron count rate measurement system for high-radiation areas that operators cannot enter.

(2) The measured neutron count rates reflected the effect of distance between the B-10 proportional counter and source and the attenuation effect of the pipe supports in the concrete cell. Accordingly, we obtained a minute neutron count rate distribution with a slight dispersion of approximately 2% (in case of 30-s measurement). These data are valid for comparison with simulation and optimization of the model.

(3) There was the correlation with the quantity of neutron (Cm) about the influence to neutron count rate by difference of solution composition. We confirmed that the neutron count rate corresponded to the quantity of neutrons.

(4) We confirmed the possibility of application to source intensity monitoring because the change in neutron count rate against source shape in the tank was constant, even when the source shape changed.

3-2-3. Feasibility evaluation for application of Pu monitoring using neutron measurements

A. Applicability of neutron count rate in concrete cell to Pu monitoring

A-1. Outline

We measured neutron count rate data by inserting a detector up to various distances inside the

concrete cell. By using the measured data, we analyzed the correlation between the measured neutron count rate and ratio of neutrons produced estimated by sampling analysis in each HALW tanks and evaluated the applicability of neutron count rate to Pu monitoring.

A-2. Nuclides for generating neutron

Table 3- 22 shows the sampling analysis results obtained in each HALW tank. The analysis was based on an evaluation of neutron generation from a representative sample of dissolved sludge in solution taken from each tank.

Table 3- 22 *Analysis results of tanks*

Analytical item	Date	2/7/2017	12/12/2017		2/8/2017	12/11/2017
	Tank	272V35	272V35*1		272V34	272V33
Acid conc. (mol/L)		2.34	2.63	-	2.24	1.73
Density (g/cm^3)		1.249	1.239	-	1.191	1.252
Cm conc. (Bq/mL)		4.10E+07	3.70E+07	4.00E+07	3.00E+07	1.60E+07
Pu conc. (mg/L)		356	326	326	250	110
U conc. (g/L)		6.65	6.46	-	5.18	2.74
^{241}Am (Bq/mL)*2		6.90E+07	7.20E+07	-	1.00E+08	5.50E+07

*1 twice implementations, *2 Undissolved

Based to these analysis results, we could identify the source that generated neutrons as Cm, Pu, U, and Am. We evaluated the neutron incidence of these nuclides by using the HALW volume of each tank and the spontaneous fission neutron incidence of each nuclide. *Table 3- 23* shows the neutron incidence of each main nuclide generating neutrons. Especially, neutron generation in the concrete cell was mostly caused by spontaneous fission from ^{244}Cm (approximately 99.9% in each tank).

Table 3- 23 *Neutron incidence of each main nuclide generating neutrons*

Nuclides	Date	2/7/2017	12/12/2017		12/11/2017	2/8/2017
	Tank	272V35	272V35		272V33	272V34
	Spontaneous fission neutron incidence [n/s/g]	Neutron incidence [n/s] (generation ratio)				
^{234}U	5.03E-3	6.87E+3 (0.00%)	6.59E+3 (0.00%)	— (0.00%)	2.60E+3 (0.00%)	5.49E+3 (0.00%)
^{235}U	2.99E-4					
^{236}U	5.49E-3					
^{238}U	1.36E-2					
^{238}Pu	2.59E+3	1.17E+7 (0.10%)	1.03E+7 (0.10%)	1.03E+7 (0.10%)	3.21E+6 (0.08%)	8.36E+6 (0.10%)
^{239}Pu	2.18E-2					
^{240}Pu	1.02E+3					
^{241}Pu	5.00E-2					
^{242}Pu	1.72E+3					
^{243}Cm	-	1.12E+10	9.98E+9	1.08E+10	4.02E+9	8.42E+9
^{244}Cm	1.08E+7	(99.90%)	(99.90%)	(99.90%)	(99.92%)	(99.90%)
^{241}Am	1.18E+0	4.94E+4 (0.00%)	5.09E+4 (0.00%)	— (—%)	3.62E+4 (0.00%)	7.35E+4 (0.00%)

A-3. Neutron incidence and neutron count rates inside concrete cell

We evaluated the correlation between neutron incidence and neutron count rate inside the concrete cell. *Figure 3- 140* shows a plot of the results measured in 3-2-2 (A-6) and the theoretical neutron count rate calculated based on the neutron incidence ratio.

$$y = \frac{Analytical\ result\ of\ Vn\ tank}{Analytical\ result\ of\ V35\ tank} \times Measured\ neutron\ conut\ rate\ of\ V35$$

(n = 33 or 34)

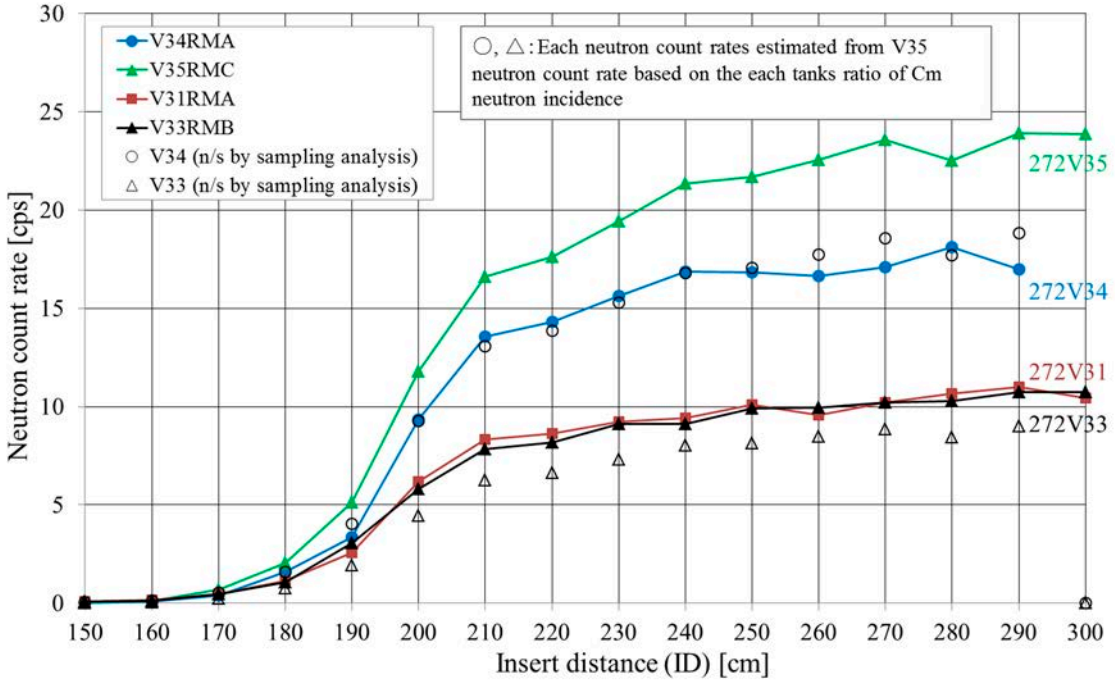

Figure 3- 140 *Comparison of neutron count rate distribution for each tank*

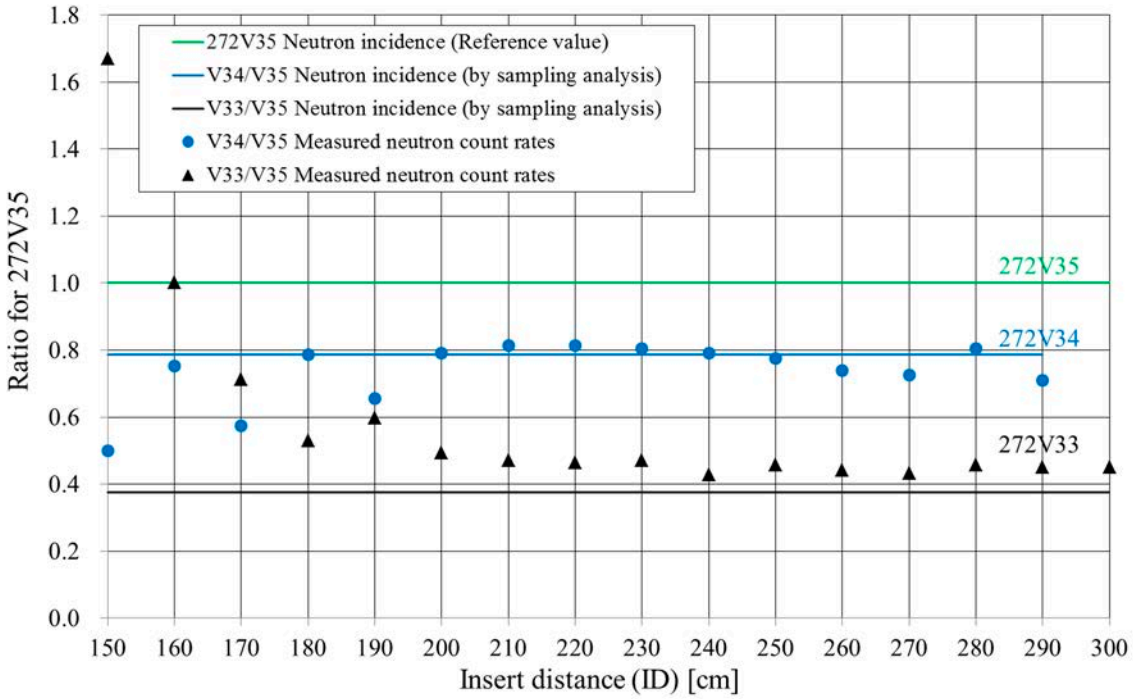

Figure 3- 141 *Ratio distributions of each tank against that of 272V35*

Figure 3- 141 shows a comparison between neutron incidence and neutron count rate based on 272V35. The measured neutron count rates of 272V34 agreed with the ratio of Cm neutron incidence evaluated by sampling analysis. Additionally, we confirmed that the case of the 272V33 tank showed good agreement in the range of less than 10%. (no sampling data are available for 272V31 tank, so it was not included in this analysis.)

According to *Figure 3- 141*, correlation of Cm quantity and neutron count rate agree well in range of less than approximately 10%. Because the error increased given the low count rate until 190 cm, we understood that effective measurement points were located beyond 200 cm, and the neutron count rate was stable.

A-4. Evaluation for Pu monitoring

We confirmed the correlation of neutron count rate and neutron incidence derived from Cm in the concrete cell, which indicated the possibility of Pu monitoring based on the neutron count rate. Therefore, we evaluated the possibility of Pu quantitation from Cm based on the results of sampling analysis.

A-4-1. Correlation of Cm and Pu

We investigated the Cm/Pu ratio obtained by sampling analysis results to consider quantitation of Pu by using the Cm/Pu ratio in the HALW tanks. *Table 3- 24* and *Figure 3- 142* shows the results of this analysis. To this end, we used the analysis data obtained considering dissolved sludge to assume neutron incidence of the entire HALW.

Table 3- 24 *Neutron incidence of Cm and Pu*

Date		2/7/2017	12/12/2017		12/11/2017	2/8/2017
Tanks		V35	V35*1		V33	V34
Nuclide	Item					
Cm	Bq/mL	4.10E+7	3.70E+7	4.00E+7	1.60E+7	3.00E+7
	Bq	3.15E+15	2.81E+15	3.04E+15	1.13E+15	2.37E+15
	n/s	1.12E+10	9.98E+9	1.08E+10	4.02E+9	8.42E+9
Pu	mg/L	356	326	326	110	250
	n/s	1.17E+7	1.03E+7	1.03E+7	3.21E+6	8.36E+6

*1 twice implementations

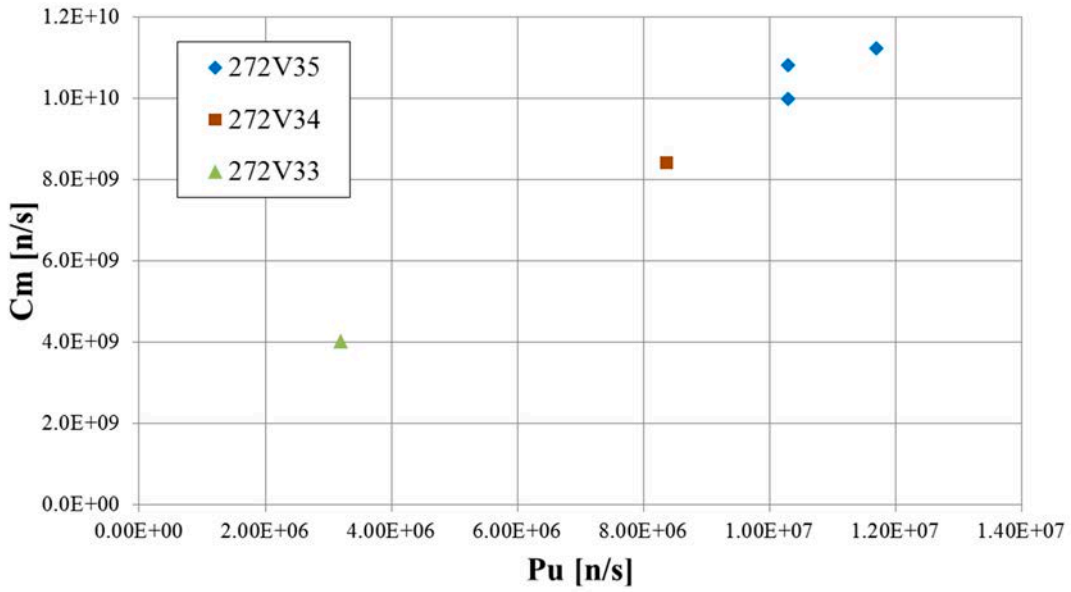

Figure 3- 142 *Correlation of Cm with Pu (Neutron incidence)*

We confirmed the correlation between Cm neutron incidence and Pu neutron incidence from *Figure 3- 142*. However, the neutron value of ^{244}Cm was 1000 times higher than that of Pu (see *Table 3- 24*).

A-4-2. Quantity of Cm and neutron incidence

We could measure the neutron count rate depending on the quantity of Cm by comparing the neutron count rate distribution in each HALW. Therefore, we considered that it is possible to monitor the quantity of Cm.

Figure 3- 143 shows the relationship between Cm neutron incidence and the neutron count rate at each measurement point. The neutron incidence was evaluated using the results of sampling analysis. We evaluated the relationship between the neutron count rate and the Cm neutron incidence for three different HALWs with different quantities of Cm.

As a result, we confirmed the (linear) correlation between the measured value and the difference in neutron count rate.

We suggest that given the large gap in neutron count rate against changes in Cm quantity at ID 290 cm, this point is useful from the viewpoint of monitoring for continuous measurement.

In addition, although the plots in *Figure 3- 142* seem to be linear, they do not reach zero. Therefore, we must collect additional HALW analytical results to validate the correlation.

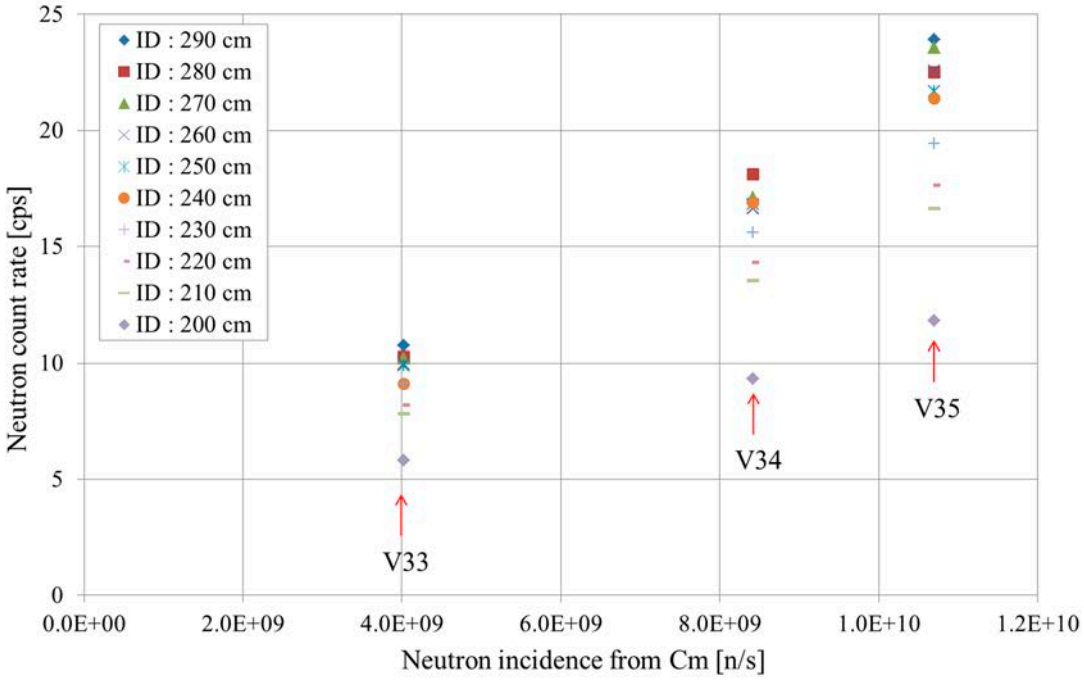

Figure 3- 143 *Relation between Cm neutron incidence and neutron count rate at measurement points.*

A-4-3. Evaluation of applicability to Pu monitoring

We confirmed

(1) the correlation between neutron incidence by Cm and the measured neutron count rate, and

(2) the correlation between Cm quantity and Pu quantity.

Then, we could perform Pu quantitation by using the neutron count rate. Additionally, we confirmed the possibility of application of neutron count rate to Pu monitoring because it changed with the quantity of Cm.

A-5. Lesson and learn

A-5-1. Quantification

We suggest a good possibility of Pu quantification from analytical and measurement data. However, a few errors, for example, sampling error, analytical error in analytical processes, and neutron count rate measurement errors, affect final value greatly. Therefore, reduction of these errors is very important to improve accuracy and precision.

A-5-2. Sampling error

Regarding sampling analysis, the data considering dissolved sludge were used. A considerable amount of Pu is transferred to sludge. If the sludge is not distributed uniformly, the sampling error

would be high. Then, the evaluated quantities of Cm and Pu will include large errors. Therefore, the sampling method must be homogeneous.

In addition, the Input Accounting Tank (IAT) contains a small quantity of sludge that is relatively homogeneous. Therefore, we evaluated the sampling error of liquid waste in IAT, and it was found to be effective for confirming the influence of homogeneity on the analysis.

A-5-3. Accumulation of measurement data

Neutron count rate data of the other HALWs are necessary to improve the accuracy and precision of Pu quantitation and Pu monitoring. In addition, verification of neutron count rates with changes in the quantity of HALW is necessary.

B. Quantification of Pu with MCNP

To investigate the sensitivity of the neutron count rate to different Pu masses, four different tank levels were simulated in MCNP. The tank level with H = 52 cm is the actual tank level for V35, which corresponds to the HALW volume provided by JAEA. This tank level was used for comparison with experimental measurements at different axial positions, as discussed in the previous section. For all tank levels, the Pu concentration was maintained constant at 0.326 g/L, and the Pu/Cm ratio was maintained constant at 26.4. *Figure 3- 144* shows a picture of the different HALW tank levels simulated with MCNP.

Tank Level [cm]	HALW Volume [L]	HALW Mass [g]	Neutron Yield [n/s]
104	9.29E+04	1.15E+08	3.50E+07
52	7.52E+04	9.28E+07	2.83E+07
2	5.82E+04	7.18E+07	2.19E+07
-54	3.91E+04	4.82E+07	1.47E+07

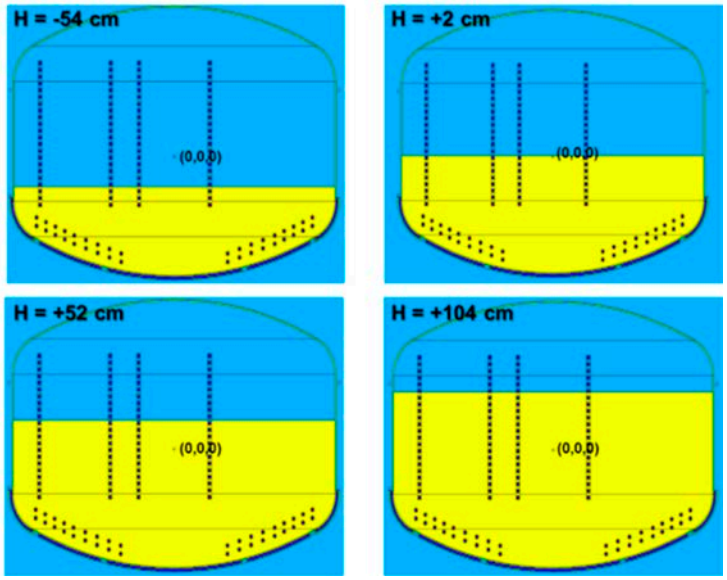

Figure 3- 144 *Different HALW tank levels simulated with MCNP*

Plots of the MCNP-simulated neutron rate versus the axial ID along the guide rail of the HALW tank are shown in *Figure 3- 145*(a). These plots show that the neutron profile as a function of axial position becomes flatter as the tank level decreases. *Figure 3- 145*(b) shows the simulated neutron rate versus Pu mass for each tank level. Based on these results, the neutron count rate decreases linearly with Pu mass (and tank level) for a constant Pu/Cm ratio and a constant Pu concentration in the HALW.

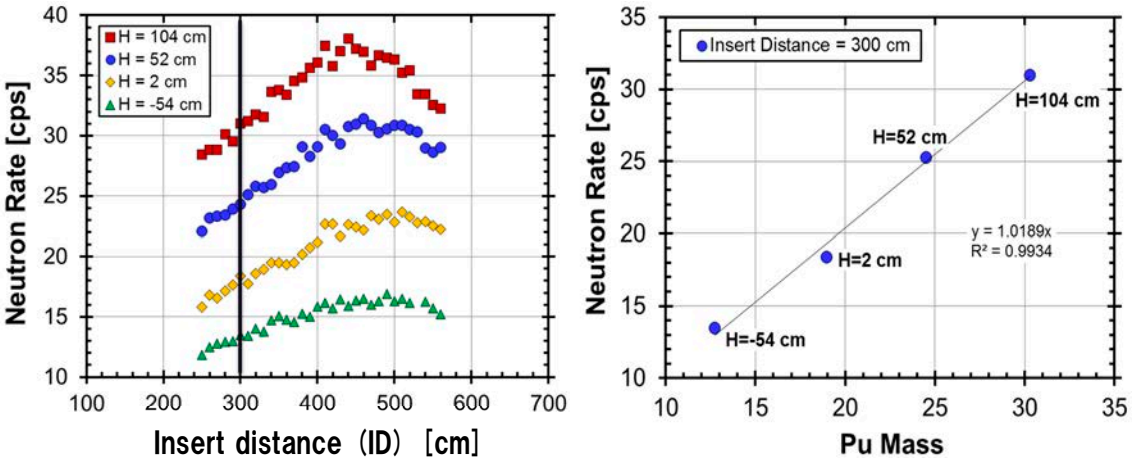

Figure 3- 145 *(a) Simulated neutron rate versus axial ID along HALW tank, and (b) simulated neutron rate versus Pu mass for each tank level*

To investigate sensitivity to changes in the Pu concentration and the Pu/Cm ratio in the HALW tank, four different TRU concentrations and four different concentrations of Cm only (constant TRU) were simulated with MCNP by employing a constant tank level of 52 cm and ID of 300 cm. The different TRU and Cm concentrations were obtained by decreasing these concentrations by 25%, 50%, and 75% relative to the original values provided by JAEA for V35. *Figure 3- 146*(a) shows the simulated neutron rate versus the Pu concentration, and *Figure 3- 146*(b) shows the neutron rate versus the Pu/Cm ratio. Based on the results shown in (a), the neutron rate decreases linearly with decreasing Pu concentration, with a y-intercept of zero. However, when changing only the amount of Cm in the HALW and maintaining the Pu concentration constant, the neutron rate decreases as a power function with increasing Pu/Cm ratio.

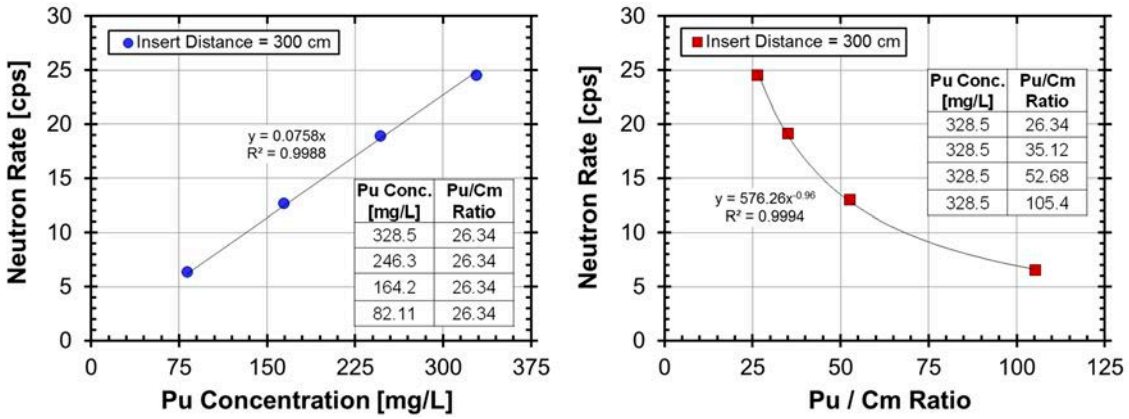

Figure 3- 146 *(a) Simulated neutron rate versus Pu concentration, and (b) simulated neutron rate versus Pu/Cm ratio*

MCNP simulations were performed by varying both the Pu/Cm ratio and the Pu concentration to simulate the different HALW compositions of V33 and V35. *Figure 3- 147* shows the simulated neutron rate versus Pu concentration for two different Pu/Cm ratios representative of the HALW in tanks V35 and V33. These results show that there are two different slopes for the different Pu/Cm ratios. Thus, different calibration curves will likely be required for different tanks with different Pu/Cm ratios.

Figure 3- 148 shows the simulated neutron rate versus Pu concentration when only Pu is varied, and the Cm concentration is kept constant. Based on these results, the simulated neutron rate barely changes over a broad range of Pu concentrations when the Cm concentration is kept constant. This is expected because Cm is the primary source of neutrons and, thus, dominates the neutron signal recorded by the detector.

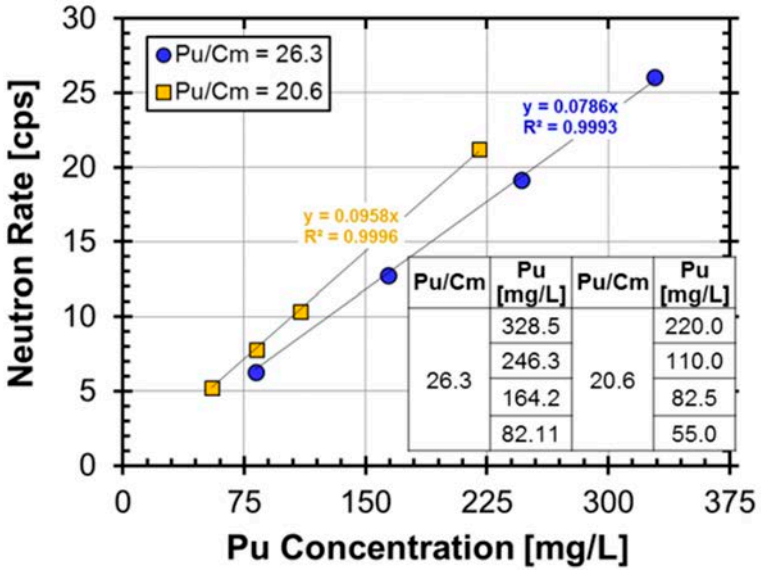

Pu/Cm	Pu [mg/L]	Pu/Cm	Pu [mg/L]
26.3	328.5	20.6	220.0
	246.3		110.0
	164.2		82.5
	82.11		55.0

Figure 3- 147 *Simulated neutron rate versus Pu concentration for two different Pu/Cm ratios*

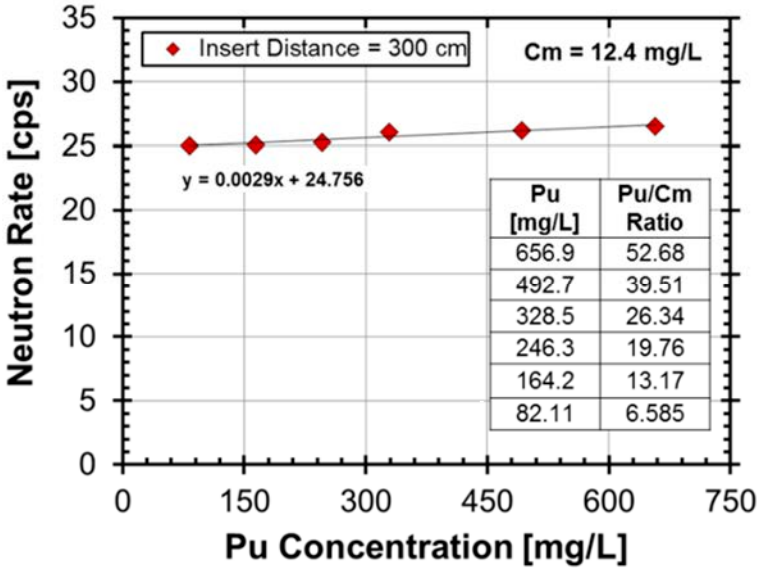

Pu [mg/L]	Pu/Cm Ratio
656.9	52.68
492.7	39.51
328.5	26.34
246.3	19.76
164.2	13.17
82.11	6.585

Figure 3- 148 *Simulated neutron rate versus Pu concentration when only Pu concentration is varied and the Cm concentration is kept constant*

We performed MCNP simulations of the neutron flux emitted from the V35 HALW tank and that detected by the B-10 holder at different axial positions along the tank height. A comparison of these MCNP simulations with the actual experimental measurements showed very good agreement, and the comparison results were used to validate the MCNP model. MCNP simulations were performed to investigate the sensitivity of the neutron measurements to different parameters (e.g., tank level, varying Pu or Cm concentration). The results showed the neutron rate varied linearly with Pu mass (by varying tank level) for fixed Pu concentration and Pu/Cm ratio, and varying the Cm content alone

to change the Pu/Cm ratio led to a decrease in the neutron rate as a power function of the increase in the Pu/Cm ratio. Notably, numerous variables can be simulated in MCNP with the validated model of the HALW tank, such as HALW density, HNO_3 concentration, tank level, Pu concentration, and Cm concentration, any of these variables can be changed simultaneously. However, the quality of the MCNP simulation results is only as good as the quality of the input information. A few variables are difficult to measure (e.g., Cm concentration) and may include large measurement errors. Furthermore, the concentrations of U, Pu, and Cm are measured from samples taken from the HALW tanks, which may have a relatively high measurement error because of the sludge at the bottom of the tank and the difficulty in obtaining a representative sample. A better understanding of these uncertainties, specifically the uncertainty in Cm concentration measurement, is needed to better assess the feasibility of using MCNP simulations to support neutron monitoring measurements of HALW tanks in general.

4. Applicability of Pu monitoring techniques and future prospects

Through this technology development of MCNP simulations and neutron/gamma-ray radiation measurements, we evaluated the applicability of Pu monitoring technologies and proposed how to use them to improve monitoring at reprocessing facilities.

According to results of MCNP simulation with changing liquid level, the effective measurement location to set the neutron detector was considered, and ID 420 cm was found to be the best location to monitor neutrons with the B-10 detector (it is applicable from ID 290 to ID 500 cm as well) because of the wider gaps between each of the sets of simulation results at the same ID, as shown in *Figure 4-1*.

Moreover, we would like to suggest that the best location to monitor gamma rays by using the B-10 or IC detectors is ID of approximately 420 cm (applicable from ID 390 to ID 450 cm) because of the wider gaps between each of the sets of simulation results at the same ID, as shown in *Figure 4- 1*. The developed B-10 detector could measure not only neutron counts but also the count rate of gamma rays. To reduce dead time for scintillator, pin hole collimator can be suggested.

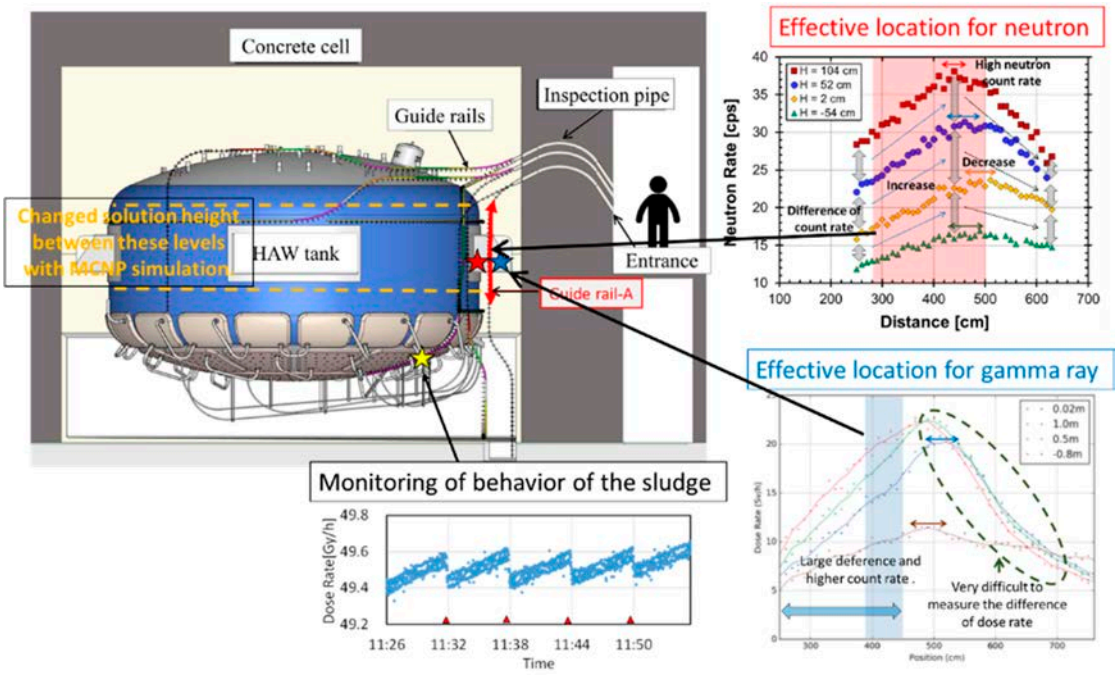

Figure 4- 1 *Suggested detector location for Pu monitoring*

Additionally, we would like to suggest setting the IC at the tank bottom to monitor sludge behavior during pulsation and transfer of HALW to the next process (Vitrification). This technique can potentially be used for facility decommissioning and safety.

5. Conclusion

LLNL, LANL, and JAEA completed all planned activities for the feasibility study of Pu monitoring. Very good experiences and valuable data were gained in the process. Though it was very challenging, we could confirm the applicability and capability of Pu monitoring to enhance reprocessing facilities that handle Pu with FPs via a feasibility study, as follows:

(1) Detector design and measurement of high radiation dose

- Test of mock-up simulating real guides are expected to help with actual measurements
- Several useful and informative techniques to design detectors were developed
- These results helped create a very reliable MCNP model.

(2) Establishment of detailed MCNP model and implementation of MCNP simulations

- Good consistency among source, model, and measurement with the MCNP model was confirmed.
- We believe that the reliable model developed herein will facilitate feasible Pu measurement and monitoring.

(3) Pu monitoring capability (Quantitative Assay)

- We confirmed the possibility of quantitative assay for Pu with FPs by MCNP simulations in a feasibility study.
- Neutron count rates decreased as the Pu concentration decreased.
- The relationship between detector location and neutron count rates was confirmed.
- Neutron count rates were proportional to a function of the analytical value of Cm.
- Gamma spectrum usage is a future challenge.

(4) Pu monitoring capability

- Possibility of quantitative assay was reflected in Pu monitoring capability as well.
- Measurement results obtained using IC highlighted a few Pu monitoring capabilities to show operational status in terms of pulsation, including sludge movement.
  These results highlight the feasibility of the Pu monitoring technology as well as its use as a decommissioning technique. (Meets safeguards requirements, maintains transparency in Pu handling)

By performing this R&D, we expected the following outcomes:

- Technology can contribute to enhancement of reprocessing safeguards and improvement of transparency.

- Remote monitoring could reduce the inspection activities required. Destructive assay (DA) for inventory/radioactive waste verification might be reduced as well. In addition, sample reduction for inventory verification might be reduced.
- This technology can be extended to monitor cleanup operations of decommissioned facilities, including Fukushima NPPs.
- This technology can be used to detect security events (unauthorized movement and sabotage).

We identified subjects to establish this technology as a safeguard device, as follows:

- Demonstration work with uncertainty evaluation, including calibration (sampling and analysis) by using a prototype detector is necessary.
- Demonstration should be conducted in the IAT or extraction cycle (higher Pu concentration than that of HALW) of reprocessing facility.
- State of health monitoring and maintenance ability should be considered.

Acknowledgments

We would like to acknowledge the Ministry of Education, Culture, Sports, Science and Technology (MEXT) of the Japanese government and the Department of Energy National Nuclear Security Administration's Office of Non-proliferation and Arms Control for supporting this work. We also would like to acknowledge the FRS at Nuclear science research institute, analysis section of Tokai reprocessing plant and CAD team at Nuclear Fuel Cycle Engineering Laboratories of JAEA and QST.

References

[1] IAEA, "IAEA Department of Safeguards Long-Term R&D Plan, 2012-2023," STR-375, Vienna, 2013.

[2] H. Nakamura, et al., "Development and future challenge for Advanced Solution Measurement and Monitoring System (ASMS)," 52nd INMM Annual Meeting Proceedings, Palm Desert, California, July 17-21, 2011, Institute of Nuclear Materials Management (2011).

[3] M. Sekine et al., "Feasibility study of advanced technology for Pu with FP solution monitoring - Overview of Research Plan and Modelling for Simulation-", ESARDA 39th Annual Meeting, EUR-28795-EN, pp788-796, (2007).

[4] J.M. Verbake, C. Hangmann, D. Wright, "Simulation of Neutron and Gamma Ray Emission from Fission," UCRL-AR-228518, Lawrence Livermore National Laboratory (2010).

[5] S. Nakamura et al., "Development of the Measurement Technique for Nuclear Data with Prompt Gamma-Ray Spectroscopy" Saokuru kiko Giho, No.16, (2002), pp.117-124.

[6] T. Goorley, et al., "Initial MCNP6 Release Overview", Nuclear Technology, 180, pp. 298-315, 2012.

[7] T. Sato, K. Niita, N. Matsuda, et al., “Particle and Heavy Ion Transport Code System PHITS, Version 2.52,” J. Nucl. Sci. Technol. 50:9, pp. 913-923 (2013).

[8] M. Newell, “Safeguards Technology Factsheet Unattended Dual Current Monitor (UDCM),” NA-241 SG Tech Fact Sheet, LA-UR-16-22490, 2016.

[9] H. Heito. et al., “Technical data on electron beam and γ-ray irradiation facilities; Electron accelerator and ^{60}Co irradiation facility,” JAEA-Technology 2008-071, 2008, 29p.（in Japanese）.

[10] RJ McConn Jr, et al., Radiation Portal Monitor Project, “Compendium of Material Composition Data for Radiation Transport Modeling”, PIET-43741-TM-943, PNNL-15870, 2011

国際単位系（SI）

表１．SI 基本単位

基本量	SI 基本単位	
	名称	記号
長さ	メートル	m
質量	キログラム	kg
時間	秒	s
電流	アンペア	A
熱力学温度	ケルビン	K
物質量	モル	mol
光度	カンデラ	cd

表２．基本単位を用いて表されるSI組立単位の例

組立量	SI 組立単位	
	名称	記号
面積	平方メートル	m^2
体積	立方メートル	m^3
速さ，速度	メートル毎秒	m/s
加速度	メートル毎秒毎秒	m/s^2
波数	毎メートル	m^{-1}
密度，質量密度	キログラム毎立方メートル	kg/m^3
面積密度	キログラム毎平方メートル	kg/m^2
比体積	立方メートル毎キログラム	m^3/kg
電流密度	アンペア毎平方メートル	A/m^2
磁界の強さ	アンペア毎メートル	A/m
量濃度(a)，濃度	モル毎立方メートル	mol/m^3
質量濃度	キログラム毎立方メートル	kg/m^3
輝度	カンデラ毎平方メートル	cd/m^2
屈折率(b)	（数字の） 1	1
比透磁率(b)	（数字の） 1	1

(a) 量濃度（amount concentration）は臨床化学の分野では物質濃度（substance concentration）ともよばれる。
(b) これらは無次元量あるいは次元１をもつ量であるが、そのことを表す単位記号である数字の１は通常は表記しない。

表３．固有の名称と記号で表されるSI組立単位

組立量	SI 組立単位			
	名称	記号	他のSI単位による表し方	SI基本単位による表し方
平面角	ラジアン(b)	rad	1 (b)	m/m
立体角	ステラジアン(b)	sr(c)	1 (b)	m^2/m^2
周波数	ヘルツ(d)	Hz		s^{-1}
力	ニュートン	N		$m\ kg\ s^{-2}$
圧力，応力	パスカル	Pa	N/m^2	$m^{-1}\ kg\ s^{-2}$
エネルギー，仕事，熱量	ジュール	J	N m	$m^2\ kg\ s^{-2}$
仕事率，工率，放射束	ワット	W	J/s	$m^2\ kg\ s^{-3}$
電荷，電気量	クーロン	C		s A
電位差（電圧），起電力	ボルト	V	W/A	$m^2\ kg\ s^{-3}\ A^{-1}$
静電容量	ファラド	F	C/V	$m^{-2}\ kg^{-1}\ s^4\ A^2$
電気抵抗	オーム	Ω	V/A	$m^2\ kg\ s^{-3}\ A^{-2}$
コンダクタンス	ジーメンス	S	A/V	$m^{-2}\ kg^{-1}\ s^3\ A^2$
磁束	ウエーバ	Wb	Vs	$m^2\ kg\ s^{-2}\ A^{-1}$
磁束密度	テスラ	T	Wb/m^2	$kg\ s^{-2}\ A^{-1}$
インダクタンス	ヘンリー	H	Wb/A	$m^2\ kg\ s^{-2}\ A^{-2}$
セルシウス温度	セルシウス度(e)	℃		K
光束	ルーメン	lm	cd sr(c)	cd
照度	ルクス	lx	lm/m^2	m^{-2} cd
放射性核種の放射能(f)	ベクレル(d)	Bq		s^{-1}
吸収線量，比エネルギー分与，カーマ	グレイ	Gy	J/kg	$m^2\ s^{-2}$
線量当量，周辺線量当量，方向性線量当量，個人線量当量	シーベルト(g)	Sv	J/kg	$m^2\ s^{-2}$
酸素活性	カタール	kat		s^{-1} mol

(a)SI接頭語は固有の名称と記号を持つ組立単位と組み合わせても使用できる。しかし接頭語を付した単位はもはやコヒーレントではない。
(b)ラジアンとステラジアンは数字の１に対する単位の特別な名称で、量についての情報をつたえるために使われる。実際には、使用する時には記号radおよびsrが用いられるが、習慣として組立単位としての記号である数字の１は明示されない。
(c)測光学ではステラジアンという名称と記号srを単位の表し方の中に、そのまま維持している。
(d)ヘルツは周期現象についてのみ、ベクレルは放射性核種の統計的過程についてのみ使用される。
(e)セルシウス度はケルビンの特別な名称で、セルシウス温度を表すために使用される。セルシウス度とケルビンの単位の大きさは同一である。したがって、温度差や温度間隔を表す数値はどちらの単位で表しても同じである。
(f)放射性核種の放射能（activity referred to a radionuclide）は、しばしば誤った用語で"radioactivity"と記される。
(g)単位シーベルト（PV,2002,70,205）についてはCIPM勧告2（CI-2002）を参照。

表４．単位の中に固有の名称と記号を含むSI組立単位の例

組立量	SI 組立単位		
	名称	記号	SI 基本単位による表し方
粘度	パスカル秒	Pa s	$m^{-1}\ kg\ s^{-1}$
力のモーメント	ニュートンメートル	N m	$m^2\ kg\ s^{-2}$
表面張力	ニュートン毎メートル	N/m	$kg\ s^{-2}$
角速度	ラジアン毎秒	rad/s	$m\ m^{-1}\ s^{-1}=s^{-1}$
角加速度	ラジアン毎秒毎秒	rad/s^2	$m\ m^{-1}\ s^{-2}=s^{-2}$
熱流密度，放射照度	ワット毎平方メートル	W/m^2	$kg\ s^{-3}$
熱容量，エントロピー	ジュール毎ケルビン	J/K	$m^2\ kg\ s^{-2}\ K^{-1}$
比熱容量，比エントロピー	ジュール毎キログラム毎ケルビン	J/(kg K)	$m^2\ s^{-2}\ K^{-1}$
比エネルギー	ジュール毎キログラム	J/kg	$m^2\ s^{-2}$
熱伝導率	ワット毎メートル毎ケルビン	W/(m K)	$m\ kg\ s^{-3}\ K^{-1}$
体積エネルギー	ジュール毎立方メートル	J/m^3	$m^{-1}\ kg\ s^{-2}$
電界の強さ	ボルト毎メートル	V/m	$m\ kg\ s^{-3}\ A^{-1}$
電荷密度	クーロン毎立方メートル	C/m^3	m^{-3} s A
表面電荷	クーロン毎平方メートル	C/m^2	m^{-2} s A
電束密度，電気変位	クーロン毎平方メートル	C/m^2	m^{-2} s A
誘電率	ファラド毎メートル	F/m	$m^{-3}\ kg^{-1}\ s^4\ A^2$
透磁率	ヘンリー毎メートル	H/m	$m\ kg\ s^{-2}\ A^{-2}$
モルエネルギー	ジュール毎モル	J/mol	$m^2\ kg\ s^{-2}\ mol^{-1}$
モルエントロピー，モル熱容量	ジュール毎モル毎ケルビン	J/(mol K)	$m^2\ kg\ s^{-2}\ K^{-1}\ mol^{-1}$
照射線量（X線及びγ線）	クーロン毎キログラム	C/kg	kg^{-1} s A
吸収線量率	グレイ毎秒	Gy/s	$m^2\ s^{-3}$
放射強度	ワット毎ステラジアン	W/sr	$m^4\ m^{-2}\ kg\ s^{-3}=m^2\ kg\ s^{-3}$
放射輝度	ワット毎平方メートル毎ステラジアン	$W/(m^2\ sr)$	$m^2\ m^{-2}\ kg\ s^{-3}=kg\ s^{-3}$
酵素活性濃度	カタール毎立方メートル	kat/m^3	$m^{-3}\ s^{-1}$ mol

表５．SI 接頭語

乗数	名称	記号	乗数	名称	記号
10^{24}	ヨタ	Y	10^{-1}	デシ	d
10^{21}	ゼタ	Z	10^{-2}	センチ	c
10^{18}	エクサ	E	10^{-3}	ミリ	m
10^{15}	ペタ	P	10^{-6}	マイクロ	μ
10^{12}	テラ	T	10^{-9}	ナノ	n
10^9	ギガ	G	10^{-12}	ピコ	p
10^6	メガ	M	10^{-15}	フェムト	f
10^3	キロ	k	10^{-18}	アト	a
10^2	ヘクト	h	10^{-21}	ゼプト	z
10^1	デカ	da	10^{-24}	ヨクト	y

表６．SIに属さないが、SIと併用される単位

名称	記号	SI 単位による値
分	min	1 min=60 s
時	h	1 h =60 min=3600 s
日	d	1 d=24 h=86 400 s
度	°	1°=(π/180) rad
分	’	1’=(1/60)°=(π/10 800) rad
秒	”	1”=(1/60)’=(π/648 000) rad
ヘクタール	ha	1 ha=1 $hm^2=10^4m^2$
リットル	L, l	1 L=1 l=1 $dm^3=10^3cm^3=10^{-3}m^3$
トン	t	1 t=10^3 kg

表７．SIに属さないが、SIと併用される単位で、SI単位で表される数値が実験的に得られるもの

名称	記号	SI 単位で表される数値
電子ボルト	eV	1 eV=1.602 176 53(14)×10^{-19}J
ダルトン	Da	1 Da=1.660 538 86(28)×10^{-27}kg
統一原子質量単位	u	1 u=1 Da
天文単位	ua	1 ua=1.495 978 706 91(6)×10^{11}m

表８．SIに属さないが、SIと併用されるその他の単位

名称	記号	SI 単位で表される数値
バール	bar	1 bar=0.1MPa=100 kPa=10^5Pa
水銀柱ミリメートル	mmHg	1 mmHg≈133.322Pa
オングストローム	Å	1 Å=0.1nm=100pm=10^{-10}m
海里	M	1 M=1852m
バーン	b	1 b=100fm^2=$(10^{-12}cm)^2$=$10^{-28}m^2$
ノット	kn	1 kn=(1852/3600)m/s
ネーパ	Np	SI単位との数値的な関係は、対数量の定義に依存。
ベル	B	
デシベル	dB	

表９．固有の名称をもつCGS組立単位

名称	記号	SI 単位で表される数値
エルグ	erg	1 erg=10^{-7} J
ダイン	dyn	1 dyn=10^{-5}N
ポアズ	P	1 P=1 dyn s cm^{-2}=0.1Pa s
ストークス	St	1 St =1$cm^2\ s^{-1}$=$10^{-4}m^2\ s^{-1}$
スチルブ	sb	1 sb =1cd cm^{-2}=10^4cd m^{-2}
フォト	ph	1 ph=1cd sr cm^{-2} =10^4lx
ガル	Gal	1 Gal =1cm s^{-2}=$10^{-2}ms^{-2}$
マクスウエル	Mx	1 Mx = 1G cm^2=10^{-8}Wb
ガウス	G	1 G =1Mx cm^{-2} =10^{-4}T
エルステッド(a)	Oe	1 Oe ≙ $(10^3/4\pi)$A m^{-1}

(a) ３元系のCGS単位系とSIでは直接比較できないため、等号「 ≙ 」は対応関係を示すものである。

表10．SIに属さないその他の単位の例

名称	記号	SI 単位で表される数値
キュリー	Ci	1 Ci=3.7×10^{10}Bq
レントゲン	R	1 R = 2.58×10^{-4}C/kg
ラド	rad	1 rad=1cGy=10^{-2}Gy
レム	rem	1 rem=1 cSv=10^{-2}Sv
ガンマ	γ	1 γ=1 nT=10^{-9}T
フェルミ		1 フェルミ=1 fm=10^{-15}m
メートル系カラット		1 メートル系カラット= 0.2 g = 2×10^{-4}kg
トル	Torr	1 Torr = (101 325/760) Pa
標準大気圧	atm	1 atm = 101 325 Pa
カロリー	cal	1 cal=4.1858J（「15℃」カロリー），4.1868J（「IT」カロリー），4.184J（「熱化学」カロリー）
ミクロン	μ	1 μ =1μm=10^{-6}m

（第8版，2006年）